

Understanding the Mechanism of Mn Emission in Quantum Dots in the Quest to Design New Materials for Optoelectronic Applications

A Thesis

Submitted for the Degree of

Doctor of Philosophy

In the Faculty of Science

by

Pradeep K R



New Chemistry Unit
Jawaharlal Nehru Centre for Advanced Scientific Research
(A Deemed University)
Bangalore – 560064

November 2020

*Dedicated to my
Parents & Wife*

DECLARATION

I hereby declare that the matter embodied in this thesis entitled “**Understanding the Mechanism of Mn Emission in Quantum Dots in the Quest to Design New Materials for Optoelectronic Applications**” is the result of the research carried out by me at the New Chemistry Unit, Jawaharlal Nehru Centre for Advanced Scientific Research, Bangalore, India, under the supervision of Prof. Ranjani Viswanatha and it has not been submitted elsewhere for the award of any degree or diploma.

In keeping with the general practices of reporting scientific observation, due acknowledgements have been made whenever the work described is based on the findings of other investigators. Any omission which might have occurred by oversight or error in judgement is regretted.

Bangalore

.....
Pradeep K R

CERTIFICATE

I hereby certify that the matter embodied in this thesis entitled “**Understanding the Mechanism of Mn Emission in Quantum Dots in the Quest to Design New Materials for Optoelectronic Applications**” has been carried out by Mr. Pradeep K R at the New Chemistry Unit, Jawaharlal Nehru Centre for Advanced Scientific Research, Bangalore, India under my supervision and that has not been submitted elsewhere for the award of any degree or diploma.

Bangalore

Prof. Ranjani Viswanatha

(Research Supervisor)

ACKNOWLEDGEMENTS

First and foremost, I would like to express my sincere gratitude to my advisor Prof. Ranjani Viswanatha for enormous freedom, constant motivation and excellent guidance throughout my Ph.D. I am extremely fortunate to have her as my advisor, who gave me the freedom to explore on my own, and at the same time monitored my progress with patience and offered constructive criticism to recover when my steps faltered. I am thankful to her for giving me an opportunity to work under her guidance.

I would like to thank Prof. C. N. R. Rao for being a constant source of inspiration throughout my PhD life. Contagious enthusiasm and vision of Prof. Rao for science has motivated me at various times. I also convey my heartfelt gratitude to him for excellent experimental resources he has provided for our department.

I would like to thank Jawaharlal Nehru Centre for Advanced Scientific Research, Bangalore for my scholarship. I thank Department of Science and Technology (DST), International Centre for Materials Science (ICMS), SSL (Sheikh Saqr Laboratory), DST, JNCASR for Funding in different scientific aspects.

I would also like to thank Prof. Chandrabhas Narayana (JNCASR), Prof. Shobhana Narasimhan (JNCASR), Prof. Umesh Waghmare (JNCASR), Prof. Guilio Cerullo (Politecnico di Milano, Italy) and Dr. Wolfgang Caliebi (Petra III, DESY, Hamburg, DE) for fruitful scientific collaborations and insightful discussions. I have been greatly benefited from their expertise, and learned a lot in the process.

I would like to thank all my Ph.D. course instructors, Prof. Umesh Waghmare, Prof. Ranjani Viswanatha, Prof. A. Sundaresan, Prof. K S Narayan and Prof. S M Shivaprasad for their instructive and enjoyable courses, and stimulating scientific interactions. I would like to thank Dr. Indumati Rao for arranging the student mentorship program.

I owe my sincere thanks to my present and past lab mates Mahima, Payel, Saptarshi, Prasenjit, Gauttam, Suhas, Murthy, Avijit, Kushagra, Amita, Anur, Subhashri, Adarsh, Gautam, Angira, Sowmeya, for their wonderful company and scientific discussions. I also thank all the visiting students, Nilesh, Savithri, Rishir, and Abinaya who worked with me.

I thank all the technical staff of JNCASR, especially, Mr. Anil, Kannan, Melisa, Mr. Peer, Mr. Mune Gowda and Mr. Dileep.

I extend my sincere thanks to the entire Academic and Administrative staff of JNCASR for their efficiency and helpfulness. Special thanks are due to the members of computer laboratory and library.

I would also like to thank the Hostel staff, Mess workers and Canteen staffs and Raju for keeping me well fed. I would also like to thank Garden Staff, Security staff and Electrical Staff for give me such a nice environment in my daily life here.

I thank all my friends in JNCASR Divya, Prem, Priyanka, Shivaram, Ravi, Rajendra, Manaswee, Sashi, Vybhav, Swati, Anusha, Usha, Malay, Deepak, Ganesh, Ashutosh, AdMa, Pawan and Manjeet. I would also like to thank all my 2015 batchmates in JNCASR for their support throughout.

I extend my sincere gratitude to my teachers Prof. P R Lalitha, Prof. G T Bhandage, Dr. J M Raj and Nageshwara Rao.

Last, but not the least, my parents and my wife for their unending support and encouragement during my up and downs. They have always believed in me, and never tied me down in any of my endeavors. I would like to thank my wife Abharana for her constant support in my academic and non-academic affairs.

Finally, I express my sincere gratitude to all those who helped me directly or indirectly.

Pradeep K R

Preface

Nanoscale materials have been investigated extensively for optoelectronic applications. Transition metal doping adds additional advantage in designing quantum dots (QDs) for various optoelectronic applications. In the era that is driven by quest for energy efficiency, understanding of the photo physics is very essential. In this thesis, we study the mechanism of Mn excitation and emission in II-VI semiconductor QDs and perovskite QDs.

Chapter 1 provides an overview of the existing literature about the opportunities and challenges of quantum dots for various optoelectronic applications. II-VI semiconductor QDs and perovskite QDs have shown great promise for optoelectronic applications like, photovoltaics, light emitting diodes, display and lasing. Due to large stokes shift minimizing the self-absorption, Mn doping have been explored extensively for lighting. Several challenges and opportunities related to Mn emission is discussed in this chapter.

Chapter 2 describes several synthesis methodologies used in this thesis to obtain Mn doped II-VI semiconductor QDs and perovskite QDs. This chapter also discusses the principles of various advanced techniques used to study the dopant host interactions like gated photoluminescence (PL), low temperature PL, transient absorption spectroscopy (TA), extended x-ray absorption fine structure (EXAFS) various other characterization techniques and their experimental details.

Part 1 elaborates the mechanism of Mn Emission in II-VI Semiconductor Quantum Dots. The mechanism of an intense emission from a spin and orbital forbidden transition in Mn (${}^4T_1 \rightarrow {}^6A_1$) have remained elusive for over two decades. The debate and the various proofs in favour of the energy transfer and charge transfer mechanisms are discussed in Chapter 3 and transient species mediated energy transfer in Mn doped II-VI semiconductor QDs is discussed in Chapter 4.

Chapter 3 focuses on energy transfer and charge transfer mechanism leading to Mn emission in II-VI semiconductor QDs. Here in this chapter, we provide a detailed overview

of the two mechanisms, bringing together the experiments in favour and against the two mechanisms to understand the origin of this excitation and emission. This chapter provides a fundamental overview of a problem that has remained elusive for several decades even though it has been extensively studied.

Chapter 4 involves the study of Mn excitation mechanism in II-VI semiconductor QDs. Based on various optical characterization techniques like gated excitation and emission with temperature dependent photoluminescence and ultrafast spectroscopy, this chapter provides a timeline of Mn excitation and emission process in II-VI semiconductor nanocrystals as well as an identification of the various transient species consistent with the selection rules.

Part 2 discusses Mn doping in Perovskite Quantum Dots for Harvesting Delayed Fluorescence. Metal halide perovskite QDs have emerged as promising contenders for next generation low cost high efficiency optoelectronic materials. Chapter 5 and 6 discusses about the structural aspects and doping in perovskites to enhance the functionalities of perovskite QDs for lighting. The last three chapters discuss about the mechanism of Mn emission and harvesting delayed fluorescence through vibrational coupling and the effect host bandgap on the dopant host interactions.

Chapter 5 provides an overview about the structural aspects of mixed halide perovskite QDs. In-depth understanding in the structure of perovskite QDs is essential to have a control on commonly faced issues like anion migration and light induced phase segregation. This chapter looks at the mixed halide perovskite QDs from various length scales using x-ray crystallography, Raman spectroscopy and EXAFS to study the structure property relations which will lead to best use of these QDs with minimal losses.

Chapter 6 discusses about the successes and challenges in doping perovskite QDs. Direct hot injection synthesis used for successful incorporation of dopants and various steps involved in purification and stabilizing doped QDs are extensively discussed in this chapter. This chapter also sheds light on local structure analysis confirming the successful incorporation of Mn in the perovskite lattice.

Chapter 7 deals with the mechanism of dopant emission in perovskite QDs. By tuning the halide composition, the host bandgap is brought closer to Mn emission energy. Detailed

analysis on delayed emission using gated PL and low temperature PL and density functional theory unravels the drip-feeding mechanism of photoexcited carriers. This electron back transfer from Mn to the host in the Mn doped perovskite QDs through vibrational coupling is termed in this chapter as vibrationally assisted delayed fluorescence (VADF).

Chapter 8 studies the effect of composition modulation and quantum confinement in Mn doped mixed halide perovskite NCs on delayed excitonic emission. The host bandgap is tuned by composition modulation and by controlling the reaction temperature to obtain various sizes with fixed halide ion concentration. This chapter also studies the temperature dependent band edge vs Mn emission efficiencies in the gated PL which is defined by entropy of VADF by looking at the rate of change of VADF with respect to temperature. Gated PLE studies also proved that the back transfer of photoexcited electrons are assisted by state specific higher excited levels.

Chapter 9 discusses the temperature and fluence dependent carrier dynamics in Mn doped perovskite QDs. Transient absorption spectroscopy studies show that due to vibrational coupling in perovskite QDs, the excited state carrier dynamics and mechanism of Mn emission is different for perovskite QDs and II-VI semiconductor QDs. Influence of Mn as a dopant in drip-feeding the photo excited carriers back to the host through VADF is validated through ultrafast carrier dynamics in this chapter.

Chapter 10 Provides a final summary of the complete thesis and also indicates future perspectives in the topics discussed in the field of research and also their applicability towards optoelectronic devices.

Abbreviations

QDs-Quantum Dots

PCE-Power Conversion Efficiency

EQE-External Quantum Efficiency

QD-LEDs- Quantum Dot -Light Emitting Diodes

PL QY- Photoluminescence Quantum Yield

LED- Light Emitting Diode

ASE- Amplified Stimulated Emission

PL- Photoluminescence

ODE- Octadecene

OIAm- Oleylamine

TOP- Trioctylphosphine

VADF- Vibrationally Assisted Delayed Fluorescence

XRD- X-Ray Diffraction

TEM- Transmission Electron Microscopy

TA- Transient Absorption

XAFS- X-ray Absorption Fine structure

PLE- Photoluminescence Excitation

TCSPC- Time-Correlated Single Photon Counting

ICP-OES- Inductively Coupled Plasma-Optical Emission Spectroscopy

XANES -X-ray absorption near edge structure

DFT - density functional theory

Contents

Declaration	iii
Certificate.....	v
Acknowledgement	vii
Preface.....	ix
Abbreviation	xiv

1. Introduction

1.1 Abstract.....	3
1.2 Evolution of Quantum Dots for Optoelectronics	3
1.3 Synthesis of Colloidal Quantum Dots.....	4
1.4 Optical Applications	6
1.4.1 Photovoltaics.....	6
1.4.2 Quantum Dot Light Emitting Diodes (QD-LEDs).....	8
1.4.3 Quantum Dots for Display Applications.....	11
1.4.4 Quantum Dot Lasing.....	12
1.4.5 Biomedical Imaging and Drug Delivery	13
1.5 Quantum Dots: Present Status and Outlook for the Future.....	15
1.6 Present Study	16
Bibliography	18

2. Methodology

2.1 UV-VIS Absorption Spectroscopy	25
2.2 Photoluminescence Spectroscopy	26
2.2.1 Steady State PL Spectroscopy	26
2.2.2 Gated PL Spectroscopy	27
2.2.3 Time Resolved Photoluminescence (TrPL)	27
2.2.4 Temperature Dependent PL Spectroscopy.....	28
2.2.5 Temperature Dependent PL Spectroscopy.....	28
2.2.6 Jacobian Transformation.....	28
2.3 X-ray diffraction (XRD)	29

2.4 Transmission Electron Spectroscopy (TEM)	29
2.5 Inductively Coupled Plasma- Optical Emission Spectroscopy (ICP-OES)	30
2.6 Transient Absorption Spectroscopy	30
2.7 X-ray Absorption Fine Structure (XAFS) Spectroscopy	31
Bibliography	35

Part I: Mechanism of Mn Emission In II-VI Semiconductor Quantum Dots

3. Mechanism of Mn Emission: Energy Transfer or Charge Transfer?

3.1 Abstract	39
3.2 Introduction	39
3.3 Discussion	40
3.3.1 Nature of Mn Emission	40
3.3.2 Is the 582 nm Peak Really the Signature of Successful Mn emission?	51
3.4 Conclusions	53
Bibliography	55

4. Transient Species Mediated Energy Transfer in Mn Doped II-VI Semiconductor Quantum Dots

4.1 Abstract	61
4.2 Introduction	61
4.3 Experimental Methods	63
4.4 Results and Discussion	65
4.5 Conclusion	76
Bibliography	77

Part II: Mn Doped Perovskite Quantum Dots for Harvesting delayed Fluorescence

5. Understanding the Structure of Mixed Halide Perovskite Quantum Dots

5.1 Abstract	83
5.2 Introduction	83
5.3 Experimental Methods	85

5.3.1 Synthesis of CsPb(Br/Cl) ₃ perovskite quantum dots (QDs)	85
5.4 Results and Discussions	85
5.5 Conclusions	96
Bibliography	97

6. Doping in Perovskite Quantum Dots: Synthesis, Stability and Local Environment

6.1 Abstract	101
7.2 Introduction	101
6.3 Experimental Methods	104
6.3.1 Materials	104
6.3.2 Preparation of Cs-Oleate	104
6.3.3 Synthesis of Undoped and Sn-doped CsPb(Br/I) ₃ QDs	105
6.3.4 Synthesis of Mn-doped CsPb(Br/Cl) ₃ perovskite QDs	105
6.3.5 Isolation and Purification of Undoped, Sn-doped and Mn-doped QDs	105
6.4 Results and Discussion	106
6.5 Conclusion	120
Bibliography	121

7. Vibrationally Assisted Delayed Fluorescence (VADF) in Mn Doped Perovskite

Quantum Dots

7.1 Abstract	127
7.2 Introduction	127
7.3 Experimental Methods	129
7.3.1 Synthesis of Undoped and Mn doped CsPb(Br/Cl) ₃ perovskite QDs	129
7.3.2 Photoluminescence Quantum Yield	129
7.3.3 Computational Details	130
7.4 Results and Discussion	130
7.5 Conclusion	142
Bibliography	143

8. Composition Modulation vs Quantum Confinement: Effect on VADF in Mn Doped Perovskite Quantum Dots

8.1 Abstract	149
8.2 Introduction	149
8.3 Experimental Methods	151
8.3.1 Synthesis of Mn doped CsPb(Br/Cl) ₃ perovskite QDs.....	151
8.4 Results and Discussion.....	152
8.5 Conclusion.....	165
Bibliography	166

9. Temperature and Fluence Dependent Carrier Dynamics in Mn Doped Perovskite Quantum Dots

9.1 Abstract	171
9.2 Introduction	171
9.3 Experimental Methods	172
9.4 Results and Discussion.....	173
9.5 Conclusion.....	180
Bibliography	181

10. Summary

10.1 Quantum Dots for Optoelectronics.....	187
10.2 Present Study	187
10.3 Mn Doped Quantum Dots: Present Status and Outlook for the Future.....	188

List of Publications..... 191

List of Publications not Part of this Thesis 192

List of Book Chapters 192

Chapter 1

Introduction

1. Introduction

1. Introduction

1.1. Abstract

Quantum dots (QDs) are typically semiconductor crystals in the size range of 2-20 nm. Due to the quantum confinement effects arising from their small size, they exhibit composition, shape and size-dependent electrical and optical properties. These highly tunable properties have driven the research for several decades into their understanding and subsequent commercial application in several fields especially for the optoelectronic devices and photovoltaics. II-VI QDs and more recently perovskite QDs have shown great promise as tunable light absorbing and/or emitting layers in LED devices and displays, in photovoltaics and imaging. Although research in this field has led to promising results, a better understanding of important factors like robustness, stability, processability, toxicity and cost effectiveness are necessary before implementing them for commercial purposes. In this chapter, the properties of QDs, studies towards commercialization for optoelectronic applications, the recent advances and future challenges are summarized.

1.2. Evolution of Quantum Dots for Optoelectronics

Quantum dots (QDs), with their unique properties have given rise to a variety of new applications that have been very useful. These semiconductor nanoparticles have electronic properties that are significantly different from their bulk counterparts as a consequence of constrained electron and hole wavefunctions. This quantum size effect was first experimentally discovered in a study of CuCl nanocrystals whose size was varied from 2 to 31 nm¹ and has since demonstrated varied unexpected magnetic, optical and opto-electronic properties that can be traced to their sizes.^{2,3} These properties are of interest both from a fundamental perspective as well as from the perspective of many practical applications.

While the early 1990s were marked by the preparation of quantum dots starting from complicated and expensive molecular beam epitaxy⁴ to the development of colloidal synthesis,⁵ the research in the past decade has been driven by practical applications. For example, most recently, the all inorganic cesium and organic hybrid lead halide perovskite QDs have dominated the field with their high quantum yields and high photo-voltaic efficiency.⁶ In fact, the broad range of applications of QDs driven by their unique properties include functional nanomaterials for photovoltaics, light emitting diodes, backlit displays, lasers, photodetectors, sensing and bioimaging. Development in the synthesis of various type of heterostructures with an increasing complexity and integrating multiple functionalities in QDs offers new applications in the field of magnetism and spintronics. However, challenges remain in reducing

1. Introduction

the toxicity of these QDs by bringing in more green chemistry in the synthesis techniques and the quest for a stable and improved performance of devices is keeping this area active. This chapter will focus on the properties driving the various applications of QDs of II-VI semiconductors and the newly emerging perovskite QDs in the area of optical and magnetic applications. The chapter concludes with a brief discussion on challenges and future perspectives of QD devices. Though a number of interesting but more specific and specialized topics have not been addressed here, we hope that this chapter provides an introduction to the field of exciting applications of QDs.

1.3. Synthesis of Colloidal Quantum Dots

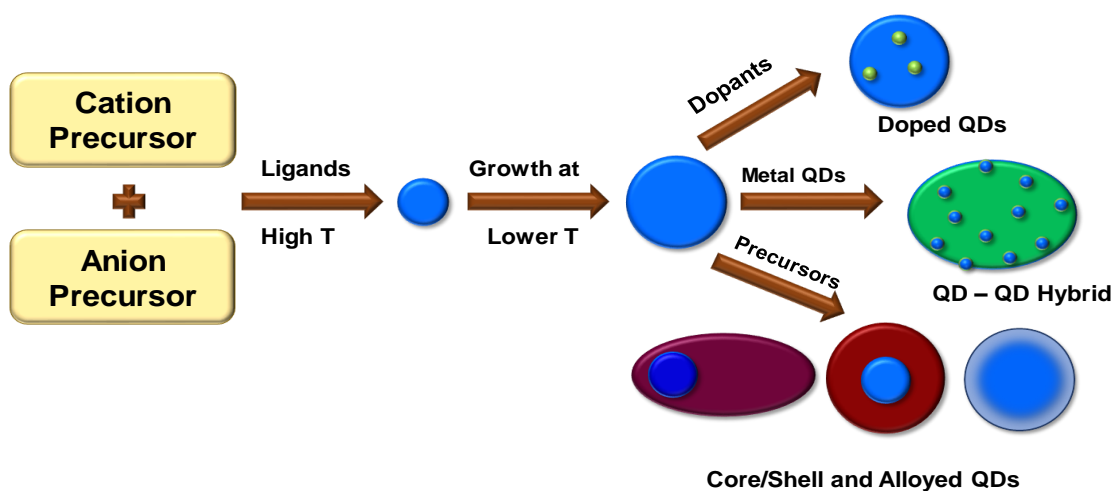


Figure 1.1 A schematic showing the synthesis of nanocrystals starting from various precursors leading to complex structures of core/shell or hybrid or doped nanocrystals.

The efficiency of applications based on colloidal QDs depends largely on the synthesis of QDs that are highly monodisperse with a narrow size distribution. Initial synthesis techniques of QDs ranged from complex, expensive methods like the molecular beam epitaxy to obtain ultrapure arrays of QDs to the solution processed micellar, hydrothermal or microwave assisted synthesis that gave rise to unstable QDs with a large size distribution. Eventually, the middle ground is stuck by the use of high temperature colloidal synthesis involving the rapid nucleation followed by the slow growth. In addition to the high quality of the sample with a good size distribution, this high temperature synthesis is also accommodative of the control over multiple reaction parameters like concentration of precursors and their reactivity, surfactants and temperature of the reaction that is useful in the synthesis of different heterostructures. A schematic showing a typical modern synthesis of colloidal QDs is shown in Figure 1.1 It is important to note here that this methodology of synthesis caters to various needs including core/shell QDs for surface passivation,^{7, 8} passivation tunability to alter the

1. Introduction

morphology and hence their optical properties as well as to dope transition metals into these QDs for magneto-optical and opto-electronic applications. The two most important parameters, namely the interface of the core/shell and the interface of the ligands with the QDs on the surface, play an important role in determining the properties of the QDs and can be accurately controlled within the high temperature synthesis route. While we discuss below the various properties driven by surface ligands, we discuss the engineering of the QD interface and their consequences on device efficiency in the later sections of this chapter.

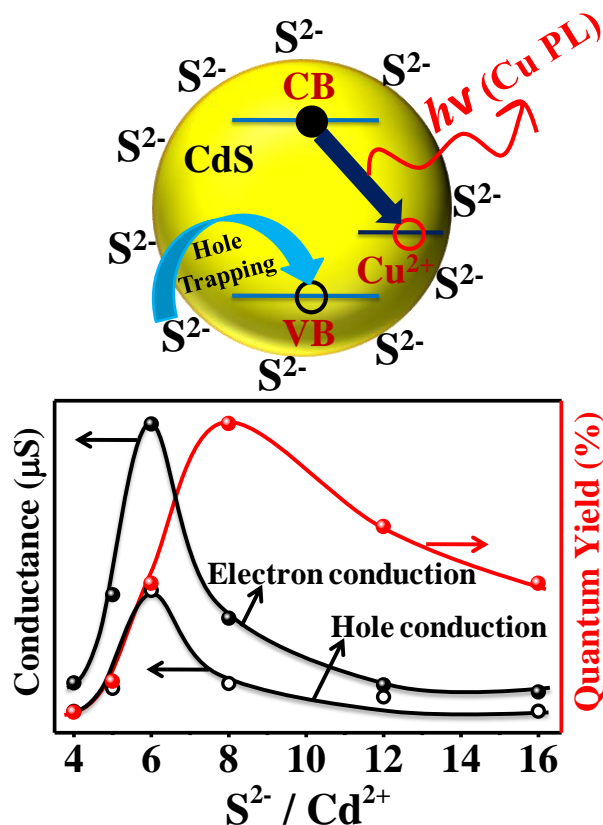


Figure 1.2 Schematic showing ligand exchanged QDs of Cu doped CdS and variation of conductance and PL quantum yield for varying S²⁻ to Cd²⁺ ratio. Reproduced with permission from Ref. ⁹. Copyright 2014 American Chemical Society.

Purification of as-synthesized QDs is also a critical step in obtaining high quality QDs as the presence of unreacted precursors or excess ligands can affect the carrier transport in devices. However, sequential precipitation and dispersion in suitable solvents can give rise to a reduced quantum yield due to the removal of ligands from the QD surface leading to trap states. Multiple purification steps can also lead to a change in the phase transformation of perovskite nanocrystals where the optically active cubic phase transforms in to an optically inactive orthorhombic phase⁶. Even though the purification of QDs after synthesis leads to complex degradation processes it is important in obtaining good performance in devices as the

1. Introduction

purification of QDs allows for obtaining good morphology by preparing pinhole free thin films.¹⁰

As synthesized QDs are typically capped with long insulating ligands (Oleic acid or Oleylamine) as these ligands are important to obtain colloiddally stable QDs. However, these long chain ligands introduce spacing between QDs which in turn lead to low density in QD films.¹¹ To obtain an improved carrier transport, ligands can be exchanged from long ligands to short as the interparticle spacing can be reduced by doing so. As shown in Figure 1.2 ligand free or sulfide capped Cu-doped CdS QDs have been synthesized to assist the transport in these QDs. These QDs are shown to be luminescent and exhibit significant conductivity.⁹ To date, the most efficient reported QD solar cell has employed a combination of partial fusing with strong passivation of the remaining surface using MPA and chloride ligands.¹² Recently high performance CsPbX₃ perovskite QD light emitting devices have been prepared via solid state ligand exchange.¹³ Similarly targeted ligand exchange chemistry on cesium lead halide perovskite QDs lead to high efficient photovoltaic devices.¹⁴

1.4. Optical Applications

Colloidal II-VI semiconductor QDs and inorganic perovskite QDs are emerging as promising materials for optoelectronic devices by virtue of their optical properties. The size and composition dependent bandgap tunability of QDs also make these materials practical for low cost, large scale devices. Here, we try to address the major advances in the area of optoelectronic applications of QDs.

1.4.1 Photovoltaics

The application of QDs in photovoltaic systems is one of the most important and promising avenues of research. The critical parameters which influence the performance of the QD photovoltaic devices are carrier mobility, doping density, trap density and diffusion length in films. The power conversion efficiency (PCE) of quantum dot photovoltaic (QD-PV) devices has increased rapidly up to 16.6 % in the past decade. The present QD-PV is currently dominated by devices based on Pb chalcogenides (PbS,¹⁵ PbSe,¹⁶ PbS_xSe_{1-x}) which exhibit a wide range of bandgap tunability in the range of NIR to visible region which is suitable for PV application. However there are reports on Cd chalcogenides QD-PV as well.¹⁷

Though QD-PV cells initially started as simple Schottky cells, heterojunction solar cells were developed to overcome the limitations of Schottky QD solar cells. A typical

1. Introduction

heterojunction solar cell consists of a highly doped n-type metal oxide in a p-n heterojunction with a p-type QD film. The typical substrate consists of a transparent base followed by a thin transparent conductive oxide layer, namely indium tin oxide (ITO). The most commonly used wide bandgap semiconductor as a n-doped junction layer is TiO_2 . The p-type QD film is coated on top of metal oxide layer and the device is coated with a back reflective contact with a deep work function metal such as gold and followed by silver or aluminum. Under this geometry, the external quantum efficiency (EQE) typically ranges between 15-25 % for a high performing device.¹⁸

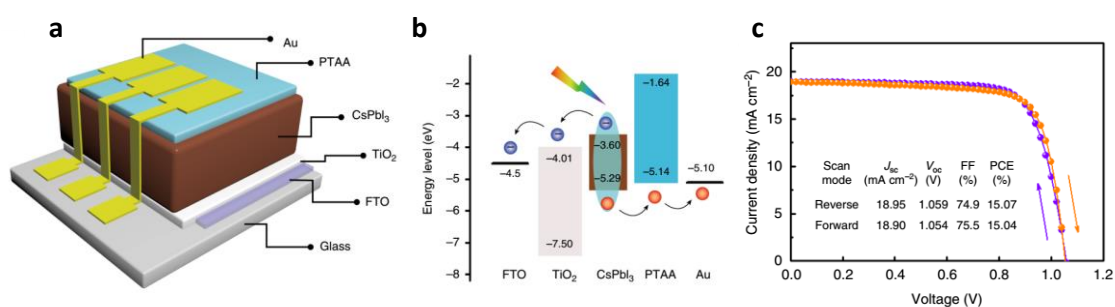


Figure 1.3 a) A schematic of a device structure and b) Energy level diagram of the CsPbI_3 PV cell. c) Current density–voltage curves of the device. Reproduced with permission from Ref.¹⁹ Copyright 2018 The Nature Publishing Group.

However, these promising results are constrained by long term stability and spectral tunability with an ideal bandgap to absorb the solar energy. Recent studies have shown that these inorganic perovskite QDs synthesized by hot injection methods are capable of performing well in the area of QD-PV.²⁰ A schematic of a typical solar cell based on perovskite QDs are shown in Figure 1.3 a) and b) respectively. Figure 1.3 c) shows the current density-voltage curve for the CsPbI_3 based device with PCE of 15.1%.¹⁹ To avoid thermal/moisture induced QDs agglomeration which is well known in perovskite QDs Wang et al. used high mobility micrometer sized graphene sheets to crosslink CsPbI_3 QDs to achieve long term stability.²¹ $\text{CsPbBr}_x\text{I}_{3-x}$ based QDs are known to show improved stability under ambient conditions compared to CsPbI_3 .²² The current record efficiency for a QD-PV is obtained by doing ligand assisted cation exchange for $\text{Cs}_{1-x}\text{FA}_x\text{PbI}_3$ QDs with photovoltaic efficiency as high as 16 % with very high photostability.²³

However, the major drawback of these materials is the toxicity of Pb that hinders these devices from commercialization. Despite, most of the first reports on quantum dot sensitized solar cells (QDSSCs) were based on Pb or Cd containing materials (CdS , CdSe , or PbS),^{24, 25}

1. Introduction

in contrast with other semiconductor solution processed photovoltaics, high performances have been attained with Pb and Cd-free materials, as CuInS_2 ,²⁶ Zn-Cu-In-S (ZCIS),²⁷ or Zn-Cu-In-Se (ZCISE).²⁷⁻²⁹ While thin-film colloidal QDs have been developed first based on PbS and PbSe QDs³⁰ and currently on lead halide perovskite QDs, with current performances $>16\%$,²³ in QDSSCs Pb and Cd-free QDs play currently a major role since most recent PCE records have been obtained with “green” QDs. TO conclude, QDSSCs are an excellent examples of the power of a focused research, starting from a concept with practically negligible photoconversion efficiency until achieve efficiencies beyond 13% in the same range as other solution-processed solar cells such as DSSCs.³¹ In summary, the performance of CsPbX_3 QD based solar cells typically have greater than 10% PCE with a large J_{sc} and V_{oc} of about 1 eV. As seen from the progress shown by all inorganic perovskite QDs based solar cells, CsPbX_3 based solar cells show promise as a strong contender for commercially available solar cells.

1.4.2 Quantum Dot Light Emitting Diodes (QD-LEDs)

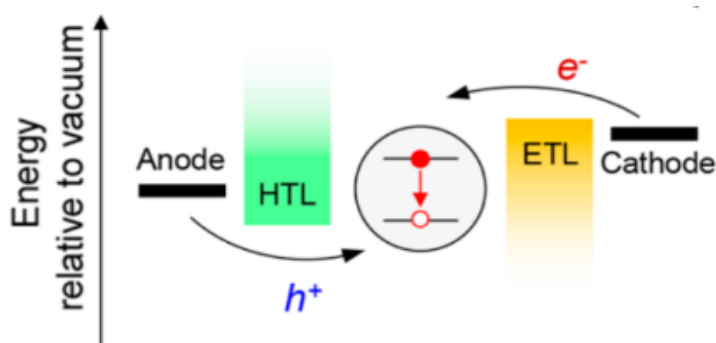


Figure 1.4 Energy level diagram for a typical QD-LED.

Electroluminescence (EL) is a phenomenon of light emission from a material excited by the electric current. When charge carriers are injected into an emissive material, like QDs through contact electrodes they recombine radiatively giving rise to EL. Similar to light emitting diodes (LEDs) QD-LEDs typically have a p-i-n structure, which comprises of an anode, a hole transporting layer, a QD active layer and an electron transport layer. Figure 1.4 shows the energy level band diagram of a typical QD-LED. Electrons from a cathode and holes from an anode are transported by the carrier transport layers and are injected to the active QD layer where they radiatively recombine.

QD-LEDs were first prepared back in 1994³² using cadmium selenide QDs. Since then, the external quantum efficiency (EQE) of QD-LEDs, defined as the ratio of the number of photons extracted from the device to the number of injected e-h pairs, has substantially

1. Introduction

improved. This is achieved by majorly focusing on high quantum yield active materials and various device architectures. The reason for low EQE devices reported in the literature is because of the low photoluminescence efficiencies (PL QY) of the QDs used as active materials.³³ Another step to improve the performance is to choose the suitable hole and electron transport materials with respect to the band alignment for smoother carrier transport.

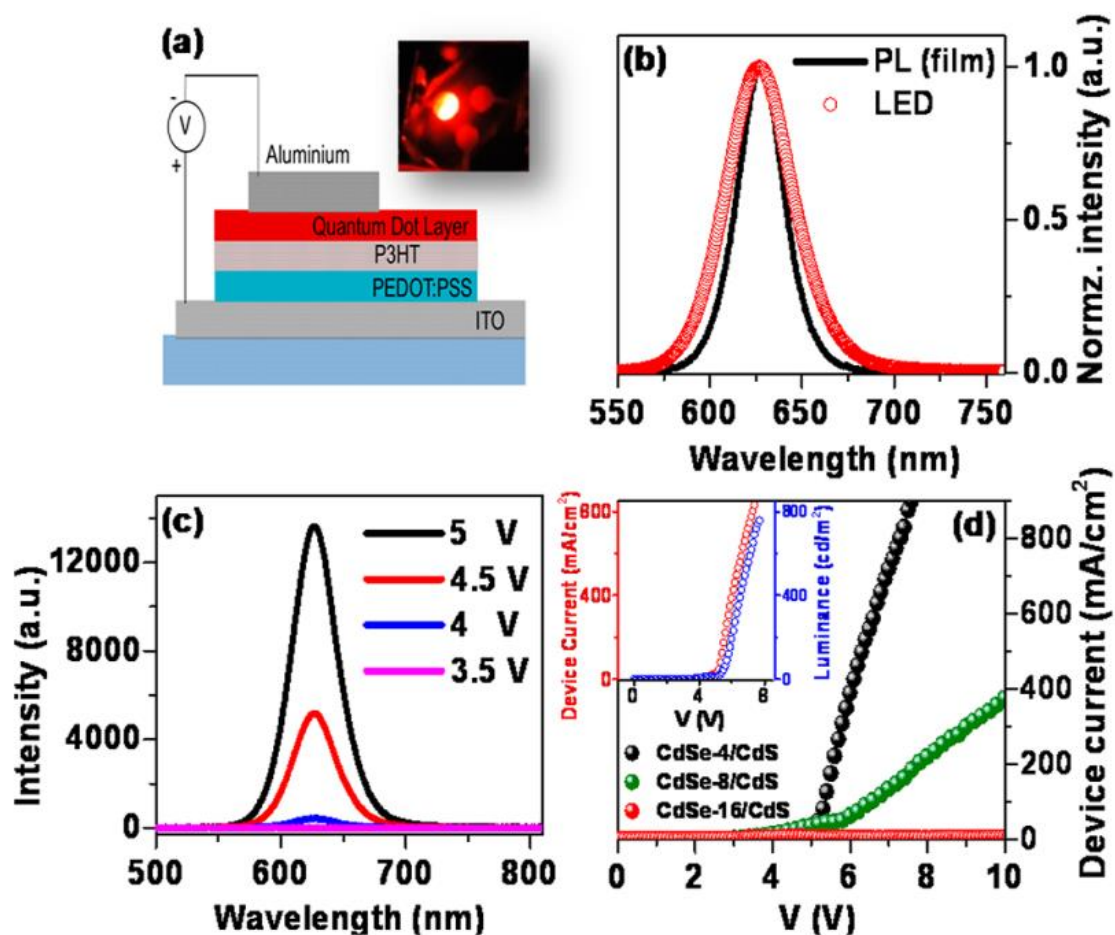


Figure 1.5 a) A schematic of the device architecture. Inset shows photograph of QD-LED. b) Spectra properties of the LED and comparison with PL. c) LED emission spectrum with various driving voltages. d) J-V characteristics of the device obtained from the QD-LEDs. Reproduced with permission from Ref. ³⁴ Copyright 2013 American Chemical Society.

Bulovic and co-workers have demonstrated QD-LEDs with an EL tunable over the entire visible spectrum by choosing different organic charge transport layers and various QDs with different bandgaps to tune the LEDs over a visible spectrum.³⁵ However, the device performance and EQE is limited by the PL QY of the active material. By carefully engineering the crystal defects, near unity QY microstructures of CdSe/CdS QDs can be synthesized

1. Introduction

demonstrating the role of interfaces in QD solids for application.³⁴ Simple unoptimized LEDs obtained from these QDs as their active layer demonstrate performances in excess of 7000 Cd/m² with a power conversion efficiency of 1.5 % lm/W. The device architecture used in the device is shown in Figure 1.5 a) This device is constructed without an electron transport layer and the hole transport layer used here is poly (3-hexyl thiophene) (P3HT). The equivalence of PL and EL indicates a common excitonic origin with the QD layer as the emission source as seen from Figure 1.5 b). As the bias voltage increases the emission intensity also increases and the emission wavelength remains unchanged as shown in Figure 1.5c). The current voltage characteristics shown in Figure 1.5 d) exhibit typical diode like features. It is also important to note here that the efficiency of the device is non-linearly proportional to the absolute PL QY emphasizing the importance of high quality QDs.

Recently all inorganic perovskite CsPbX₃ QDs have emerged as a new class of optoelectronic materials with PL QY up to 90%.⁶ Unlike hybrid organic inorganic halide perovskite materials inorganic perovskite QDs are highly stable at ambient conditions making them excellent candidates for high performance LEDs.³⁶ In 2015 Song et al.³⁷ for the first time reported CsPbX₃ QDs based LEDs with a typical device structure composed of ITO/PEDOT:PSS/PVK/CsPbX₃ QDs/TPBi/LiF/Al. Here, the CsPbX₃ QDs were synthesized through the hot-injection method discussed earlier and the bandgap is tuned by the halide composition. The luminance and EQE values were reported to be 742,946, and 528 cd/m² and 0.07%, 0.12 %, and 0.09% respectively for blue, green and orange CsPbX₃ QD-LEDs. However, besides the toxicity, one needs to consider crucial contribution from ligands to obtain high quality QD-LEDs with perovskite QDs as active layers. While a high concentration of ligands are needed for better passivation and hence high PL QY, environmental and phase stability, their presence hinders electric conductivity due to their long hydrophobic tail.³⁸ Hence it is essential to obtain optimal balance between surface passivation and charge carrier injection by the ligand density control as well as the ligand exchange by shorter ligands on CsPbX₃ QDs.³⁹ Yet another way of improving the electro/photoluminescence efficiency of perovskite QDs is the doping of transition metals. Yao et al.⁴⁰ proposed a high-performance LED by Ce³⁺ doping into the CsPbX₃ QDs. QD-LED based on these samples showed an improvement in EQE clocking up to 4.5% with almost a 100% increase compared to their undoped counterparts.

Along with the optimizations of the active layer, the HTL and ETL also play an important role in improving the performance of QD-LEDs. Subramanian et al.⁴¹ reported a CsPbBr₃ QDs based LED with inverted LED architecture where ETL is Li doped TiO₂. Li

1. Introduction

doping facilitates the charge carrier balance between ETL and HTL leading to superior green emitting LED with enhanced EQE. Although CsPbI₃ based LED showed promising results, the stability of these QDs in an ambient environment still remains as a challenge. In fact, several challenges remain in the path for the LED application of perovskite QDs based LEDs, more efforts need to be put to tackle the challenges and exciting developments are expected to continue in the upcoming decade.

1.4.3 Quantum Dots for Display Applications

One very important application of LEDs with excellent color purity is in display applications wherein mixed proportions of sources of primary colors (RGB) are required. The most economical and efficient structure for displays available in the market is constructed by the blue InGaN LED with a yellow phosphor (Ce-doped YAG). But the lack of color purity makes it inefficient to express the natural colours.⁴² Hence currently, white LEDs are attracting a great deal of interest in the commercialization of displays, especially for backlights in liquid-crystal displays. There have been many efforts to develop QD color converters for LEDs for general purposes after Bawendi's report on QD-polymer composites.⁴³ Y. Kim and co-workers have synthesized highly luminescent multi-shell structured green CdSe//ZnS/CdZnS QDs and red CdSe/CdS/ZnS/CdZnS QDs which showed almost 100% quantum efficiency.⁴⁴ White LEDs for the display backlights were prepared by combining the above QDs with blue LEDs. The EQEs of green and red QD-LEDs reached up to 72 % and 34 % respectively and the QD-LED maintained a high efficiency and stability over a long period of time up to 2500 hrs.

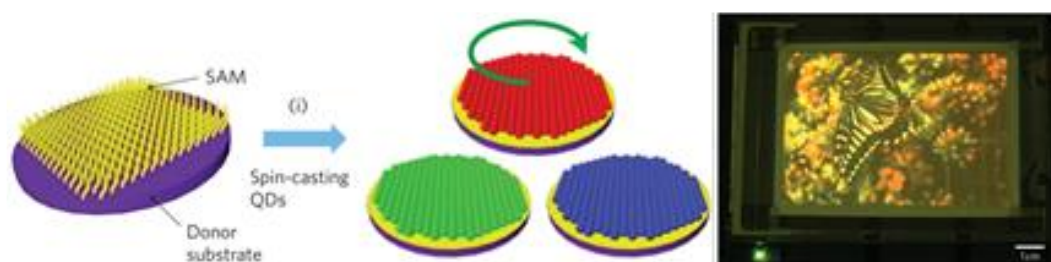


Figure 1.6 Schematic illustration of spin casting different QDs on to donor substrate and electroluminescence image of a 4-inch full colour QD-display using a TFT backplane with a 320*240-pixel array. Reproduced with permission from Ref. 36 Copyright 2011 Nature Publishing Group.

1. Introduction

Figure 1.6 shows a schematic of the process of fabrication of spin cast QD LED display device and electroluminescence image of a prototype 4-inch full colour QD-display on a 320*240-pixel array of TFT backplane.⁴⁵ The development of these EL devices strongly relies on the precise band engineering of multi core/shell QDs. Alternative materials with a simple synthesis would be valuable for future development. Recent developments in the EL properties of perovskite QDs make them excellent contenders for II-VI semiconductors based EL devices for display applications. With all the advantages of wide colour tunability, inherent narrow band emission, high PLQY, and low-cost production, perovskite QDs are very promising candidates for display applications.⁴⁶ Recently H.C. Wang et al.⁴⁷ created mixed green and red perovskite QDs in silicon resin and subjected them to excitation using a blue InGaN chip. The green emitting CsPbBr₃ QDs were coated with mesoporous silica to avoid anion exchange with red emitting CsPbI₃ QDs. In the LED packaging, the red emitting CsPb(Br/I)₃ was mixed with this coated green CsPbBr₃ and then dropped in the blue LED chip. The obtained spectra were found to be pure with a NTSC value of 113 % which is more than 104 % NTSC value reported by II-VI semiconductor QDs earlier.⁴⁴ However the low stability and high toxicity are still concerns for perovskite QDs from commercialization and far away from practical applications for daily usage.

1.4.4 Quantum Dot Lasing

Lasing in QDs were observed in the early 90's where QDs were grown by epitaxial techniques using optical and electrical pumping.⁴⁸ The difficulty in achieving lasing on colloidal QDs is due to the high nonradiative carrier losses arising due to surface defects. An important milestone in the area of QD lasing was when the researchers realized that the optical gain in QDs mostly relies on emission not from single excitons but biexcitons and other multiexcitons of higher orders.⁴⁹ A simplified scheme of biexciton generation is depicted in Figure 1.7 a). In order to obtain optical gain, one must excite two electrons to the conduction band and generate biexcitons as shown in the figure. But due to the highly efficient Auger recombination, the optical gain depletes which in turn leads to more complication especially when QDs are in a solution.⁴⁹ The experiment that lead to the first successful demonstration of the amplified stimulated emission (ASE) in QDs is in QD films and excited by femtosecond pulses.⁴⁹ Since then multiple efforts in improving the performance of QD lasers, mostly concentrating on improving the sample emission and excitonic generation by reducing the surface defects and improvisation by introducing thick shell and other architectures⁵⁰ are underway. A typical

1. Introduction

series of PL spectra showing the first and second order laser emission in CdSe/CdS films recorded as a function of pump intensity is shown in Figure 1.7b).⁵¹

Recent advances and early research suggest that the perovskite QDs are emerging as a new research paradigm in photonics and will compete favorably with both conventional CdSe-based QDs and organic- inorganic hybrid halide perovskites as optical gain media.^{52, 53}

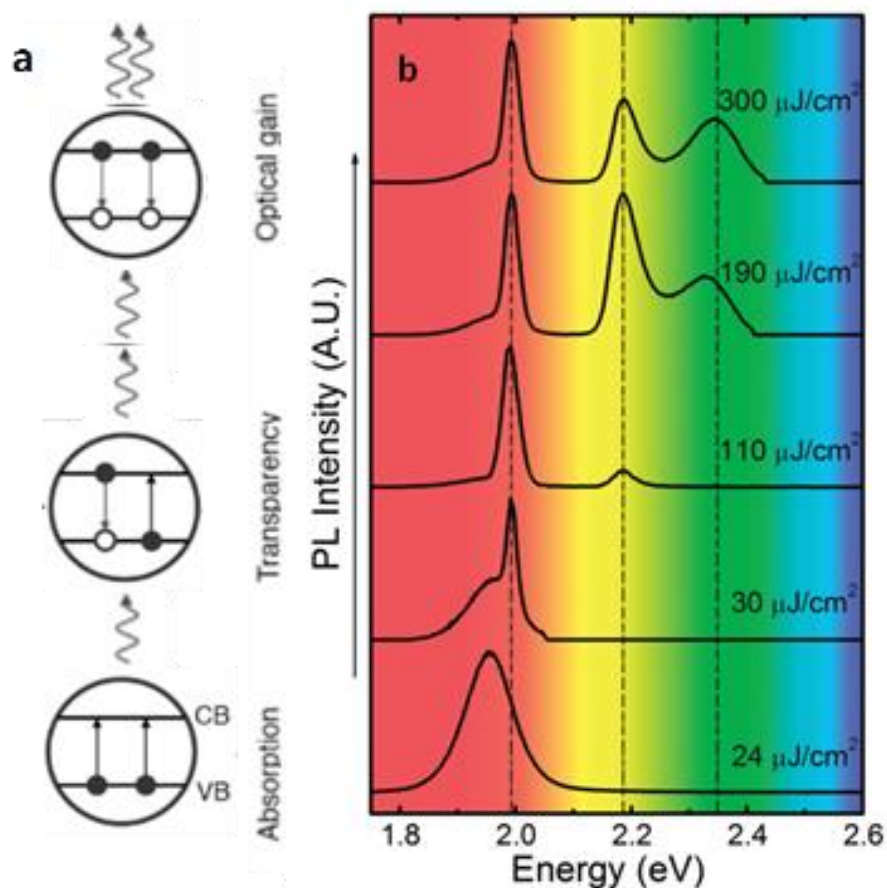


Figure 1.7 a) Simplified scheme illustrating biexciton generation leading to stimulated emission. b) PL spectra showing first and second order laser emission in CdSe/CdS films recorded as a function of pump intensity. Reproduced with permission from Ref. 42 Copyright 2013 American Chemical Society.

1.4.6 Biomedical Imaging and Drug Delivery

QDs, with their dimensional similarities with biomolecules such as proteins and nucleic acids, size dependent optical properties and resistance against photo bleaching, make them potential candidates for imaging and theranostic applications.⁵² Their improved signal brightness compared to the conventional organic dyes has been used for bio imaging.⁵⁴ However, their major drawback in biological applications is the presence of heavy elements as well as blinking.

1. Introduction

Extensive research has been carried out to prepare heavy-metal free biocompatible QDs possessing favorable fluorescent properties such as the long fluorescence lifetime, large Stokes shift and the narrow emission band.⁵⁵ Recently, the synthesis and application of lead-free ternary I-III-VI chalcogenide QDs (Cu-In-S, Cu-In-Se) have taken centre stage owing to the multiple recombination channels present in their system.⁵⁶ Also, coating QDs with a wide band gap semiconductor shell like ZnS (~3.6 eV) forming a core-shell structure has been adapted efficiently not only to enhance the stability of the core but also to encapsulate the heavy-metal rich core like CdSe. In this aspect, Klimov et al (2017), reported a CuInS₂/ZnS system achieving narrow emission line widths up to 60 meV in NIR I and NIR II regions extending its robustness, overcoming a serious limitation of a large photoluminescence (PL) line width (typically >300 meV).⁵⁷ Though CuInS₂ and CuInSe₂ systems have attracted notable attention, they suffer from fairly low PL QY compared to other QDs. However, a quaternary QD system ZnAgInSe⁵⁸ is known to be heavy metal free with high PL QY (~70%). In fact, in 2017, Deng et al, demonstrated ZnAgInSe/ZnS core-shell QD conjugated with sulfobetaine-poly(isobutylene-altmaleic anhydride)-histimine (SPH) polymer and a cyclic RGD peptide for its significant application in cancer imaging.⁵⁹

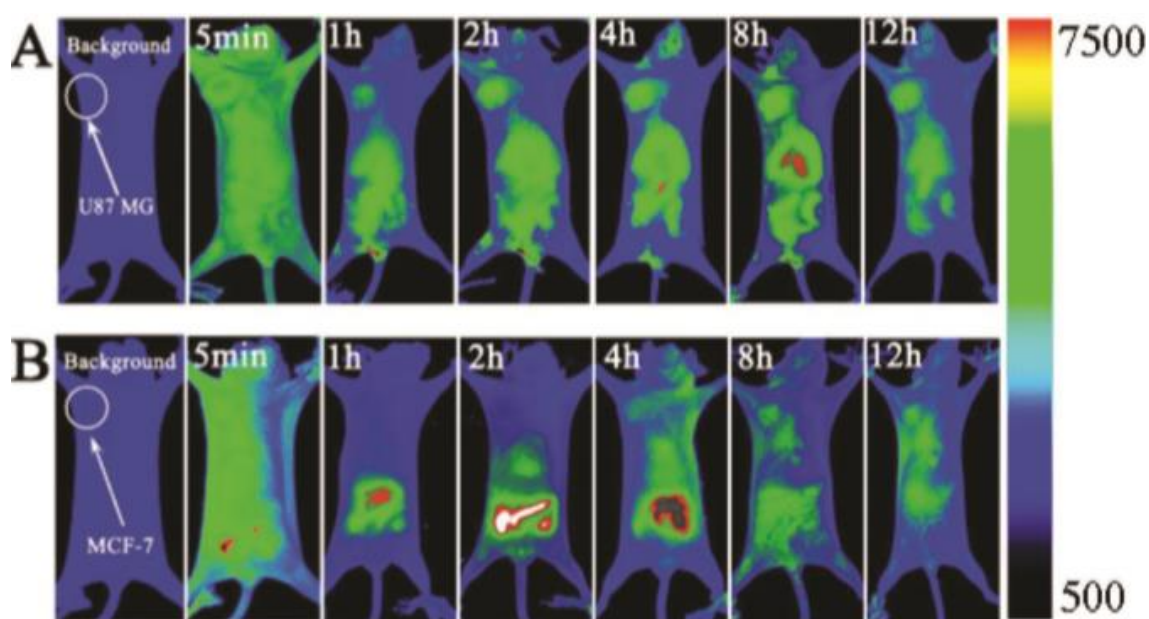


Figure.1.9 Longitudinal distribution of RGD–SPH ZnAgInSe/ZnS QDs-clusters in nude mice bearing A) glioblastoma B) breast cancer, detected using NIR QD imaging ($\lambda_{ex} = 660 \text{ nm}$, $\lambda_{em} = 740 \text{ nm}$). Reproduced with permission from Ref. 49 Copyright 2017 American Chemical Society.

1. Introduction

This was injected in glioblastoma or breast cancer tumor bearing mice; NIR images were taken up to 72h post-injection as shown in Figure 1.9. QD cores providing a structural scaffold for drug delivery is also well established in recent years. QDs possessing good biocompatibility, inertness towards drugs, loading capacity with high in-vivo residence time and a suitable particle size and shape with stability are excellent choices as successful drug carriers. Thus, this wide possibility of tuning material characteristics opens up an interesting platform to engineer the drug carrier materials with high selectivity and superior physical properties such as size, cell transfection, charge etc.⁶⁰

Utilization of QDs as drug carriers for therapeutics range from cancer, neurological disorders, hypertension and also gene therapy.⁶¹ QDs with Lipofectamine™2000 and small interfering RNA (siRNA) as a gene therapeutic approach was discussed by Chen and his co-workers.⁶² Another nano-vehicle for the anticancer drug was established in 2017, by L Zhang et al⁶³ based on a self-assembled quantum dot DNA hydrogel system that exhibited both enzyme-responsive drug delivery of doxorubicin and cell-specific targeting.

1.5. Quantum Dots: Present Status and Outlook for the Future

Despite its history of more than 30-years, the science of colloidal QDs still represents an exciting area of research that appeals to scientists with a various range of backgrounds, including inorganic and colloidal chemistry, condensed matter physics, optoelectronics, biological and medical sciences. With the introduction of perovskite inorganic QDs the possibility is further increased by a recent demonstration of their applications in different technologies ranging from photovoltaics, QD-LEDS, lasers, bio-imaging etc. Colloidal QDs are rapidly generating attention not only in the scientific community but also engineering and entrepreneurial communities due to their potential in various applications.

QDs in real life applications are at developmental stages for some applications, some applications like QD based down-converting displays have already become a commercial reality. However, there are a lot of major issues and concerns that need to be addressed to make these applications to become part of our daily lives.

The stability of colloidal QDs and thin films are some of the major issues here. A brief exposure of QDs solid to oxygen or moisture may entirely modify the landscape of surface trapping state thus affecting its conductivity as well as the optical properties. In case of perovskite QDs a slight exposure to air, moisture, UV light can fasten the degradation of these cubic crystals to orthorhombic phase which is an optical inactive phase leading to inefficiency

1. Introduction

in these devices. Even though the cell encapsulation can reduce the ill effects of oxygen and water contamination, it is useless against thermodynamic instability.

The removal of long chain organic ligands accelerates degradation on densely packed QDs and eventually causes aggregation and transformation to optically inactive and inefficient stages. Stability issues are attended to an extent by the encapsulation of QDs in a polymer matrix like PMMA, or silica coating air stable QDs with a high performance needs to be engineered.

Additionally, the cost of manufacturing and the lack of scalability hinders some of these materials to come out of the laboratory scale to an industrial large-scale production. A majority of highly efficient colloidal QDs are synthesized either using heavy metals like Cd, Hg, Pb etc. The social and environmental concerns regarding toxicity of these heavy metals are still a huge concern in bringing these technologies to real life applications. Replacing heavy metals from these QDs using lesser toxic elements like Sn and Cu have been partially successful, however their optoelectronic performance compared to the native QDs have been really poor. For example, all inorganic perovskite Sn based CsSnX_3 are synthesized using high temperature colloidal synthesis but these QDs are highly unstable and exhibit a negligible PL QY. Hence for the commercialization of Cd or Pb based QD devices in the near future, efficient policies in recycling have to be first formulated and followed.

1.6 Present Study

II-VI semiconductor QDs and perovskite QDs have been investigated extensively for optoelectronic applications. Transition metal doping adds additional advantage in designing quantum dots (QDs) for various optoelectronic applications. In the era that is driven by quest for energy efficiency, understanding of the photo physics is very essential. The thesis is divided into nine chapters along with methodology chapter where experimental techniques employed throughout these chapters are discussed. Rest of the thesis is divided in to two parts. The first part discusses about the decade long debate about mechanism of Mn emission in Mn doped II-VI semiconductors and the second part of the thesis discusses about various issues related to stability and structure of perovskite QDs and harvesting delayed fluorescence using Mn as a dopant in mixed halide perovskite QDs.

Part 1 elaborates the mechanism of Mn Emission in II-VI Semiconductor Quantum Dots. **Chapter 3** focuses on energy transfer and charge transfer mechanism leading to Mn emission in II-VI semiconductor QDs. This chapter provides a fundamental overview of a problem that has remained elusive for several decades even though it has been extensively studied. In

1. Introduction

Chapter 4 we study the Mn excitation mechanism in II-VI semiconductor QDs. This chapter provides a timeline of Mn excitation and emission process in II-VI semiconductor nanocrystals as well as an identification of the various transient species consistent with the selection rules.

Part 2 discusses Mn doping in Perovskite Quantum Dots for Harvesting Delayed Fluorescence.

Chapter 5 and 6 discusses about the structural aspects and doping in perovskites to enhance the functionalities of perovskite QDs for lighting. The last three chapters discuss about the mechanism of Mn emission and harvesting delayed fluorescence through vibrational coupling.

Chapter 5 provides an overview about the structural aspects of mixed halide perovskite QDs.

This chapter looks at the mixed halide perovskite QDs from various length scales using x-ray crystallography, Raman spectroscopy and EXAFS to study the structure property relations which will lead to best use of these QDs with minimal losses. **Chapter 6** discusses about the successes and challenges in doping perovskite QDs. This chapter also sheds light on local structure analysis confirming the successful incorporation of Mn in the perovskite lattice.

Chapter 7 deals with the mechanism of dopant emission in perovskite QDs. By tuning the halide composition, the host bandgap is brought closer to Mn emission energy. Detailed analysis on delayed emission using gated PL and low temperature PL and density functional theory unravels the drip-feeding mechanism of photoexcited carriers. Due to the strong vibrational coupling between the dopant and the host, there exists an electron back transfer from Mn to the host in the Mn doped perovskite QDs, leading to vibrationally assisted delayed fluorescence (VADF). This chapter discusses about harvesting delayed fluorescence in detail using VADF which helps to improve the emission efficiency of the perovskite QDs.

Chapter 8 studies the effect of composition modulation and quantum confinement in Mn doped mixed halide perovskite NCs on delayed excitonic emission. This chapter also studies the temperature dependent band edge vs Mn emission efficiencies in the gated PL which is defined by entropy of VADF by looking at the rate of change of VADF with respect to temperature. In **Chapter 9** we study the temperature and fluence dependent carrier dynamics in Mn doped perovskite QDs. Influence of Mn as a dopant in drip-feeding the photo excited carriers back to the host through VADF is validated through ultrafast carrier dynamics in this chapter. **Chapter 10** Provides a final summary of the complete thesis and also indicates future perspectives in the topics discussed in the field of research and also their applicability towards optoelectronic devices.

1. Introduction

Bibliography

1. Ekimov, A. I.; Onushchenko, A. A. *JETP Lett.* **1981**, 34, (6), 345-349.
2. Norris, D. J.; Bawendi, M. *Phys. Rev. B* **1996**, 53, (24), 16338.
3. Ekimov, A. I.; Hache, F.; Schanne-Klein, M.; Ricard, D.; Flytzanis, C.; Kudryavtsev, I.; Yazeva, T.; Rodina, A.; Efros, A. L. *J. Opt. Soc. Am.* **1993**, 10, (1), 100-107.
4. Alferov, Z. I. *Semiconductors* **1998**, 32, (1), 1-14.
5. Murray, C.; Norris, D. J.; Bawendi, M. G. *J. Am. Chem. Soc.* **1993**, 115, (19), 8706-8715.
6. Protesescu, L.; Yakunin, S.; Bodnarchuk, M. I.; Krieg, F.; Caputo, R.; Hendon, C. H.; Yang, R. X.; Walsh, A.; Kovalenko, M. V. *Nano Lett.* **2015**, 15, (6), 3692-3696.
7. Hines, M. A.; Guyot-Sionnest, P. *J. Phys. Chem. A* **1996**, 100, (2), 468-471.
8. Peng, X.; Schlamp, M. C.; Kadavanich, A. V.; Alivisatos, A. P. *J. Am. Chem. Soc.* **1997**, 119, (30), 7019-7029.
9. Grandhi, G. K.; Swathi, K.; Narayan, K.; Viswanatha, R. *J. Phys. Chem. Lett.* **2014**, 5, (13), 2382-2389.
10. Sanehira, E. M.; Marshall, A. R.; Christians, J. A.; Harvey, S. P.; Ciesielski, P. N.; Wheeler, L. M.; Schulz, P.; Lin, L. Y.; Beard, M. C.; Luther, J. M. *Sci. Adv.* **2017**, 3, (10).
11. Remacle, F. *J. Phys. Chem. A* **2000**, 104, (20), 4739-4747.
12. Carey, G. H.; Levina, L.; Comin, R.; Voznyy, O.; Sargent, E. H. *Adv. Mater.* **2015**, 27, (21), 3325-3330.
13. Suh, Y.-H.; Kim, T.; Choi, J. W.; Lee, C.-L.; Park, J. *ACS Appl. Nano Mater.* **2018**, 1, (2), 488-496.
14. Wheeler, L. M.; Sanehira, E. M.; Marshall, A. R.; Schulz, P.; Suri, M.; Anderson, N. C.; Christians, J. A.; Nordlund, D.; Sokaras, D.; Kroll, T. *J. Am. Chem. Soc.* **2018**, 140, (33), 10504-10513.
15. Speirs, M.; Balazs, D.; Fang, H.-H.; Lai, L.-H.; Protesescu, L.; Kovalenko, M. V.; Loi, M. *J. Mater. Chem. A* **2015**, 3, (4), 1450-1457.
16. Crisp, R. W.; Kroupa, D. M.; Marshall, A. R.; Miller, E. M.; Zhang, J.; Beard, M. C.; Luther, J. M. *Sci. Rep.* **2015**, 5, 9945.
17. Pan, Z.; Zhao, K.; Wang, J.; Zhang, H.; Feng, Y.; Zhong, X. *ACS Nano* **2013**, 7, (6), 5215-5222.

1. Introduction

18. Ip, A. H.; Thon, S. M.; Hoogland, S.; Voznyy, O.; Zhitomirsky, D.; Debnath, R.; Levina, L.; Rollny, L. R.; Carey, G. H.; Fischer, A. *Nat. Nanotechnol.* **2012**, 7, (9), 577.
19. Wang, K.; Jin, Z.; Liang, L.; Bian, H.; Bai, D.; Wang, H.; Zhang, J.; Wang, Q.; Shengzhong, L. *Nat. Commun.* **2018**, 9, (1), 4544.
20. Park, B. W.; Philippe, B.; Zhang, X.; Rensmo, H.; Boschloo, G.; Johansson, E. M. *Adv. Mater.* **2015**, 27, (43), 6806-6813.
21. Wang, C.; Chesman, A. S.; Jasieniak, J. J. *ChemComm* **2017**, 53, (1), 232-235.
22. Ghosh, D.; Ali, M. Y.; Chaudhary, D. K.; Bhattacharyya, S. *Sol. Energy Mater Sol. Cells* **2018**, 185, 28-35.
23. Hao, M.; Bai, Y.; Zeiske, S.; Ren, L.; Liu, J.; Yuan, Y.; Zarrabi, N.; Cheng, N.; Ghasemi, M.; Chen, P. *Nature Energy* **2020**, 5, (1), 79-88.
24. Santra, P. K.; Kamat, P. V. *J. Am. Chem. Soc* **2012**, 134, (5), 2508-2511.
25. Pan, Z.; Zhang, H.; Cheng, K.; Hou, Y.; Hua, J.; Zhong, X. *ACS Nano* **2012**, 6, (5), 3982-3991.
26. Pan, Z.; Mora-Seró, I. n.; Shen, Q.; Zhang, H.; Li, Y.; Zhao, K.; Wang, J.; Zhong, X.; Bisquert, J. *J. Am. Chem. Soc* **2014**, 136, (25), 9203-9210.
27. Rao, H.; Zhou, M.; Pan, Z.; Zhong, X. *J. o. M. C. A. J. Mater. Chem. A* **2020**, 8, (20), 10233-10241.
28. Du, J.; Du, Z.; Hu, J.-S.; Pan, Z.; Shen, Q.; Sun, J.; Long, D.; Dong, H.; Sun, L.; Zhong, X. *J. Am. Chem. Soc* **2016**, 138, (12), 4201-4209.
29. Du, J.; Singh, R.; Fedin, I.; Fuhr, A. S.; Klimov, V. I. *Nature Energy* **2020**, 5, (5), 409-417.
30. Carey, G. H.; Abdelhady, A. L.; Ning, Z.; Thon, S. M.; Bakr, O. M.; Sargent, E. H. *Chem. Rev.* **2015**, 115, (23), 12732-12763.
31. Mora-Seró, I. *Adv. Energy Mater* **2020**, 10, (33), 2001774.
32. Colvin, V.; Schlamp, M.; Alivisatos, A. P. *Nature* **1994**, 370, (6488), 354.
33. Niu, Y.-H.; Munro, A. M.; Cheng, Y. J.; Tian, Y.; Liu, M. S.; Zhao, J.; Bardecker, J. A.; Jen-La Plante, I.; Ginger, D. S.; Jen, A. Y. *Adv. Mater.* **2007**, 19, (20), 3371-3376.
34. Saha, A.; Chellappan, K. V.; Narayan, K.; Ghatak, J.; Datta, R.; Viswanatha, R. *J. Phys. Chem. Lett.* **2013**, 4, (20), 3544-3549.
35. Anikeeva, P. O.; Halpert, J. E.; Bawendi, M. G.; Bulovic, V. *Nano Lett.* **2009**, 9, (7), 2532-2536.

1. Introduction

36. Lin, K.; Xing, J.; Quan, L. N.; de Arquer, F. P. G.; Gong, X.; Lu, J.; Xie, L.; Zhao, W.; Zhang, D.; Yan, C. *Nature* **2018**, 562, (7726), 245-248.
37. Song, J.; Li, J.; Li, X.; Xu, L.; Dong, Y.; Zeng, H. *Adv. Mater.* **2015**, 27, (44), 7162-7167.
38. Yang, D.; Li, X.; Zeng, H. *Adv. Mater. Interfaces* **2018**, 5, (8), 1701662.
39. Pan, J.; Sarmah, S. P.; Murali, B.; Dursun, I.; Peng, W.; Parida, M. R.; Liu, J.; Sinatra, L.; Alyami, N.; Zhao, C. *J. Phys. Chem. Lett.* **2015**, 6, (24), 5027-5033.
40. Yao, J.-S.; Ge, J.; Han, B.-N.; Wang, K.-H.; Yao, H.-B.; Yu, H.-L.; Li, J.-H.; Zhu, B.-S.; Song, J.-Z.; Chen, C. *J. Am. Chem. Soc.* **2018**, 140, (10), 3626-3634.
41. Subramanian, A.; Pan, Z.; Zhang, Z.; Ahmad, I.; Chen, J.; Liu, M.; Cheng, S.; Xu, Y.; Wu, J.; Lei, W. *ACS Appl. Mater. Interfaces* **2018**, 10, (15), 13236-13243.
42. Berns, R. S., *Billmeyer and Saltzman's principles of color technology*. Wiley New York: 2000.
43. Lee, J.; Sundar, V. C.; Heine, J. R.; Bawendi, M. G.; Jensen, K. F. *Adv. Mater.* **2000**, 12, (15), 1102-1105.
44. Jang, E.; Jun, S.; Jang, H.; Lim, J.; Kim, B.; Kim, Y. *Adv. Mater.* **2010**, 22, (28), 3076-3080.
45. Kim, T.-H.; Cho, K.-S.; Lee, E. K.; Lee, S. J.; Chae, J.; Kim, J. W.; Kim, D. H.; Kwon, J.-Y.; Amaratunga, G.; Lee, S. Y. *Nat. Photonics* **2011**, 5, (3), 176.
46. Bai, Z.; Zhong, H. *Sci. Bull.* **2015**, 60, (18), 1622-1624.
47. Wang, H. C.; Lin, S. Y.; Tang, A. C.; Singh, B. P.; Tong, H. C.; Chen, C. Y.; Lee, Y. C.; Tsai, T. L.; Liu, R. S. *Angew. Chem. Int. Ed* **2016**, 55, (28), 7924-7929.
48. Kirstaedter, N.; Ledentsov, N.; Grundmann, M.; Bimberg, D.; Ustinov, V.; Ruvimov, S.; Maximov, M.; Kop'ev, P. S.; Alferov, Z. I.; Richter, U. *Electron. Lett.* **1994**, 30, (17), 1416-1417.
49. Klimov, V. I.; Mikhailovsky, A. A.; McBranch, D.; Leatherdale, C. A.; Bawendi, M. G. *Science* **2000**, 287, (5455), 1011-1013.
50. Pietryga, J. M.; Park, Y.-S.; Lim, J.; Fidler, A. F.; Bae, W. K.; Brovelli, S.; Klimov, V. I. *Chem. Rev.* **2016**, 116, (18), 10513-10622.
51. García-Santamaría, F.; Chen, Y.; Vela, J.; Schaller, R. D.; Hollingsworth, J. A.; Klimov, V. I. *Nano Lett.* **2009**, 9, (10), 3482-3488.
52. Wang, Y.; Li, X.; Song, J.; Xiao, L.; Zeng, H.; Sun, H. *Adv. Mater.* **2015**, 27, (44), 7101-7108.

1. Introduction

53. Zhu, H.; Fu, Y.; Meng, F.; Wu, X.; Gong, Z.; Ding, Q.; Gustafsson, M. V.; Trinh, M. T.; Jin, S.; Zhu, X. *Nat. Mater.* **2015**, 14, (6), 636-642.
54. Zrazhevskiy, P.; Sena, M.; Gao, X. *Chem. Soc. Rev.* **2010**, 39, (11), 4326-4354.
55. Weissleder, R.; Pittet, M. J. *Nature* **2008**, 452, (7187), 580.
56. Zhong, H.; Bai, Z.; Zou, B. *J. Phys. Chem. Lett.* **2012**, 3, (21), 3167-3175.
57. Zang, H.; Li, H.; Makarov, N. S.; Velizhanin, K. A.; Wu, K.; Park, Y.-S.; Klimov, V. I. *Nano Lett.* **2017**, 17, (3), 1787-1795.
58. Zhang, J.; Xie, R.; Yang, W. *Chem. Mater.* **2011**, 23, (14), 3357-3361.
59. Deng, T.; Peng, Y.; Zhang, R.; Wang, J.; Zhang, J.; Gu, Y.; Huang, D.; Deng, D. *ACS Appl. Mater. Interfaces* **2017**, 9, (13), 11405-11414.
60. Xiao, S.; Zhou, D.; Luan, P.; Gu, B.; Feng, L.; Fan, S.; Liao, W.; Fang, W.; Yang, L.; Tao, E. *Biomaterials* **2016**, 106, 98-110.
61. Jia, N.; Lian, Q.; Shen, H.; Wang, C.; Li, X.; Yang, Z. *Nano Lett.* **2007**, 7, (10), 2976-2980.
62. Chen, A. A.; Derfus, A. M.; Khetani, S. R.; Bhatia, S. N. *Nucleic Acids Res.* **2005**, 33, (22), e190-e190.
63. Zhang, L.; Jean, S. R.; Ahmed, S.; Aldridge, P. M.; Li, X.; Fan, F.; Sargent, E. H.; Kelley, S. O. *Nat. Commun.* **2017**, 8, (1), 381.

1. Introduction

Chapter 2

Methodology

2. Methodology

2. Methodology

There are several types of experimental set ups and characterization techniques, which have been employed to study the various nanocrystal systems in present work: UV-VIS absorption spectroscopy, Photoluminescence (PL) Spectroscopy, X-ray diffraction (XRD), transmission electron microscopy (TEM), inductively coupled plasma-optical emission spectroscopy, transient absorption (TA) spectroscopy and X-ray absorption of fine structure spectroscopy (XAFS). In this chapter, the details of all these experimental techniques that were used in this thesis are described in detail.

2.1. UV-VIS Absorption Spectroscopy

UV-VIS absorption spectroscopy is a powerful tool for the characterization of semiconductor nanocrystals. This technique is also used to obtain the bandgap of the quantum dots (QDs). Absorption of ultraviolet and visible ray is associated with the excitation of electron from lower to higher energy level, specifically from valence band to conduction band in case of semiconductor. We have used Beer-Lamberts law to determine the concentration of sample and it is given by

$$A = \epsilon \cdot c \cdot l$$

Where A = Absorbance, ϵ = molar absorption co-efficient, c = concentration of the sample, l = sample thickness

When light passes through a sample the Absorbance can be measured by the photodetector using formula

$$A = \log (I_0/I)$$

The molar absorptivity can be calculated using the Beer-Lambert law.

The energy of the radiation should be equal or more than the band gap of the semiconductor QDs. The shift in the absorption edge is used to study the change in the band gap in various samples. Additionally, due to the quantum confinement effect shown by QDs, we observe a size dependent bandgap change which is also observed using UV-VIS absorption spectroscopy.

In this work UV-VIS absorption spectroscopy has been used to monitor the band gap and absorption characteristics of different QDs. The samples were dissolved in hexane and the measurements were carried out in Agilent 8453 UV-visible spectrometer.

2. Methodology

2.2. Photoluminescence Spectroscopy

When a molecule or fluorophores absorbs a light, the molecule gets excited and creates exciton (electron-hole pair). The radiative recombination of this exciton pairs results emission light known as photoluminescence (PL). PL spectroscopy is extensively used in this thesis to study the photo-physics of the semiconductor QDs.

2.2.1 Steady state PL spectroscopy

Photoluminescence is defined as the spontaneous emission of light from material under optical excitation. The whole photophysical process occurs in three stages as described below in Figure 2.1.

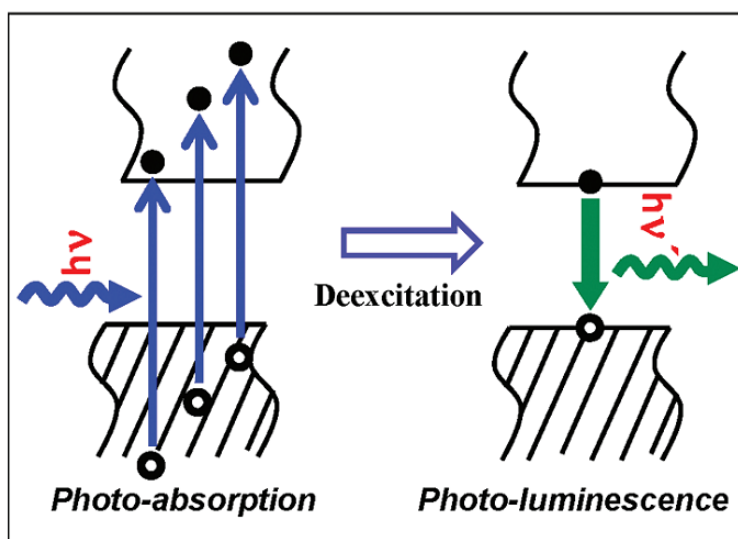


Figure 2.1 Schematic of Photoluminescence process. Reprinted with permission from ref¹ (Copyright 2010 American Chemical Society).

When external light with energy $h\nu_{\text{ex}} > E_g$ (E_g is the band gap) incident on QDs, the QDs absorb the light generating excitons. The deexcitation process of the excited electron can occur through either non-radiative recombination in the form of heat or by recombining with the hole in the valance band giving rise to radiative recombination. The radiative recombination process occurs in 10^{-9} - 10^{-7} sec. As the excited electron dissipates some energy in form of heat, the energy of the emitted photon ($h\nu_{\text{em}}$) is always less than the excitation photon ($h\nu_{\text{ex}}$) creating a difference in energy or wavelength which is called as Stokes' shift. To identify the origin of the multiple peak structures in PL spectra can be identified by PL excitation (PLE) spectra. In PLE we fixed emission wavelength and measures emission at this wavelength from the sample with varying excitation wavelength. This provides information on absorption properties but

2. Methodology

with improved signal-to-noise ratio compared to conventional absorption measurements in transmission geometry.

2.2.2. Gated PL spectroscopy

The PL emission decay lifetime can vary for different emissions observed in a sample. To identify the long-lived delayed PL emissions, a technique integrated to the PL emission spectrometer can be used. The emission spectra are recorded with a time delay of few microseconds to record only the long-lived emissions. Similarly, the origin of the long-lived delayed emission is also obtained by gated PLE spectra. Gated PLE is performed by fixing the emission wavelength and measures the delayed emission at the wavelength from the sample with varying excitation wavelength. Gated PLE corresponds to the energy levels responsible only for the delayed emission from the sample.

2.2.3. Time Resolved Photoluminescence (TrPL)

Time Resolved Photo-Luminescence (TrPL) is an experimental technique that provides the relaxation dynamics of charge carrier as a function of time after excitation using a short laser pulse. The time resolution can be attained in a number of ways which depends on the required sensitivity and time resolution. TCSPC (Time-Correlated Single Photon Counting) is one of them and it is a digital counting technique which counts photons that are time-correlated in relation to a short excitation light pulse. This technique is used to find radiative and non-radiative lifetimes of exciton pairs in semiconductor QDs. The average time in the excited state $\langle t \rangle$ is obtained by averaging t over the intensity decay of the QDs,

$$\langle t \rangle = \frac{\int_0^{\infty} tI(t)dt}{\int_0^{\infty} I(t)dt}$$

For a single exponential decay, the average time in the excited state is equal to the lifetime τ .² However, for a multiexponential decay, average time in the excited state can be a complex function with several parameters from the above equation. We have quantified the average time in the excited state across various QDs by considering the time taken by the intensity to reach 37 % of its original value upon the excitation of QDs.

450 W xenon lamp is used as the source on the FLSP920 spectrometer, Edinburgh instrument, for the excitation of the QDs, while the photoluminescence decay dynamics (Time resolved PL) measurements were carried out using the EPL-405 ps pulsed diode laser. The micro flash lamp is used to record the long-lived delayed emission lifetime.

2. Methodology

All the solution-based measurements were performed by dissolving the QDs in hexane collected using 450 W xenon lamp as the excitation source on the FLSP920 spectrometer, Edinburgh Instruments.

2.2.4 Temperature dependent PL spectroscopy

Here, the PL spectra and the lifetime are measured as a function of temperature. As the electron phonon interaction usually decreases at low temperature. This leads to lesser non radiative recombination at low temperature resulting in enhanced PL intensity and average lifetime.

The QDs dispersed in hexane were drop casted on a glass substrate and the solvent were allowed to evaporate leaving behind the QDs on the thin film. Low temperature PL emission, gated PL emission, TrPL, PLE and gated PLE measurements were done using ARS cryostat with liquid helium cooling. NCs films were cooled down to 10K and measurements were done at every 20K interval while increasing temperature to 290K. The subsequent chapters will discuss this in detail.

2.2.5 PL quantum yield (PLQY)

The ratio of the number of photons emitted to the number of photons absorbed is known as the PL QY. Unity QY will be obtained when there are no non radiative recombination losses and all the excited electrons decay radiatively to the ground state. Accurate quantum yield for both thin film and solution were obtained by using integrating sphere. The absolute determination of the emission quantum yield of the QDs requires the precise measurement of the emission spectrum of the sample and the measurement of the absorbed number of photons. The latter is performed by two spectral (emission) scans, namely sample scatter and blank scatter, with the emission monochromator scanning over the Rayleigh scattered light from the sample and from a 100% diffuse reflecting reference. The intensity difference in the scattering spectra of the solvent over sample gives the number of photons absorbed by the sample. The number of photons emitted by the sample is obtained from the emission spectrum. Once the number of photons absorbed and photons emitted are obtained, the absolute PL QY for the QDs is calculated.

2.2.6. Jacobian Transformation

Conventional PL spectra is recorded and plotted with respect to wavelength units whereas in the materials science the most preferred unit is in energy units and presentation of data as a function of energy provides better physical insight. However, the bandpass in energy is not

2. Methodology

constant when the spectrum is recorded with constant wavelength resolution.² Direct conversion of wavelength to energy will end up in improper interpretation of the data. To correct this possible inclusion of error, the scaling factor hc/E^2 which is known as the Jacobian transformation³ to be used while converting a plot from wavelength scale to energy scale units.

This conversion is very important when the spectra are broad enough to cover a wide range of energies compared to the ones which are having narrow full width half maximum (fwhm). In case of QDs with broad dopant emission band along with the band edge PL, the transformation significantly alters the spectrum with a slight redshift and intensity change. We have applied this correction to all the PL spectra shown in the thesis.

2.3. X-ray diffraction

X-ray diffraction is most commonly used technique⁴ for the determination of crystal structure and symmetry. In addition, this technique also provides an estimate of nanocrystal size. X-ray diffraction is based on constructive interference of monochromator radiation coming from different diffraction planes of the crystalline sample. X-ray diffraction obeys Bragg's law which states that constructive interference would occur if the path difference between the x-rays scattered from parallel planes is an integer number of the wavelength of radiation. If the planes of atoms, separated by a distance 'd', make an angle θ with incident beam as shown in figure, then the path difference would be $2d\sin\theta$. So, for constructive interference, the Bragg's law must be satisfied

$$\text{i.e.} \quad n\lambda = 2d\sin\theta \quad n = 1, 2, 3, \dots$$

where λ = wavelength of the x-ray radiation

We have carried out powder X-ray diffraction experiments on the samples using Bruker D8 Advance diffractometer using Cu-K α radiation having wavelength 1.5406 Å. Powder or precipitates of sample were placed on a glass plate sample holder during measurement. As the diffraction peak intensity from the QDs is very weak, we have taken scan for sufficient intensity with a slow scan rate to get a reasonable signal to noise ratio. The bulk XRD patterns were obtained from the inorganic crystal structure database for the crystal structure analysis.

2.4. Transmission Electron Microscopy

The transmission electron microscopy (TEM) is one of the important tools in material science for characterization of microscopic structure of nanomaterials. A TEM image represents a two-

2. Methodology

dimensional projection of a three-dimensional (3D) object. TEM is used to study the monodispersity, shape, quality and size of the QDs. TEM works on the same principles as the visible light microscope, however uses electrons instead of light, having much lower wavelength, which makes it possible to get a resolution of about thousand times better than a visible light microscope. When the electron beam passes through a thin specimen, it gets absorbed or diffracted by the specimen. The variation of intensity of electron diffraction across the specimen called the 'diffraction constant' is used in imaging of defects such as dislocation, interfaces and secondary phase particles. An image is formed from the interaction of the electrons transmitted through the specimen. The image is magnified and focused onto a fluorescent screen or a photographic film. Now a days, CCD camera is used to record the TEM images. TEM can be used in recording electron diffraction pattern. Although the XRD pattern provides more quantitative information than electron diffraction pattern, TEM has a greater advantage that the electron beam can be focused easily to any part of specimen. So, this electron diffraction data from different area of specimen can give us more details about the accurate local structure of the sample study.

Samples for TEM were prepared by drop casting very dilute solution of the QDs dissolved in a solvent (hexane) onto a carbon-coated copper grid. The grids were then dried under IR lamp for few hours. TEM was carried out using Technai F30 UHR version electron microscope, using a field emission gun (FEG) operating at an acceleration voltage of 300 kV.

2.5. Inductively Coupled Plasma Optical Emission Spectrometry (ICP-OES)

ICP-OES is widely used in analytical laboratories to determine the composition of elements in a sample using plasma and a detector. It is based on Atomic Emission Spectroscopy in which the sample is excited with high temperature plasma (up to 8000 K), generated at the end of a quartz torch. When the excited electron returned to lower energy state, energy released as light and the corresponding photon wavelength is measured. Every element has its own characteristics emission spectrum. The element type is determined based on the wavelength of the photon rays, and the concentration of each element is determined based on the rays' intensity.

Here, we have used Perkin Elmer optima 7000 DV ICP-OES machine to determine the elemental concentration in our samples. Samples were dissolved in 2-5% of HNO₃ solution, and different elemental concentrations were measured against high purity known standards.

2. Methodology

2.6. Transient absorption spectroscopy

Transient absorption (TA) spectroscopy, is a pump-probe spectroscopic technique utilised to measure the photogenerated excited state absorption energies and associated lifetimes of molecules, materials, and devices. The pump-probe technique can be described by a sample being photo-excited by an ultrafast light source (pump pulse), whereby a second light source (probe pulse) is measured for changes in absorption as a function of wavelength and time. The technique focuses on electron and energy transfer mechanisms.

Ultrafast transient absorption measurements were performed by an amplified Ti:Sapphire laser (Coherent Libra) generating 100-fs pulses at 800 nm and 2 kHz repetition rate. Pump pulses at 400 nm were generated by frequency doubling the fundamental wavelength by a 2-mm-thick β -barium borate crystal; they were modulated at 1 kHz by a mechanical chopper and focused in a spot of $(400 \times 180) \mu\text{m}^2$ on samples dispersed in hexane. UV-visible probe pulses were produced by white light supercontinuum generation focusing a part of the fundamental beam in a calcium fluoride plate. Chirp-free differential transmission spectra $\Delta T/T = (T_{\text{on}} - T_{\text{off}})/T_{\text{off}}$, T_{on} and T_{off} being the transmission of the probe through the perturbed and unperturbed sample, were acquired at different pump-probe delays by a fast-optical multichannel analyser operating at the full laser repetition rate. The temporal resolution of the setup is ≈ 100 fs. Measurements were carried out at room temperature.

2.7. X-ray Absorption Fine Structure (XAFS) Spectroscopy

X-ray absorption fine structure spectroscopy⁵⁻⁷ is an important tool to characterize the local structure of nanocrystals. This technique has been extensively used to probe the evolution of the local structure of various undoped and doped QDs in this thesis. XAFS gives information about how X-rays are absorbed by a specific element (atoms) of its near and above the core binding energy through “photoelectric effect”. Usually, the energy range of X-ray used for the XAFS covers from 500 eV to 50 keV. When high energy X-rays incident on the sample (X-ray energy higher than the binding energy), the oscillating electric field of the electromagnetic radiation interacts with bound electrons of the absorbing atom and remove from its quantum level to the continuum. This results in absorption of X-ray energy and an emission of a photoelectron, from the atom. In XAFS we study the probability of X-ray absorption coefficient (μ) as a function of X-ray energy.

2. Methodology

X-ray diffraction (XRD), which relies on long range ordering of atomic planes to probe crystalline structure at a length scale of approximately 50 Å or more. X-ray absorption spectroscopy probes the immediate environment of the selected element, within about 6 Å.

The number of X-rays transmitted (I) through a sample is given by the intensity of X-rays impinging on the sample (I_0) decreased exponentially by the thickness of the sample (t) and the absorption coefficient of the sample (μ)

According to Beer-Lambert law the energy absorption,

$$I=I_0 e^{-\mu t}$$

Where I_0 and I are incident and transmitted x-ray intensity respectively, t is sample thickness

Usually the absorption co-efficient μ is can be expressed as,

$$\mu \approx \frac{\rho z^4}{AE^3}$$

Where ρ = sample density, z = atomic number, A = atomic mass and E = energy of X-ray

The probability for absorption increases sharply when the incident X-ray energy equals the energy required to excite an electron to an unoccupied electron orbital. These steps in the absorption coefficient are termed absorption edges.

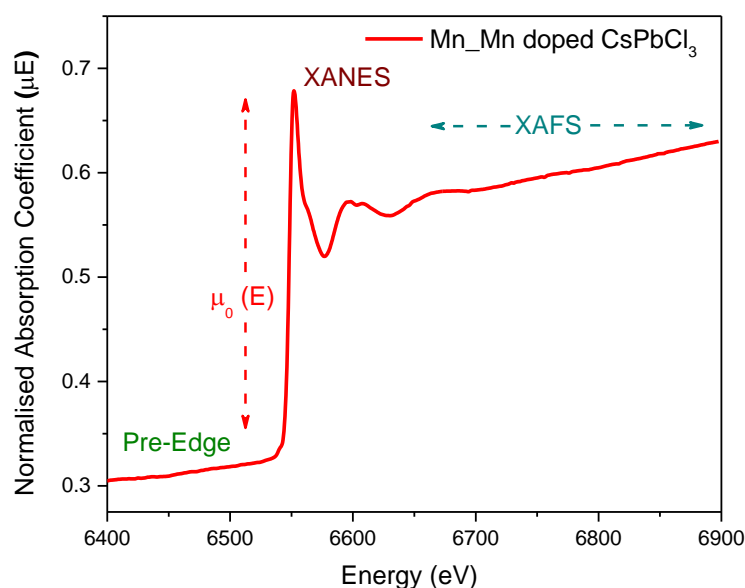


Figure 2.2 XAFS spectrum of Mn edge for Mn doped CsPbCl₃ showing different region of energy.

2. Methodology

A typical XAFS spectrum is shown in figure 2.2. It is generally divided into two sections (i) X-ray absorption near edge structure (XANES) which extend from just below the edge to about 30 eV and (ii) extended X-ray absorption fine structure spectroscopy (EXAFS) which starts after XANES and continues up to 1000 eV above the edge. As, XANES occurs at lower energy, when the transition happens, it provides information about electronic properties, oxidation states, the density of available states etc. However, the EXAFS provides information about the neighbours and the local structure around the absorbing atom. Moreover, it also gives the information about local defects and can extract site specific structural information.

EXAFS can be represented as primary quantity $\chi(k)$, the oscillatory variation of photoelectron wavenumber. To emphasize the oscillation, at early/late length scales, depending on the requirement of the problem, $\chi(k)$ is often represented as k^2 or k^3 .

Scattering from different surrounding neighbouring atoms give rise to different frequencies and the EXAFS oscillation $\chi(k)$ can be expressed as

$$\chi(k) = \sum \frac{N_j f_j(k) e^{-2k^2 \sigma_j^2}}{k R_j^2} \sin[2k(R_j + \delta_j(k))]$$

where $f(k)$ and $\delta(k)$ are scattering properties of the neighbouring atoms, R is the distance of the interacting neighbor, N is the coordination number and σ^2 is the Debye-Waller factor. By appropriate modeling of EXAFS spectra one can determine N , R , σ^2 from this equation knowing the scattering amplitude $f(k)$ and phase shift $\delta(k)$.

XAFS data processing: The obtained data from synchrotron beamline represent the variation of μ as a function of energy which can be transformed in wavevector in k -space by changing energy to photoelectron wavenumber k [$k = (2m(E-E_0)/\hbar^2)^{1/2}$]. This spectrum has more physical consequence than when it represents in terms of radial function (R) i.e. in R -space by applying Fourier transformation on the k -space EXAFS.

In this thesis we followed the following steps to process our data-

- 1. Pre-edge background correction.** Due to intensity of the incident x-ray and detector efficiency there always exist some background intensity before the absorption edge. This pre-edge background should be removed before processing the data. The pre-edge spectrum should be fitted with some functional form and extrapolating this function into the post edge.

2. Methodology

2. **Deglitching.**⁸ The post absorption edge or the EXAFS region of the raw spectrum often consist of some sharp spikes due to reflection (Bragg scatter) from crystalline monochromator or the diffraction from the sample. These sharp spikes contribute a lot in Fourier transformed R-space spectrum and hence it is necessary to remove or deglitch them before processing further. These glitches can be removed by removing those defecting points carefully and fitting with a polynomial to interpolate the region of glitch.
3. **Normalization.** The EXAFS spectra recorded is contribution from multiple absorbing atoms. To obtain the contribution from a single atom and more quantitative information the data should be normalized.
4. **Conversion to k-space.** To convert the E-space spectrum to k-space $\chi(E)$ need to convert into $\chi(k)$. It can be changed by changing the x-axis using the relation $k = [(2m(E-E_0)/\hbar^2)^{1/2}]$.
5. **Conversion to R-space.** The k-space spectrum can be converted to R-space by Fourier transformation. The R-space spectrum represents the radial position of the neighbouring atom. It should be noted that the peak position does not give exactly the bond length due to the phase shift term $\delta(k)$ in EXAFS equation. Typically, the bond length is 0.3-0.5 Å shorter than the peak position.
6. **Fitting.** Finally the R-space data is modeled by providing known crystal structure information using known crystal structure information as well as the various paths using abinitio calculation of FEFF code.⁷

2. Methodology

Bibliography

1. Pradhan, N.; Sarma, D. D. *J. Phys. Chem. Lett.* **2011**, 2, (21), 2818-2826.
2. Lakowicz, J. R., *Principles of fluorescence spectroscopy*. Springer science & business media: 2013.
3. Mooney, J.; Kambhampati, P. *J. Phys. Chem. Lett.* **2013**.
4. Klug, H. P.; Alexander, L. E., *X-Ray Diffraction Procedures: For Polycrystalline and Amorphous Materials*. Wiley: 1974.
5. Sayers, D. E.; Stern, E. A.; Lytle, F. W. *Phys. Rev. Lett.* **1971**, 27, (18), 1204.
6. Rehr, J. J.; Albers, R. C. *Rev. Mod. Phys.* **2000**, 72, (3), 621-654.
7. Newville, M. *J. Synchrotron Rad.* **2001**, 8, (2), 322-324.
8. Zhuchkov, K. N.; Shuvaeva, V. A.; Yagi, K.; Terauchi, H. *J. Synchrotron Radiat.* **2001**, 8, (2), 302-304.

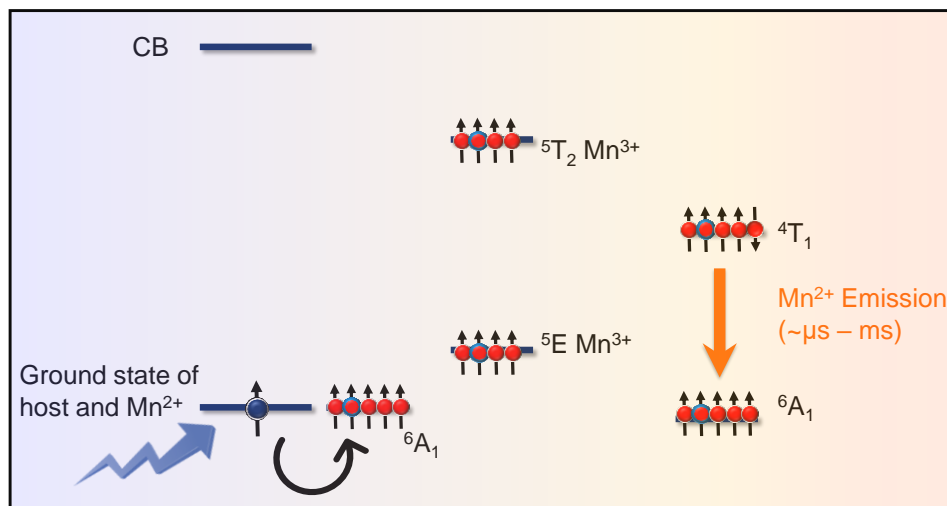
2. Methodology

Part I

Mechanism of Mn Emission in II-VI Semiconductor Quantum Dots

Chapter 3

Mechanism of Mn Emission: Energy Transfer or Charge Transfer?



The following papers have been published based on work presented here:

Pradeep K R, and R. Viswanatha. "Mechanism of Mn emission: Energy transfer vs charge transfer dynamics in Mn-doped quantum dots." *APL Materials* 8, 2 (2020): 020901.

3. Mechanism of Mn Emission: Energy Transfer or Charge Transfer?

3. Mechanism of Mn Emission: Energy Transfer or Charge Transfer?

3.1. Abstract

In a quest for new functional materials, transition metal doping in semiconductors has attracted significant attention wherein introduction of dopant atoms alters a range of physical properties of the host like its optical, magnetic and electronic properties. Hence the choice of appropriate dopants to meet the current challenges makes semiconductor doping highly versatile field. In the past, Mn doping in II-VI semiconductors has been extensively studied. The interest in these systems arises from a prominent orange emission from an optically forbidden state. An extended debate in literature spanning last three decades has so far shed light on various anomalous properties of Mn emission, specifically in quantum-confined systems leading to more questions. In this chapter, we review the literature with specific emphasis on the mechanism of Mn emission and an understanding of the electron-hole pathway during the excitation and de-excitation process in doped quantum dots. We explore various phenomena of energy and charge transfer mechanisms along with experiments in support of these phenomena which can eventually lead to a better understanding of spin driven optoelectronics.

3.2. Introduction

Transition metal-doped semiconductor quantum dots have attracted significant attention as a new class of materials, where the interaction of the dopant with the host leads to unique ways of tuning the electronic, optical and magnetic properties.¹⁻⁶ Enhancement of dopant related material properties, as well as the observation of new properties in doped quantum dots (QDs) that is not observed in their bulk counterparts due to a strong interaction of the dopant ions with quantum confined host is an established phenomena.^{5, 7} For instance, Mn-doped colloidal quantum dots exhibit high photoluminescence (PL) quantum yield (QY) with an intense Mn d-d emission centred around 585 nm unlike the conventional bulk dilute magnetic semiconductors (DMSs)⁸ despite the d-d transition being spin forbidden.⁹⁻¹⁵ Mn²⁺ ions doped in II-VI or perovskite semiconductor host QDs can function as a highly efficient energy acceptor and act as a storehouse for the excitons generated in the semiconductor host.^{4, 6} The long lifetime of the excited state of the dopant also provides excellent opportunities either for extracting the excitonic energy for use as energy storehouse for various other light emitting applications¹⁶ or its use as charge carriers for photonic applications.¹⁷⁻¹⁹ For this purpose, it is important to know the nature of the transition, specifically if it is an energy transfer or a charge transfer process. The violation of selection rules for this intense transition has given rise to various challenges in understanding the nature of this emission and has been the subject of

3. Mechanism of Mn Emission: Energy Transfer or Charge Transfer?

intense research in the last few decades. Despite this, many questions remain unanswered and connections to the missing links do not allow for unleashing the full potential of this emission as an active tool in optoelectronic applications. Few of the questions include complete absence of band edge emission in Mn-doped II-VI semiconductor QDs,⁹ anomalous polarization of Mn d-d emission in presence of magnetic field,²⁰ magnetic polaron formation in Mn²⁺ doped CdSe QDs,^{21, 22} light-induced spontaneous magnetization in Mn-doped CdSe QDs at zero external magnetic field,²³ tunable Mn emission from epitaxial strain,²⁴ ultra-narrow and widely tunable Mn emission from ZnS-CdS alloy QDs.²⁵ More recently, Mn-doped perovskite QDs¹⁵ have shown the absence of Mn emission at room temperature. Lack of comprehensive understanding in the mechanism of excitation and emission is the core reason behind such large number of unanswered anomalies.

In this chapter, we give a brief overview of the Mn doping in nanocrystals, followed by a detailed discussion on the physics behind this excitation and emission process. The Mn excitation is proposed to occur through one of the two mechanisms, namely direct energy transfer or the charge transfer by the host or the organic ligand from the surface.²⁶ We discuss the physics behind these two pathways, the selection rules and thermodynamics pertaining to energy and charge transfer processes. We then review recent developments focusing on the dynamics of the energy and charge transfer processes in Mn-doped II-VI semiconductor QDs and Mn-doped perovskite QDs. We look at various experiments that are well explained by the process of energy transfer and a few, wherein energy transfer mechanism is unable to provide an understanding. We also probe the charge transfer mechanism which involves a transient change in the oxidation state of Mn²⁺ ion and its energetics to understand the viability of these processes followed by a discussion on the so-far unexplained properties of Mn-doped QDs to provide better understanding of the spin driven optoelectronics. We then discuss and present Mn doping in perovskites which is known to behave differently than their II-VI QD counterparts and has been widely studied in the last two to three years. The physics behind the Mn doping in perovskite is further intriguing and gives rise to various unsolved challenges that will be elucidated in this article.

3.3. Discussion

3.3.1. Nature of Mn emission

Mn²⁺ doped semiconductor QDs leads to high luminescence efficiencies with dopant associated yellow-orange emission typically centred within 580 - 600 nm as shown by a typical spectra in Figure 3.1 a).²⁷ The decay life-time of Mn emission, unlike excitonic and/or surface state

3. Mechanism of Mn Emission: Energy Transfer or Charge Transfer?

emission, is quite long-lived ($\sim \mu\text{s}$ to ms) as shown in Figure 3.1 b). It is widely accepted in literature that the presence of this long-lived 585 nm emission is a signature of successful Mn doping in QDs. Extensive studies have assigned this peak to arise from the ${}^4\text{T}_1 - {}^6\text{A}_1$ d-d transition, the two lowest energy multiplets of Mn^{2+} ions within a tetrahedral crystal field splitting. It should be noted that in accordance with the selection rules, an allowed transition should have a change in the orbital quantum number, Δl of ± 1 while it is zero in this case. Similarly, the change in spin quantum number Δs is expected to be zero for the spin conservation rules while this transition demonstrates a non-zero change of spin. Hence this transition is both orbital and spin forbidden and the long emission lifetime is as per the selection rules. However, while the emission lifetime can be understood relatively easily, the excitation of Mn^{2+} ions is not yet understood. Remarkably, the Mn d-states cannot be directly excited and these states are only sensitized through the excitation of the host QDs. Hence the presence of photo-excited electron and hole pair within the host matrix is known to play a role in the excitation of the Mn d-states. The detailed photo-absorption process is described extensively in ref.¹⁰ Briefly, the total energy of ground state is shown by state <1> in Figure 3.1 c) which contains the ground state of the host QDs along with the ground state multiplet configuration of the Mn^{2+} states. During the photo-absorption phase, generation of excitons occurs and subsequently, they decay non-radiatively to the lowest energy. This process of excitation is very rapid. However, an understanding of the excitation of the Mn d- states that is also forbidden by the selection rules has intrigued researchers for several decades. Recent results have shown that in presence of Mn^{2+} ions, the photo-excited electron-hole pair within the host is known to decay very quickly, in the order of a few hundred femtoseconds (fs) suggesting an extremely quick transfer to Mn^{2+} ions.^{28,29} It should be noted here that the excited states have two possible states at two different energies, namely the electron-hole excited host along with the Mn in the ${}^6\text{A}_1$ state, which are shown as the continuum of energies, marked by <2>, and another lower energy excited state wherein Mn^{2+} state is sensitized to the ${}^4\text{T}_1$ state with a non-radiative recombination of any excited electron-hole pair in the host as marked by <3> in the figure. A high energy photon primarily causes electron-hole excitations within the host, as shown in Figure 3.1 c) which trickles down quickly to <2> as shown in Figure. 1 d) and is incapable of directly reaching state <3> even though that is lower in energy as the Mn state cannot be directly sensitized. However, this state is known to be populated in literature and the probable mechanisms of population of this state will be discussed below. Eventually, the excited $\text{Mn}^{2+} {}^4\text{T}_1$ state decays radiatively to the ground state configuration of the ${}^6\text{A}_1$ state (<3>

3. Mechanism of Mn Emission: Energy Transfer or Charge Transfer?

→ $\langle 1 \rangle$, as shown by the vertical orange arrow in Figure 3.1 d), giving rise to the 580 nm orange dopant emission.

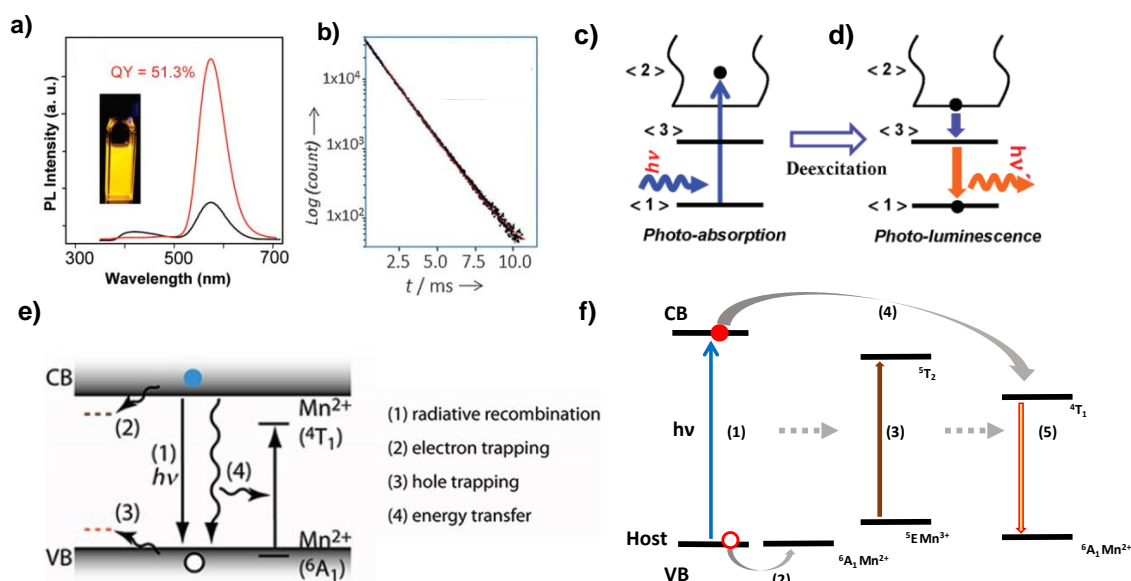


Figure 3.1 a) PL spectra of Mn-doped ZnSe QDs. (Ref. 27) (red spectra show PL after adding ZnSe shells) b) PL lifetime decay plot of Mn-doped ZnSe QDs. (Ref. 30) c) and d) Schematic of total energy diagram of excitation and de-excitation process in Mn-doped QDs. (Ref. 10) Schematic of the e) energy transfer processes (Ref. 28) and f) charge transfer processes. Reproduced with permission from the American Chemical Society and Wiley VCH.

The two probable mechanisms that leads to a population in state $\langle 3 \rangle$ from state $\langle 2 \rangle$ include an energy transfer or a charge transfer. In the case of an energy transfer, the photo-excited electron-hole pair of the host follows non-radiative Auger-like recombination, transferring the energy from the host to Mn for exciting the Mn²⁺ ground state $6A_1$ to its excited $4T_1$ state. A schematic of the various photophysical processes involved in the process of energy transfer after the generation of excitons in Mn-doped QDs is shown in Figure 3.1 e). The first process is radiative recombination giving rise to excitonic PL, and second and third process involves trapping of carriers which leads to losses followed by energy transfer from the host to Mn states. This energy transfer process should be very rapid and typically expected to occur within a timescale of a few femtoseconds (fs). In the case of charge transfer, the photoexcited hole can quickly relocate to the Mn site giving it a transient Mn³⁺ nature. Since the Mn³⁺ ions have a ground state of $5E$ and the first excited state corresponds to $5T_2$ state, spin is conserved and we observe a selection rules allowed absorption from $5E$ to $5T_2$ state, wherein the photo-excited electron is later captured to reach a more stable Mn²⁺ state as shown in Figure 3.1 f). This process is known as charge transfer and it is well known that while the population in the

3. Mechanism of Mn Emission: Energy Transfer or Charge Transfer?

excited 4T_1 state is driven by selection rules in case of charge transfer, the same may not be true for energy transfer. Recently, it has been observed that the excitonic absorption survives for about a few picoseconds (ps) before transferring energy/charge to the dopant.²⁶ As this is on higher end of a normal energy transfer process and the lower end of the charge transfer process, it is necessary to probe further about the nature of the transition. Even though historically researchers have assumed this transition to be an energy transfer, in this chapter we present various experimental details, mostly in the last decade and discuss their consequences in terms of energy transfer or charge transfer to understand the mechanism.

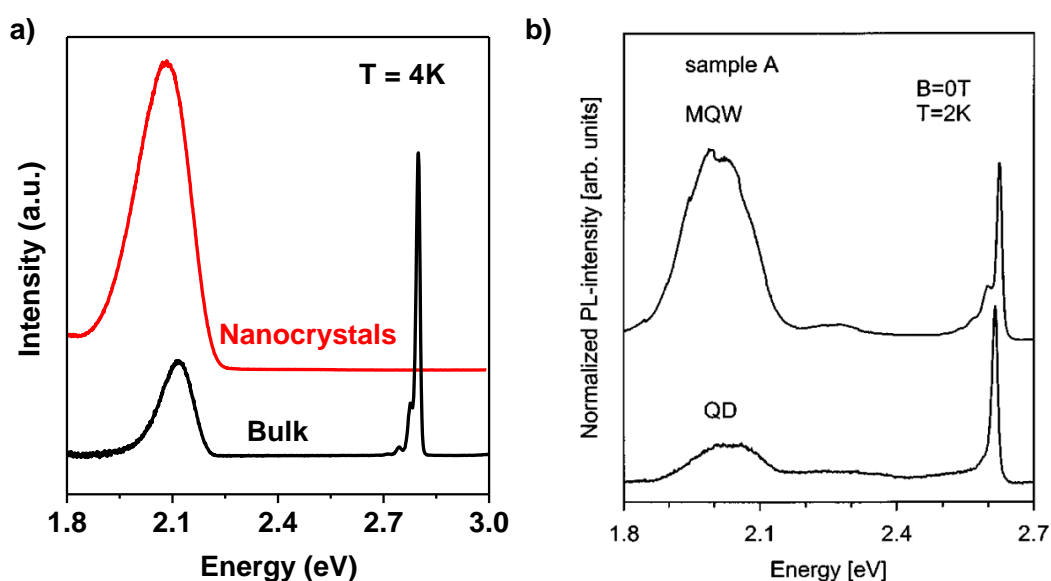


Figure 3.2 PL spectra of a) nanocrystalline and b) bulk Mn-doped ZnS (Ref. 8). Reproduced with permission from the American Physical Society.

Historically, Mn-doping was mostly explored in systems grown using molecular beam epitaxy until development in colloidal synthesis of QDs gained lot of attention. The whole process of colloidal synthesizing Mn-doped QDs has evolved over time with various modifications adapted from new methods to synthesize colloidal undoped II-VI semiconductor QDs. One of the earliest reports on Mn-doped ZnS QDs exhibiting 18 % PL QY was from Bhargava et al.³¹ and few years later colloidal synthesized ZnSe with Mn as a dopant gave PL QY of 22 % reported by Norris et al.³² Advances over the years in the colloidal synthesis strategies have led to high quality Mn-doped QDs with QY above 50 %.^{27, 33} Some of the landmark techniques that led to a change in the design strategy include hot-injection method by injecting the dopant precursor and the host precursors to pre-heated solvent at high temperature to form Mn-doped QDs, but it suffered from low doping yield due to the expulsion of the dopant ions to the surface of the QDs leading to poor dopant related features.² To tackle

3. Mechanism of Mn Emission: Energy Transfer or Charge Transfer?

these problems, lowering the reaction temperature, step by step separation of crystal growth and doping process were employed.³⁴ Mn ions were diffused by taking a core of MnSe in a shell of ZnSe to elevated temperature which is termed as “nucleation doping” and is developed by Peng’s group.³³ By taking high concentration of Mn²⁺ in the core, higher dopant concentration was achieved despite the loss of dopant during the diffusion of Mn²⁺ ions. Recently, the layer by layer growth of Mn-doped QDs evolved sufficiently to achieve the required control over the size, dopant concentration, location of dopant.^{35,36} Structural tuning of the QDs and dopant location in the QDs plays important role in giving rise to remarkable dopant related features and is important in understanding the energy and/or charge transfer dynamics from the host to dopant.

Mn emission in QDs is known to be substantially different than their bulk counterparts. For example, complete absence of band-edge emission in Mn-doped QDs is observed (Figure 3.2 a) unlike that in the bulk wherein both the band edge emission and the Mn emission are observed as seen from Figure 3.2 b).⁸ Initially this led Bhargava et. al³¹ to propose that the reported intense Mn d-d emission from the host excitation on Mn doped ZnS nanocrystals arises as a result of strong sp-d mixing due to localization of electron and hole in the Mn²⁺ ion in the quantum confined regime³¹ and hence leading to a substantial shortening of lifetime of Mn. However, this elucidation was later confirmed to be wrong.³⁷ Bol et. al showed that the emission and PLE spectra for Mn doped ZnS synthesized by two different methods such as organometallic synthesis and inorganic synthesis are not different from previous reports and the characteristic 590 nm emission was attributed to ⁴T₁-⁶A₁ transition of the Mn dopant. Lifetime studies from time resolved spectroscopy revealed that the decay lifetime of the Mn d-d emission is indeed long and in the range of 1-3 ms range like Mn d-d emission in the bulk Mn-doped ZnS. Hence it was deemed necessary to probe further to understand the nature of Mn emission.

One of the major arguments in literature in favor of energy transfer apart from the selection rules is the lack of sensitivity of Mn emission to the nature of the host except for the lattice strain. The insensitivity of the energy of Mn emission as a function of host energy gap suggests a possible energy transfer to the Mn levels wherein the atomic-like states of Mn are unaffected by the size and band gap of the host. However, for a given anion, local lattice strain resulting from the heterointerface of Mn ions as well as the hydrostatic pressure alters the Mn d-d splitting energy. It has since been proved by Hazarika *et al.* that by modifying the lattice strain on purpose by providing a hetero-interface, and locating the Mn ions at different radial positions, it is possible to achieve the entire rainbow emission (Figure 3.3 a)).²⁴ Other groups

3. Mechanism of Mn Emission: Energy Transfer or Charge Transfer?

have also shown limited tunability between 560 nm to 610 nm on addition of thiolate ligands to Mn doped ZnS QDs⁹ even though they have not explicitly correlated the tunability to lattice strain. This is not surprising as the energy of the ligand field transition is determined by the strength of the ligand field that is normally dictated by the coordination structure around the Mn²⁺ ions.³⁸ The strength of ligand field, spin-orbit coupling and the inter-dopant exchange interactions³⁹ have been the guiding factors in determining the energy of the Mn d-d transition. However, the relatively broad spectral width of these transitions from an atomic-like state have boggled researchers for several years. Strikingly, even in the case of rainbow emission from Mn doping, not only the peak position, but also the peak width of the Mn emission is very different. This wide transition has since been attributed to a convolution of several spectra, each having full width at half maximum of approximately 60-70 meV by performing single QD spectroscopy²⁵ as shown in Figure 3.3 b). This opened up the possibility to not only tune the position of the Mn spectra but also that this emission indeed carries information about the host lattice.

The second factor in favor of energy transfer is the high quantum yield of the Mn emission indicating an extremely efficient energy/charge transfer in spite of several competing charge trapping processes. If this transition is indeed an energy transfer process, it should be mediated through the exchange interaction between Mn²⁺ d electrons and the excitons as a dipole coupled energy transfer, which would give rise to a weak overlap between the donor and the acceptor. Also since the exchange interactions depend on wavefunction overlap between the two states, the rate of energy transfer should be strongly dependent on the relative location of the dopant with the QD as well as the doping concentration.²⁸ The rate of transfer of energy/charge from the exciton to the Mn states was originally assumed to be in sub-femtoseconds and was calculated earlier from the radiative and non-radiative rate constants.^{40, 41} However, in a heterogeneous environment, wherein the position of the Mn²⁺ ion cannot be precisely controlled, this is not very reliable. In the past, location and features of the dopant Mn were generally characterized using electron paramagnetic resonance (EPR) spectroscopy and inductive coupled plasma (ICP) techniques to quantify the dopant concentration. However, this widely used techniques can only distinguish between a tetrahedral and octahedral environment from the EPR line-splitting along with the prediction of Mn-Mn interactions from the broad linewidths.⁴² This information is insufficient to determine the nature of Mn atomic-like states excitation. Hence the use of optical and magneto-optical spectroscopy along with some local probe like extended x-ray absorption spectroscopy (EXAFS) are necessary to obtain detailed information on the location of the Mn ion in the host lattice. However, one of the

3. Mechanism of Mn Emission: Energy Transfer or Charge Transfer?

factors that came out of this study was the order of magnitude of the transition lifetimes. It was found that these transition times were not in the sub-fs regime as originally assumed but rather in a few picoseconds (ps).

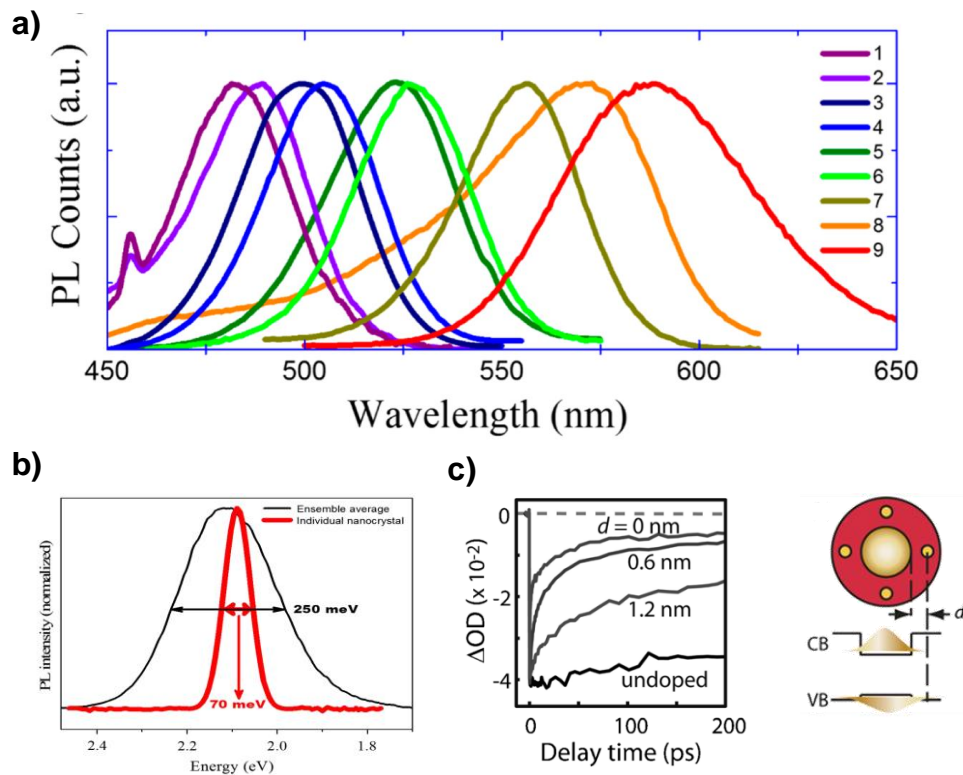


Figure 3.3 a) Mn emission spectra from doped QDs showing Mn emission tunability by doping Mn at various radial positions. (The numbers 1–9 indicate emission patterns from samples with Mn located at different distances from the ZnSe/CdSe interface. In samples 1–4, Mn is situated exactly at the interface. The CdSe thickness is different in each case. Samples 5–8 have Mn doped at different positions. Sample 9 is a Mn-doped ZnSe QD (zero CdSe thickness)). (Ref. 24). b) Comparison of PL spectra of single QD (thick line) with the ensemble (Ref. 25) c) Dynamics of band-edge bleach recovery of undoped and Mn-doped CdS/ZnS QDs with different doping locations at $n_{Mn} = \sim 6$. (Ref. 28) Reproduced with permission from American Physical Society and American Chemical Society respectively.

Direct measure of transition time ranging from a few hundred fs to a few ps can be probed through pump-probe techniques such as transient absorption wherein direct information regarding ultra-fast processes can help in resolving the fast process of excitation and emission. Son's group has probed both the band edge and intra-band electron absorption, for Mn doped CdS/ZnS using transient absorption spectroscopy.^{28, 43} By comparing the dynamic bleach recovery of the undoped and Mn doped QDs at the band edge, energy transfer rate can be

3. Mechanism of Mn Emission: Energy Transfer or Charge Transfer?

estimated. To understand the energy transfer in Mn doped QDs, various modifications in the parameters which directly depends on the optical performance can be made, such as studying the bleach recovery for samples with various doping location, host with varying sizes and structures, intentional introduction of various hole traps are some of them. Figure 3.3 c) shows the dynamic bleach recovery for the Mn doped and undoped QDs where the location of dopant is varied. By moving the dopant location closer to the core of the QDs, better overlap of the Mn wavefunction is expected and that would increase the energy transfer rate. It also to be noted here that rate of energy transfer is directly correlated to the quantum yield of the photoemission in these doped systems. Linear dependence in the doping location dependent energy transfer rate with the time scale of transfer between a single pair of exciton and Mn^{2+} was determined to be ~ 60 ps.²⁹ While this does give a better understanding of the transfer rate, this data is equally valid for either an energy transfer or a charge transfer. Though the original paper reports it as an energy transfer, it should be noted that the transfer time in the order of 4-80 ps is much longer than the normal energy transfer processes, especially considering such an efficient transfer. In fact, trap states would easily be able to compete with this transfer rate as was also found in this work wherein the hole traps occurred at 50-100 ps time scale.

The third argument in favour of energy transfer is that it is believed that doped Mn^{2+} ions in CdS/ZnS host function as energy acceptors rather than charge carrier acceptors because the charge transfer between a Mn^{2+} ion and valence or conduction band is energetically more expensive than the bandgap transition.⁴³ However, we show that in chapter 4 that the first principle density functional theory calculations in excited state to verify the probability of transformation of the Mn^{2+} ion to the Mn^{3+} ion by the removal of a relatively tightly bound 3d electron. We estimated the exciton formation energy, i.e., the energy required to remove the electron from the valence band forming an electron-hole pair, in ZnSe and Mn-doped ZnSe QDs (not equivalent to the exciton binding energy), of excitons in ZnSe QDs and Mn-doped ZnSe QDs to be respectively 1.8 eV and 885 meV suggesting an active involvement of the Mn ion in the excited state formation, thus favoring a charge transfer state. Hence so far, even though it has largely been assumed in literature as an energy transfer, there has been no convincing evidence in its favor.

It should be noted here that there have been several reports in literature^{7, 21, 44} wherein the bandgap is same or lower than the Mn emission energy, for example in Mn doped CdSe. These reports have discussed the formation of excitonic magnetic polarons,²³ wherein the charge carrier photoexcitation initiates formation of magnetic polaron formation as well as the

3. Mechanism of Mn Emission: Energy Transfer or Charge Transfer?

non-standard excitonic behavior in these materials. However, due to the spectral overlap of the Mn emission as well as the excitonic feature, it is non-trivial to obtain the origin of the observed spectral peak. Hence, we have refrained from commenting on these aspects.

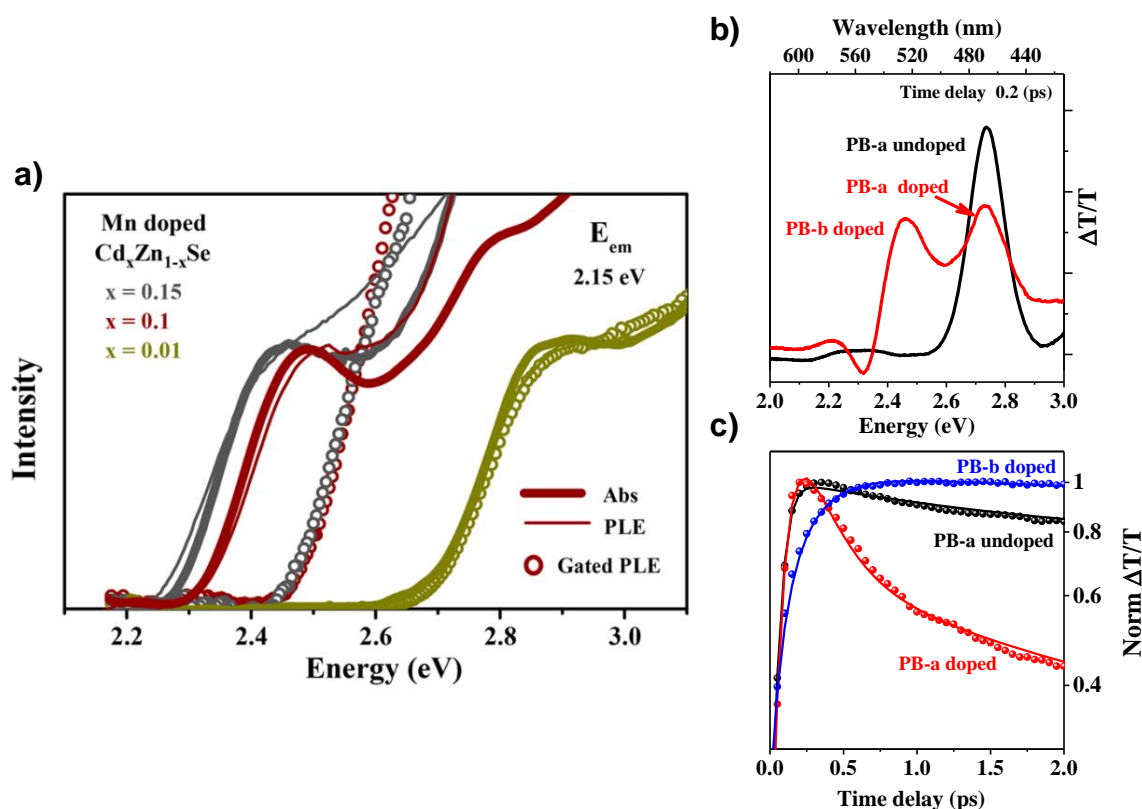


Figure 3.4 a) Gated PLE and time integrated PLE spectra for doped QDs taken at Mn d-d emission wavelength. b) differential transmission dynamics for the Mn doped and undoped QDs and c) differential transmission dynamics for the Mn doped and undoped QDs in the 0.2 ps region. Reproduced from Ref. 26 with permission from American Chemical Society.

However, light induced polaron formation was not just the work that challenged existing explanations for understanding the dopant related emission mechanism compared to bulk DMS systems, undoped and Mn doped studies. Recent reports have explored Mn emission mechanism in hosts whose band gaps are in resonance with the Mn emission energy. We demonstrated direct observation of the Mn excited state for the first time using gated photoluminescence excitation (PLE) and ultra-fast transient absorption techniques on QDs of bandgap closer to the Mn emission energy as discussed in chapter 4. Studies of PLE and gated PLE measurements as shown in Figure 3.4 a) gives important evidence towards the presence of a transient species. For samples with bandgap lower than 2.5 eV, the gated PLE goes to zero around 2.5 eV indicating the minimum energy required to excite the Mn which could be arising due to the presence of a transient species. Figure 3.4 b) compares the transient absorption

3. Mechanism of Mn Emission: Energy Transfer or Charge Transfer?

spectra (0.2 ps after the excitation) with the undoped QDs, (PB-a band) and the newly formed band in Mn doped QDs (PB-b band). Figure 3.4 c) reveals the early time of the species suggesting the growth of PB-b band at the cost of decay of PB-a species. Further, in a typical semiconductor QDs, addition of charge carrier traps like surface states leads to quenching of luminescence. For instance, it has been seen in literature that the transfer to Mn is most efficient and quick when the location of Mn is in the centre of the QD as seen in Figure 3.3 c), both due to a better wavefunction overlap as well as a low influence of trap states.

However, the most direct evidence of charge transfer state is when information coded in the excitonic charge carriers is transferred to the Mn emission. Two ways the information can be coded into the photo-excited electrons are by the spin polarization of the excitons and the transfer of long-lived photoexcited electron to sensitize the active layer and hence improve the power conversion efficiency of QD based solar cells. The concept of spin polarization is rather straight forward in doped semiconductors which are known to produce large Zeeman effect with g values of the order of 1000, demonstrating high excitonic polarisation. In Mn doped bulk semiconductors, wherein both Mn and excitonic emission are observed, application of magnetic field lead to the decay of Mn emission in both directions while the excitonic emission is highly polarised as shown in Figure 3.5 a). This is widely observed in the reports studied on bulk DMS and was considered as universal characteristic of DMS based materials.^{45, 46} This led researchers to conclude that excitonic emission was assisting the Mn emission with an overall conservation of spin. As soon as the excitonic spin is polarised and hence unable to compensate for the change of Mn spin, the transition becomes forbidden and hence decays quickly. However, later work on Mn doped semiconductor quantum dots have shown qualitatively different results even though the reason for these differing results have not been covered in these papers.^{20, 47} The interaction strength between the dopant ions and excitons depends on the spatial overlap of the two wavefunctions. In comparison to bulk, QDs provide more probability of overlap between the dopant and exciton wavefunctions which can lead to stronger interactions that provides more opportunities for tuning or enhancing the properties by structural variations.^{23, 28, 48}

In the case of Mn doped ZnSe/CdSe core-shell QDs, at zero field, only Mn d-d emission is observed even though the dopant percentage is less than 1 % demonstrating an efficient transfer from host to the dopant. In presence of external magnetic field, the Mn luminescence develops a sizable circular polarization.²⁰ Mn emission shows polarization both in intensity as well as energy of the peak position, and the PL is not suppressed as seen from Figure 3.5 b). Interestingly, as seen from Figure 3.5 c) the circular polarization of the Mn^{2+} follows Brillouin-

3. Mechanism of Mn Emission: Energy Transfer or Charge Transfer?

like paramagnetic magnetization behavior as measured from magnetic circular dichroism (MCD) data suggesting a transfer of excitonic spin polarization on to the Mn energy levels. The circular polarisation has been shown to scale with the independently measured MCD data as a function of temperature and magnetic field. Later work by a different group on Mn doped QDs in high Mn^{2+} concentration have shown a ferromagnetic alignment of the Mn^{2+} - Mn^{2+} dimers, with a 100% circular polarization as observed from time resolved magnetic circularly polarized PL arising from the polarization of the photo-excited charge carriers.⁴⁷ These data point direct evidence towards the charge transfer mechanism of electrons during the Mn emission.

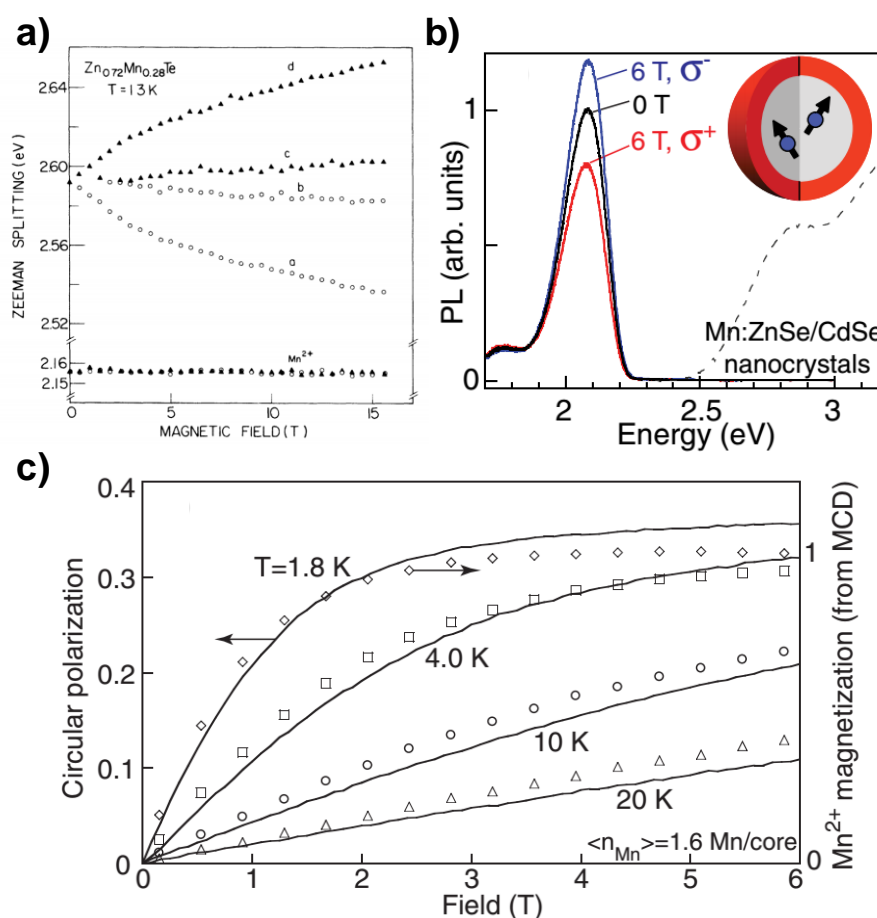


Figure 3.5 a) Magnetic field dependence of the Zeeman components of the free exciton and Mn d-d transitions in bulk $\text{Zn}_{0.72}\text{Mn}_{0.28}\text{Te}$ at 1.3 K (Solid triangles and open circles denote the transitions for σ^- and σ^+ polarization, respectively.) (Ref. ⁴⁹) b) Magneto PL from Mn doped ZnSe/CdSe QDs (Ref. 20). c) The circular polarization of the Mn^{2+} PL from Mn doped ZnSe/CdSe QDs versus field and temperature (lines; left axis). Circular polarization tracks the Brillouin-like Mn^{2+} magnetization (independently measured by MCD; points, right axis). (Ref. 20) Reproduced with permission from American Physical Society.

3. Mechanism of Mn Emission: Energy Transfer or Charge Transfer?

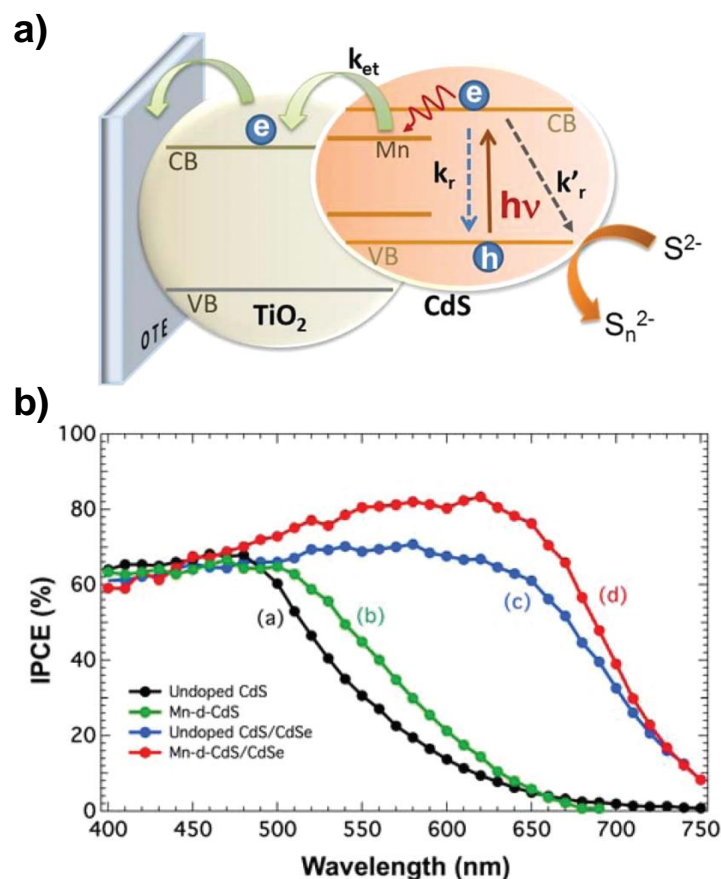


Figure 3.6 a) Schematic diagram of illustrating the electron transfer. b) The incident-photon-to-carrier conversion-efficiency (IPCE) spectra for undoped and Mn doped QD sensitized solar cells. Reproduced from Ref. ⁵⁰ with permission from American Chemical Society.

Finally, the use of Mn doped QDs in QD sensitized solar cells have demonstrated an improvement of power conversion efficiency by 20% compared to its undoped counterpart due to the long-lived nature of the Mn emission as well as a probable electron and/or hole acceptor.⁵⁰ If it was indeed an energy transfer, it would not have been able to transfer the charge to the TiO₂ (as per the schematic in Figure 3.6 a)) and hence show an improvement in the charge conversion efficiency as shown in Figure 3.6 b). Similarly in a study by Ghosh and co-workers, Mn center has been used as an electron storage tank.⁵¹ While these studies have existed in the past, reviews on this topic have claimed these studies as inconclusive evidence.³⁸ However, the capability of Mn to retain the spin information in presence of magnetic field in addition to these data as well as the observation of transient species in near resonant band gap materials suggest the involvement of charge carriers in the signature Mn emission peak.

3.3.2 Is the 580 nm peak really the signature of successful Mn emission?

Recently, a new class of materials aka inorganic perovskite QDs with high PL QY and narrow emission with wide tunability of bandgap over entire visible region by composition modulation

3. Mechanism of Mn Emission: Energy Transfer or Charge Transfer?

have gained lots of attention.^{52, 53} Due to their ease of solution processability, perovskite QDs are one of the ideal systems for Mn doping to testify energy or charge transfer mechanism. Mn doping in high bandgap CsPbCl₃ QDs show intense Mn emission having the potential to open up new era of research in the field of light emitting materials.^{15, 54}

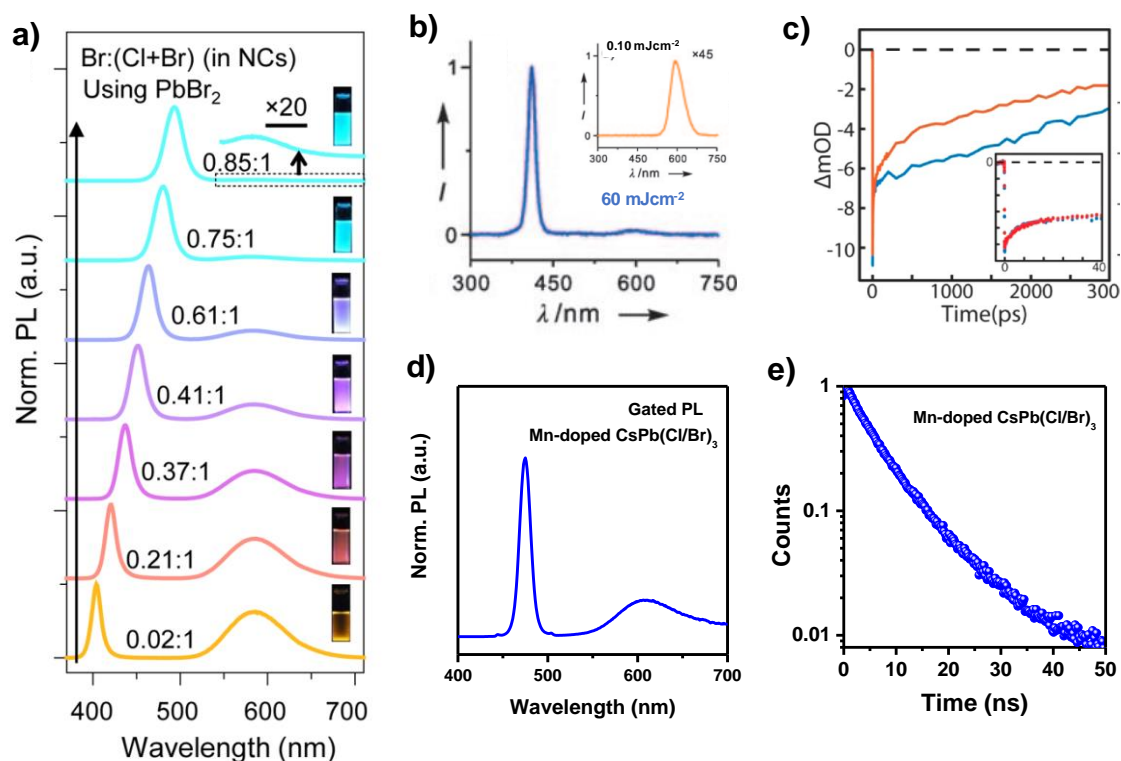


Figure 3.7 a) Decreasing Mn emission upon Br incorporation in Mn doped mixed halide perovskite QDs. (Ref. 15) b) PL spectra for Mn doped CdS/ZnS QDs at high excitation fluence of 60 mJ cm^{-2} with the inset showing the same spectra at 0.10 mJ cm^{-2} . (Ref. 55) c) Transient absorption for the undoped and Mn doped perovskite CsPbCl₃ QDs. (Ref. 6) d) Gated PL spectra and e) PL lifetime at band edge for Mn doped CsPb(Cl/Br)₃. Reproduced with permission from American Chemical Society and Wiley VCH.

However, the major difference observed between II-VI semiconductor QDs and perovskite QDs as a host for Mn doping is the presence of small band edge emission in spite of improvements in the synthesis techniques. It is to be noted here that while hosts like CsPbCl₃ have shown a dominant Mn emission, as the band gap approaches closer to the Mn emission energy, we see a decrease in the Mn emission with a complete absence of Mn d-d emission in lower bandgap hosts like CsPbBr₃ as shown in Figure 3.7 a).¹⁵ It is also noteworthy here that even II-VI semiconductors have shown the presence of band edge emission at high fluence as observed in Figure 3.7 b) even though they show an efficient Mn emission at low fluence (Inset to Figure 3.7 b)).⁵⁵ Hence even though the signature of successful Mn doping in QDs is

3. Mechanism of Mn Emission: Energy Transfer or Charge Transfer?

classified by typical orange emission peak at 580 nm, by varying the fluence it has been possible to suppress this emission.⁵⁶ There are also various cases in II-VI semiconductor QDs wherein the band gap is smaller than the Mn emission energy and has demonstrated thermally assisted back transfer at low temperature leading to the presence of strong band edge emission.⁴

However, the absence of Mn d-d emission in perovskite systems, even at single excitonic excitation and at room temperature wherein the host band gap is larger than the Mn emission energy, can arise either due to inefficient doping or lack of proper pathways to excite Mn levels. Detailed understanding of the excitation mechanism of Mn in perovskite hosts is necessary to understand the complex process involved in the field of doped QDs. Compared to Mn doped CdS/ZnS QDs, CsPbCl₃ shows weaker exchange coupling due to lack of strong confinement effects in perovskite QDs.⁶ Transient absorption studies on undoped and Mn doped perovskite QDs as seen from Figure 3.7 c) show similar charge carrier dynamics in undoped and Mn doped perovskite QDs with a notable absence of the fast decay component in doped perovskites unlike II-VI semiconductor QDs. Even more surprisingly, gated PL measurements on these Mn doped perovskite QDs within the mixed halide composition and a gating time of several microseconds (200 μ s) show the presence of a band-edge emission even though the lifetime of the band edge emission is observed to be a few nanoseconds (\sim 20-100 ns)⁵² as shown respectively in Figure 3.7 d) and Figure 3.7 e). This has been shown to arise due to drip-feeding of photoexcited electrons from Mn²⁺ to the host conduction band through vibrational coupling as vibrationally assisted delayed fluorescence (VADF) as discussed later in this thesis. This state specific presence of band edge emission in Mn doped perovskite QDs opens up new challenges in understanding the complex photophysical properties involved in transition metal doped QDs with the prominent unanswered question being is the 580 nm emission the signature peak of successful Mn incorporation as well as the mechanism of the emission.

3.4. Conclusions

In summary, here we have discussed the physics behind Mn emission, selection rules and thermodynamics of photons and charge carriers associated with dopants in photoexcited colloidal QDs. We have then discussed the pathways of energy or charge flow in the excited states. While the interest in doped QDs has been focused largely on the efficiency of dopant emission and on the spectral tunability of the luminescence, little emphasis has been given in literature to understand the physics behind these transitions even though these transitions provide a useful platform for exploring the nature and strength of the sp-d coupling between

3. Mechanism of Mn Emission: Energy Transfer or Charge Transfer?

the host and the dopant ions. Additionally, magnetism carried by the dopant and its ability to provide large magneto-optical signatures could be used as a useful tool to understand the nature of these transitions. The progress made in the understanding of the photons and charge carriers involved is the combined efforts of developing synthetic methodologies as well as designing new novel experiments to pin down the processes involved. Just as we were reaching a conclusion on the mechanism of Mn emission and excitation after decades of research, the advent of Mn doped perovskites has thrown fresh challenges in the field. An understanding of the underlying principles at the nanoscopic level will continue to be crucial for future research in this field.

3. Mechanism of Mn Emission: Energy Transfer or Charge Transfer?

Bibliography

1. Norris, D. J.; Efros, A. L.; Erwin, S. C. *Science* **2008**, 319, (5871), 1776-1779.
2. Erwin, S. C.; Zu, L.; Haftel, M. I.; Efros, A. L.; Kennedy, T. A.; Norris, D. J. *Nature* **2005**, 436, (7047), 91.
3. Chen, W.; Zhang, J. Z.; Joly, A. G. *J. Nanosci. Nanotechnol.* **2004**, 4, (8), 919-947.
4. Beaulac, R.; Archer, P. I.; van Rijssel, J.; Meijerink, A.; Gamelin, D. R. *Nano Lett.* **2008**, 8, (9), 2949-2953.
5. Sarma, D. D.; Viswanatha, R.; Sapra, S.; Prakash, A.; Garcia-Hernandez, M. J. *Nanosci. Nanotechnol.* **2005**, 5, (9), 1503-1508.
6. Rossi, D.; Parobek, D.; Dong, Y.; Son, D. H. *J. Phys. Chem. C* **2017**, 121, (32), 17143-17149.
7. Beaulac, R.; Archer, P. I.; Ochsenbein, S. T.; Gamelin, D. R. *Adv. Funct. Mater.* **2008**, 18, (24), 3873-3891.
8. Falk, H.; Hübner, J.; Klar, P. J.; Heimbrodt, W. *Phys. Rev. B* **2003**, 68, (16), 165203.
9. Pradhan, N.; Peng, X. *J. Am. Chem. Soc.* **2007**, 129, (11), 3339-3347.
10. Pradhan, N.; Sarma, D. D. *J. Phys. Chem. Lett.* **2011**, 2, (21), 2818-2826.
11. Bol, A. A.; Meijerink, A. *Phys. Rev. B* **1998**, 58, (24), R15997.
12. Ithurria, S.; Guyot-Sionnest, P.; Mahler, B.; Dubertret, B. *Phys. Rev. Lett.* **2007**, 99, (26), 265501.
13. Nag, A.; Cherian, R.; Mahadevan, P.; Gopal, A. V.; Hazarika, A.; Mohan, A.; Vengurlekar, A.; Sarma, D. D. *J. Phys. Chem. C* **2010**, 114, (43), 18323-18329.
14. Mir, W. J.; Jagadeeswararao, M.; Das, S.; Nag, A. *ACS Energy Lett.* **2017**, 2, (3), 537-543.
15. Liu, W.; Lin, Q.; Li, H.; Wu, K.; Robel, I.; Pietryga, J. M.; Klimov, V. I. *J. Am. Chem. Soc.* **2016**, 138, (45), 14954-14961.
16. He, M.; Cheng, Y.; Shen, L.; Shen, C.; Zhang, H.; Xiang, W.; Liang, X. *Applied Surface Science* **2018**, 448, 400-406.
17. Farrow, B.; Kamat, P. V. *J. Am. Chem. Soc.* **2009**, 131, (31), 11124-11131.
18. Haque, S. A.; Palomares, E.; Cho, B. M.; Green, A. N.; Hirata, N.; Klug, D. R.; Durrant, J. R. *J. Am. Chem. Soc.* **2005**, 127, (10), 3456-3462.
19. Sukhovatkin, V.; Hinds, S.; Brzozowski, L.; Sargent, E. H. *Science* **2009**, 324, (5934), 1542-1544.

3. Mechanism of Mn Emission: Energy Transfer or Charge Transfer?

20. Viswanatha, R.; Pietryga, J. M.; Klimov, V. I.; Crooker, S. A. *Phys. Rev. Lett.* **2011**, 107, (6), 067402.
21. Bacher, G.; Schneider, L.; Beaulac, R.; Archer, P. I.; Gamelin, D. R. *J. Korean Phys. Soc.* **2011**, 58, (51), 1261-1266.
22. Rice, W. D.; Liu, W.; Pinchetti, V.; Yakovlev, D. R.; Klimov, V. I.; Crooker, S. A. *Nano Lett.* **2017**, 17, (5), 3068-3075.
23. Beaulac, R.; Schneider, L.; Archer, P. I.; Bacher, G.; Gamelin, D. R. *Science* **2009**, 325, (5943), 973-976.
24. Hazarika, A.; Pandey, A.; Sarma, D. D. *J. Phys. Chem. Lett.* **2014**, 5, (13), 2208-2213.
25. Hazarika, A.; Layek, A.; De, S.; Nag, A.; Debnath, S.; Mahadevan, P.; Chowdhury, A.; Sarma, D. D. *Phys. Rev. Lett.* **2013**, 110, (26), 267401.
26. Gahlot, K.; R, P. K.; Camellini, A.; Sirigu, G.; Cerullo, G.; Zavelani-Rossi, M.; Singh, A.; Waghmare, U. V.; Viswanatha, R. *ACS Energy Lett.* **2019**, 4, (3), 729-735.
27. Srivastava, B. B.; Jana, S.; Karan, N. S.; Paria, S.; Jana, N. R.; Sarma, D. D.; Pradhan, N. *J. Phys. Chem. Lett.* **2010**, 1, (9), 1454-1458.
28. Chen, H.-Y.; Maiti, S.; Son, D. H. *ACS Nano* **2012**, 6, (1), 583-591.
29. Chen, H.-Y.; Chen, T.-Y.; Son, D. H. *J. Phys. Chem. C* **2010**, 114, (10), 4418-4423.
30. Das Adhikari, S.; Dutta, S. K.; Dutta, A.; Guria, A. K.; Pradhan, N. *Angew. Chem.* **2017**, 56, (30), 8746-8750.
31. Bhargava, R. N.; Gallagher, D.; Hong, X.; Nurmikko, A. *Phys. Rev. Lett.* **1994**, 72, (3), 416.
32. Norris, D. J.; Yao, N.; Charnock, F. T.; Kennedy, T. A. *Nano Lett.* **2001**, 1, (1), 3-7.
33. Pradhan, N.; Goorskey, D.; Thessing, J.; Peng, X. *J. Am. Chem. Soc.* **2005**, 127, (50), 17586-17587.
34. Archer, P. I.; Santangelo, S. A.; Gamelin, D. R. *Nano Lett.* **2007**, 7, (4), 1037-1043.
35. Yang, Y.; Chen, O.; Angerhofer, A.; Cao, Y. C. *J. Am. Chem. Soc.* **2006**, 128, (38), 12428-12429.
36. Yang, Y.; Chen, O.; Angerhofer, A.; Cao, Y. C. *J. Am. Chem. Soc.* **2008**, 130, (46), 15649-15661.
37. Bol, A.; Meijerink, A. *Phys. Rev. B* **1998**, 58, (24), R15997.
38. Qiao, T.; Parobek, D.; Son, D. H. *J. Mater. Chem. C* **2019**.
39. Boulanger, D.; Parrot, R.; Cherfi, Z. *Phys. Rev. B* **2004**, 70, (7), 075209.
40. Andersen, D. R.; Kolodziejski, L. A.; Gunshor, R. L.; Datta, S.; Kaplan, A. E.; Nurmikko, A. V. *Appl. Phys. Lett.* **1986**, 48, (23), 1559-1561.

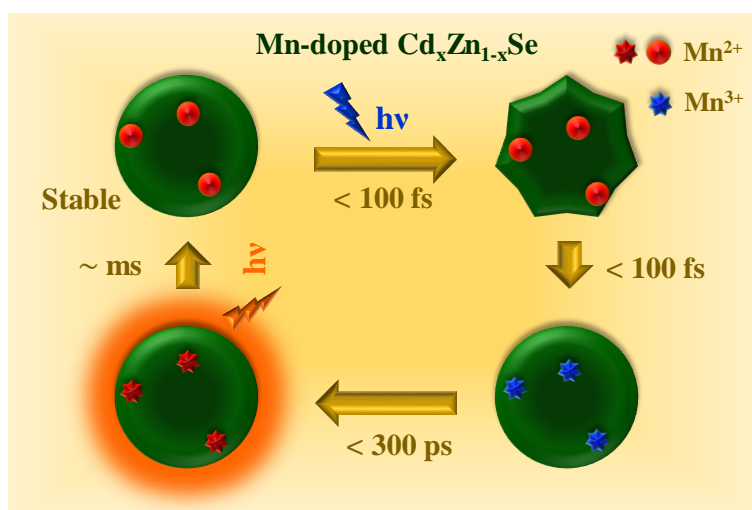
3. Mechanism of Mn Emission: Energy Transfer or Charge Transfer?

41. Seufert, J.; Bacher, G.; Scheibner, M.; Forchel, A.; Lee, S.; Dobrowolska, M.; Furdyna, J. K. *Phys. Rev. Lett.* **2001**, 88, (2), 027402.
42. Ji, T.; Jian, W.-B.; Fang, J. *J. Am. Chem. Soc.* **2003**, 125, (28), 8448-8449.
43. Chen, H. Y.; Son, D. H. *Isr. J. Chem.* **2012**, 52, (11-12), 1016-1026.
44. Nelson, H. D.; Bradshaw, L. R.; Barrows, C. J.; Vlaskin, V. A.; Gamelin, D. R. *ACS nano* **2015**, 9, (11), 11177-11191.
45. Furdyna, J. K. *J. Appl. Phys.* **1988**, 64, (4), R29-R64.
46. Lee, S.; Dobrowolska, M.; Furdyna, J. K. *Phys. Rev. B* **2005**, 72, (7), 075320.
47. Bradshaw, L. R.; May, J. W.; Dempsey, J. L.; Li, X.; Gamelin, D. R. *Phys. Rev. B* **2014**, 89, (11), 115312.
48. Maksimov, A. A.; Bacher, G.; McDonald, A.; Kulakovskii, V. D.; Forchel, A.; Becker, C. R.; Landwehr, G.; Molenkamp, L. W. *Phys. Rev. B* **2000**, 62, (12), R7767.
49. Lee, Y. R.; Ramdas, A. K.; Aggarwal, R. L. *Phys. Rev. B* **1988**, 38, (15), 10600.
50. Santra, P. K.; Kamat, P. V. *J. Am. Chem. Soc.* **2012**, 134, (5), 2508-2511.
51. Debnath, T.; Maity, P.; Maiti, S.; Ghosh, H. N. *J. Phys. Chem. Lett.* **2014**, 5, (16), 2836-2842.
52. Nedelcu, G.; Protesescu, L.; Yakunin, S.; Bodnarchuk, M. I.; Grotevent, M. J.; Kovalenko, M. V. *Nano Lett.* **2015**, 15, (8), 5635-5640.
53. Diroll, B. T.; Nedelcu, G.; Kovalenko, M. V.; Schaller, R. D. *Adv. Funct. Mater.* **2017**, 27, (21), 1606750.
54. Pradhan, N. *J. Phys. Chem. Lett.* **2019**.
55. Chen, O.; Shelby, D. E.; Yang, Y.; Zhuang, J.; Wang, T.; Niu, C.; Omenetto, N.; Cao, Y. C. *Angew. Chem.* **2010**, 49, (52), 10132-10135.
56. Sun, Q.; Wang, S.; Zhao, C.; Leng, J.; Tian, W.; Jin, S. *J. Am. Chem. Soc.* **2019**.

3. Mechanism of Mn Emission: Energy Transfer or Charge Transfer?

Chapter 4

Transient Species Mediated Energy Transfer in Mn Doped II-VI Semiconductor Quantum Dots



The following papers have been published based on work presented here:

Gahlot, K, Pradeep K R, A. Camellini, G. Sirigu, G. Cerullo, M. Rossi, A. Singh, U.V. Waghmare, and R. Viswanatha. "Transient Species Mediating Energy Transfer to Spin-Forbidden Mn d States in II–VI Semiconductor Quantum Dots." *ACS Energy Lett.* (2019), 4, 729-735.

4. Transient Species Mediated Energy Transfer

4. Transient Species Mediated Energy Transfer

4.1. Abstract

The nature of the transient species leading to emission from the spin/orbital forbidden Mn *d-d* transition in doped semiconductor quantum dots has intrigued scientists for a long time. This understanding is important in the quest for energy efficiency as the energy from the conduction band is transferred efficiently to Mn in femtosecond timescale overcoming other non-radiative recombination pathways. In this chapter, we have shown the presence of the transient species using materials with band gaps in resonance with the energy of the Mn emission to understand the nature of the absorbing, transient and emitting species. Detailed studies lead to the emergence of transient Mn³⁺ state that is further corroborated with spin dependent density functional theory calculations. This opens up a unique opportunity to realize a reversible photochemical reaction and high radiative efficiency in a semiconductor nanostructure by controlling the spin state of the magnetic ion by external illumination.

4.2. Introduction

Luminescent materials are characterized by the emission of light with energy beyond thermal equilibrium. In spite of the great strides made in this field, specifically using quantum dots (QDs), optimization of emission energy efficiency has been the driving force for the still challenging research in this field. In this context, the presence of spin forbidden transitions, like the Mn *d-d* emission, has long been recognized as a hindrance to energy efficiency. Remarkably, Mn doped semiconductors, specifically three-dimensionally confined colloidal QDs, present high photoluminescence (PL) quantum yield (QY) in spite of the spin forbidden nature of the Mn *d-d* emission.¹⁻⁶ Mn emission has an intense orange-yellow color, apparently invariant at around 2.15 eV (585 nm) with limited tunability (<150 meV).⁷⁻¹⁰ However among the many questions that remain unanswered for more than a decade, are the QDs specific properties like complete absence of band edge emission,⁴ anomalous polarization in magnetic fields,¹¹ wave-function engineering of exchange constants,^{12, 13} excitonic magnetic polarons,^{14,} ¹⁵ light-induced spontaneous magnetization,¹⁶ epitaxial strain and crystal field induced broad tunability of the Mn emission.^{17, 18}

Central to such a large number of unexpected anomalous properties, is the excitation and emission mechanism. Despite the spin and orbital forbidden nature of both Mn excitation and emission, this emission at 2.15 eV has been universally considered as a signature of Mn doping in II-VI semiconductors. The excitation dynamics of Mn can happen by two competing parallel pathways which can either be energy transfer or charge transfer by the host or the organic

4. Transient Species Mediated Energy Transfer

ligand on the surface. It has been widely argued in literature that the Mn emission occurs by the energy transfer processes rather than the charge transfer.^{19, 20} One of the first proposed explanations for this intense emission, enhanced in QDs, was the strong *sp-d* mixing due to localization of the electron and hole in the Mn²⁺ ion leading to a shortening of the lifetime of Mn emission;²¹ this assumption was however later proven to be wrong.⁶ Since then various explanations including Auger-like energy transfer to Mn²² and total spin conservation through the excitonic emission^{23, 24} have been put forward. However, although theories like non-radiative Auger-like energy transfer to Mn *d* states explain properties of bulk materials,^{23, 24} they fail to explain QDs specific properties like polarization of Mn emission in presence of magnetic fields.¹¹ Even though there have been several anomalous observations that are not explained by the process of energy transfer, there has been no direct observation of the charge transferred state in literature until now. Recently a few studies²⁵⁻³⁰ have shown that the exciton-dopant transfer time decreases in presence of Mn doping, effectively competing with both radiative and nonradiative relaxation of exciton and opening an ultrafast (< 100 fs) one-way channel for the localization of the photo-excited electron into the Mn *d*-states. Though indirect evidences for the presence of such a species have been presented and probable pathways are predicted²⁹, this transient species has neither been observed nor are its properties understood. Hence it is believed that the charge transfer is energetically unfavourable as it involves changing of the oxidation state of the metal. However, similar transfer of charge from nanomaterial core to surface with electron transfer has been discussed in literature.^{31, 32} Many of these open questions can be addressed by understanding the nature of the transient species mediating this transfer. Further, this efficient extraction can be utilized to channel the electrons into energy efficient pathways, possibly back towards the radiative pathways of the host. This understanding of the mechanism of Mn emission has an immediate consequence in overcoming internal energy losses and spin driven opto-electronics may be a new strategy for designing optimal devices for photo-emissive and photo-voltaic applications.³³⁻³⁵

In this chapter, we demonstrate for the first-time direct observation of the charge transfer state using transient absorption spectroscopy when the band gap is in resonance with the atomic-like Mn *d*-states. We address this long-standing puzzle by spectroscopic studies on Mn-doped Cd_xZn_{1-x}Se QDs, prepared by slow addition of Cd precursor at high temperature to Mn-doped ZnSe.⁴ Detailed characterization is shown in Figure 4.1. Steady-state and gated PL and ultrafast transient absorption (TA) spectroscopy were used to study the QDs. QDs with band gaps (E_g) in the range of 2.3- 2.9 eV, tuned by varying the Cd concentration, showed a dual wavelength emission, which we interpret in terms of a transient species mediating energy

4. Transient Species Mediated Energy Transfer

transfer to the Mn *d* states. Additionally, in QDs with bandgap comparable to the Mn emission the lifetime of the transient species was increased and its growth and decay were resolved using ultrafast TA spectroscopy. This work substantiates the characteristic point that tuning the band gap of host nanocrystals in proximity to Mn levels leads to the excitation of Mn by transfer of electron within tens of ps. We use low temperature PL spectra to demonstrate the population transfer kinetics and the activation barrier as a function of temperature. These results provide new insights into the Mn absorption and emission mechanism in doped semiconductor QDs. A mechanism involving transient charge transfer was proposed and its possibility was verified using first-principles calculations based on spin dependent density functional theory (DFT). Further, when the excitonic gap is in complete resonance with the Mn emission energy or lower, we observed greater than 10-fold increase in absolute QY of the material even though the signature Mn peak was absent. We show possibly for the first time a slow and state specific back transfer to the excitonic states providing a new pathway for energy efficiency. It is also important to note that the long-lived nature of Mn states has potential applications in storing and extracting electronic states as separated charge carriers.³⁶

4.3. Experimental Methods

Briefly, Mn-doped ZnSe QDs was prepared using modified literature methods.⁴ Initially, Mn precursor with octadecene (ODE) was taken in a three necked round bottom flask and degassed for an hour at 100 °C and followed by purging of Ar and then the temperature is raised to 280 °C. TOP-Se was then added instantly and the reaction mixture was kept for an hour at 260 °C. Later, Zn precursor was added dropwise and after 4 min, 1:1 mixture of ODE and Oleylamine was added. The temperature was brought down to 140 °C and appearance of bright orange emission under UV light confirms Mn doping. Host bandgap tuning was achieved by the addition of cadmium precursor using a syringe pump for an hour at constant rate and the collection of aliquots at different time intervals. These samples were thoroughly washed, characterized using x-ray diffraction to determine the crystal structure, as shown in Figure 4.1 a). Peak shift in the X-ray diffraction (XRD) pattern confirms Cd-doping in the zinc blend structure of ZnSe. Transmission electron microscopy (TEM) is used to determine the size of the Mn doped QDs as shown in Figure 4.1 b) and c). The average size of the Mn doped QDs are 4.7 nm as seen from the size distribution histogram. and inductively coupled plasma optical emission spectroscopy (ICP-OES) was employed to determine the percentage of Mn and Cd

4. Transient Species Mediated Energy Transfer

with respect to Zn. Mn in all the doped samples was found to be about 1% of the cation concentration.

To determine the electronic and atomic structure of ZnSe and Mn-doped ZnSe nano-clusters, we have used first-principles calculations based on density functional theory (DFT) as implemented in Quantum Espresso code³⁷, modeling the interaction between ionic cores and valence electrons with norm-conserving pseudopotentials.^{38, 39} We treated the exchange-correlation energy of electrons within a local density approximation (LDA) using a functional form parametrized by Perdew, and Zunger⁴⁰. In the self-consistent field (SCF) calculations, we truncated the plane wave basis with cut-off energies of 70 Ry and 280 Ry in representations of Kohn-Sham wave functions and charge density, respectively. We relaxed the geometry of each structure fully until atomic forces converged within $0.03 \text{ eV}\text{\AA}^{-1}$ are obtained. To simulate an isolated (free) cluster, we used a $20 \text{ \AA} \times 20 \text{ \AA} \times 20 \text{ \AA}$ periodic cubic cell, and only the wavefunctions at Γ point (Bloch vector = $(0,0,0)$). We simulated ZnSe cluster of diameters is about 10 \AA made of 20 atoms (10 Zn atoms and 10 Se atoms) (refer Figure 4.2 a)). We replaced one Zn atom in ZnSe nanocluster by a Mn atom to construct Mn-doped ZnSe nanocluster (NC) (see Figure 4.2 b)), and simulated it with spin dependent DFT.

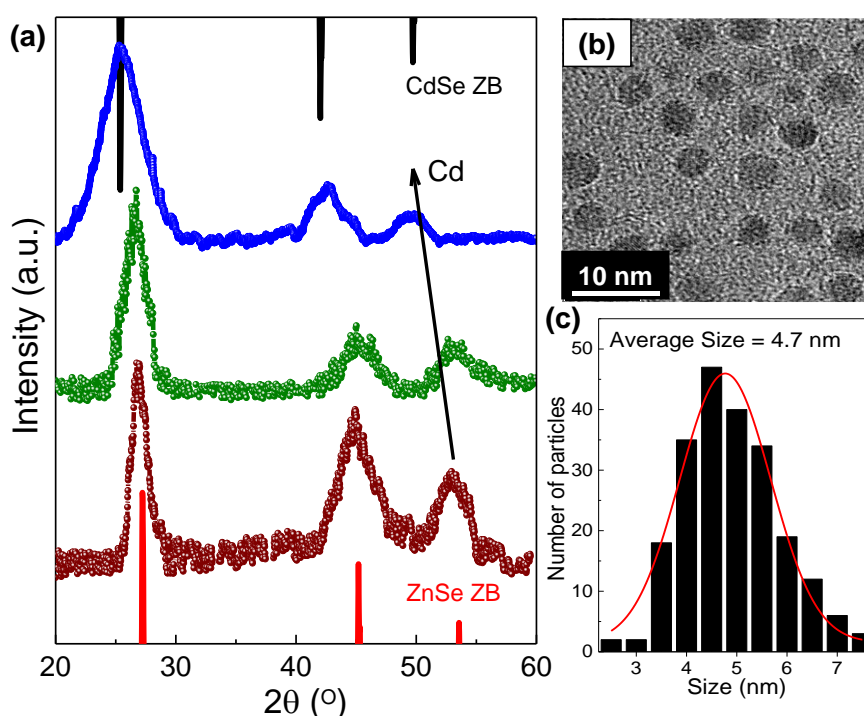


Figure 4.1 (a) XRD pattern for Mn doped $\text{Cd}_x\text{Zn}_{1-x}\text{Se}$ QDs. (b) TEM image of Mn doped $\text{Cd}_x\text{Zn}_{1-x}\text{Se}$ QDs ($x = 0.05$, Scale bar – 10 nm) (c) Size distribution histogram of the same showing average size to be 4.7 nm.

4. Transient Species Mediated Energy Transfer

We determined the exciton formation energy of ZnSe and Mn-doped ZnSe nanoclusters starting with a N-particle ground state, where all the electrons occupy valence states at zero temperature. We have used constrained occupation number method to model an exciton, in which we excite an electron from the highest occupied molecular orbital (HOMO) to lowest unoccupied molecular orbital (LUMO) creating a pair of hole and an electron. The exciton formation energy (E_{form}) can be estimated using:

$$E_{\text{Form}}=E_{\text{es}}-E_{\text{gs}}$$

where E_{es} and E_{gs} are the energies of N particle excited and ground states respectively. The supernatant comprising the QDs was then stored under refrigeration.

4.4. Results and Discussion

In order to understand the nature of Mn emission, we use four samples with E_g ranging from 2.3-2.9 eV (obtained from maxima of the first derivative of the absorption spectrum) as shown by the absorption spectra of doped and undoped $\text{Cd}_x\text{Zn}_{1-x}\text{Se}$ QDs as shown Figure 4.2. Figure 4.3 a) shows the room temperature steady state PL spectra of Mn-doped (thin solid lines) and undoped (dotted lines) $\text{Cd}_x\text{Zn}_{1-x}\text{Se}$ QDs for E_g ranging from 2.3 to 2.9 eV.

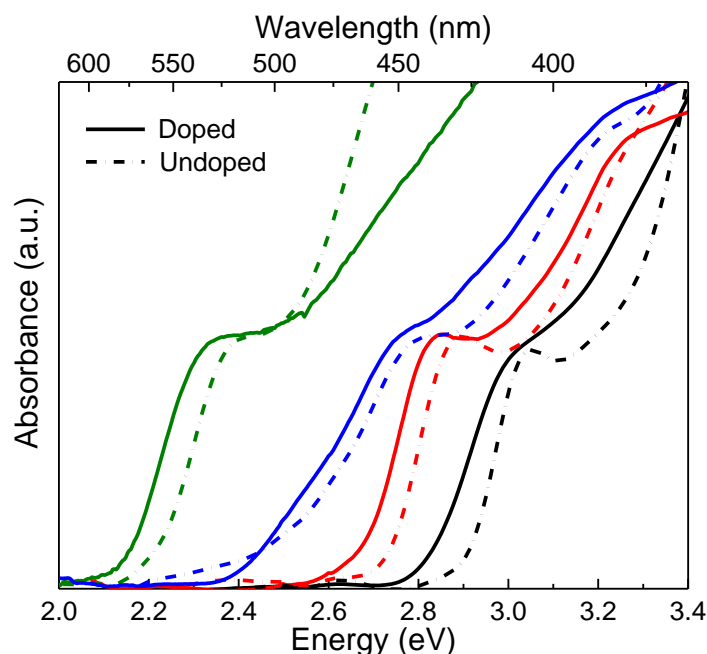


Figure 4.2 Optical absorption spectrum of Mn doped $\text{Cd}_x\text{Zn}_{1-x}\text{Se}$ and $\text{Cd}_x\text{Zn}_{1-x}\text{Se}$ QDs for x values ranging from 0 to 0.2

4. Transient Species Mediated Energy Transfer

From this data, it is evident that Mn doped higher E_g materials (> 2.8 eV) are characterized by an intense single peak at 2.15 eV. However smaller E_g materials show the presence of a second peak at higher energy (Peak II). Earlier literature reports have assigned this new peak to the band edge emission from the undoped fraction of the QDs.⁴¹ However, the band edge emission occurs at much higher photon energy for materials with similar E_g (dotted lines in Figure 4.3 b)) negating the previous assignment. Observation of this peak II in homogenous systems like CdSe⁴¹⁻⁴³ and the absence of lattice strain required to tune the Mn emission to 2.5 eV^{17, 18} excludes the possibility of the emission from the fraction of strained QDs.

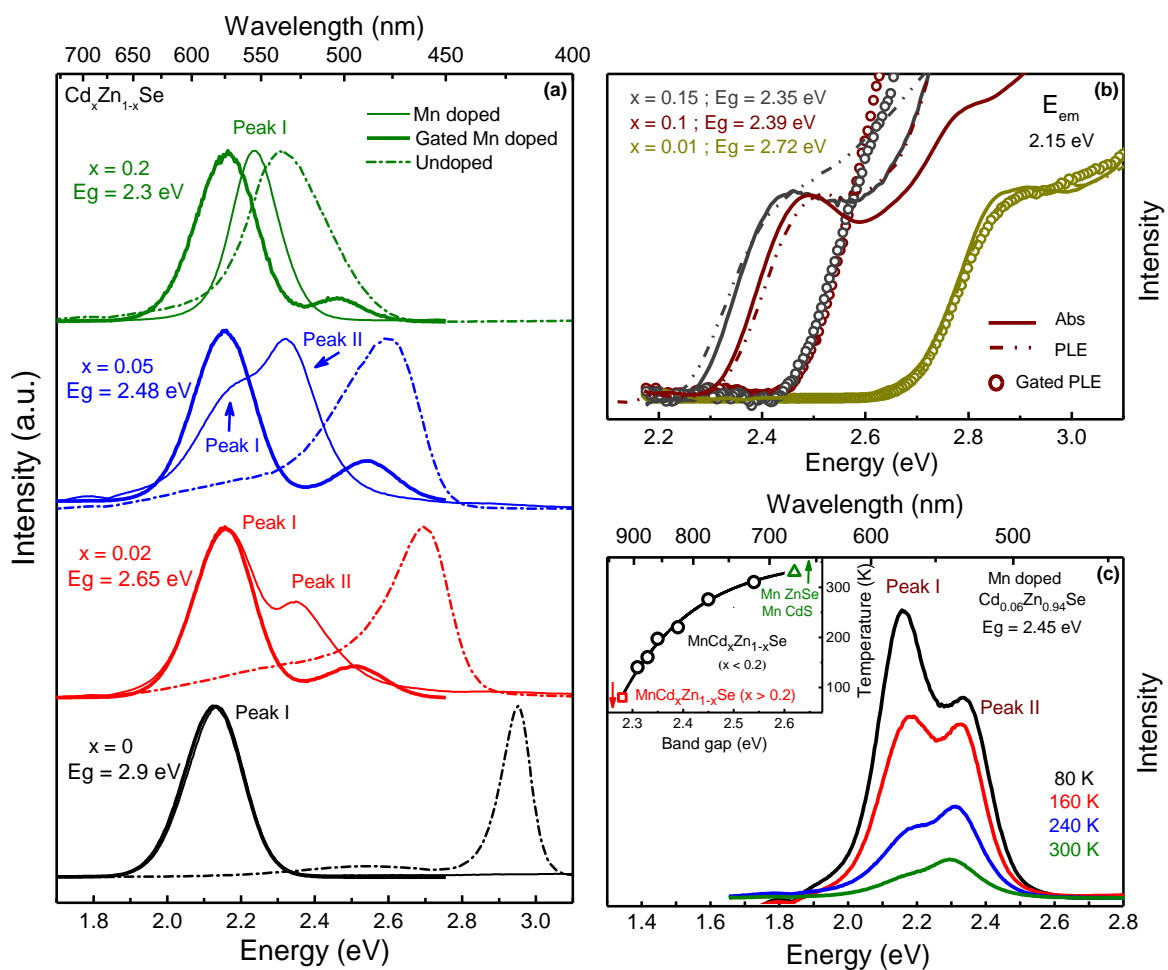


Figure 4.3 (a) Steady state and gated PL of doped QDs (thin lines and thick lines respectively). dotted lines show steady state PL of the undoped QDs. (b) Gated PLE with a delay of 100 μ s and time-integrated PLE spectra of doped QDs taken at 2.15 eV. (c) Temperature dependence of steady state PL measurements for doped QDs with E_g of 2.45 eV ($x = 0.06$). Inset shows the plot of T_c , as a function of E_g of the host material. Solid line is a guide to the eye.

4. Transient Species Mediated Energy Transfer

In order to understand the nature of this peak II, we measured PL of Mn-doped samples collected after 100 μ s (gated emission) and the results are shown as thick lines in Figure 4.3 a). We note here that there exist two peaks even in the gated PL emission at relatively invariant positions (~ 2.15 and ~ 2.5 eV) indicating two species, one long lived and another that is either long lived or is electronically coupled to the long-lived Mn emission. The variable energy peak II observed in steady state PL could be a convolution of peak I with the ~ 2.5 eV peak, with the actual position and intensity depending on the relative ratios of the two peaks. We tentatively assign the peak at ~ 2.5 eV to a short-lived transient species that is electronically coupled to the long-lived Mn emission peak.

PL excitation (PLE) and gated PLE spectra measured at a PL emission of 2.15 eV have been used to understand the origin of the Mn excitation and the nature of this new transient species. Interestingly, for E_g lower than 2.5 eV (brown and dark grey curves in Figure 4.3 b)), we observe that, irrespective of the value of E_g , the gated PLE intensity goes to zero at around 2.5 eV, demonstrating that there is a minimum energy required to excite Mn, possibly arising from the excitation of the transient species. This transient species would then be responsible for the excitation of the spin forbidden 2.15 eV Mn $d-d$ transition. It should be noted that for E_g higher than 2.5 eV both the time integrated and gated PLE spectra match with the absorption spectra as expected (green curve in Figure 4.3 b)).

The observation of this peak II, only in similar E_g materials suggests a thermally activated pathway for energy transfer, further confirmed by low temperature PL spectroscopy experiments shown in Figure 4.3 c).³⁶ From the figure, it is evident that in the intermediate E_g materials the intensity ratio of Peak II to Peak I decreases substantially with decreasing temperature. We interpret these changes and hence lifetime of the transient species, in terms of a thermally driven back-transfer process from the transient Mn species to the host material which is quenched by reducing the temperature and is more relevant for lower bandgaps. At lower temperature the intensity of peak-I emission increases due to the reduction of back transfer and the two-peak structure of the PL spectrum is recovered. In fact, the critical temperature T_c , determined as the minimum temperature above which we observe the onset of the back-transfer process, leading to the two peak structure in PL for materials with E_g ranging from 2.3 to 2.8 eV, is shown to increase with increasing E_g as seen in the inset to Figure 4.3 c), demonstrating the increase of lifetime of transient species in mid E_g materials. This trend is further confirmed by the observation of only one peak at room temperature for lower E_g materials (~ 2.35 eV), that can be deconvoluted into the peak II and a tiny peak-I emission

4. Transient Species Mediated Energy Transfer

(Figure 4.4). High E_g materials (Figure 4.5) only show an increase in absolute PL intensity with decreasing temperature due to decrease in the non-radiative pathways.⁴¹ It is interesting to note that this quasi-thermal equilibrium through low temperature PL and time-resolved PL will provide better insight into the energetics and rate of thermally activated pathway for energy transfer. However, that is not the emphasis of this work but rather to find the nature of this transient species.

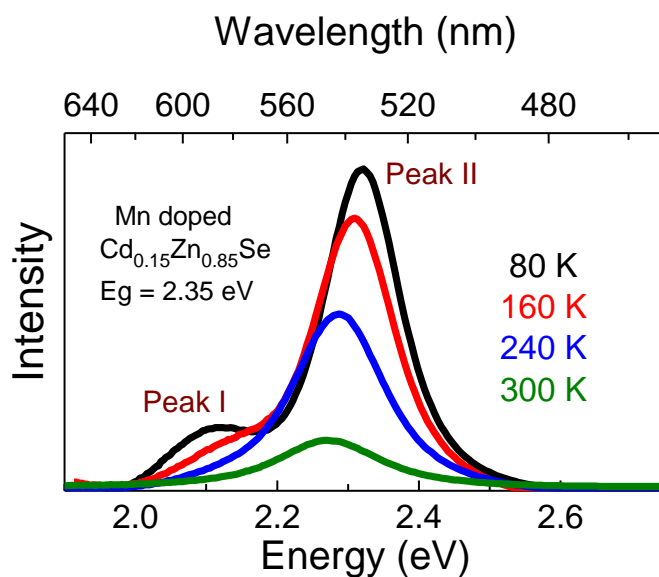


Figure 4.4 Temperature dependent PL spectra of the doped QDs with band gap $\sim 2.35 \text{ eV}$ ($x = 0.15$).

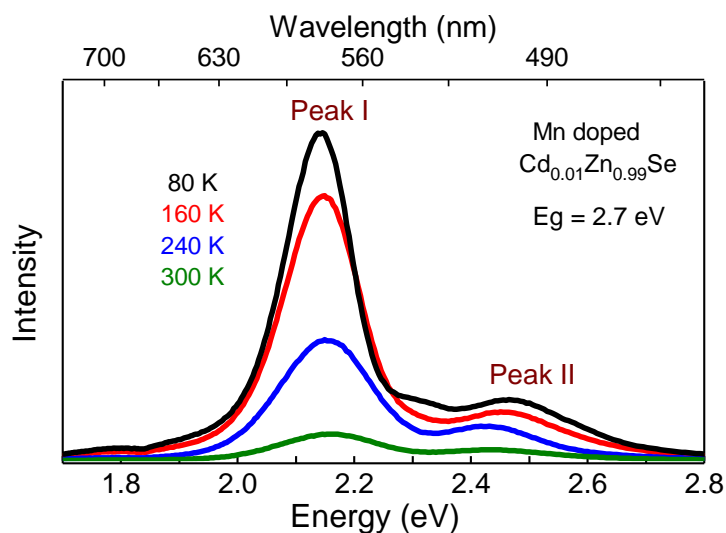


Figure 4.5 Temperature dependent PL spectra of the doped QDs with band gap $\sim 2.7 \text{ eV}$ ($x = 0.01$).

4. Transient Species Mediated Energy Transfer

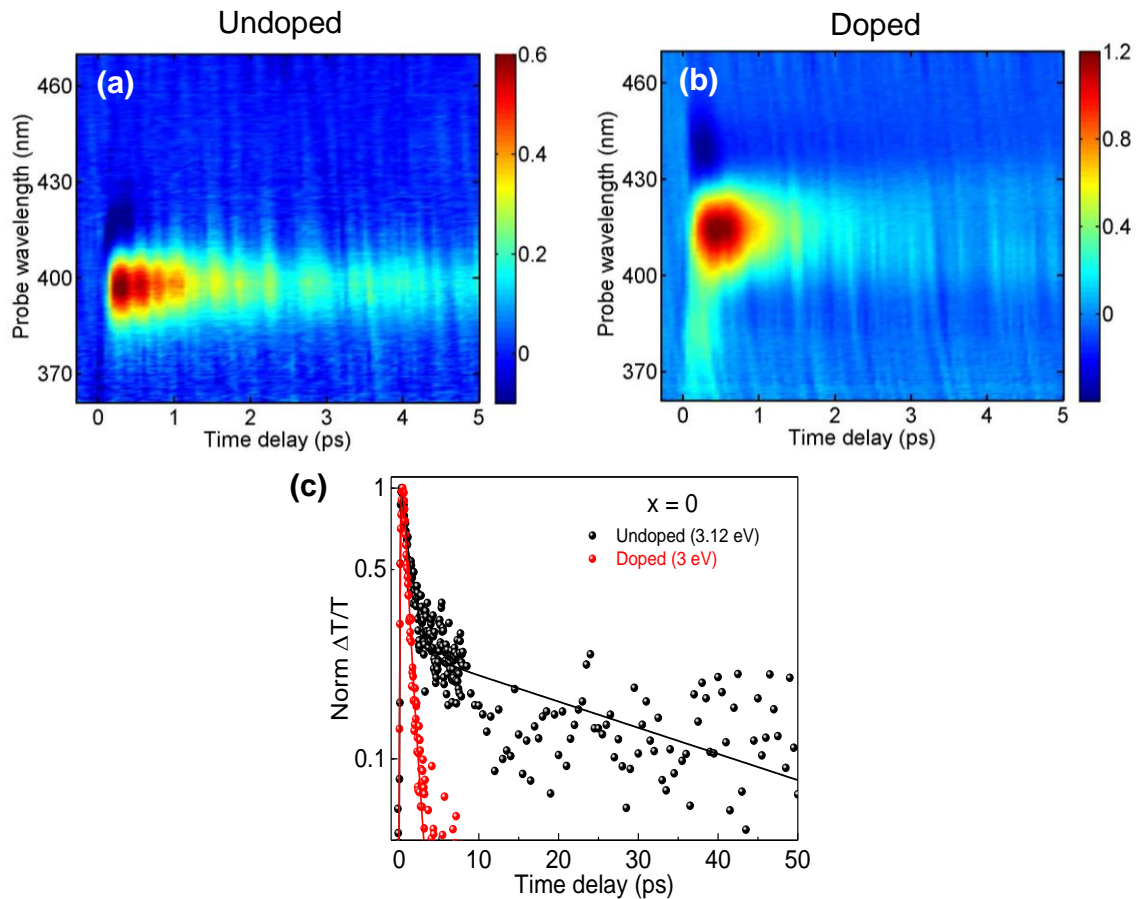


Figure 4.6 (a) and (b) $\Delta T/T$ maps as a function of probe wavelength and time delay for ZnSe and Mn doped ZnSe QDs respectively. (c) Decay profile at the band edge absorption near 3.1 eV (400 nm) with multiexponential fit of the curves (dashed lines).

Ultrafast optical spectroscopy has the capability to observe and trace the origin of this, so far elusive, transient species and its role in energy transfer, paving the way to the understanding of the mechanism of Mn emission. Ultrafast TA measurements on doped and undoped ZnSe QDs as a function of pump-probe delay are shown in Figure 4.6. Similar to earlier reported literature on Mn-doped CdS/ZnS structures^{25,26} and Mn-doped ZnS QDs,²⁷⁻³⁰ we observe a single positive peak assigned to photo-bleaching (PB) of the ZnSe with no evidence of the transient species. The fast decay in doped QDs has been explained by the presence of an additional transfer channel from the exciton to the dopant, possibly a spin allowed relaxation as the transfer occurs in sub-picosecond timescales. Surprisingly, as the host bandgap decreases, the TA spectra on the Mn-doped and undoped $\text{Cd}_x\text{Zn}_{1-x}\text{Se}$ samples look completely different. As a representative example, $\Delta T/T$ spectra at various pump-probe delays for the case of undoped and Mn-doped $\text{Cd}_x\text{Zn}_{1-x}\text{Se}$ for a bandgap of 2.65 eV ($x = 0.02$) are shown in the Figure 4.7 a) and 4.7 b) respectively. The TA spectra of both samples consist of

4. Transient Species Mediated Energy Transfer

all the regular salient features observed in QDs like the Stark effect,²⁵⁻²⁷ correspondence of the PB peaks with the absorption peaks²⁶ as shown by the second derivative peaks of the linear absorption (grey regions in Figure 4.7 a) and 4.7 b)), long lived photo-induced absorption denoting the lack of defects and the good quality of the samples. The $\Delta T/T$ dynamics are independent of the pump fluence, suggesting the suppression of Auger recombination.²⁸

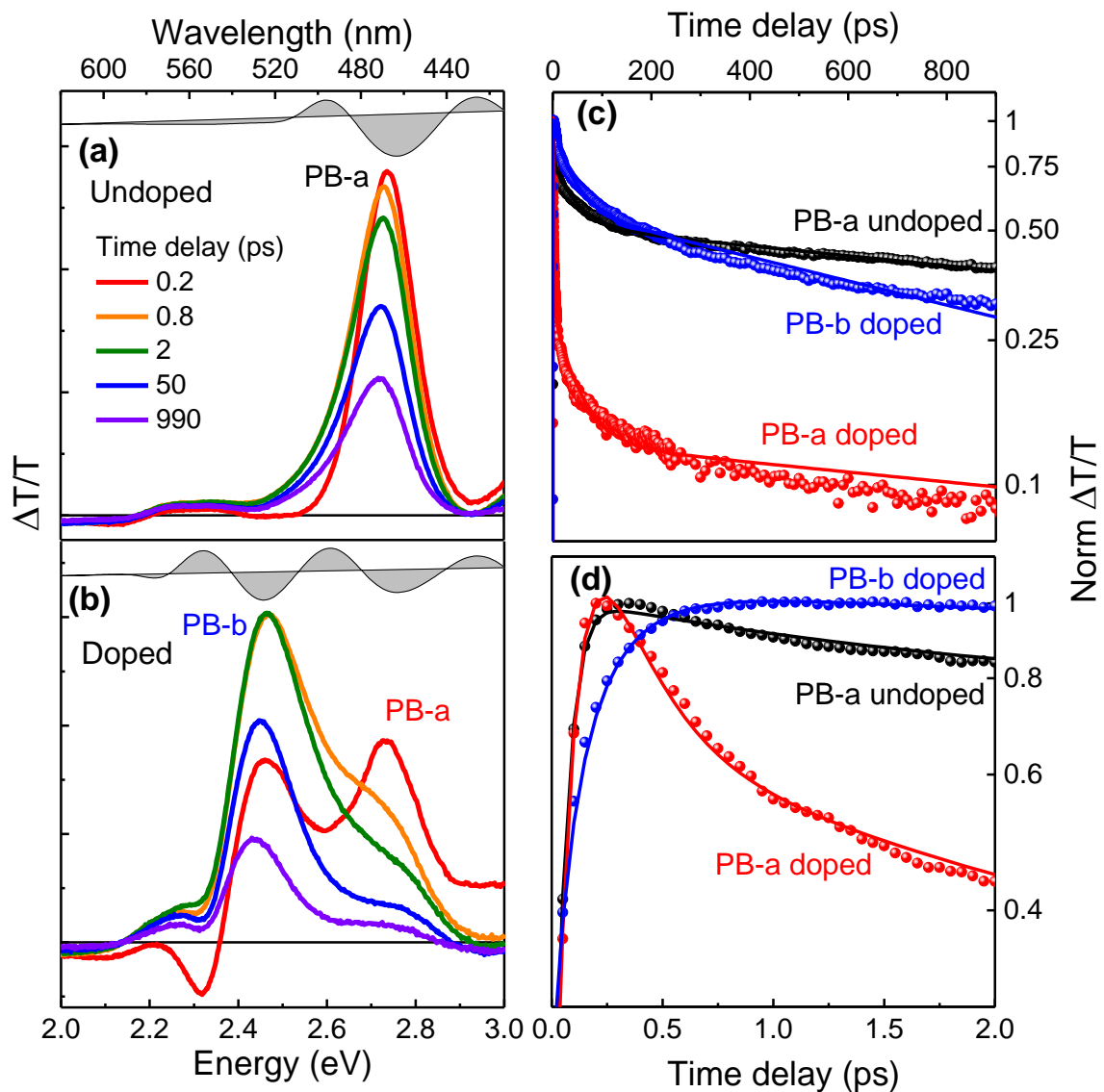


Figure 4.7 Differential transmission spectra at different delay times for the (a) undoped and (b) doped QDs with E_g of 2.65 eV ($x=0.02$), pumping at 3.1 eV, $\langle N \rangle = 1$. (c) Differential transmission dynamics for doped and undoped QDs and (d) the zoom in 2 ps region of (c). Grey area shows the second order derivative of the linear absorption of the same sample.

4. Transient Species Mediated Energy Transfer

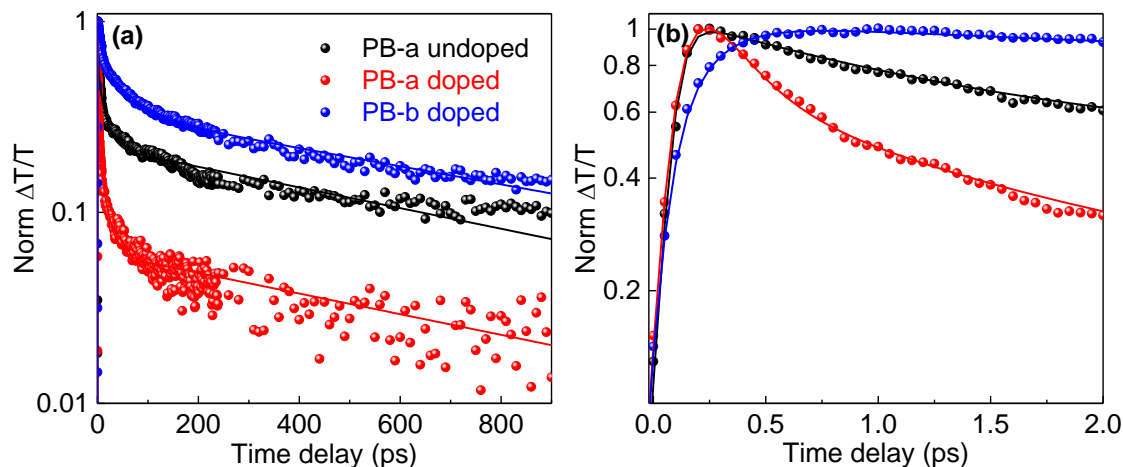


Figure 4.8 (a) $\Delta T/T$ dynamics for un-doped (black line) and Mn doped QDs (red and blue lines) with a band gap of 2.75 eV ($x = 0.005$) at the photobleaching peaks (b) the zoomed 2ps region of (a).

Additionally, while the PB band centered at ≈ 2.75 eV (PB-a) in both the undoped and doped cases can be assigned to the band-edge absorption of $\text{Cd}_x\text{Zn}_{1-x}\text{Se}$, we observe the evolution of a second PB band at ≈ 2.45 eV (PB-b) in doped QDs (see Figure 4.7 b)) similar to gated PL results shown in Figure 4.2 a). The temporal evolution of the PB peaks shown in Figure 4.7 c) reveals that the PB-a band in undoped QDs could be fitted with a multi-exponential function with an instantaneous rise time and a three-exponential decay. However, doped QDs required the inclusion of a further decay component, with a time constant, $\tau_{\text{trans}} \cong 210$ fs, in addition to the previous ones (which remained unchanged). This suggests the presence of a new decay channel in the doped QDs. Interestingly, upon zooming the $\Delta T/T$ dynamics at initial time scales (Figure 4.7 d)), it can be observed that the build-up time of the PB-b band is longer than the instrumental response function (IRF) and can be fitted by an exponential function with a rise time $\tau_{\text{rise}} \cong 210$ fs. The observation of similar time constants for the decay of the PB-a band, τ_{trans} , and the rise time of the PB-b band τ_{rise} suggests an ultrafast transfer of excitonic energy from one species to the other. Secondly, the decay of the PB-b band could be fitted to three exponential decay with an average time constant of 750 ps. It is evident that the transient species is unstable in larger E_g materials and is possibly instantaneously converted back as this species is not observed in these cases. Hence this lifetime should be entirely compensated due to thermally allowed back transfer to the host as also observed from the temperature dependent Mn $d-d$ excitation and emission study.

4. Transient Species Mediated Energy Transfer

Upon increasing E_g from 2.65 eV to 2.75 eV (see Figure 4.8) the time constant of both the decay of the PB-a band and the rise of the PB-b band decreases to $\tau \cong 160$ fs. This lifetime further decreases below the IRF upon increasing the E_g to 2.9 eV in Mn-doped ZnSe and all the other host materials. Similarly, the average decay time of the transient species at 2.5 eV decreases from 750 ps to 330 ps upon increasing E_g from 2.65 eV to 2.75 eV and could not be observed within the time resolution for Mn doped ZnSe at about 3 eV.

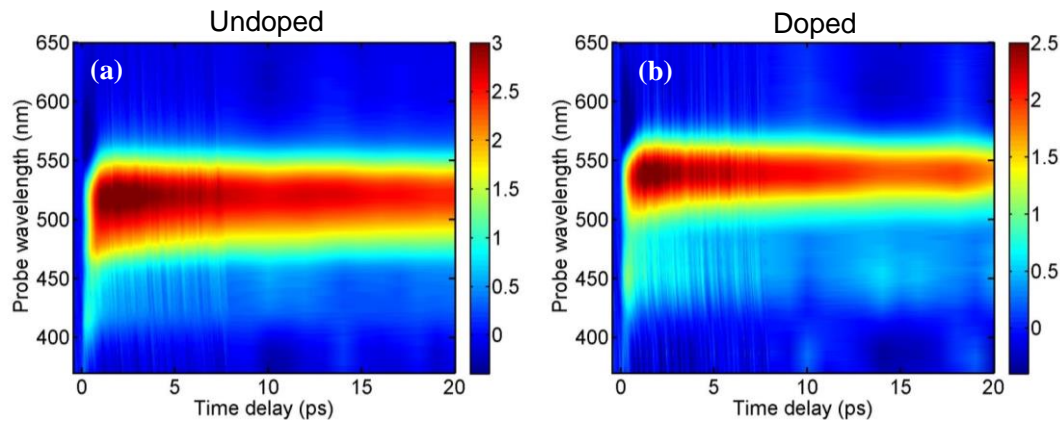


Figure 4.9 $\Delta T/T$ maps as a function of probe wavelength (nm) and time delay (ps) for (a) undoped and (b) Mn doped QDs ($x = 0.2$) respectively.

Decrease in E_g below the Mn excitation energy of 2.5 eV resulted in similar spectra for both undoped and doped counterparts as shown in Figure 4.9 with a 10 fold increase in the quantum yield in presence of Mn doping. A weak Mn emission observed under gated emission at this E_g as shown in Figure 4.2 a) is the only direct confirmation for the presence of uniformly doped Mn in the QDs. However, it is interesting to note that when we achieve resonance between the Mn excitation energy and the band gap, this spin allowed species mediates the transfer of energy between the host and the spin-forbidden Mn^{2+} species reversibly and exclusively coupled to the conduction band of the host. This spin driven opto-electronics could play an important role in overcoming energy losses such as non-radiative recombination losses as well as overpotential losses in photovoltaic applications. Hence it is imperative to understand the nature of this transient species.

It should be noted here that the involvement of a transient species which leads to the excitation of Mn is first such claim to the best of our knowledge. The emergence of a new peak under spectral projection is remarkable mainly because of the transient nature of the phenomena. It is possible to observe a peak only when the peak is long lived. However, it has been observed that when the states are not in resonance, the transient peak is so short lived that

4. Transient Species Mediated Energy Transfer

it is unable to detect them even in femto-second timescales. Similarly, it can be predicted that when the back electron transfer is efficient, we would again not observe the transient species as the back electron transfer has to be efficient on a similar time frame. Hence observation of this species is limited to the resonance of the states but not enough to have a back electron transfer. Hence observation of this species is indeed very remarkable. Taken together, these data suggest the presence of transient species with a spin allowed transition around 2.5 eV that can be excited by energy transfer from the photoexcited electron-hole pair of the host semiconductor. Study of various Mn transitions in literature⁴³⁻⁴⁶ shows that the Mn^{3+} gives rise to a spin allowed $d-d$ transition ${}^5\text{E} \rightarrow {}^5\text{T}_2$ around 20000 cm^{-1} or 2.50 eV. However, our steady state dopant has been unmistakably identified to be Mn^{2+} and not Mn^{3+} .⁴¹ Both cases are only consistent with a two-step energy transfer process. The photo-excited hole decays on the sub-picosecond timescale from the host valence band to the Mn^{2+} ions creating a transient Mn^{3+} state, which is then responsible for the PB-b band at 2.5 eV observed in Figure 4.7 b). This transient Mn^{3+} species absorbs energy to form the spin allowed ${}^5\text{T}_2$ state (visible in TA) which upon the capture of photo-excited electron returns to the spin forbidden excited ${}^4\text{T}_1$ state of Mn^{2+} . Further decay to the ground state has been extensively studied^{4, 5} and will not be discussed in this chapter. A schematic picture of the process is shown in Figure 4.10.

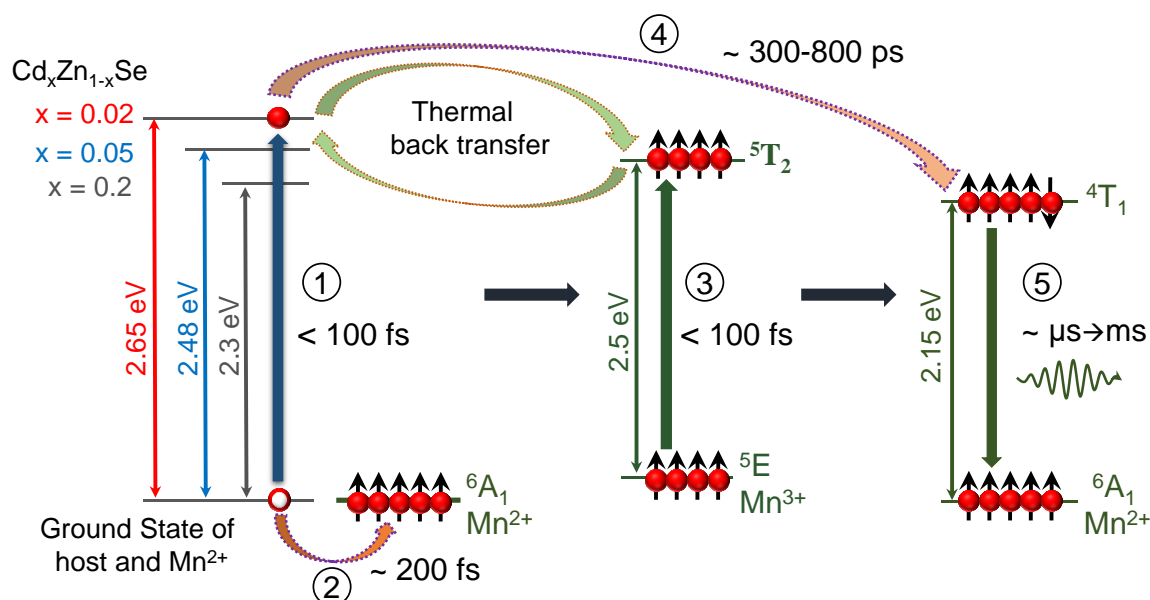


Figure 4.10 Schematic of the energy levels involved in the two-step process leading to Mn^{2+} emission.

4. Transient Species Mediated Energy Transfer

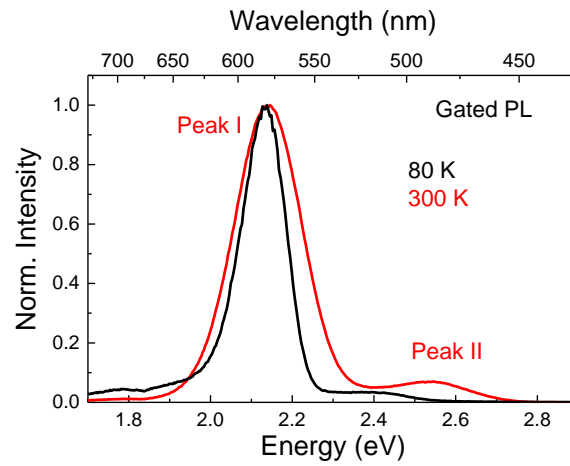


Figure 4.11 Temperature dependent gated PL measurement for sample with band gap of 2.7 eV ($x = 0.01$).

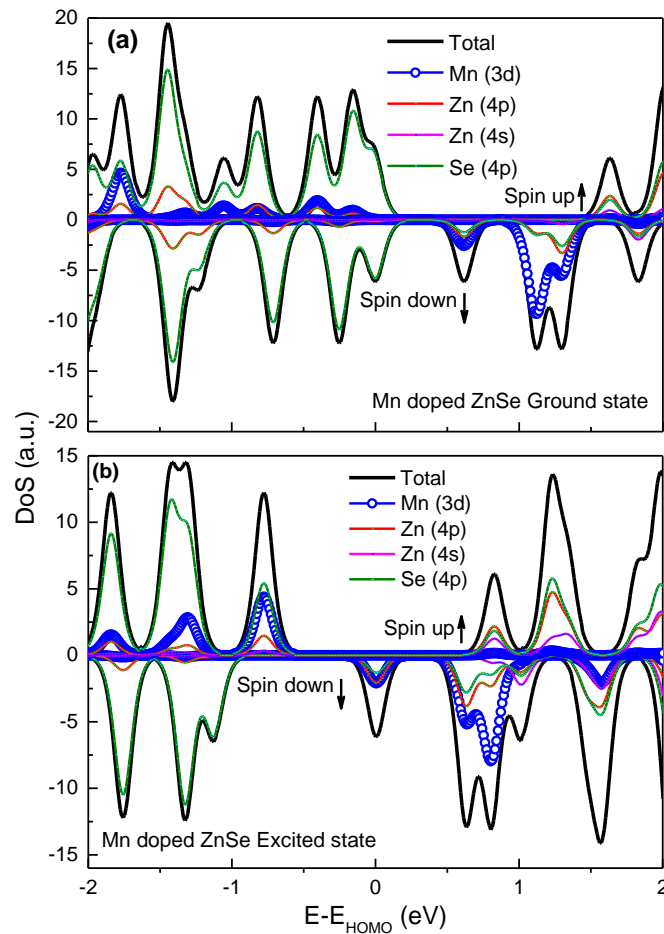


Figure 4.12 (a) Spin dependent Partial DOS of Mn doped ZnSe in the ground state. (b) Spin dependent total and partial DOS of Mn doped ZnSe in the excited state.

4. Transient Species Mediated Energy Transfer

4.5. Conclusions

In conclusion, the short-lived transient Mn species responsible for the excitation of the spin forbidden Mn *d-d* transition in II-VI semiconductor QDs has been observed by increasing its lifetime by tuning the host E_g energy to be in thermal equilibrium with the transient species. The growth and decay of this species is resolved by ultrafast TA spectroscopy. Based on these observations, we propose the formation of transient Mn^{3+} species with a spin-allowed transition into the 5T_2 state as the source of excitation of the Mn dopant ions. An important consequence of this understanding is the requirement of 2.5 eV excitation energy for the Mn emission previously believed to be 2.15 eV. Furthermore, the transfer of the photo-excited hole to the Mn atom is more efficient in QDs compared to bulk or nanowires due to the stronger overlap of wave functions, leading to incompletely suppressed band edge emission in these bulk materials. This understanding of the mechanism of Mn emission has an immediate consequence in overcoming internal energy losses like Auger recombination, overpotential losses and so on. Spin driven opto-electronics may be a new strategy for designing optimal devices for photo-emissive and photo-voltaic applications utilizing the fundamental spin conservation laws.

4. Transient Species Mediated Energy Transfer

Bibliography

1. Moro, F.; Turyanska, L.; Granwehr, J.; Patane, A. *Phys. Rev. B* **2014**, *90*, (20), 205428.
2. Ochsenbein, S. T.; Feng, Y.; Whitaker, K. M.; Badaeva, E.; Liu, W. K.; Li, X.; Gamelin, D. R. *Nat. Nanotechnol.* **2009**, *4*, (10), 681-687.
3. Qu, F.; Hawrylak, P. *Phys. Rev. Lett.* **2005**, *95*, (21), 217206.
4. Pradhan, N.; Peng, X. *J. Am. Chem. Soc.* **2007**, *129*, (11), 3339-3347.
5. Pradhan, N.; Sarma, D. D. *J. Phys. Chem. Lett.* **2011**, *2*, (21), 2818-2826.
6. Bol, A. A.; Meijerink, A. *Phys. Rev. B* **1998**, *58*, (24), R15997.
7. Ithurria, S.; Guyot-Sionnest, P.; Mahler, B.; Dubertret, B. *Phys. Rev. Lett.* **2007**, *99*, (26), 265501.
8. Nag, A.; Cherian, R.; Mahadevan, P.; Gopal, A. V.; Hazarika, A.; Mohan, A.; Vengurlekar, A. S.; Sarma, D. D. *J. Phys. Chem. C* **2010**, *114*, (43), 18323-18329.
9. Mir, W. J.; Jagadeeswararao, M.; Das, S.; Nag, A. *ACS Energy Lett.* **2017**, *2*, (3), 537-543.
10. Liu, W.; Lin, Q.; Li, H.; Wu, K.; Robel, I.; Pietryga, J. M.; Klimov, V. I. *J. Am. Chem. Soc.* **2016**, *138*, (45), 14954-14961.
11. Viswanatha, R.; Pietryga, J. M.; Klimov, V. I.; Crooker, S. A. *Phys. Rev. Lett.* **2011**, *107*, (6), 067402.
12. Bussian, D. A.; Crooker, S. A.; Yin, M.; Brynda, M.; Efros, A. L.; Klimov, V. I. *Nat. Mater.* **2009**, *8*, (1), 35-40.
13. Archer, P. I.; Santangelo, S. A.; Gamelin, D. R. *Nano Lett.* **2007**, *7*, (4), 1037-1043.
14. Bacher, G.; Schneider, L.; Beaulac, R.; Archer, P. I.; Gamelin, D. R. *J. Kor. Phys. Soc.* **2011**, *58*, (51), 1261-1266.
15. Rice, W.; Liu, W.; Pinchetti, V.; Yakovlev, D.; Klimov, V.; Crooker, S. *Nano Lett.* **2017**, *17*, (5), 3068-3075.
16. Beaulac, R.; Schneider, L.; Archer, P. I.; Bacher, G.; Gamelin, D. R. *Science* **2009**, *325*, (5943), 973-976.
17. Hazarika, A.; Layek, A.; De, S.; Nag, A.; Debnath, S.; Mahadevan, P.; Chowdhury, A.; Sarma, D. D. *Phys. Rev. Lett.* **2013**, *110*, (26), 267401.
18. Hazarika, A.; Pandey, A.; Sarma, D. D. *J. Phys. Chem. Lett.* **2014**, *5*, (13), 2208-2213.
19. Chen, H. Y.; Son, D. H. *Isr. J. Chem* **2012**, *52*, (11-12), 1016-1026.

4. Transient Species Mediated Energy Transfer

20. Hsia, C.-H.; Wuttig, A.; Yang, H. *ACS nano* **2011**, 5, (12), 9511-9522.
21. Bhargava, R. N.; Gallagher, D.; Hong, X.; Nurmikko, A. *Phys. Rev. Lett.* **1994**, 72, (3), 416.
22. Chernenko, A. V.; Dorozhkin, P. S.; Kulakovskii, V. D.; Brichkin, A. S.; Ivanov, S. V.; Toropov, A. A. *Phys. Rev. B* **2005**, 72, (4), 045302.
23. Lee, Y. R.; Ramdas, A. K.; Aggarwal, R. L. *Phys. Rev. B* **1988**, 38, (15), 10600.
24. MacKay, J. F.; Becker, W. M.; Spaek, J.; Debska, U. *Phys. Rev. B* **1990**, 42, (3), 1743.
25. Klimov, V.; Hunsche, S.; Kurz, H. *Phys. Rev. B* **1994**, 50, (11), 8110.
26. Klimov, V. I. *J. Phys. Chem. B* **2000**, 104, (26), 6112-6123.
27. Kambhampati, P. *J. Phys. Chem. C* **2011**, 115, (45), 22089-22109.
28. Taguchi, S.; Ueda, A.; Tayagaki, T.; Matsuda, K.; Kanemitsu, Y. *Phys. Status Solidi C* **2010**, 7, (3-4), 735-738.
29. Chen, H.-Y.; Maiti, S.; Son, D. H. *ACS nano* **2012**, 6, (1), 583-591.
30. Chen, H.-Y.; Chen, T.-Y.; Son, D. H. *J. Phys. Chem. C* **2010**, 114, (10), 4418-4423.
31. Kambhampati, P. *Chem. Phys.* **2015**, 446, 92-107.
32. Krause, M. M.; Mooney, J.; Kambhampati, P. *ACS nano* **2013**, 7, (7), 5922-5929.
33. Wang, Q.; Zhang, X.; Jin, Z.; Zhang, J.; Gao, Z.; Li, Y.; Liu, S. F. *ACS Energy Lett.* **2017**, 2, (7), 1479-1486.
34. Meinardi, F.; Akkerman, Q. A.; Bruni, F.; Park, S.; Mauri, M.; Dang, Z.; Manna, L.; Brovelli, S. *ACS Energy Lett.* **2017**, 2, (10), 2368-2377.
35. Akkerman, Q. A.; Meggiolaro, D.; Dang, Z.; De Angelis, F.; Manna, L. *ACS energy letters* **2017**, 2, (9), 2183-2186.
36. Mooney, J.; Krause, M. M.; Kambhampati, P. *J. Phys. Chem. C* **2014**, 118, (14), 7730-7739.
37. Giannozzi, P.; Baroni, S.; Bonini, N.; Calandra, M.; Car, R.; Cavazzoni, C.; Ceresoli, D.; Chiarotti, G. L.; Cococcioni, M.; Dabo, I. *J. Phys.: Condens. Matter* **2009**, 21, (39), 395502.
38. Goedecker, S.; Teter, M.; Hutter, J. *Phys. Rev. B* **1996**, 54, (3), 1703.
39. Hartwigsen, C.; Goedecker, S.; Hutter, J. *Phys. Rev. B* **1998**, 58, (7), 3641.
40. Perdew, J.; Zunger, A. *Phys. Rev. B* **1981**, 23, 5048.
41. Beaulac, R.; Archer, P. I.; Gamelin, D. R. *J. Sol. Stat. Chem.* **2008**, 181, (7), 1582-1589.

4. Transient Species Mediated Energy Transfer

42. McLaurin, E. J.; Vlaskin, V. A.; Gamelin, D. R. *J. Am. Chem. Soc.* **2011**, 133, (38), 14978-14980.
43. Vlaskin, V. A.; Janssen, N.; van Rijssel, J.; Beaulac, R.; Gamelin, D. R. *Nano Lett.* **2010**, 10, (9), 3670-3674.
44. Alam, T. M.; Jenkins, J. E.; Farrukh, M. A., *Advanced Aspects of Spectroscopy*. INTECH: India, 2012; Vol. Chap. 1, p 279-306.
45. Durga, D. K.; Veeraiah, N. *J. Phys. Chem. Solids* **2003**, 64, (1), 133-146.
46. Beaulac, R.; Ochsenein, S. T.; Gamelin, D. R.; Klimov, V. I., *Colloidal Transition-Metal-Doped Quantum Dots*. 2010; Vol. 2, p 398.

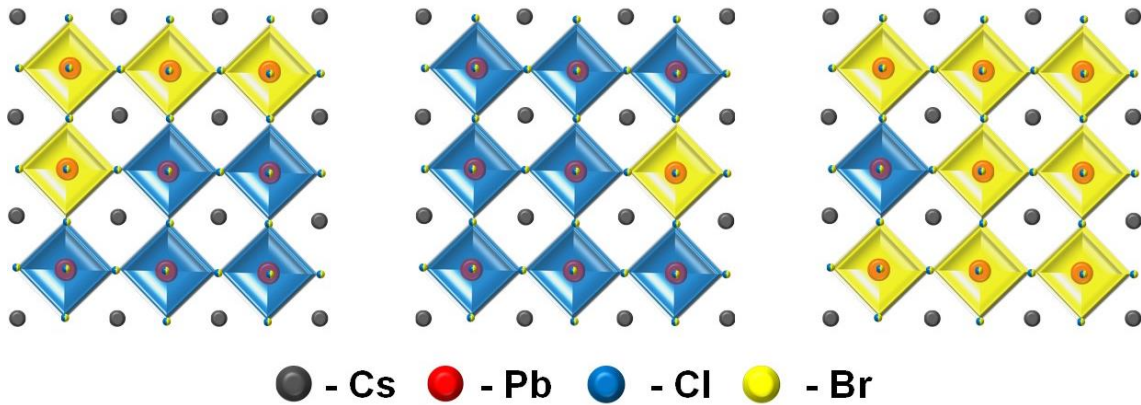
4. Transient Species Mediated Energy Transfer

Part II

Mn Doped Perovskite Quantum Dots for Harvesting delayed Fluorescence

Chapter 5

Understanding the Structure of Mixed Halide Perovskite Quantum Dots



5. Structure of Mixed Halide Perovskite Quantum Dots

5. Structure of Mixed Halide Perovskite Quantum Dots

5.1. Abstract

Lead halide perovskite quantum dots (QDs) are interesting semiconductors for photovoltaic and optoelectronic applications due to their low cost, efficient external quantum efficiencies and bandgap tunability. Clear understanding of the internal structure and bonding of the mixed halide perovskite QDs is necessary to design stable materials for applications. Using a combination of optical absorption and emission spectroscopy, X-ray diffraction (XRD), Extended X-ray absorption fine structure (EXAFS), and Raman spectroscopy, we probe the extent of alloying and phase segregations in these mixed halide perovskites at three different length scales. The internal structure of mixed halide perovskite QDs are identified as domain-free mixed halide solid solutions with randomly distributed halide ions about the Pb centre with up to seven possible distinct but dynamically changing $[\text{PbCl}_x\text{Br}_{6-x}]^{4-}$ environments with only Pb-Cl and Pb-Br bonds which are also sensitive to the changes in the unit cell dimensions resulting from the substitution of Br by Cl, obeying Vegard's law. However, it has been observed that the weak bonding within the octahedra is responsible for the dynamic nature of this environment. Better optoelectronic devices with enhanced stability and performance may be realized through careful manipulation of the different phases present in these materials.

5.2. Introduction

Colloidally synthesized QDs of cesium lead halides (CsPbX_3 X: Cl, Br, I) are highly promising for light emitting applications. Since the discovery of lead halide perovskite QDs by using thin films for optoelectronic¹⁻⁵ and photovoltaic applications⁶⁻⁸ there have been great deal of interest in studying the structure-property correlations. Colloidal synthesis of perovskite QDs have utilized the ability of solution processability and cost effectiveness to gain enormous interest among the scientific community. As an additional advantage these systems exhibit extremely high photoluminescence and sharp absorption edges. The bandgap tunability in the entire visible range for perovskite QDs are obtained by the variation in the halide composition.⁹ However, stability of these QDs in the ambient environment due to light induced phase segregation,^{10, 11} and inability to maintain optically active cubic phase⁹ is still a major concern in the well-studied area of perovskite QDs.

Apart from the structural issues, mixed halide perovskite materials are known to undergo anion exchange in solution,^{12, 13} photo induced phase separation¹⁴ and other unusual properties largely due to, fast rate of diffusion and high mobility of the halide ions through the

5. Structure of Mixed Halide Perovskite Quantum Dots

crystalline lattice of lead halides.^{15, 16} More research is needed to understand whether mixed halide perovskites form alloys, and if so their stability and other factors that trigger phase segregation, and how it has influence on the optoelectronic properties. Additionally, clear understanding about lead halide octahedra for the pure and mixed halides which are the building blocks of the perovskite QDs are important to design high performance devices.

Conflicting reports in the literature regarding the crystal structure of CsPbBr₃ QDs as cubic⁹ and orthorhombic^{17, 18} still exists and benchtop XRD to determine the accurate crystal structure is limited due to the peak broadening arising from smaller nanocrystal size, and high background due to the presence of ligands. The unanswered questions in phase segregation include recognizing the channels that facilitate ion migration and phase segregation dynamics of the lead halide octahedra, differentiating between alloys and solid solutions with several possibilities of individual halide compositions.

To date, most of the mixed halide hybrid perovskite structural studies have relied broadly on diffraction-based methods.¹⁹ Recently, Rosales et.al have used solid state nuclear magnetic resonance (NMR) spectroscopy to investigate phase segregation and alloying nature of organolead mixed halide perovskite, but the understanding of the microstructure and extend of alloying in the mixed halides remains incomplete.²⁰ However, Karmakar *et. al* identified seven distinct Pb octahedral environments in the Br/Cl mixed halide perovskites using one and two-dimensional NMR spectroscopy.²¹ Even though solid state NMR spectroscopy is a powerful tool to probe the local chemical environment of NMR active nuclei, it cannot give detailed local structural environment around the atoms including lead-halide bond distances and octahedral arrangements.

In this chapter, we investigate the structural properties of perovskite QDs at a macro, micro and atomic level length scale with the help of XRD, Raman spectroscopy, and local structure analysis (EXAFS). X-ray diffraction approaches are excellent for the determination of the long-range crystal structure, while EXAFS is one of the few characterization tools capable of measuring atomic level nearest neighbour environment providing direct information regarding the local structure of mixed halide perovskites. But EXAFS is limited to the nearest neighbour environment and not a suitable tool to provide the extent of mixing in the octahedra of mixed halide perovskites. Raman spectroscopy is an excellent tool to understand the nature of octahedral coordination in the mixed halide perovskites and can shed light on to the extent of mixing of various halides within the octahedra in mixed halide perovskite QDs. Here we

5. Structure of Mixed Halide Perovskite Quantum Dots

discuss a detailed analysis on the local structure of mixed halide perovskite QDs and correlate the findings from the X-ray crystallography, with Raman spectroscopy results providing a detailed understanding on the structure of mixed halide perovskites at various length scales with suitable experimental probes at each length scales.

5.3. Experimental Methods

Chemicals used in the experiments include Cs_2CO_3 (99.99%), octadecene (ODE, 90%), oleic acid (OA, 90%), oleylamine (OLAm, 70%), PbBr_2 (99.999%), PbCl_2 (99.999%), n-hexane (>97.0%), trioctylphosphine (TOP), and are used straight after purchasing from Sigma Aldrich. All solvents and reagents were of analytical grade and directly used without further purification.

Cesium oleate was prepared using standard literature methods⁹ using Cs_2CO_3 and OA in presence of ODE at high temperature of 150 °C until all Cs_2CO_3 reacted with OA forming a clear solution of Cs-oleate.

5.3.1 Synthesis of $\text{CsPb}(\text{Br}/\text{Cl})_3$ perovskite quantum dots (QDs): Perovskite QDs were prepared according to the method described by Protesescu *et al.*⁹ Stoichiometric mixtures of PbCl_2 and PbBr_2 , were taken for the synthesis of both size and composition modulation of $\text{CsPb}(\text{Br}/\text{Cl})_3$ perovskite QDs. ODE (5mL) and the required Pb salts were loaded into a 3-neck flask and dried under vacuum for 1 hour at 120°C. Dried OLAm (1.5 mL), dried OA (1.5 mL) and TOP (1 mL) were injected at 120°C under Argon flow. After the complete solubilization of the precursors added and obtaining a clear solution, the temperature was raised up to 180°C for composition modulation and Cs-oleate solution (0.4mL preheated to 100°C) was quickly injected and 5 seconds later the reaction mixture was cooled down by ice water bath. For the sized variation sample Cs-oleate is injected at lower temperature (120-180 °C). The QDs were purified by centrifuging the crude solution for 10 minutes at 5000 rpm. The precipitated QDs were redispersed in hexane and centrifuged for 5min at 10000 rpm. Following this the precipitate, containing unreacted precursors, larger QDs and agglomerates, was discarded. The supernatant comprising the QDs was then stored under refrigeration.

5.4. Results and Discussion

We have first synthesized a series of pure and mixed halide perovskite QDs (P0-P100) following the hot injection method adapted from the literature⁹ by taking stoichiometric mixture lead halide salts. Figure 5.1 displays the absorption and photoluminescence spectra of the perovskite QDs. Pristine CsPbCl_3 (P0) QDs emit near UV-blue PL at wavelength of 404

5. Structure of Mixed Halide Perovskite Quantum Dots

nm whereas pristine CsPbBr₃ (P100) emits bright green PL at a wavelength of 512 nm. PL emission of the mixed halide perovskites ranges between 404 to 512 periodically red shifting in accordance with the composition modulation.

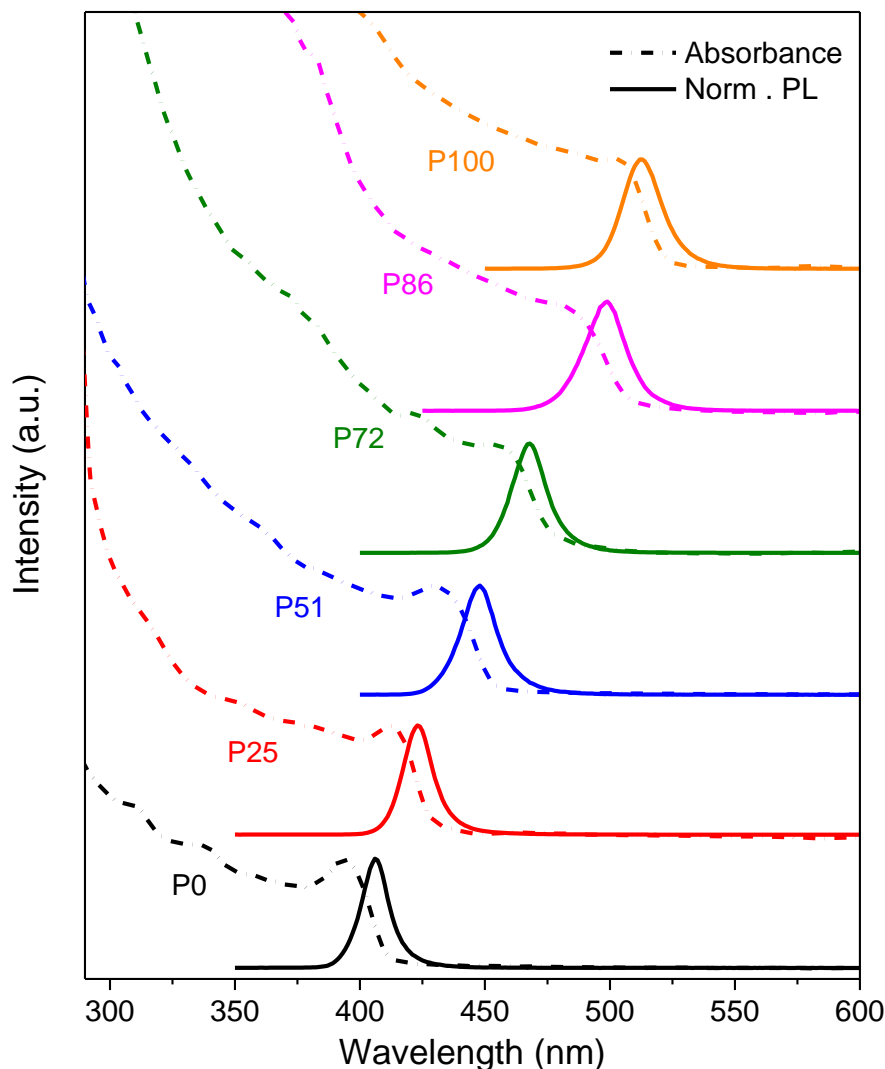


Figure 5.1 Absorption and steady state PL emission spectra for mixed halide perovskite QDs. P0 is CsPbCl₃ and P100 is CsPbBr₃ and P0-P100 shows various combination of mixed halide composition.

To investigate the internal structure of the mixed halide perovskite QDs for different compositions we employed local structure analysis using XAFS spectroscopy. To accomplish this goal, we studied XANES and EXAFS as a probe to study the variation of co-ordination number and different bond contribution between the halides. A series of XAFS fluorescence spectra were collected at Pb-L_{III}-edges for various samples starting from CsPbCl₃ to CsPbBr₃.

5. Structure of Mixed Halide Perovskite Quantum Dots

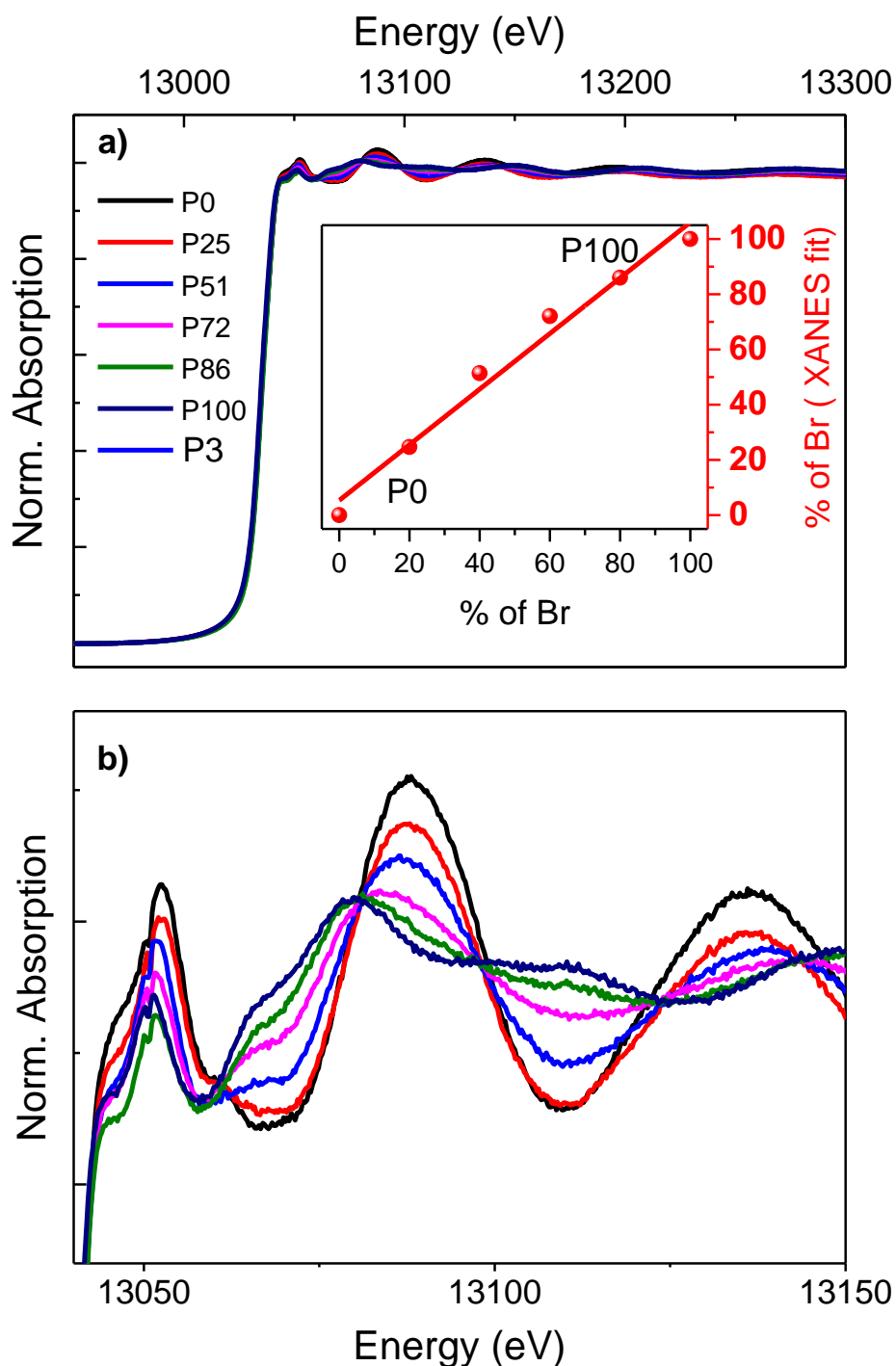


Figure 5.2 QDs. a) Pb-L_{III}-edge XANES spectra for CsPb(Cl/Br)₃. Inset shows the comparison of the stoichiometric variation in the bromide ion content to the variation obtained from the linear combination fit of the XANES spectra for the mixed halide CsPb(Cl/Br)₃ QDs. b) Zoomed XANES spectra for mixed halide CsPb(Cl/Br)₃ (P0-P100).

The data were processed using ATHENA software²² and the Pb-L_{III} edge XANES spectra are shown in Figure 5.2 a). In order to get the quantitative values for the same, we perform a linear combination fit of the experimental XANES data for the mixed halide perovskite by

5. Structure of Mixed Halide Perovskite Quantum Dots

comparing with the same from pure lead halide perovskite QDs. The analysis gives rise to the actual variation in the halide composition with respect to the stoichiometric mixture of lead halides taken during the synthesis. Inset of Figure 5.2 a) shows that difference between the halide content in the mixed halide systems taken during the synthesis and the results obtained from the linear combination fit between CsPbCl_3 and CsPbBr_3 . The red line shows a linear fit to the data and it is evident that the shift from the ideal behaviour is minimal suggesting formation of mixed halide systems in the desired range. The results obtained from linear combination fit of XANES is used as the accurate halide compositions for the further analysis.

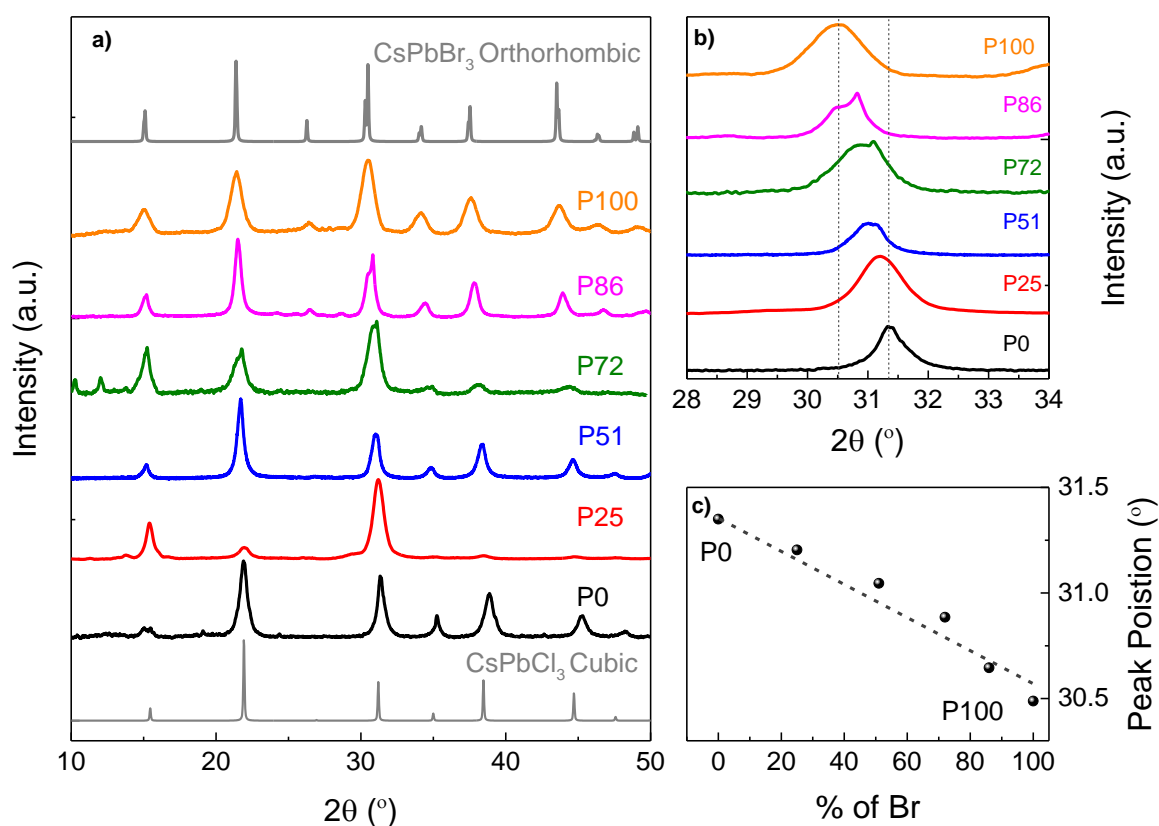


Figure 5.3 a) XRD patterns for pure and mixed halide perovskite QDs. Experimental data is compared to the bulk cubic structure of CsPbCl_3 and cubic and orthorhombic structure of CsPbBr_3 . b) Shift in the XRD peaks for $\text{CsPb}(\text{Cl}/\text{Br})_3$ QDs. c) shift in the XRD peak vs Br ion content in the $\text{CsPb}(\text{Cl}/\text{Br})_3$ QDs.

A close look at the XANES spectra as shown in the Figure 5.2 a), for the mixed halide (Figure 5.2 b)) shows several isosbestic points. Presence of isosbestic points in the spectra indicates that the mixture constitutes a combination only two paths namely, Pb-Cl or Pb-Br bonds and in a single environment. Isosbestic points in the mixed halide perovskite also confirms that there are no other environments present in the mixed halide perovskite structure.

5. Structure of Mixed Halide Perovskite Quantum Dots

To understand the crystal structure of the mixed halide perovskite QDs in comparison to the bulk lead halide perovskites, powder XRD measurements were performed at room temperature of the drop casted films of samples P0 to P100. Even though conflicting literature on the crystal structure of CsPbBr₃ (P100) are available, our results show that the orthorhombic structure provides a better match than the cubic structure for CsPbBr₃. XRD patterns for all the samples are shown in Figure 5.3 a). The XRD pattern for the pristine CsPbCl₃ (P0) shows the same characteristic peaks as the cubic CsPbCl₃ bulk structure and the mixed halide perovskite QDs (P25 -P86) shows a periodic shift in the peaks which is due to change of halide composition. Figure 5.3 b) shows the observed 2θ shift in the XRD peak for the QDs and plotted against the Br ion content in the mixed halide CsPb(Cl/Br)₃ QDs. Absence of mixture of peaks originating from the respective individual CsPbCl₃ and CsPbBr₃ structures in the mixed halide systems indicates the formation of alloyed structure with an effective lattice parameter ranging between CsPbCl₃ and CsPbBr₃ following Vegard's law.²³ Cubic CsPbCl₃ and orthorhombic CsPbBr₃ can alloy due to the smaller lattice mismatch (4.5 %) ²⁰ and are not going to phase-segregate in spite orthorhombic structure of CsPbBr₃ as it arises due to slight rotation of octahedra and is unlikely to disrupt the perovskite structure in the mixed halides. The solid solution behaviours of the mixed halide perovskite QDs can be observed from the linear behaviour of the peak positions observed for QDs from P0 to P100 as shown in Figure 5.3 c).

While detailed analysis on the XRD provided information on crystal structure of mixed halide perovskites, XRD techniques are limited to macroscopic scale. Minor changes locally in the systems cannot be understood by a global technique like XRD. However, Pb-Cl and Pb-Br bonds within the mixed halide CsPb(Cl/Br)₃ lattice can be studied using the quantitative EXAFS analysis of the nearest neighbours. While the XANES region is known to give information about the oxidation state of the Pb ion, the information regarding the local first and second shell structure around the absorbing atom (Pb) can be obtained from analysing the EXAFS region of the data. The evolution of the local structure around Pb with the addition of PbBr₆ octahedra is thus studied for the series of CsPb(Cl/Br)₃ samples. Pb-L_{III}-edge $\chi(k)$ data for all the samples have been shown in Figure 5.4 a). From the plot it is evident that the as the Br content increases, the k-space oscillations periodically shift towards Br-rich environment eventually matching the k-space oscillations of pure CsPbBr₃. This confirms that there are indeed 2 paths, Pb-Cl and Pb-Br bonding. For further confirmation, the data from these samples were Fourier transformed and plotted in R-space as shown by open circles in Figure 5.5 a – e). Visual inspection of these real (R) space EXAFS plots signals that the local structure around

5. Structure of Mixed Halide Perovskite Quantum Dots

Pb is gradually converting from CsPbCl_3 to CsPbBr_3 through different stages of halide incorporation. However, in order to obtain more quantitative information on the bonds involved, we modelled the EXAFS spectra with a theoretical standard and generated the relevant paths using FEFF6 within the ARTEMIS program.²⁴ The theoretical model consisted of CsPbCl_3 in its cubic form with space group $\text{pm}3\text{m}$ and CsPbBr_3 in the orthorhombic crystal structure with space group Pnma . The solid lines represent the best fit obtained from this procedure, whereas the thin lines depict the component paths necessary to achieve this fit.

Figure 5.5 a – e) shows the experimental data and the fit for mixed halide $\text{CsPb}(\text{Cl}/\text{Br})_3$ QDs. It is evident from the plots that the dominant contributions are coming from only Pb-Cl and Pb-Br path and there exists no intermediate bond in the mixed halide perovskites.

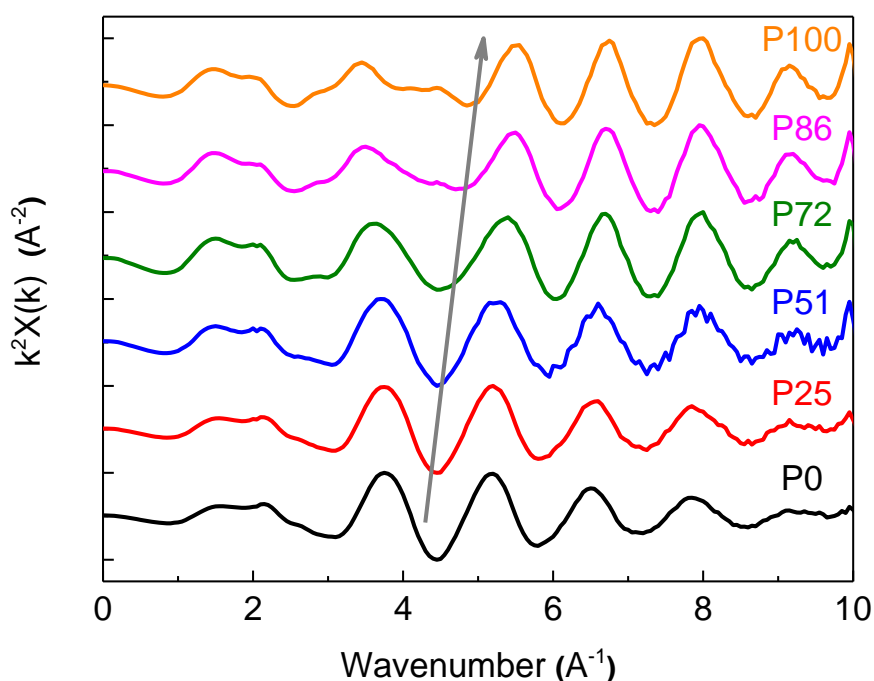


Figure 5.4 k^2 -Weighted $\chi(k)$ oscillations for Pb-L_{III}-edge for different samples of $\text{CsPb}(\text{Cl}/\text{Br})_3$ (P0-P100).

The EXAFS fitting is performed over a R range of 1-4 Å for all the samples to study the gradual changes observed going from pure CsPbCl_3 structure to CsPbBr_3 . It is evident from the figure that the gradual evolution of the Pb-Br path is seen as we go from CsPbCl_3 and there are four parameters in the model: the coordination number (CN), the energy shift (ΔE_0), the adjustment of the half-path length (ΔR), and the mean-square relative displacement of absorber and backscatter atoms (σ^2).²⁴ The related fitting results of the EXAFS spectra are summarized in Table 5.1. The R factors of both samples are far less than 0.02, corroborating the accuracy of

5. Structure of Mixed Halide Perovskite Quantum Dots

fittings. From the Table 1 it is seen that the coordination number (CN) for CsPbBr₃ is 5.93 which is close to optimum value of 6 for the perovskite structure. In contrast for Cl rich systems the CN is lesser than the optimum value. This demonstrates that CsPbCl₃ based systems have halide vacancies whereas CsPbBr₃ have minimal defects and halide vacancies. Taken on whole the EXAFS data provides a strong evidence that the mixed halide perovskite systems are built on only Pb-Cl and Pb-Br bonds. In addition to that, EXAFS also provides more information regarding halide deficiencies in Cl rich QDs and are directly correlated to the halide ion migration in mixed halide QDs resulting in low quantum yield.

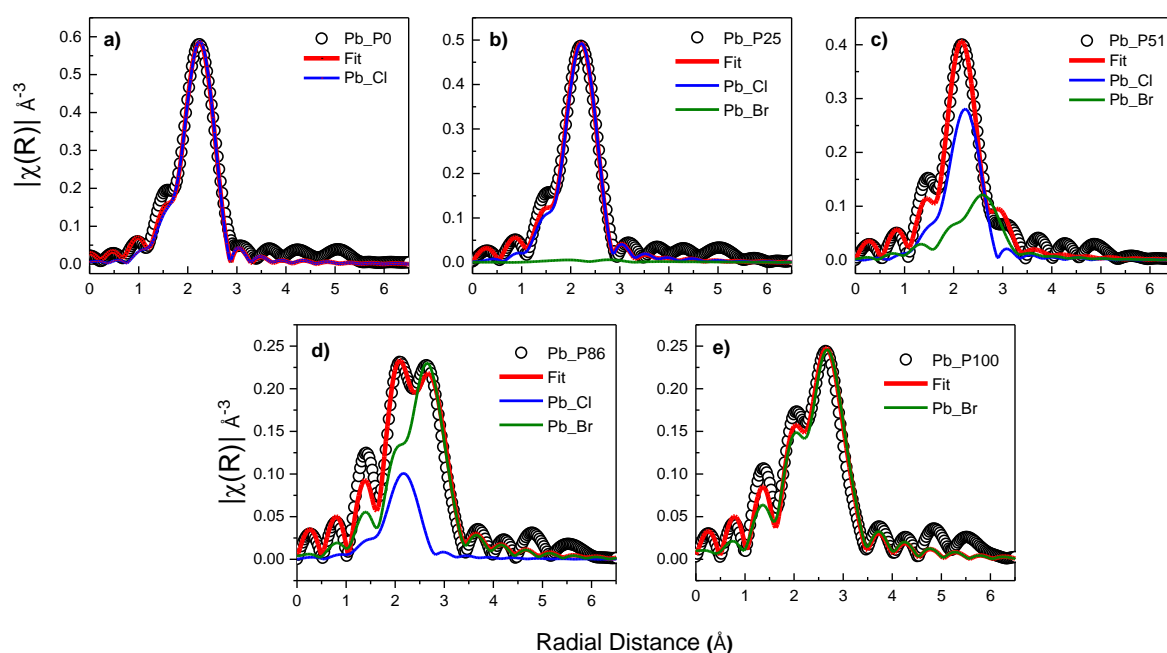


Figure 5.5 a-e) Magnitude of Fourier-transformed Pb-L_{III}-edge EXAFS spectra (open symbols) and their best fit (solid line) for P0-P100 (CsPb(Cl/Br)₃). Thin lines show their component fitting paths.

Structural analysis of mixed halide perovskite QDs of various halide composition using both XRD studies and EXAFS reveal several information about the internal chemical bonding and the long-range order of the chloride and bromide perovskite QDs, but the key information about the arrangement of the octahedra in the mixed halide perovskites cannot be understood using the above-mentioned techniques. As both XRD and EXAFS average out the result and give a global perspective about the overall lattice arrangements and local environment around Pb atom, both the techniques fails to explain the nature of mixing of the halide octahedra and how it changes as more and more Br atoms are introduced.

5. Structure of Mixed Halide Perovskite Quantum Dots

Sample	R (Å)	N	(σ^2)	ΔE (eV)	R - factor
P0	2.25±0.03	4.33	0.01±001	-1.71±0.86	0.021
P25	2.19±0.05	3.50+0.87=4.37	0.06± 0.001	-2.49±1.84	0.012
	2.69±0.03		0.01±0.03	4.89±0.58	
P51	2.23±0.06	2.34+2.47=4.81	0.01± 0.002	-3.25±1.78	0.022
	2.59±0.04		0.02±0.005	1.98±1.76	
P72	2.16±0.07	1.38+3.66=5.04	0.01± 0.002	-4.37±0.87	0.021
	2.68±0.04		0.02±0.001	1.10±1.55	
P86	2.17±0.07	0.72+4.50=5.22	0.01± 0.004	-4.80±0.14	0.019
	2.65±0.05		0.01±0.001	0.11±1.26	
P100	2.68±0.04	5.93	0.01±0002	0.73±0.907	0.020

Table 5.1 Main fitting results of the fits performed on the Pb L_{III}-Edge k^2 -weighted EXAFS spectra for CsPb(Cl/Br)₃ QDs.

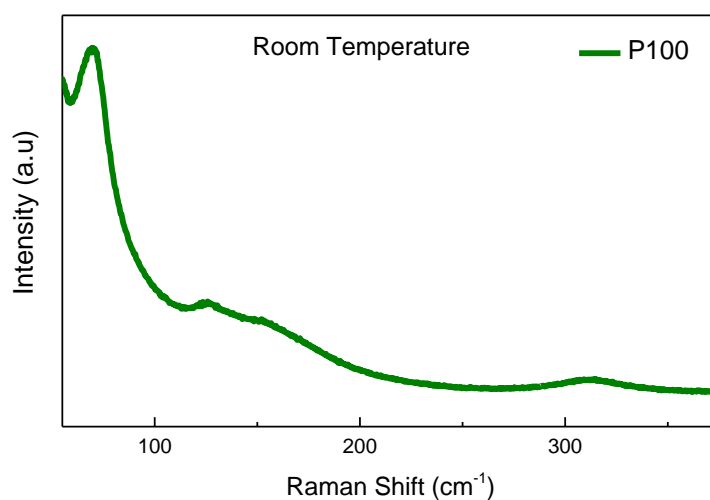


Figure 5.6 Room temperature Raman spectra for CsPbBr₃ (P100).

5. Structure of Mixed Halide Perovskite Quantum Dots

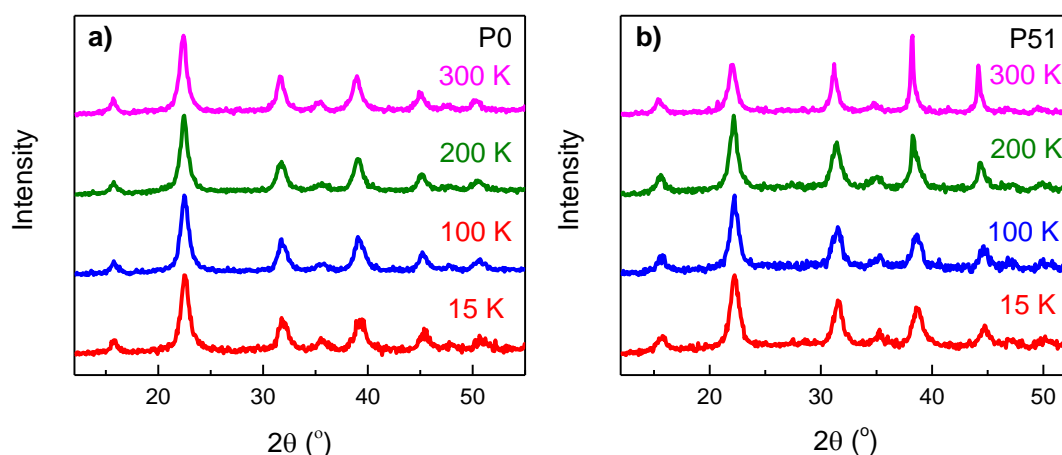


Figure 5.7 Temperature dependent XRD patterns for CsPbCl_3 (P0) and mixed halide $\text{CsPb}(\text{Cl}/\text{Br})_3$ (P51) QDs.

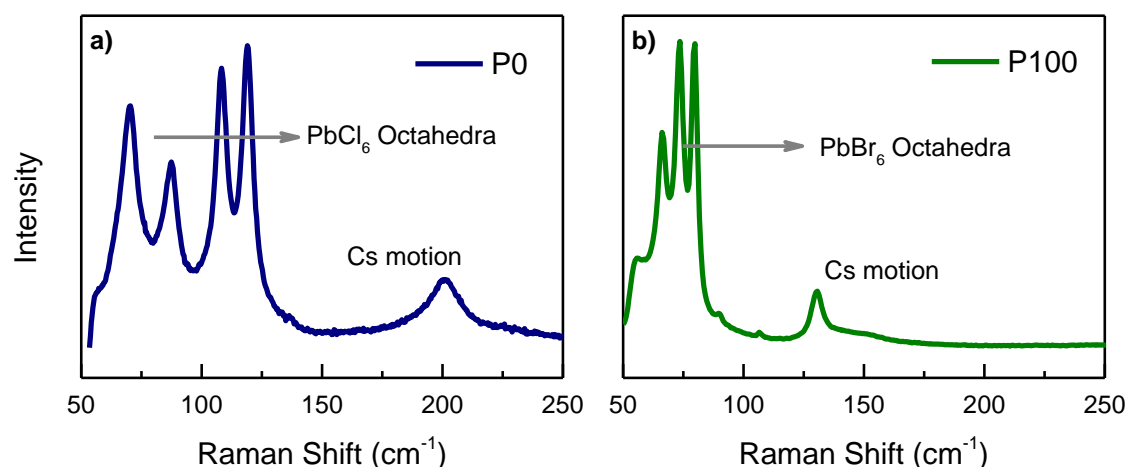


Figure 5.8 a) and b) Raman spectra for CsPbCl_3 (P0) and CsPbBr_3 (P100) QDs at 77 K.

Raman spectroscopy, is used to study the chemical environment around octahedra in mixed halide QDs. Figure 5.6 shows typical Raman spectra for CsPbBr_3 (P100) at room temperature. As the octahedral modes are not observable at room temperature due to thermal effects, the Raman spectroscopy is performed at 77 K. In addition to the reduction of thermal effects, laser induced anion migration is also reduced at 77 K. We perform temperature dependent XRD is performed for mixed halide perovskite QDs as shown in Figure 5.7 a) and b) to confirm that there is no phase change going from room temperature to 77 K. As seen from the figure, there is no phase change or new phases arising at low temperature, suggesting that

5. Structure of Mixed Halide Perovskite Quantum Dots

the Raman spectra collected at 77 K is indeed for the same QDs with no change in octahedral environment. Figure 5.8 a) and b) shows Raman spectra for CsPbCl₃ (P0) and CsPbBr₃ (P100) QDs at 77 K. From the resonant Raman studies, the sharp peaks arising at 72 and 90 cm⁻¹ is assigned to PbCl₆ octahedral rotations matching the literature.²⁵ The Raman modes observed at 110, 121 and 200 cm⁻¹ are assigned to the Cs-motion. Similarly, Raman peak corresponding to PbBr₆ octahedra is assigned at 78 cm⁻¹ as seen from Figure 5.8 b).

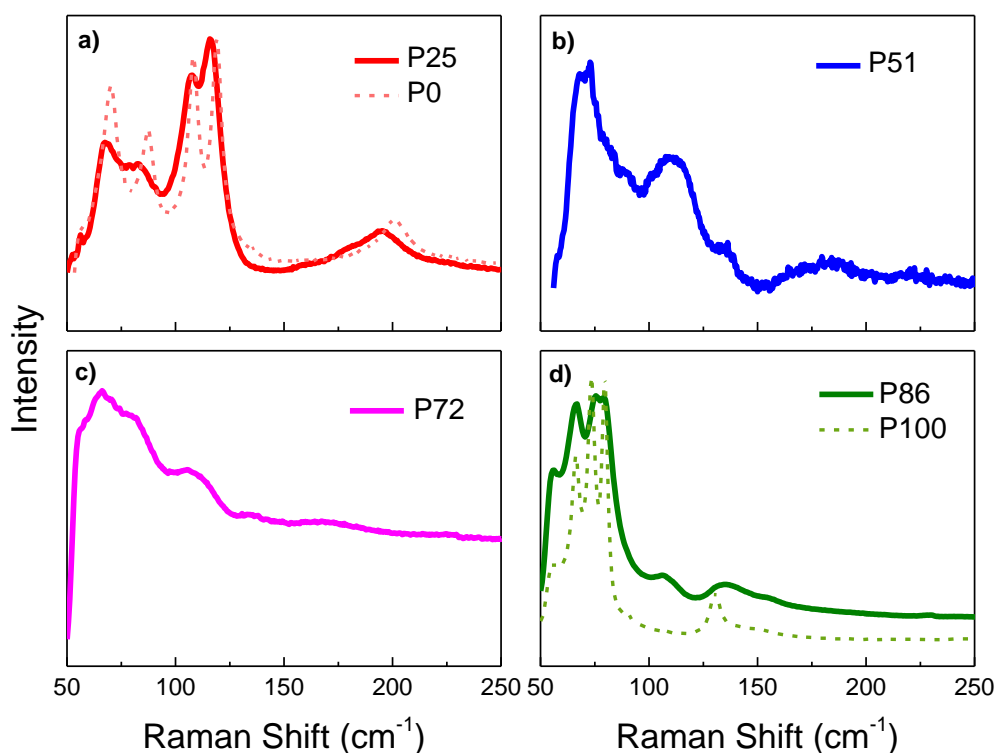


Figure 5.9 a)- d) Raman spectra for CsPb(Cl/Br)₃ (P25-P86) QDs at 77 K. Raman spectra for (P0 and P100) are shown in a) and d) as thin dotted lines for comparison.

The results summarized in Figure 5.9 are those for a material with very fluid properties with dynamic octahedra whose chemical structure can readily be altered to randomly accommodate any combination of halide anions. Even at relatively lower level halide substitutions (i.e., $\leq 25\%$), the halide ion transitions into the lattice replacing a Br for Cl (or Cl for Br) immediately affect the lattice parameters of the solid-solution and the corresponding octahedral modes of [PbBr₆]⁴⁻ or [PbCl₆]⁴⁻, reflecting the sensitivity of Raman spectroscopy as seen from Figure 5.9 a) and d). As Br replaces Cl, the Raman spectra gets broader due to the formation of new Pb-X bonds as seen from the Figure 5.9 a). As the halide substitution increases up to 50%, the Raman peaks get broader where the octahedral modes can be identified. This observation of broad peaks as seen in Figure 5.9 b) and c) in QDs confirms that

5. Structure of Mixed Halide Perovskite Quantum Dots

the sample is a solid solution, since neither phase-separated materials nor micro/nano domains could be identified. It also can create a highly disordered local $[\text{PbX}_x\text{X}'_{6-x}]^{4-}$ octahedral environment due to rearrangements of bond lengths and angles about the Pb centre. These assignments correspond to probable mixtures of individual lead coordination environments comprised of $[\text{PbCl}_5\text{Br}]^{4-}$, $[\text{PbCl}_4\text{Br}_2]^{4-}$, $[\text{PbCl}_3\text{Br}_3]^{4-}$, $[\text{PbCl}_2\text{Br}_4]^{4-}$, and $[\text{PbBr}_5\text{Cl}]^{4-}$ octahedra, respectively, which are bound by weak chemical bonds that can be easily altered by exposure to light.

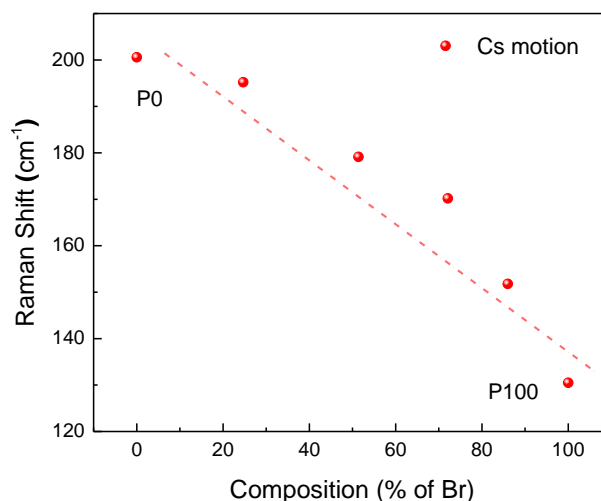


Figure 5.10 Cs motion obtained from Raman spectra for $\text{CsPb}(\text{Cl}/\text{Br})_3$ (P0-P100) QDs at 77 K.

However, effect on Cs-motion as seen in Figure 5.10 can be correlated with the effect caused by the changing composition. The observed shifts reveal a linear relationship, decreasing systematically as Cl anions are replaced by Br anions from $[\text{PbCl}_6]^{4-}$ to $[\text{PbBr}_6]^{4-}$ (Figure 5.10). The linear shift observed in the Cs-motion for the mixed halide perovskites upon composition modulation also is in well agreement with the linear increase in the actual composition tuning that is obtained from the XANES fit as seen from Figure 5.2.

To summarize, we have shown using systematic analysis of structure property correlations in perovskite QDs by using different characterization techniques of various length scales such as XRD and EXAFS and Raman spectroscopy. In particular, we have demonstrated that XAFS can provide valuable information on the internal local structure in perovskite QDs from an elemental perspective. These findings concerning the local structure environment around the Pb octahedra have important consequences regarding their photoluminescence properties. Also, systematic shift in the bandgap and lattice parameter as halide replacement occurs supporting the assumption that these materials exhibit alloy behaviour, readily adjusting

5. Structure of Mixed Halide Perovskite Quantum Dots

their local ($[\text{PbX}_x\text{X}'_{6-x}]^{4-}$) octahedra. The relative ease of rotation of the dynamically changing octahedral environment explains why slight external trigger such as external light exposure that can hasten the anion migrations and eventually lead to phase segregation. We expect that this idea can be used to probe the internal structure of the nanostructures and can provide new insight to designing new and improved optoelectronic devices.

5.5. Conclusions

These findings further support our conclusion that mixed halide perovskite QDs produces a homogeneous halide mixture. A periodic shift in the bandgap as halide substitution occurs supports the conclusion that these materials exhibit solid solution behaviour, readily adjusting their local ($[\text{PbX}_x\text{X}'_{6-x}]^{4-}$) as evident from Raman spectra and long-range (lattice constant) structure as Cl is replaced by Br. To determine that these materials are not phase-separated or located as micro scale domains, we investigated these materials using local structure EXAFS and Raman spectroscopy method. While ongoing development of mixed halide perovskite QDs will require careful characterization, our study has shown that the combination of both X-ray diffraction, EXAFS and Raman spectroscopy, are vital to properly characterize these intrinsically simple yet complex materials.

5. Structure of Mixed Halide Perovskite Quantum Dots

Bibliography

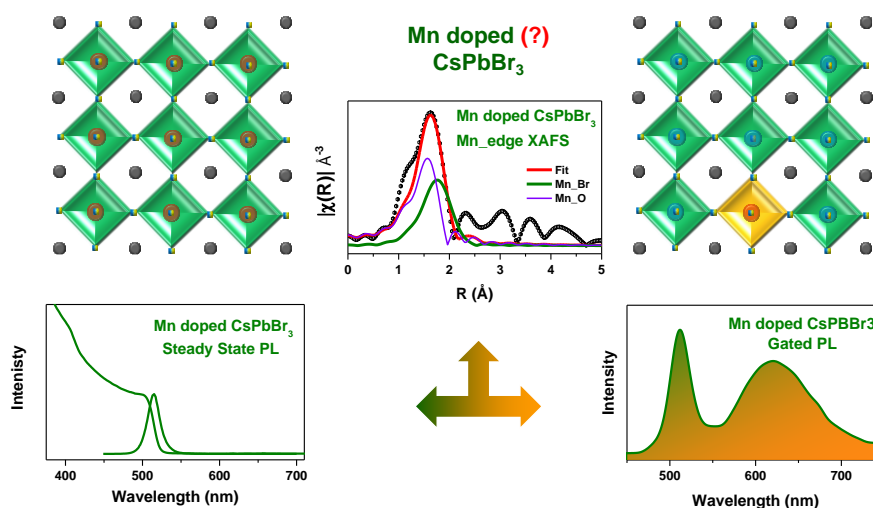
1. Kovalenko, M. V.; Protesescu, L.; Bodnarchuk, M. *Science* **2017**, 358, (6364), 745-750.
2. Zhou, Y.; Chen, J.; Bakr, O. M.; Sun, H.-T. *Chem. Mater.* **2018**, 30, (19), 6589-6613.
3. Fu, Y.; Zhu, H.; Chen, J.; Hautzinger, M. P.; Zhu, X.-Y.; Jin, S. *Nat. Rev. Mater.* **2019**, 4, (3), 169-188.
4. Zhao, Y.; Zhu, K. *Chem. Soc. Rev.* **2016**, 45, (3), 655-689.
5. Chen, Q.; De Marco, N.; Yang, Y. M.; Song, T.-B.; Chen, C.-C.; Zhao, H.; Hong, Z.; Zhou, H.; Yang, Y. *Nano Today* **2015**, 10, (3), 355-396.
6. Beal, R. E.; Slotcavage, D. J.; Leijtens, T.; Bowring, A. R.; Belisle, R. A.; Nguyen, W. H.; Burkhard, G. F.; Hoke, E. T.; McGehee, M. D. *J. Phys. Chem. Lett.* **2016**, 7, (5), 746-751.
7. Swarnkar, A.; Marshall, A. R.; Sanhira, E. M.; Chernomordik, B. D.; Moore, D. T.; Christians, J. A.; Chakrabarti, T.; Luther, J. M. *Science* **2016**, 354, (6308), 92-95.
8. Wang, Y.; Zhang, T.; Kan, M.; Zhao, Y. *J. Am. Chem. Soc.* **2018**, 140, (39), 12345-12348.
9. Protesescu, L.; Yakunin, S.; Bodnarchuk, M. I.; Krieg, F.; Caputo, R.; Hendon, C. H.; Yang, R. X.; Walsh, A.; Kovalenko, M. V. *Nano Lett.* **2015**, 15, (6), 3692-3696.
10. Slotcavage, D. J.; Karunadasa, H. I.; McGehee, M. D. *J. Am. Chem. Soc.* **2016**, 138, (6), 1199-1205.
11. Brennan, M. C.; Draguta, S.; Kamat, P. V.; Kuno, M. *ACS Energy Lett.* **2017**, 3, (1), 204-213.
12. Guerrero, A.; You, J.; Aranda, C.; Kang, Y. S.; Garcia-Belmonte, G.; Zhou, H.; Bisquert, J.; Yang, Y. *ACS Nano* **2016**, 10, (1), 218-224.
13. Hoke, E. T.; Slotcavage, D. J.; Dohner, E. R.; Bowring, A. R.; Karunadasa, H. I.; McGehee, M. D. *Chem. Science* **2015**, 6, (1), 613-617.
14. Steele, J. A.; Lai, M.; Zhang, Y.; Lin, Z.; Hofkens, J.; Roeffaers, M. B.; Yang, P. *Acc. Mater. Res.* **2020**.
15. Li, G.; Ho, J. Y.-L.; Wong, M.; Kwok, H. S. *J. Phys. Chem. C* **2015**, 119, (48), 26883-26888.
16. Yuan, Y.; Huang, J. *Acc. Chem. Res.* **2016**, 49, (2), 286-293.
17. Cottingham, P.; Brutchey, R. L. *Chem. Comm.* **2016**, 52, (30), 5246-5249.

5. Structure of Mixed Halide Perovskite Quantum Dots

18. Brennan, M. C.; Kuno, M.; Rouvimov, S. *Inorg. Chem.* **2018**, 58, (2), 1555-1560.
19. Rehman, W.; McMeekin, D. P.; Patel, J. B.; Milot, R. L.; Johnston, M. B.; Snaith, H. J.; Herz, L. M. *Energy Environ. Sci.* **2017**, 10, (1), 361-369.
20. Rosales, B. A.; Men, L.; Cady, S. D.; Hanrahan, M. P.; Rossini, A. J.; Vela, J. *Chem. Mater.* **2016**, 28, (19), 6848-6859.
21. Karmakar, A.; Askar, A. M.; Bernard, G. M.; Terskikh, V. V.; Ha, M.; Patel, S.; Shankar, K.; Michaelis, V. K. *Chem. Mater.* **2018**, 30, (7), 2309-2321.
22. Newville, M. *J. Synchrotron. Radiat.* **2001**, 8, (2), 322-324.
23. Jacob, K.; Raj, S.; Rannesh, L. *Int. J. Mater. Res.* **2007**, 98, (9), 776-779.
24. Ravel, B.; Newville, M. *J. Synchrotron Radiat.* **2005**, 12, (4), 537-541.
25. Calistru, D. M.; Mihut, L.; Lefrant, S.; Baltog, I. *J. Appl. Phys.* **1997**, 82, (11), 5391-5395.

Chapter 6

Doping in Perovskite Quantum Dots: Synthesis, Stability and Local Environment



The following papers have been published based on work presented here:

Pradeep K R, S. Chakraborty, R. Viswanatha, "Stability Sn of Based Inorganic Perovskite Quantum Dots" *Mater. Res Express*, (2019), 6, 114004.

Pradeep K R, R. Viswanatha, "Doped or Not Doped? Importance of the Local Structure of Mn (II) in Mn Doped Perovskite Nanocrystals" *Mater. Res Bulletin*, (2021), (Under review).

6. Doping in Perovskite QDs: Synthesis and Stability

6. Doping in Perovskite QDs: Synthesis and Stability

6.1. Abstract

Metal halide perovskite crystal structures have emerged as a class of optoelectronic materials, which combine the ease of solution processability with excellent optical absorption and emission qualities. However, even though the optical and crystal structure stability in some of the inorganic perovskites leaves much room for improvement, so far there has been no studies on the structure property correlation. Further the most promising perovskite structures rely on lead as a cationic species, thereby hindering commercial application. The replacement of lead with non-toxic alternatives such as tin has been studied in bulk but not in quantum dots. Also doing with transition metals such as manganese adds additional functionality to tune their optical properties. In this chapter, we first obtain the structure property correlation in CsPbI₃ and CsPbBr₃ perovskite structures. We then use these correlations to study the stability of Sn doped perovskites. We synthesize Sn and Pb based alloy perovskite quantum dots by direct synthesis method by of taking mixture of Pb and Sn precursors in the desired ratio leading to quantum dots (QDs) of CsPb_{1-x}Sn_xBr_yI_{3-y} with successful Sn incorporation into the host lattice. As colloidal stability of these QDs is a crucial factor for device applications, we have studied the stability of the QDs under different conditions for these Sn based QDs and have found them to degrade faster upon using anti-solvents during washing process. In order to stabilize them, we have devised a purification method that is discussed in this chapter. We then study their structural purity and their optical stability which was found to be extremely stable across the series of compounds for up to three months. Once the Purification strategy is developed and stability is obtained, the same method is employed to obtain Mn doped QDs. Transition metal doping of semiconductor QDs can generate new optical, magnetic, properties through dopant-host interaction. Although Mn²⁺ doping in semiconducting QDs has been studied for decades, Mn doped perovskite QDs have opened up new avenues for optoelectronic applications due to signature Mn d-d emission. However, Mn doping in bromide-based perovskite QDs have not shown this signature peak sowing doubts about the efficient doping in these systems. Here, we demonstrate that the chemical bonding and local environment of Mn obtained using electron paramagnetic resonance (EPR) and X-ray absorption fine structure (XAFS) is similar to that of chloride-based perovskites.

6.2. Introduction

Intense development of organometallic and inorganic lead halide systems have led to a dramatic surge in the efficiency of the opto-electronic applications including photovoltaics,^{1 2}

6. Doping in Perovskite QDs: Synthesis and Stability

light emitting diodes (LEDs)³ and lasers.⁴ This is largely powered by sustained research interest to produce cost-competitive, facile, and environmentally friendly technologies. Among these, the perovskite systems exhibit numerous advantages like abundance of materials, flexibility, and simple processing leading to low production cost which directly contributes to the competitiveness with other commercial technologies like indium tin oxide. Additionally, doping lead halide perovskite QDs with transition metals is also explored improve the stability and optical properties.⁵⁻⁸ In this context, aiming for the retention of optoelectronic properties, tin based perovskites and transition metal doped perovskites have attracted most attention due to its similar ionic radii. And in terms of transition metal doping, Mn is most studied due to the stoke shifted intense Mn d-d emission at 580 nm.^{7,9}

The success of Mn doping in II-VI semiconductors made it a natural extension to address a similar doping strategy to modify the spectroscopic properties of highly emissive perovskite QDs as well.^{6, 10, 11} However, although doping with Mn in inorganic perovskite QDs have also shown improved PLQY,^{12, 13} structural stability,^{14, 15} and improved size distribution¹⁶, it is plagued with the presence of band edge emission leading researchers to believe that there exists a small percentage of undoped QDs population in spite of best efforts to overcome the same.¹¹ Additionally, Mn emission has not been observed in hosts with lower bandgaps such as CsPb(Cl/Br)₃ and CsPbBr₃¹⁷⁻²⁰ although doping in similar band gap II-VI semiconductor QDs have shown very promising results.²¹ This anomalous behaviour of retaining the advantages of Mn doping but lack of the optical signatures of successful Mn doping in perovskite QDs indicate that relying on optical signature to confirm successful incorporation of Mn as a dopant may not be valid in the case of perovskite QDs as a host.

But there are several challenges in the synthesis of doped QDs due to the difficulties in obtaining uniformly doped QDs. Primarily due to the fact that the dopant precursor needs to be introduced in the initial stage of the reaction and its nearly impossible to replace lead with Mn post synthesis unlike the synthesis strategies used for doping in II-VI semiconductor QDs. Secondly, high dopant to host precursor ratio need to be used for successful incorporation of Mn into the perovskite structure which affects the reaction conditions. Drastically increasing the dopant precursor amount in the reaction brings down the colloidal stability and reduced emission with lots of unreacted precursors in the mixture. However, Mn doped QDs are relatively stable compared to Sn doped perovskite QDs. Hence standardising the stabilizing and purifying strategies with Sn as a dopant can help in improving the quality of Mn doped QDs further and can obtain QDs with enhanced emission properties.

6. Doping in Perovskite QDs: Synthesis and Stability

Despite the impressive progress in lead-halide perovskites, several challenges related to stability upon prolonged exposure to light, humidity, and high temperature as well as the development of suitable large-scale manufacturing processes are yet to be addressed. In this context, the most unsettling flaw of these perovskite materials, that is also a stumbling block for the large-scale applications, is the toxicity of the dissolvable lead leading to environmental concerns. This has led to a great deal of interest in replacing Pb with less toxic metals such as Bi²², Sn²³, Ge²⁴ but the efforts have largely been unsuccessful due to the highly unstable nature of these compounds under ambient conditions.

A quick inspection of fundamental physical properties of tin based perovskites lead to remarkable similarities with their lead-based counterparts. Therefore, Pb substitution by Sn should cause no obvious lattice distortion in perovskites²⁵. Cesium tin iodide (CsSnI₃) has direct bandgap of around 1.3 eV²⁶, which is even narrower and more attractive for NIR applications than those of their Pb-based analogues. After exposure to ambient air, the Sn-based perovskites degrade to Sn⁴⁺ becoming SnO₂, which is an environment-friendly material. Though, recently, Pb free CsSnX₃ QDs have been reported to exhibit visible to NIR bandgap tunability (2.8-1.8 eV) they failed to perform in the field of optoelectronic devices due to very low PL QY and poor stability²⁷.

Hence though in principle we expect to reproduce similar efficiencies of these materials, the tin based perovskites are known to be extremely unstable. While a lot of research has gone into exploring how to stabilize and improve the efficiency of tin based perovskites, the fundamental reason for this instability has not been explored. In this chapter we study the structural correlation in a wide range of lead-based perovskites ranging from highly stable and luminescent materials like CsPbBr₃ to the unstable CsPbI₃. We then dope tin in lead-based perovskites to understand if similar structural features lead to decay of its optical properties. Then, we look for stabilizing the Sn doped cesium lead halide systems by maintaining the structural phases to study its optical properties. Once the purification strategy is developed and stability is obtained, the same method is employed to obtain Mn doped QDs. Here, in this work we compare various characterisation techniques used in Mn doped nanostructures to confirm successful incorporation of Mn as a dopant and analyse their reliability in doped perovskite QDs, in the absence of PL emission features from Mn doped QDs. The lack of clarity and minimal information provided by structural characterisation and inefficiency of PL emission spectroscopy to confirm the successful incorporation of dopant to perovskite QDs are discussed. To confirm the presence of uniformly doped Mn in the QDs, one of the most

6. Doping in Perovskite QDs: Synthesis and Stability

extensively used techniques in early literature was the X-band electron paramagnetic resonance (EPR) spectra. EPR spectra can also be used to determine the location of the dopant in the QDs since the hyperfine splitting is strongly dependent on the local environment.²⁸ However, the expectation of an octahedral lattice for the Mn replacing Pb in the Pb-halide octahedra further complicates the analysis of the local structure as the surface bound Mn ions are also expected to have an octahedral geometry owing to O_2^- geometry.²⁹ Though local structure analysis has been used in literature as an excellent tool to understand the environment around the dopants, X-ray absorption fine structure (XAFS) has not been studied so far to realize the local coordination environment around Mn. Insight into the local structure of Mn using XAFS in Mn doped perovskite mixed halide perovskite QDs can address several of the open challenges in this class of compounds. This knowledge can also facilitate the information to unravel the missing links between the dopant emission mechanism and chemical bonding in Mn doped perovskite mixed halide QDs.

6.3. Experimental Methods

Although optical properties of colloidal perovskite QDs can easily be tailored through halide exchange reactions,³⁰⁻³¹ cation exchange to obtain mixture of Pb and other metals have been rarely attempted. Recently, replacing a small percentage of Pb with divalent atoms such as Mn^{2+} , has been tried by taking mixture of Pb and Mn precursors to achieve characteristic Mn dopant emission.⁹ Post synthetic cation exchange on $CsPbBr_3$ by Sn, Cd, Zn to replace Pb has also been reported recently.¹⁸ However, direct synthesis of perovskite QDs based on Sn/Pb mixture has been attempted very rarely.³² Here, in this chapter, we take mixture of Pb and Sn precursors in the desired ratio to replace Pb with Sn leading to QDs of $CsPb_{1-x}Sn_x(Br/I)_3$ with successful Sn incorporation into the host lattice.

6.3.1. Materials

Chemicals used in the experiments include Cs_2CO_3 (99.99%), octadecene (ODE, 90%), oleic acid (OA, 90%), oleylamine (OLAm, 70%), PbI_2 (99.999%), $MnBr_2$ (99.9%), $MnCl_2 \cdot 4H_2O$ (99%), n-hexane (> 97.0%), trioctylphosphine (TOP), and SnI_2 (99%) used directly after purchasing from Sigma-Aldrich. $SnBr_2$ (99.999%) was purchased from Alfa-Aesar. All solvents and reagents were of analytical grade and directly used without further purification.

6.3.2. Preparation of Cs-Oleate

Cesium oleate was synthesized using standard literature methods³³ using Cs_2CO_3 and OA in presence of ODE at high temperature of 150 °C until all Cs_2CO_3 reacted with OA forming Cs-oleate.

6. Doping in Perovskite QDs: Synthesis and Stability

6.3.3. Synthesis of Undoped and Sn doped CsPb(Br/I)₃ QDs.

Perovskite QDs were prepared according to the method described by Protesescu et al³⁴. Stoichiometric mixtures of PbI₂ and PbBr₂ were used for the synthesis of undoped QDs, whereas stoichiometric mixtures of PbI₂ and PbBr₂ with SnI₂ and SnBr₂ were taken for the synthesis of Sn doped CsPb(Br/I)₃ perovskite QDs. Tin precursor was prepared in a glove box under Ar atmosphere by dissolving SnBr₂ in the mildly reducing solvent TOP and sonicated for 5min for complete dissolution of SnBr₂ salts in 1 mL TOP. ODE (5mL) and the required Pb/Sn salts were loaded into a 3-neck flask and dried under vacuum for 1 hour at 120°C. Dried OlAm (1 mL), and dried OA (1 mL) were injected at 120°C under Argon flow. After complete solubilisation of Pb/Sn salts, the temperature was raised up to 180°C and Cs-oleate solution (0.4mL preheated to 100°C) was quickly injected and 5 seconds later the reaction mixture was cooled down by ice water bath.

6.3.4. Synthesis of Mn-doped CsPb(Br/Cl)₃ perovskite quantum dots (QDs):

Stoichiometric mixtures of PbCl₂ and PbBr₂, with MnCl₂.4H₂O and MnBr₂ were taken for the synthesis of both size and composition modulation of Mn-doped CsPb(Br/Cl)₃ perovskite QDs. ODE (5mL) and the required Pb/Mn salts were loaded into a 3-neck flask and dried under vacuum for 1 hour at 120°C. Dried OlAm (1.5 mL), dried OA (1.5 mL) and TOP (1 mL) were injected at 120°C under Argon flow. After the complete solubilization of the precursors added and obtaining a clear solution, the temperature was raised up to 180°C for composition modulation and Cs-oleate solution (0.4mL preheated to 100°C) was quickly injected and 5 seconds later the reaction mixture was cooled down by ice water bath.

6.3.5. Isolation and purification of the Undoped and Sn doped CsPb(Br/I)₃ QDs and Mn doped CsPb(Cl/Br)₃ QDs

The QDs were first washed by adding tert-butanol to the crude solution and centrifuging at speed of 5000 rpm for 5 minutes. The supernatant was discarded and the particles were re-dispersed in hexane. For obtaining colloidally stable QDs, the crude solution was cooled down by water bath and QDs were separated by centrifuging for 10 minutes at 5000 rpm. The precipitated QDs were dispersed in hexane and this suspension was centrifuged again for 5 min at 10000 rpm, after which the precipitate, containing unreacted precursors, larger QDs and agglomerates, was discarded. The supernatant containing the QDs was then stored under refrigeration.

6.4. Results and Discussion

Structure property correlation in lead halide perovskites are first studied to understand the source of instability of optical properties. It has been well known in literature³⁵ that among the halides, iodides are known to be optical unstable when exposed to air and moisture. Hence, we first characterized the CsPbI₃ QDs as shown in Figure 6.1. Figure 6.1 a) shows the absorbance and PL of CsPbI₃ measured immediately after synthesis (red plots) and measured after 10 days. It is clearly evident that not only the PL intensity died down within this period but the absorption was heavily blue-shifted similar to available literature³⁵ showing clear transformation from optically active to inactive phase. This could possibly be due to a phase transition during this period as CsPbI₃ QDs are known to be stabilized in both cubic and orthorhombic phases. This was further verified by XRD patterns of these two samples taken over a period of 10 days that is shown in Figure 6.1 b) which shows structurally unstable CsPbI₃ transforming from cubic to orthorhombic phase under ambient conditions matching the available literature³⁵. Hence even though stabilising the cubic phase is a challenging task, the difference in structural information between both the crystal phases and PL features can be a useful tool to study effect of Sn doping taking CsPbI₃ as starting host QDs. The PL emission peak at 695 nm for cubic CsPbI₃ which is dark brown in colour transforms to the yellow orthorhombic phase that is PL inactive under continuous exposure to air, atmosphere and moisture. However due to the speed of decomposition and the instability of cesium lead iodides, doping Sn in CsPbI₃ to study the structure property correlation is non-trivial, even though CsSnI₃ is of higher relevance in applications.

In order to overcome this shortcoming, we started doping Sn in CsPbBr₃ as it is well known in literature that CsPbBr₃ is more stable than the CsPbI₃ allowing a better chance to correlate the properties with the structural information. Sn doped CsPbBr₃ for varying Sn concentrations were characterized by XRD as shown in Figure 6.2 a). From the figure, it is evident that the Sn-doped CsPbBr₃ shows same characteristic diffraction peaks as undoped CsPbBr₃ without the presence of any impurities. Similarly, the band gap of CsPbBr₃ in both the cubic and orthorhombic phases are very similar and optically active. Figure 6.2 b) shows the optical absorption and PL data upon Sn incorporation which shows blueshift in both the absorbance and steady state photoluminescence spectra. Undoped CsPbBr₃ has a band gap of 509 nm (2.44 eV) which upon Sn doping up to 10%, blueshifts systematically up to 496 nm (2.5 eV). Further increase in Sn percentage leads to severe shift in the band gap, possibly due to phase segregation or due to the breakdown on the perovskite structure. In addition, it is

6. Doping in Perovskite QDs: Synthesis and Stability

evident that attempt to increase the Sn dopant in the host system leads to optically unstable QDs. This is not surprising as partial replacement of Pb^{2+} by several isovalent ions like Sn^{2+} , Cd^{2+} , and Zn^{2+} is known to give rise to blueshift in the optical spectra which is attributed to the lattice contractions.¹⁸

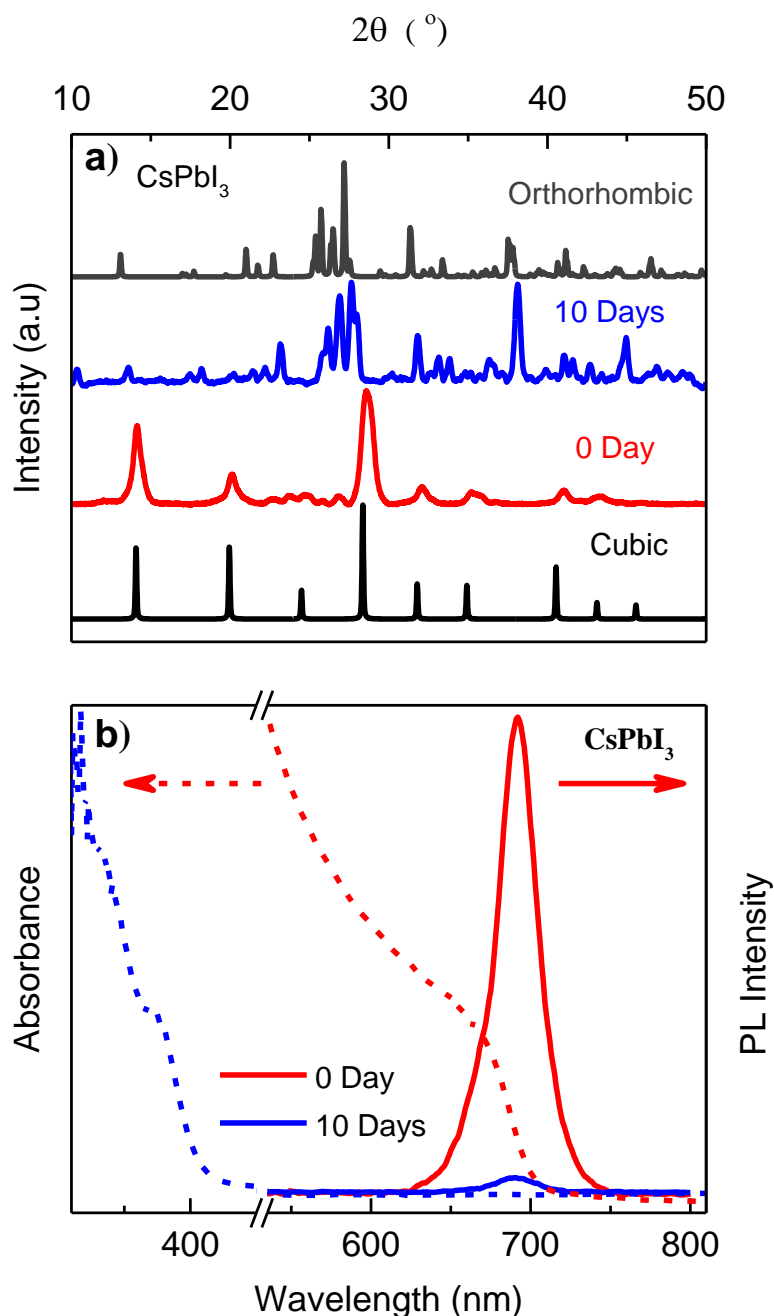


Figure 6.1 a) XRD patterns for freshly prepared cubic CsPbI_3 QDs and orthorhombic QDs after 10 days undergoing phase transformation. Reference XRD for the bulk CsPbI_3 is also shown for comparison. b) Absorbance and steady state PL spectra for cubic and orthorhombic QDs taken during the span of 10 days showing degradation.

6. Doping in Perovskite QDs: Synthesis and Stability

However, in contrast to CsPbI₃ wherein direct evidence about stable phase could be obtained from XRD and optical absorption data, from the perspective of structure property correlation, the XRD pattern and the band gap of this system does not prove to be very useful. The band gap of CsPbBr₃ is not different for both cubic and orthorhombic phase unlike CsPbI₃. Additionally, it is nearly impossible to differentiate between the cubic and orthorhombic phases between QDs of CsPbBr₃ due to similarities in the XRD patterns of the bulk as also shown in Figure 6.2 a). Hence direct correlation between structural stability and PL emission cannot be studied.

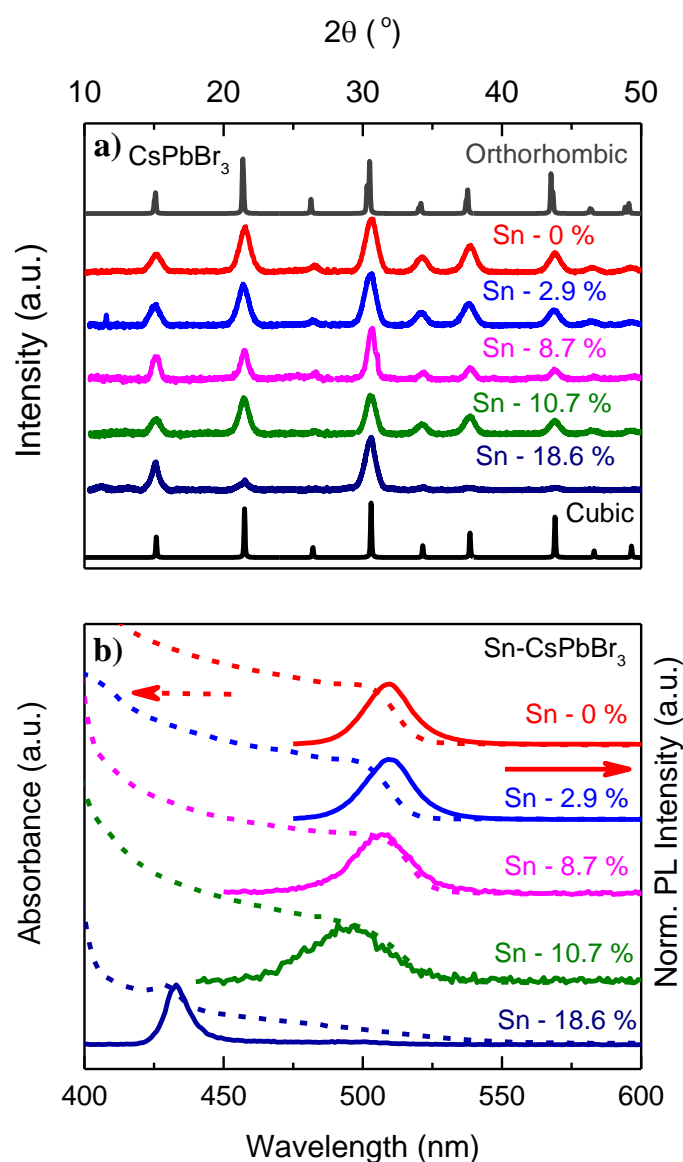


Figure 6.2 a) XRD patterns for Sn doped CsPbBr₃ in comparison with reference patterns for cubic and orthorhombic phases of bulk CsPbBr₃ b) Absorption and PL emission for undoped and Sn doped CsPbBr₃.

6. Doping in Perovskite QDs: Synthesis and Stability

In order to overcome both these shortcomings, we studied stability of mixed halide systems as a function of Sn doping with special emphasis on sample purification. In order to achieve this, we used SnBr₂ as a cation precursor source in the synthesis such that in addition to Sn incorporation, anionic mixing between Br and I can improve the structural stability and optical stability.

Stoichiometric mixtures of SnBr₂ and PbI₂ was used for synthesis of Sn-doped CsPb(Br/I)₃ QDs. Normal purification techniques involve washing the as prepared samples using 1:1 mixture of tert-butanol with crude solution and centrifuged at 5000 rpm for 10 min. However, these antisolvents like tert-butanol not only precipitate the QDs and the excess unreacted precursors³⁴ but also facilitate removal of the surface ligands which can lead to exposure of QDs to air and moisture, thus enhancing the rate of degradation. Presence of unreacted precursors are favourable for well-known ion migrations giving rise to phase segregated perovskite QDs reported earlier.³⁶ Hence it is important to introduce an effective way of purifying as synthesized QDs which can be both structurally and optically stable.

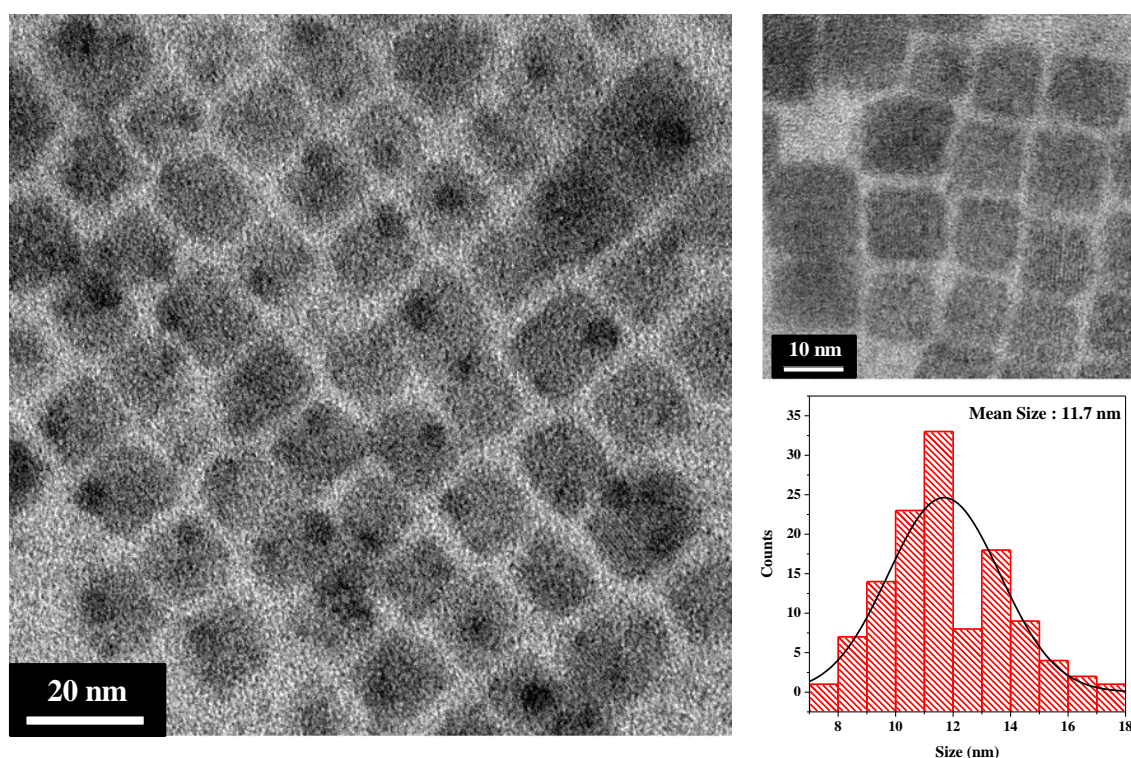


Figure 6.3 Representative high resolution TEM images for 2.1 % Sn doped CsPb(Br/I)₃ QDs with average size of 11.7 nm.

6. Doping in Perovskite QDs: Synthesis and Stability

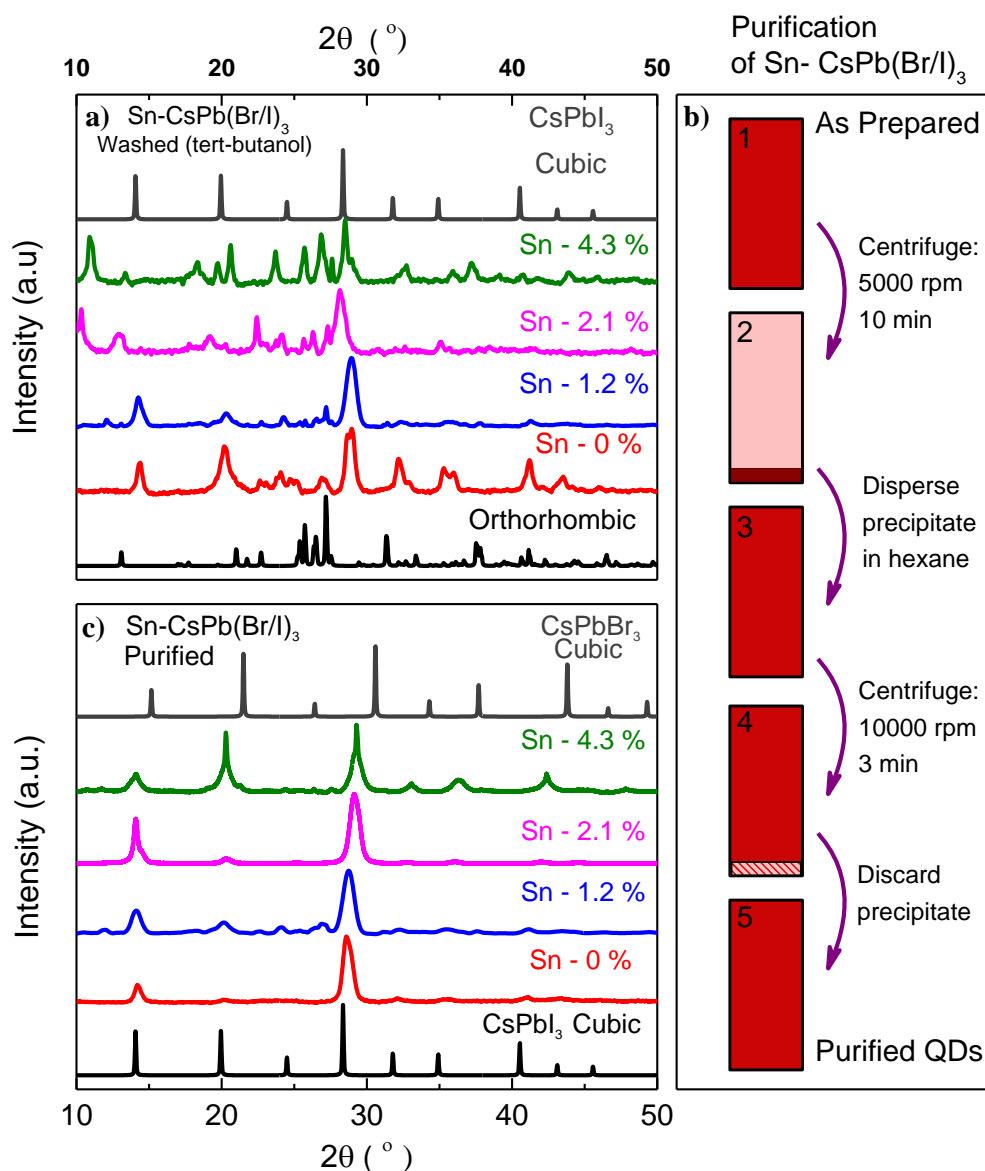


Figure 6.4 a) XRD patterns for Sn doped CsPb(Br/I)₃ QDs washed using tert-butanol. b) modified purification method to obtain colloiddally stable QDs. c) XRD for QDs purified using method shown in b) showing no impurity and highly crystalline cubic phases.

Representative TEM and HRTEM images for 2.1 % Sn doped CsPb(Br/I)₃ QDs are shown in Figure 6.3 with QDs showing average size of 11.7 ± 1.5 nm. Typical XRD patterns of Sn doped CsPb(Br/I)₃ QDs for various Sn dopant percentages is shown in Figure 6.4 a). The sizes as obtained from the broadening of the XRD peaks is estimated to be about 11.5 ± 1 nm from the Scherrer formula in accordance with the sizes obtained from TEM images. From the Figure 6.4 a) it is evident that upon Sn incorporation it is seen that orthorhombic peaks started arising which, in turn, led to less intense PL emission compared to their cubic counterparts.

6. Doping in Perovskite QDs: Synthesis and Stability

Further presence of small mixture of orthorhombic phase led to faster degradation and ion migrations of the QDs at ambient conditions. Hence, we developed a modified purification strategy of the Sn-doped QDs for the conservation of the structural integrity. The as synthesized QDs were centrifuged at high speed for around 10 min to precipitate the QDs and the supernatant containing solvents like ODE was discarded. The precipitate contained both Sn doped perovskite QDs and excess ligands and precursor complexes. To remove all the unnecessary components that are known to hinder the QDs performance were removed by dissolving the precipitate in hexane and centrifuging at high speed (10000 rpm) for 3 min. By doing this, unreacted precursors precipitated out of hexane. Further the supernatant was collected and the process was repeated multiple times to remove the unreacted precursors. The schematic of the purification process is shown in Figure 6.4 b). These samples are referred as purified samples in the rest of the chapter.

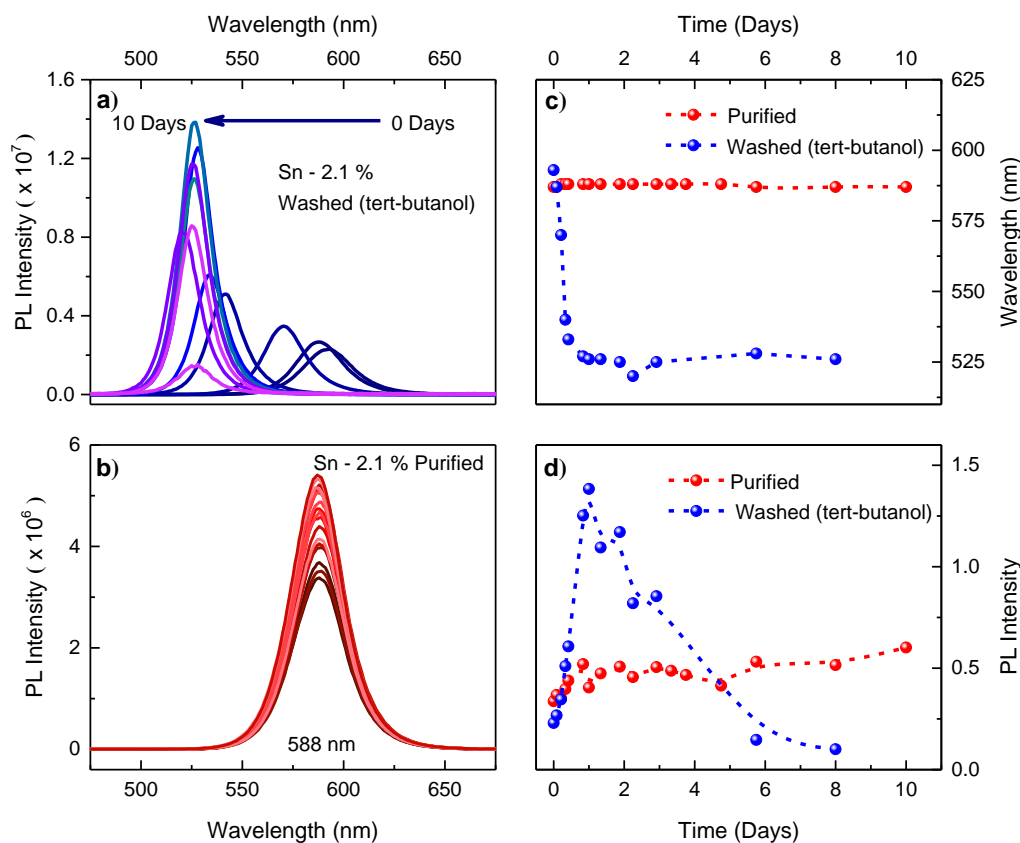


Figure 6.5 a) PL spectra for 2.1 % Sn doped $\text{CsPb}(\text{Br/I})_3$ QDs washed using tert-butanol showing blueshift in emission and fluctuations in PL emission. b) PL spectra for purified QDs of 2.1 % Sn doped $\text{CsPb}(\text{Br/I})_3$ showing stable 588 nm emission peak over 10 days with high colloidal stability. c) and d) shows variation of PL emission and its intensity over a period of 10 days demonstrating very high colloidal stability for Sn doped perovskite QDs.

6. Doping in Perovskite QDs: Synthesis and Stability

The purified samples were preserved in refrigerator for longer stability. XRD patterns of Sn-doped QDs purified by above method is shown in Figure 6.4. c) which show that all the samples retain cubic crystal structure and do not contain any of the impurity peaks. Hence by selective and careful precipitation of the QDs after the reaction, cubic Sn doped CsPb(Br/I)₃ QDs can be synthesized.

Optical stability of the QDs were studied over a period of 10 days kept under ambient conditions and were compared with QDs washed using tert-butanol. The results are summarized in Figure 6.5. Figure 6.5 a) shows the PL spectra for Sn-2.1% washed using tert-butanol. Over a period of 10 days we see that the PL blueshifts in addition to reduced PL intensity. The facile phase segregation in this group of systems are well known in literature³⁷⁻⁴⁰ and reduced ligands can further hasten this process. Hence this blueshift in the spectra could possibly arise due to phase segregation of the QDs and phase transition of the iodine rich phase into the optically inactive orthorhombic phase. Due to this phase segregation, the ratio of optically active phase contains an increased Br/I ratio resulting in the blueshift of the spectra in addition to deterioration of the PL intensity. In contrast to this highly unstable QDs, purification using repeated centrifugations leads to more stable QDs with no shift in PL emission spectra and minimal intensity fluctuations giving an emission peaked at 588 nm as shown in Figure 6.5 b). Figure 6.5 c) shows variation in PL emission wavelength plotted over a period of 10 days for the samples washed using tert-butanol as well as the purified samples. As observed from the spectra, samples washed with tert-butanol showed a continuous blueshift while the purified samples showed very high colloidal stability and the PL emission wavelength was invariant for over 10 days. Similarly, PL intensity variation showed uniform emission intensity for purified QDs while the samples washed by tert-butanol demonstrated a dramatic variation in its intensity as also shown in Figure 6.5 c).

However, having good colloidal stability and optical emission quality over a period of 10 days are not sufficient for device application perspective. Hence it is important to know the structural stability of these QDs over long term. As we have seen that PL emission is directly correlated to structural properties, even presence of minor surface degradation and exposure can lead to huge changes in emission quality and PL quantum yield (QY). Additionally, for device applications, these QDs have to be spin coated to a film and once they are cast on a film, the chances of reduction in PL QY and transformation from cubic (known as the black phase) to orthorhombic phase (optically inactive yellow phase) transition are much higher.

6. Doping in Perovskite QDs: Synthesis and Stability

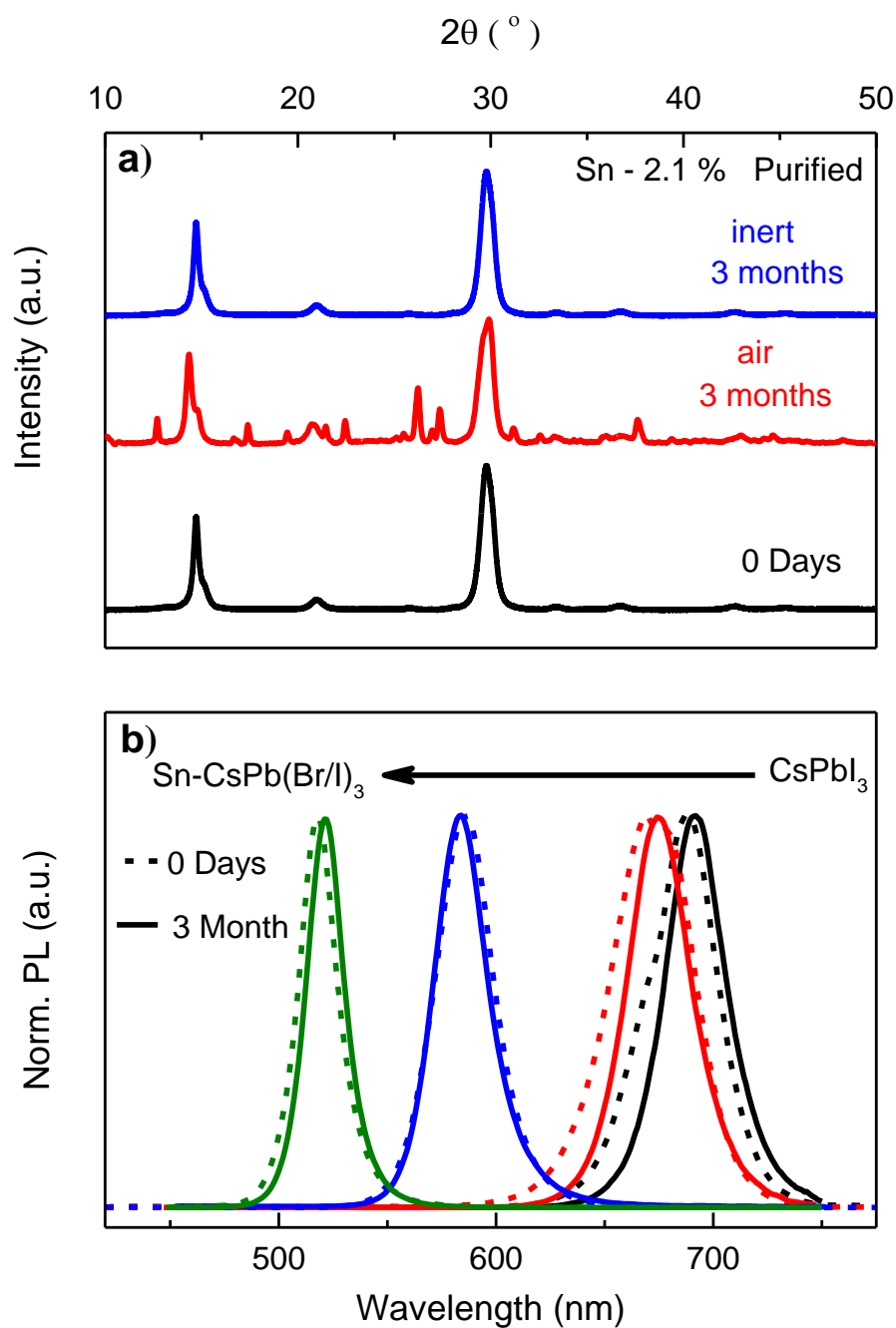


Figure 6.6 a) XRD spectra for 2.1 % Sn doped $\text{CsPb}(\text{Br/I})_3$ QDs showing long term structural stability over 3 months. b) Normalised PL spectra taken after 3 months in comparison to freshly prepared Sn-doped $\text{CsPb}(\text{Br/I})_3$ QDs.

To understand the long-term stability of the Sn doped QDs, we performed XRD and PL spectra after 3 months and the results are shown in Figure 6.6 a) and b) respectively. The films exposed to air, moisture and ambient light kept at room temperature showed signatures of slight degradation and showed presence of slow but definite phase transition. Prolonged exposure to

6. Doping in Perovskite QDs: Synthesis and Stability

ambient light and moisture and atmosphere is shown to degrade the structural features and PLQY and it has been shown that the encapsulation of these QDs within polymer matrices enhances the stability.⁴¹ The stability of these QDs is also enhanced by the use of various methods like embedding the QDs in silica microsphere^{42,43} or in PMMA polymer matrix.^{34,44} Interestingly, we observed ultra-high structural stability for these QDs preserved in glovebox as seen from Figure 6.6 a). Hence it is recommended to preserve the QDs, especially films under inert atmospheres for long term stability. Figure 6.6 b) shows normalised PL spectra for all the Sn doped CsPb(Br/I)₃ taken after 3 months showing no blueshift and maintain narrow emission linewidth with high PLQY.

Once synthesis, purification methods are standardised for Sn based QDs and the reasons for degradation is understood and long term colloiddally stable QDs are obtained, it becomes easier for preparing Mn doped mixed halide perovskite QDs. Mn doped perovskite QDs were prepared via hot injection method by taking various ratios of Pb and Mn halides. Figure 6.7 (a) shows a typical TEM image for Mn doped lead halide QDs showing uniform size distribution of about 10 nm. XRD measurements were performed on various Mn concentrations to understand the effect of Mn doping on the structure, with specific emphasis to the shift in the XRD peaks as well as the probable presence of independent dopant clustering peaks. Figure 6.7 (b) and (c) shows the Mn doped CsPbCl₃ (MP0) QDs for 0% Mn to 7.2 % Mn doped QDs as obtained from inductively coupled plasma – optical emission spectroscopy (ICP-OES). From the figure, it is evident that Mn doped QDs possess similar crystal structure as that of cubic CsPbCl₃ with small shifts arising from the successful doping of Mn with very small shift for lesser Mn doping into the lattice. Figure 6.7 (d) shows the lattice contraction arising due to the substitution of the larger Pb²⁺ (133 pm) ions by smaller Mn²⁺ (97 pm) ions further demonstrating the successful incorporation of Mn into the perovskite lattice. Additionally, the absence new impurity peaks indicate the absence of independent clusters of Mn impurity. Further, we observe from Figure 6.7 (e) and (f) that this shift is consistent across the entire mixed halide series suggesting that the Mn doping has crystallographically similar effect across the entire series of halides from chlorides to bromides. However, the presence/absence of the shift in these QDs is often not confirmatory test in QDs due to the broadness of the peak arising from its small size especially for QDs with smaller concentration of Mn.

6. Doping in Perovskite QDs: Synthesis and Stability

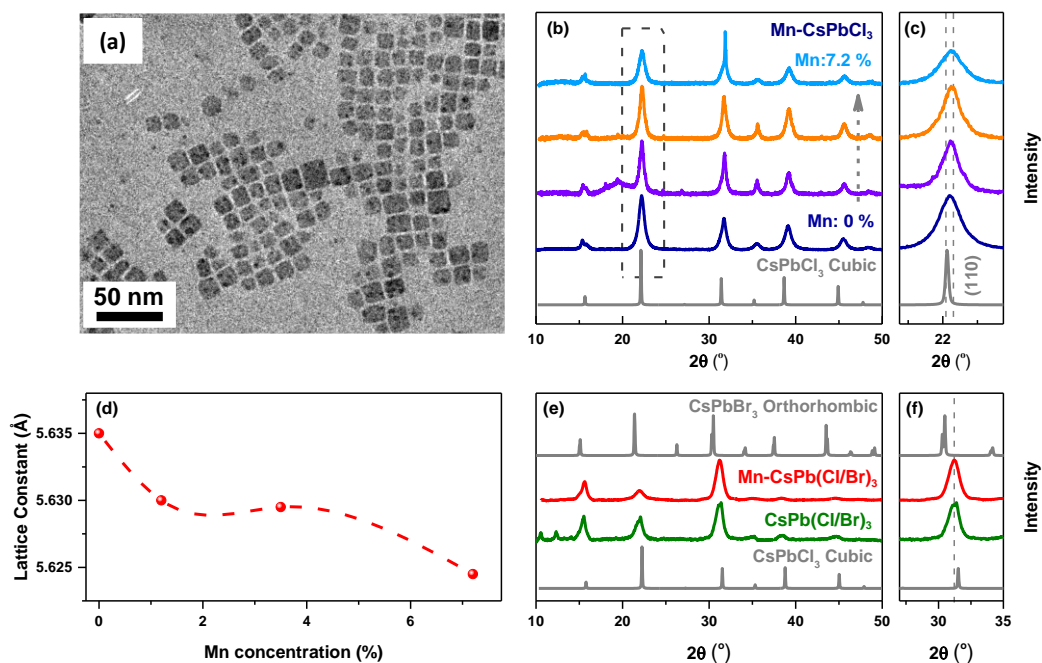


Figure 6.7 (a) Representative high resolution TEM images of Mn doped CsPbCl_3 QDs. (b) XRD patterns for pure (CsPbCl_3) and Mn doped halide perovskite QDs with various Mn: Pb precursor ratio. experimental data is compared to the bulk cubic structure of CsPbCl_3 . (c) expanded view of the (110) peak indicating the shift (d) Lattice contraction arising due to Mn doping. (e) XRD patterns for Br-rich undoped and Mn doped $\text{CsPb}(\text{Cl}/\text{Br})_3$ perovskite QDs. experimental data is compared to cubic CsPbCl_3 and orthorhombic CsPbBr_3 . (f) expanded view of the XRD patterns for the same indicating the shift.

Understanding the actual location of the dopant distribution in the QDs is critical to the observation of the signature optical properties. Hence, we performed X-band EPR spectra for MP0-MP100 (MP0 - Mn doped CsPbCl_3 and MP100 - Mn doped CsPbBr_3) and the results are shown in Figure 6.8. From the figure, we observe a clear signature of Mn at the prescribed magnetic field of 3200 G. We observe a broad feature with small hyperfine splitting pattern of an isolated Mn ion in its 2+ oxidation state in the case of all the NC ranging from MP0-MP100. The presence of a broad feature corresponds to the presence of large Mn concentration within the QDs and is identical for most of the cases from MP0 to MP100. The hyperfine splitting constant of 86G suggests the presence of an octahedral coordination consistent with previous reports for an octahedral coordination for Mn in the system, suggesting an absence of clustering and any other environment for the Mn^{2+} ion. EPR spectra have been traditionally used in systems that form a tetrahedral environment within the lattice and an octahedral environment for the species lying outside. In these cases, hyperfine splitting constant has been used to detect

6. Doping in Perovskite QDs: Synthesis and Stability

Mn²⁺ in tetrahedral lattice or the octahedral surface.^{45, 46} However, as both the internal lead halide lattice as well as the surface lattices form an octahedral environment, EPR spectra is unable to differentiate the exact location of Mn as a dopant and further analysis is required to decode the local environment around Mn.

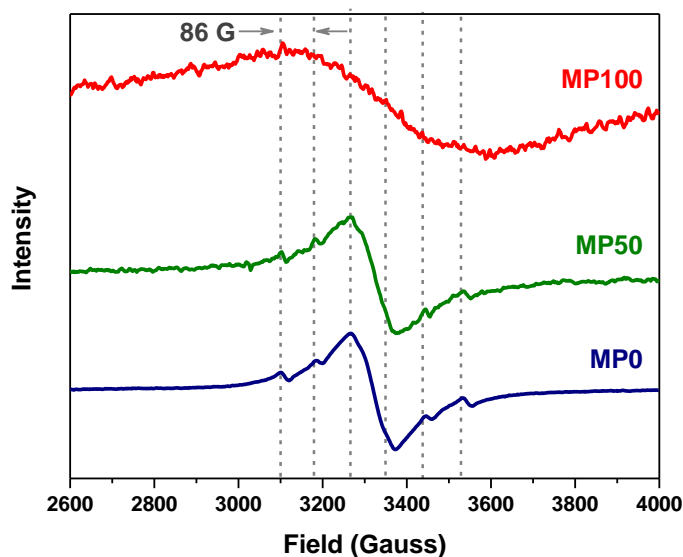


Figure 6.8 Room temperature X band EPR spectra for Mn doped perovskite QDs (MP0-P100).

Thus, with the background that structurally MP0 and MP100 show similar results following the introduction of Mn into the lattice, we study the optical properties that yield completely different results. So far, the broad Mn emission at ~580 nm has been considered as a signature of doped Mn semiconductors. Figure 6.9 (a) shows the PL emission spectra for MP0 with various Mn: Pb ratios. The undoped QDs exhibit a PL centred at 404 nm. The 580 nm emission arising from the Mn doping increases in intensity when compared to the host emission with increase in Mn concentration till 3.2 % Mn, following which we observe a decrease due to Mn-Mn interactions. However, it is interesting to note that even though the band edge emission decreases with increasing Mn percentage, it does not go down to zero unlike other II-VI semiconductors. This behaviour is further exemplified with the introduction of the bromide ions to substitute the chloride ions as shown in Figure 6.9 (b). Figure 6.9 (b) shows the absorption and steady state PL spectra for Mn doped CsPb(Cl/Br)₃ mixed halide perovskite QDs (MP0-MP100) at room temperature. The consistent redshift in the absorbance is due to composition modulation obtained by Br incorporation in Mn doped mixed halide perovskite QDs. Similar to earlier reports,^{11, 47} decrease in intensities of Mn d-d emission is also observed upon decreasing the host bandgap by Br incorporation. The inset shows a typical

6. Doping in Perovskite QDs: Synthesis and Stability

PL lifetime of Mn emission indicating long lived emission ($\tau \sim$ few ms) in all cases wherever the signal exists. The dramatic reduction in the Mn emission with increasing Br content was attributed to removal of Mn from the QDs, which was proven to be wrong as the Mn emission recovered by doing reverse anion exchange eventually leading to Cl rich QDs.¹¹ ICP-OES as well as XRD shifts suggests substantial doping in MP100 confirming the presence of Mn in the QDs. Clear differences in the mechanism of Mn emission in II-VI semiconductor QDs as host and mixed halide perovskite QDs⁴⁸ suggest that presence of strong Mn emission irrespective of host bandgap is no longer a clear signature of Mn doping.

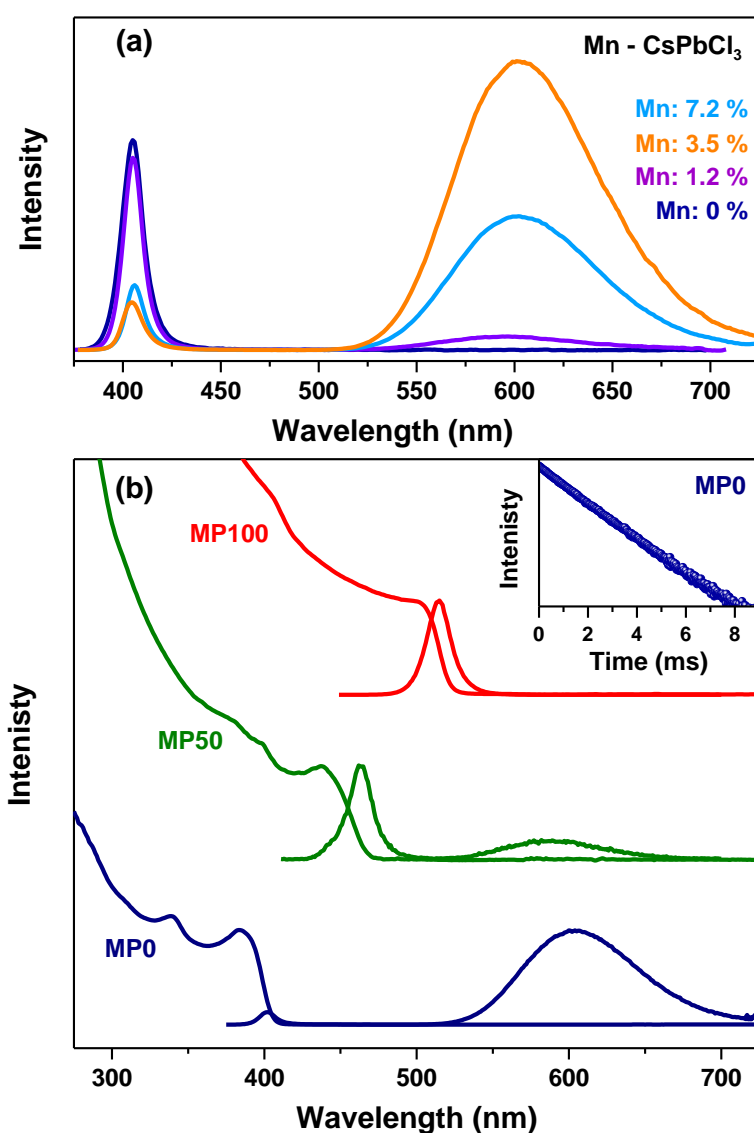


Figure 6.9 (a) PL emission spectra for Mn doped CsPbCl₃ with various Mn: Pb precursor ratio. (b) Optical absorption and steady state PL emission spectra for the Mn doped CsPb(Cl/Br)₃ (MP0 -MP100) QDs. Inset shows long lived emission lifetime of dopant emission for MP0 (Mn doped CsPbCl₃) QDs

6. Doping in Perovskite QDs: Synthesis and Stability

In order to understand these controversial structural and optical properties, we further investigate the local environment around Mn in MP100 by measuring Mn k-edge XAFS. Figure 6.10 shows the XAFS region of k-edge spectra of Mn in R-space. The structural information around Mn is obtained by performing a multi-shell fitting to the XAFS data. The XAFS fit over a k-range of 1-11 \AA^{-1} suggests that the Mn^{2+} in the QDs reside in two sites in Pb-halide lattice. One site is the interior Pb site replacing the Pb^{2+} and the other being possibly a surface state of octahedral geometry. The Mn k-edge XAFS fit suggests that significant number of Mn^{2+} ions in the QDs occupy Pb^{2+} in the lattice. However, Mn^{2+} lack full first shell coordination of Br, which is an indication of the presence of Mn^{2+} at the surface as well. An Mn-O path was later added to better fit the data. Our XAFS fitting concludes that Mn is coordinated to six bromides, with an average the Mn-Br bond length of 2.38 \AA which is substantially smaller than 2.67 \AA observed for Mn-Br in MnBr_2 . This suggests that the Mn is well dispersed within the lattice and the Mn-Br bond length is reduced to accommodate Mn within the perovskite structure. Nevertheless, although this is significantly shorter than the Pb-Br bond length, we observe that it fits the data well within the perovskite crystal structure.

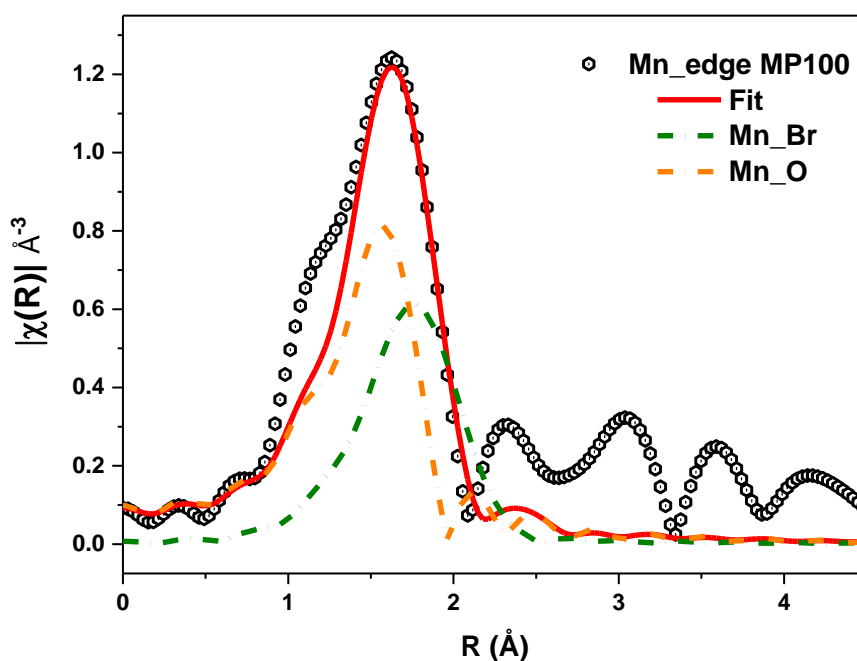


Figure 6.10 Fourier transform of Mn K-edge EXAFS spectra (circles) and their fits (red solid line) for Mn doped CsPbCl_3 . Orange and green dotted lines are different fitting paths.

6. Doping in Perovskite QDs: Synthesis and Stability

Taken together, even in the absence of significant Mn emission from optical studies, XAFS fit shows that a large percentage of Mn^{2+} indeed replaces Pb^{2+} but creates a locally distorted environment around Mn with a shorter Mn-Br bond length even in MP100, although optical signatures are not observed.

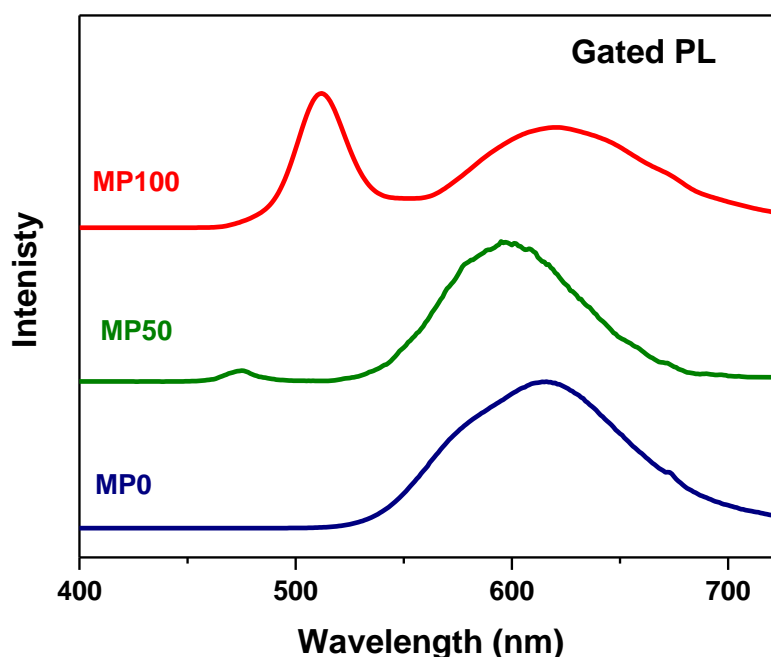


Figure 6.11 Room temperature gated PL emission spectra for MP0-MP100.

To further confirm this from optical studies we perform gated emission spectra wherein the emission persistent after a certain delay time is observed. This would be useful to understand the nature of Mn emission as the Mn emission is well-known to have long lifetimes (\sim few μs) unlike band edge emission (few tens of ns). This could lead to an understanding of the discrepancy between the local structure understanding and the optical property study. Figure 6.11 shows room temperature gated PL emission spectra for Mn doped mixed halide perovskite QDs clearly showing Mn emission even in MP100. Interestingly, this also shows that although the band edge lifetime is significantly smaller, we observe a strong band edge peak for MP 100 suggesting that there is a high possibility of transfer back to the band edge emission. These transfer probabilities have been extensively studied in literature.³¹ However, these studies clearly demonstrate that although Mn is efficiently doped in CsPbBr_3 as observed from structural characterization, signature Mn emission peak is not observed due to the new back transfer probability. This suggests that due to a significantly different Mn emission

6. Doping in Perovskite QDs: Synthesis and Stability

mechanism compared to the II-VI semiconductor QDs and the common notions followed to identify the dopant strategies using optical signatures are no longer valid.^{47, 48} Hence, even though Mn emission is absent in MP100, various other structural characterisation tools could identify the presence and exact location of dopants in MP100. As the PL lifetime for both the excitonic emission and Mn emission are of different order, performing gated PL with a delay time can also shed light on Mn emission features in MP100.

6.5. Conclusions

In summary, direct synthesis of Sn doped CsPb(Br/I)₃ and Mn doped CsPbCl₃ by hot injection method is demonstrated and fast degradation of cubic phase to orthorhombic phase is systematically studied by directly correlating the structural information with PL emission characteristics. Presence of unreacted precursors and removal of surface ligands are found to be accelerators of structural transformation and modified purification of as synthesized QDs were employed to obtain colloidal stability. Long term stability of these QDs over a period of 3 months were studied and it is found that continuous exposure to ambient air, moisture and light can lead to partial degradation and it is preferred to store the films of QDs in inert atmosphere. Colloidal stability study of these QDs under different conditions reveal their stability under ambient conditions which is apt for various device applications such as LEDs, photo detectors and lasers. By incorporating dopants like Sn, Mn into the lattice of Pb based perovskite QDs, these new class of materials may prove beneficial for a number of applications.

Bibliography

1. Lee, M. M.; Teuscher, J.; Miyasaka, T.; Murakami, T. N.; Snaith, H. J. *Science* **2012**, 338, (6107), 643-647.
2. Jeon, N. J.; Noh, J. H.; Yang, W. S.; Kim, Y. C.; Ryu, S.; Seo, J.; Seok, S. I. *Nature* **2015**, 517, (7535), 476-480.
3. Tan, Z.-K.; Moghaddam, R. S.; Lai, M. L.; Docampo, P.; Higler, R.; Deschler, F.; Price, M.; Sadhanala, A.; Pazos, L. M.; Credgington, D. *Nat. Nanotechnol.* **2014**, 9, (9), 687-692.
4. Yakunin, S.; Protesescu, L.; Krieg, F.; Bodnarchuk, M. I.; Nedelcu, G.; Humer, M.; De Luca, G.; Fiebig, M.; Heiss, W.; Kovalenko, M. V. *Nat. Commun.* **2015**, 6.
5. Rossi, D.; Parobek, D.; Dong, Y.; Son, D. H. *J. Phys. Chem. C* **2017**, 121, (32), 17143-17149.
6. Parobek, D.; Roman, B. J.; Dong, Y.; Jin, H.; Lee, E.; Sheldon, M.; Son, D. H. *Nano Lett.* **2016**, 16, (12), 7376-7380.
7. Pradhan, N. *J. Phys. Chem. Lett.* **2019**, 10, (10), 2574-2577.
8. Zhou, Y.; Chen, J.; Bakr, O. M.; Sun, H.-T. *Chem. Mater.* **2018**, 30, (19), 6589-6613.
9. Liu, W.; Lin, Q.; Li, H.; Wu, K.; Robel, I.; Pietryga, J. M.; Klimov, V. I. *J. Am. Chem. Soc.* **2016**, 138, (45), 14954-14961.
10. Van der Stam, W.; Geuchies, J. J.; Altantzis, T.; Van Den Bos, K. H.; Meeldijk, J. D.; Van Aert, S.; Bals, S.; Vanmaekelbergh, D.; de Mello Donega, C. *J. Am. Chem. Soc.* **2017**, 139, (11), 4087-4097.
11. Liu, W.; Lin, Q.; Li, H.; Wu, K.; Robel, I.; Pietryga, J. M.; Klimov, V. I. *J. Am. Chem. Soc.* **2016**, 138, (45), 14954-14961.
12. Pradeep, K.; Acharya, D.; Jain, P.; Gahlot, K.; Yadav, A.; Camellini, A.; Zavelani-Rossi, M.; Cerullo, G.; Narayana, C.; Narasimhan, S. V., Ranjani. *ACS Energy Lett.* **2019**, 5, (2), 353-359.
13. Das Adhikari, S.; Guria, A. K.; Pradhan, N. *J. Phys. Chem. Lett.* **2019**, 10, (9), 2250-2257.
14. Zou, S.; Liu, Y.; Li, J.; Liu, C.; Feng, R.; Jiang, F.; Li, Y.; Song, J.; Zeng, H.; Hong, M. *J. Am. Chem. Soc.* **2017**, 139, (33), 11443-11450.
15. Chen, D.; Fang, G.; Chen, X.; Lei, L.; Zhong, J.; Mao, Q.; Zhou, S.; Li, J. *J. Mater. Chem. C* **2018**, 6, (33), 8990-8998.

6. Doping in Perovskite QDs: Synthesis and Stability

16. Paul, S.; Bladt, E.; Richter, A. F.; Döblinger, M.; Tong, Y.; Huang, H.; Dey, A.; Bals, S.; Debnath, T.; Polavarapu, L.; Feldmann, J. *Angew. Chem.* **2020**, 59, (17), 6794-6799.
17. Liu, M.; Zhong, G.; Yin, Y.; Miao, J.; Li, K.; Wang, C.; Xu, X.; Shen, C.; Meng, H. *Adv. Sci.* **2017**, 4, (11), 1700335.
18. Van der Stam, W.; Geuchies, J. J.; Altantzis, T.; Van Den Bos, K. H.; Meeldijk, J. D.; Van Aert, S.; Bals, S.; Vanmaekelbergh, D.; de Mello Donega, C. *J. Am. Chem. Soc.* **2017**, 139, (11), 4087-4097.
19. Guria, A. K.; Dutta, S. K.; Adhikari, S. D.; Pradhan, N. *ACS Energy Lett.* **2017**, 2, (5), 1014-1021.
20. Xu, K.; Meijerink, A. *Chem. Mater.* **2018**, 30, (15), 5346-5352.
21. Gahlot, K.; Pradeep, K. R.; Camellini, A.; Sirigu, G.; Cerullo, G.; Zavelani-Rossi, M.; Singh, A.; Waghmare, U. V.; Viswanatha, R. *ACS Energy Lett.* **2019**, 4, (3), 729-735.
22. Park, B. W.; Philippe, B.; Zhang, X.; Rensmo, H.; Boschloo, G.; Johansson, E. M. *Adv. Mater.* **2015**, 27, (43), 6806-6813.
23. Marshall, K. P.; Walton, R. I.; Hatton, R. A. *J. Mater. Chem. A* **2015**, 3, (21), 11631-11640.
24. Chen, Q.; De Marco, N.; Yang, Y. M.; Song, T.-B.; Chen, C.-C.; Zhao, H.; Hong, Z.; Zhou, H.; Yang, Y. *Nano Today* **2015**, 10, (3), 355-396.
25. Zuo, F.; Williams, S. T.; Liang, P. W.; Chueh, C. C.; Liao, C. Y.; Jen, A. K. Y. *Adv. Mater.* **2014**, 26, (37), 6454-6460.
26. Stoumpos, C. C.; Malliakas, C. D.; Kanatzidis, M. G. *Inorg. Chem.* **2013**, 52, (15), 9019-9038.
27. Jellicoe, T. C.; Richter, J. M.; Glass, H. F.; Tabachnyk, M.; Brady, R.; Dutton, S. n. E.; Rao, A.; Friend, R. H.; Credginton, D.; Greenham, N. C. *J. Am. Chem. Soc.* **2016**.
28. Kennedy, T.; Glaser, E.; Klein, P.; Bhargava, R. *Phys. Rev. B* **1995**, 52, (20), R14356.
29. Norman, T. J.; Magana, D.; Wilson, T.; Burns, C.; Zhang, J. Z.; Cao, D.; Bridges, F. *J. Phys. Chem. B* **2003**, 107, (26), 6309-6317.
30. Nedelcu, G.; Protesescu, L.; Yakunin, S.; Bodnarchuk, M. I.; Grotevent, M. J.; Kovalenko, M. V. *Nano lett.* **2015**, 15, (8), 5635.
31. Akkerman, Q. A.; D'Innocenzo, V.; Accornero, S.; Scarpellini, A.; Petrozza, A.; Prato, M.; Manna, L. *J. Am. Chem. Soc.* **2015**, 137, (32), 10276-10281.

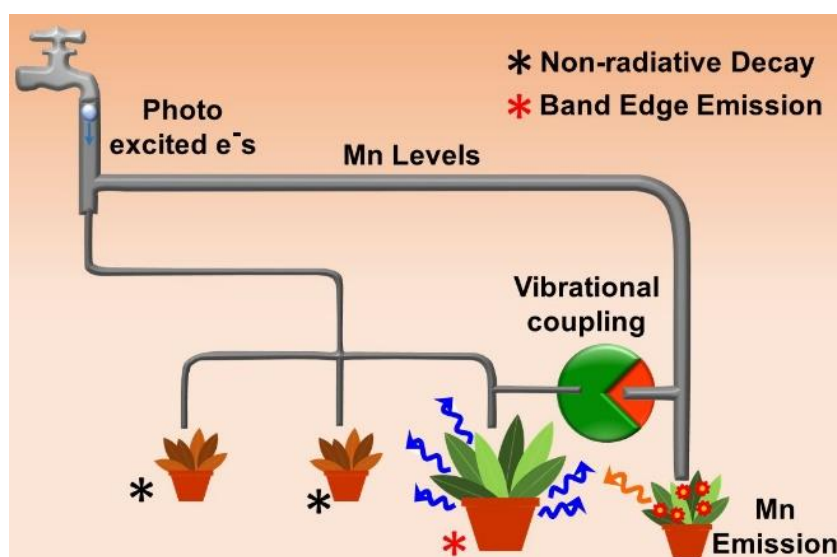
6. Doping in Perovskite QDs: Synthesis and Stability

32. Vitoreti, A. B. F.; Agouram, S.; Solis de la Fuente, M.; Muñoz-Sanjosed, V.; Schiavon, M. A. n.; Mora-Seró, I. n. *J. phys. Chem. C* **2018**, 122, (25), 14222-14231.
33. Protesescu, L.; Yakunin, S.; Bodnarchuk, M. I.; Krieg, F.; Caputo, R.; Hendon, C. H.; Yang, R. X.; Walsh, A.; Kovalenko, M. V. *Nano Lett.* **2015**, 15, (6), 3692-3696.
34. Protesescu, L.; Yakunin, S.; Bodnarchuk, M. I.; Krieg, F.; Caputo, R.; Hendon, C. H.; Yang, R.; Walsh, A.; Kovalenko, M. V. *Nano Lett.* **2015**, 15, (6), 3692-3696.
35. Swarnkar, A.; Marshall, A. R.; Sanehira, E. M.; Chernomordik, B. D.; Moore, D. T.; Christians, J. A.; Chakrabarti, T.; Luther, J. M. *Science* **2016**, 354, (6308), 92-95.
36. Vashishtha, P.; Halpert, J. E. *Chem. Mater.* **2017**, 29, (14), 5965-5973.
37. Zhang, H.; Fu, X.; Tang, Y.; Wang, H.; Zhang, C.; William, W. Y.; Wang, X.; Zhang, Y.; Xiao, M. *Nat. Commun.* **2019**, 10, (1), 1088.
38. Brennan, M. C.; Draguta, S.; Kamat, P. V.; Kuno, M. *ACS Energy Lett.* **2017**, 3, (1), 204-213.
39. Draguta, S.; Sharia, O.; Yoon, S. J.; Brennan, M. C.; Morozov, Y. V.; Manser, J. S.; Kamat, P. V.; Schneider, W. F.; Kuno, M. *Nat. Commun.* **2017**, 8, (1), 200.
40. Yoon, S. J.; Draguta, S.; Manser, J. S.; Sharia, O.; Schneider, W. F.; Kuno, M.; Kamat, P. V. *ACS Energy Lett.* **2016**, 1, (1), 290-296.
41. Raja, S. N.; Bekenstein, Y.; Koc, M. A.; Fischer, S.; Zhang, D.; Lin, L.; Ritchie, R. O.; Yang, P.; Alivisatos, P. *ACS Appl. Mater. Interfaces* **2016**.
42. Dirin, D. N.; Protesescu, L.; Trummer, D.; Kochetygov, I. V.; Yakunin, S.; Krumeich, F.; Stadie, N. P.; Kovalenko, M. V. *Nano Lett.* **2016**, 16, (9), 5866-5874.
43. Wang, H. C.; Lin, S. Y.; Tang, A. C.; Singh, B. P.; Tong, H. C.; Chen, C. Y.; Lee, Y. C.; Tsai, T. L.; Liu, R. S. *Angew. Chem.* **2016**, 55, (28), 7924-7929.
44. Meyns, M.; Perálvarez, M.; Heuer-Jungemann, A.; Hertog, W.; Ibáñez, M.; Nafria, R.; Genç, A.; Arbiol, J.; Kovalenko, M. V.; Carreras, J. *ACS Appl. Mater. Interfaces* **2016**, 8, (30), 19579-19586.
45. Norman, T. J.; Magana, D.; Wilson, T.; Burns, C.; Zhang, J. Z.; Cao, D.; Bridges, F. *J. Phys. Chem. B* **2003**, 107, (26), 6309-6317.
46. Hofmann, A.; Graf, C.; Boeglin, C.; Rühl, E. *ChemPhysChem* **2007**, 8, (13), 2008-2012.
47. Pradeep, K.; Acharya, D.; Jain, P.; Gahlot, K.; Yadav, A.; Camellini, A.; Zavelani-Rossi, M.; Cerullo, G.; Narayana, C.; Narasimhan, S.; Viswanatha, R. *ACS Energy Lett.* **2019**, 5, (2), 353-359.
48. Pradeep KR; Viswanatha, R. *APL Materials* **2020**, 8, (2), 020901.

6. Doping in Perovskite QDs: Synthesis and Stability

Chapter 7

Vibrationally Assisted Delayed Fluorescence (VADF) in Mn Doped Perovskite Quantum Dots



The following papers have been published based on work presented here:

Pradeep K R, D. Acharya, P. Jain, K. Gahlot, A. Yadav, A. Camellini, M. Zavelani-Rossi G. Cerullo, C. Narayana, S. Narasimhan, R. Viswanatha. "Harvesting Delayed Fluorescence in Perovskite Nanocrystals Using Spin-Forbidden Mn d States." *ACS Energy Letters* (2019) 5, 353-359.

7. Vibrationally Assisted Delayed Fluorescence

7. *Vibrationally Assisted Delayed Fluorescence*

7.1. Abstract

Opto-electronic devices based on all-inorganic perovskite systems are an energy efficient source of lighting due to their high photoluminescence quantum yield (QY). However, dominant surface trapping continues to plague the field, despite their high defect tolerance, as evidenced by the several fold improvements in the external quantum efficiency of perovskite quantum dots (QDs) upon appropriate surface passivation or physical confinement between high band gap materials. Here, we introduce the concept of drip feeding of photo-excited electrons from an impurity-induced spin-forbidden state to address this major shortcoming. An increased and delayed (about several milliseconds) excitonic QY, Raman spectroscopy demonstrating specific vibrational modes of the PbX_6 octahedra and density functional theory establish the electron back-transfer signifying an efficient recombination. We term this electron back-transfer from Mn^{2+} to the host conduction band in this prototypical example of Mn-doped CsPbX_3 ($X = \text{Cl}, \text{Br}$) QDs through vibrational coupling as Vibrationally Assisted Delayed Fluorescence (VADF).

7.2. Introduction

Smart electronic devices demand highly functional, cost and energy efficient solutions and major strides in this direction can be achieved by the reduction of energy loss pathways. Non-radiative recombination processes like Auger recombination¹ and surface defect trapping^{2, 3} contribute to the major source of energy loss in the field of lighting. Even the all-inorganic perovskite quantum dots (QDs), known for their energy-efficiency,⁴⁻⁷ show several fold improvement in external quantum efficiency^{8,9} upon surface processing, despite their high defect tolerance. This indicates that the energy decay pathways are still dominated by surface trapping.

One of the ways of avoiding trapping of photo-excited electrons on the surface is to capture the photo-excited charges internally through a quick pathway and drip-feed the same from within the QDs to radiative states of the host QDs. The realization of this concept involves quick extraction of the photo-excited electrons into long-lived impurity levels, slow back-transfer through finite vibrational coupling of the impurity levels with the host, followed by radiative recombination of the electrons. However, so far this concept has not been realized in any real extended solids though a similar path known as the thermally activated delayed fluorescence (TADF) has shown high degree of success in organic molecules. The use of spin in the pioneering work of Adachi *et al.*¹⁰ led the way to harvesting the spin selective losses in

7. *Vibrationally Assisted Delayed Fluorescence*

organic molecules. Despite extensive use of TADF in organic molecules since then, harvesting the non-radiative losses in solids has not been hitherto attempted in inorganic systems primarily due to the lack of one single prominent pathway that is faster than other non-radiative losses, unlike the spin selective (triplet) losses in organic molecules. In this chapter, we introduce the concept of VADF in inorganic materials to harvest delayed fluorescence. Towards this end, it is well known in the literature^{7, 11-14} that Mn doping in QDs leads to fast transfer of charge/energy from the excitonic excitation, typically within a few hundred femtoseconds,^{11, 15} and is retained for several μs to ms within the excited state of Mn. Based on the recent evidence of the observation of the excited state,¹¹ in this chapter we aim to deliberately play with excited state dynamics to detrapp these charges from the Mn and return them to the radiative excited state of the host within the fluorescence lifetime of Mn to achieve our aim of VADF. It should be noted that the thermally activated back and forth energy transfer from Mn levels lying above the conduction band minimum has been demonstrated long back.¹⁶ However, two major drawbacks of this technique are the absence of selection rules as well as the mandatory requirement of low temperature, providing minor reduction of loss pathways (if at all) at room temperature. Hence targeted hopping of electrons driven by internal selection rules, as well as the creation and exploitation of an internal electron storeroom, are not only of fundamental importance towards our understanding of Mn emission, but also offer a powerful strategy to increase the efficiency of opto-electronic devices by reducing the overpotential and non-radiative decay losses.

For the charge detrapping study with vibrational assistance we chose Mn-doped perovskite QDs as a prototype due to the anomalous properties observed in this class of materials.^{12-14, 17} For example, despite extensive efforts spanning over a hundred papers, Mn emission has not been observed in hosts with lower band gaps (E_g), such as $\text{CsPb}(\text{Cl}/\text{Br})_3$ and CsPbBr_3 QDs^{3, 7, 13, 14, 17-19} and the complete absence of excitonic emission has been elusive in all materials. This has been attributed to reasons like the disparity of M-Br ($M = \text{Pb}, \text{Mn}$) bond dissociation energies,⁷ clustering of Mn atoms,²⁰ surface defects,³ and lattice instabilities arising from size mismatch of the anion and cation.¹³ However, when the E_g of the QDs is higher, for example, in nanoplatelets of CsPbBr_3 ,¹⁷ irrespective of the composition, Mn emission has been observed. Secondly, the absence of Mn emission occurs in perovskites with E_g that is in resonance or near resonance with the Mn excitation energy (500 nm).¹¹ In this chapter, we study the Mn excitation and emission mechanism for Mn-doped perovskite QDs with specific emphasis on the coupling of Mn with the host, leading to back transfer of photo-

7. *Vibrationally Assisted Delayed Fluorescence*

excited electrons to the host and hence an improved QY giving rise to an intrinsically new class of materials

7.3. Experimental Methods

Chemicals used in the experiments include Cs_2CO_3 (99.99%), octadecene (ODE, 90%), oleic acid (OA, 90%), oleylamine (OLAm, 70%), PbBr_2 (99.999%), PbCl_2 (99.999%), MnBr_2 (99.9%), $\text{MnCl}_2 \cdot 4\text{H}_2\text{O}$ (99 %), n-hexane (>97.0%), trioctylphosphine (TOP), and are used directly after purchasing from Sigma Aldrich. All solvents and reagents were of analytical grade and directly used without further purification. Cesium oleate was synthesized using standard literature methods²¹ using Cs_2CO_3 and OA in presence of ODE at high temperature of 150 °C until all Cs_2CO_3 reacted with OA forming Cs-oleate.

7.3.1 Synthesis of Undoped and Mn-doped $\text{CsPb}(\text{Br/Cl})_3$ perovskite quantum dots (QDs)

Perovskite QDs were prepared according to the method described by Protesescu *et al.*²¹ Stoichiometric mixtures of PbCl_2 and PbBr_2 were used for the synthesis of undoped QDs, whereas stoichiometric mixtures of PbCl_2 and PbBr_2 with MnCl_2 or MnBr_2 were taken for the synthesis of Mn-doped $\text{CsPb}(\text{Br/Cl})_3$ perovskite QDs. ODE (5mL) and the required Pb/Mn salts were loaded into a 3-neck flask and dried under vacuum for 1 hour at 120°C. Dried OLAm (1.5 mL), dried OA (1.5 mL) and TOP (1 mL) were injected at 120°C under Argon flow. After complete solubilisation of Pb/Mn salt, the temperature was raised up to 180°C and Cs-oleate solution (0.4mL preheated to 100°C) was quickly injected and 5seconds later the reaction mixture was cooled down by ice water bath. For the MP40-LT sample Cs-oleate is injected at lower temperature (125 °C). The QDs were purified by centrifuging the crude solution for 10 minutes at 5000 rpm. The precipitated QDs were redispersed in hexane and centrifuged for 5min at 10000 rpm. Following this the precipitate, containing unreacted precursors, larger QDs and agglomerates, was discarded. The supernatant containing the QDs was then stored under refrigeration.

7.3.2 Photoluminescence quantum yield (PLQY)

The QY was obtained on drop-casted thin films using an integrating sphere. It should be noted here that the QY as obtained from the measurement ranged from 70-100% like earlier literature. However, these uncorrected QYs showed an increase when doped with Mn leading to > 100%. However, while they may be useful to perform a comparative study, they would not be relevant for any other issue as they are not absolute numbers. Hence, we have used only corrected QY to rid the spectra from instrumental artifacts in the entire paper.

7. *Vibrationally Assisted Delayed Fluorescence*

7.3.3 Computational Details

Our calculations have been performed using *ab initio* density functional theory (DFT)^{22, 23}, as implemented in the Quantum ESPRESSO package.²⁴ To describe the exchange-correlation interactions a generalized gradient approximation of the PBE form was used.²⁵ Electronic wavefunctions were expanded using a plane wave basis set, with cutoffs of 40 Ry and 400 Ry for the wavefunctions and charge density, respectively. The interactions between the ionic cores and valence electrons were described using ultrasoft pseudopotentials.²⁶ Structural optimizations were performed using the Broyden-Fletcher-Goldfarb-Shanno (BFGS) scheme until the Hellmann-Feynman forces on all the atoms being relaxed were less than 0.001 Ry/bohr. Marzari-Vanderbilt cold smearing²⁷ with a width of 0.001 Ry was used for better convergence. It has been shown that for perovskite QDs larger than 7 nm, the state filling happens similar to bulk.²⁸ Further DFT calculations for QDs in real space are known to be very compute intensive and are not fully reliable. Since the size of our QDs were about 12-16 nm, all DFT calculations were done for a bulk crystal. The Brillouin zone was sampled with a Monkhorst-Pack mesh²⁹ of 8×8×8 k-points for the primitive unit cell of CsPbBr₃.

A large unit-cell where one of 8 Pb atoms was substituted by Mn, was constructed to reduce the Mn concentration down to 12.5%, but we note that this concentration is still substantially higher than < 5% Mn in the experimental samples, as determined from inductively coupled plasma optical emission spectroscopy. Theoretical calculations were performed for the cubic structure of bulk CsPbBr₃ and Mn doped CsPbBr₃ based on the experimental XRD and TEM data. The lattice constant of CsPbBr₃ was obtained to be 6.01 Å similar to earlier literature.³⁰ This discrepancy from an experimental value of 5.85 Å is presumably due to the use of the Generalized Gradient Approximation, which is known to underbind. The calculated band gap of CsPbBr₃ is 1.79 eV. We note that the underestimation of the band gap is a well-known shortcoming of standard DFT calculations. Phonon calculations were performed by DFPT.³¹

7.4. Results and Discussion

Undoped (P0-P100) and Mn-doped (MP0-MP100) CsPb (Cl/Br)₃ QDs with varying Cl to Br ratios were synthesized by direct hot injection method using a mixture of lead halide, manganese halide and cesium oleate precursors according to literature reports.²¹ After purification, QDs were characterized by TEM images of the Mn-doped QDs shown in Figure 7.1; these indicate the existence of a monodisperse highly crystalline and cubic morphology, similar to that of the undoped perovskite QDs. X-ray diffraction (XRD) (Figure 7.2) shows

7. Vibrationally Assisted Delayed Fluorescence

high crystallinity along with retaining the cubic structure. Elemental analysis using inductively coupled plasma optical emission spectroscopy (ICP-OES) shows less than 5% Mn within the QDs. The E_g s were obtained from the absorption spectra and are shown in Figure 7.3

Sample	Br (%)	E_g (eV)	Sample	Br (%)	E_g (eV)
P0	0	3.08	MP0	0	3.10
P20	20	2.95	MP20	20	3.00
P40	40	2.78	MP40	40	2.87
P60	60	2.65	MP60	60	2.67
P80	80	2.48	MP80	80	2.56
P100	100	2.41	MP000	100	2.42
			MP40 LT	40	3.15

TABLE 7.1 Sample compositions for both undoped and Mn-doped $\text{CsPb}(\text{Cl}/\text{Br})_3$ perovskite QDs

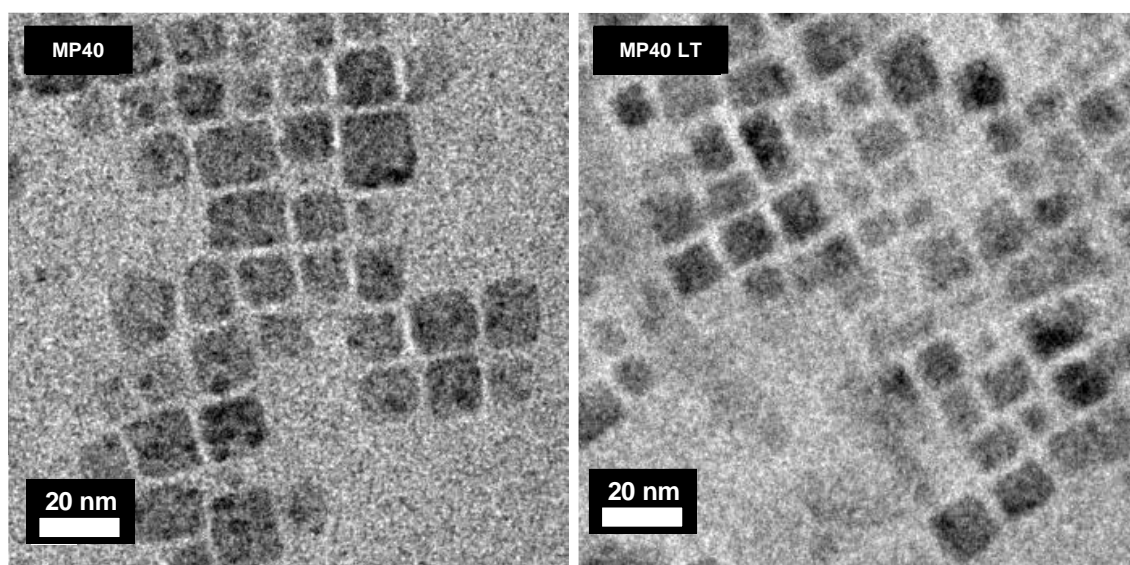


Figure 7.1 a) TEM images of MP40 perovskite QDs. b) TEM images of MP40 LT perovskite QDs with smaller size synthesized at 125°C (Scale bar - 20 nm).

7. Vibrationally Assisted Delayed Fluorescence

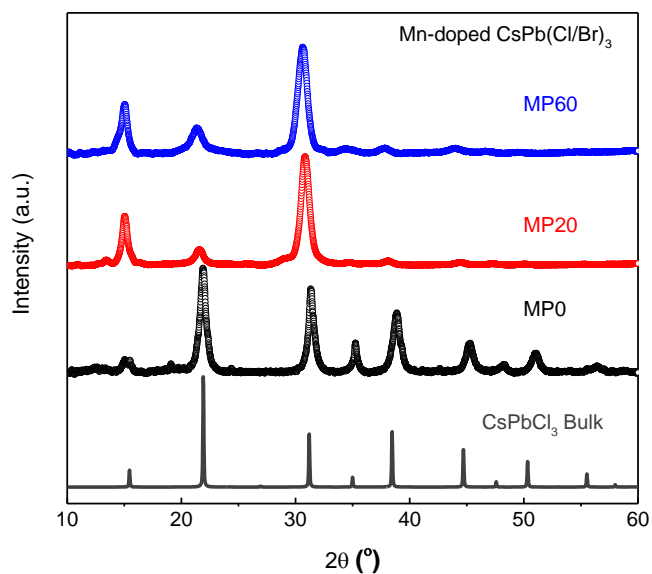


Figure 7.2 XRD patterns of Mn-doped $\text{CsPb}(\text{Cl}/\text{Br})_3$ perovskite QDs with reference data for cubic phase of bulk CsPbCl_3 .

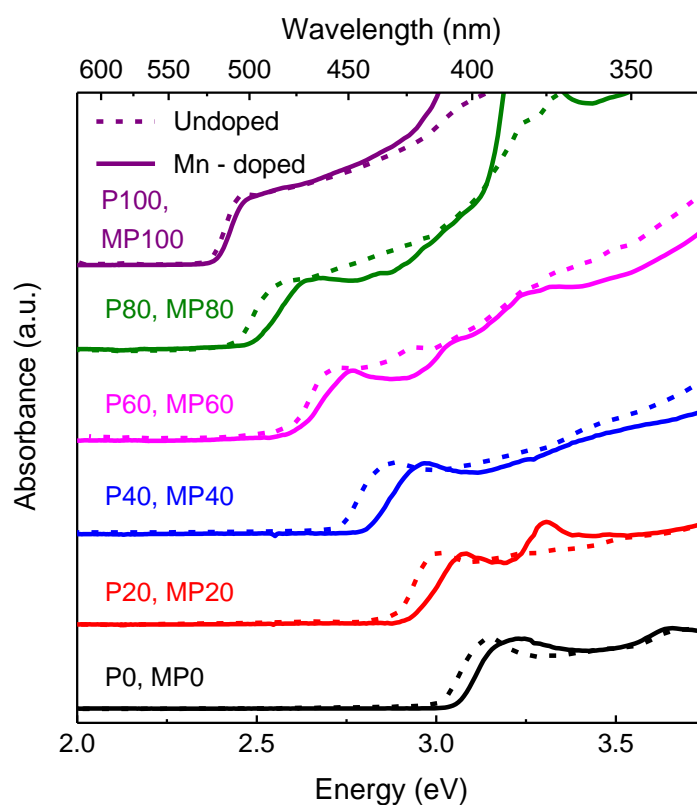


Figure 7.3 Absorption spectra for Undoped and Mn-doped $\text{CsPb}(\text{Cl}/\text{Br})_3$ perovskite QDs

7. *Vibrationally Assisted Delayed Fluorescence*

Figure 7.4 1 a) shows the steady-state photoluminescence (PL) spectra of undoped (P0-P100) and Mn-doped (MP0-MP100) QDs of $\text{CsPb}(\text{Cl}/\text{Br})_3$ at room temperature; the compositions are given in Table 7.1 and the corresponding absorption spectra are shown in Figure 7.3. The absorbance spectra of the doped and undoped samples are very similar suggesting no major electronic structure changes at the bottom of conduction band and top of valence band. The presence of higher energy peaks in the absorbance spectra of the doped QDs at higher energy could either be due to bidisperse size distribution or due to the higher order excitonic absorption. Hence the most likely origin of the additional higher energy peaks to be due to higher order excitations. Like earlier reports, Br-incorporation into the QDs shifts the exciton PL towards lower energy both in undoped and Mn-doped QDs. In addition, Mn-doped samples with larger E_g show broad emission at 590 nm (2.1 eV), arising from the spin forbidden 4T_1 to 6A_1 transition. We further characterized the samples with other methods with typical results being shown for P40 and MP40, wherein both excitonic and Mn emission peaks are observed. Femtosecond transient absorption measurements on P40 and MP40, reported in Figure 7.4 b), show similar photobleaching with a noticeable absence of the fast component ($\sim 200 - 400$ fs) that is characteristic of Mn doping,¹¹ in spite of a Mn emission peak at 590 nm (2.1 eV). This could be the signature of a very efficient fast transfer, taking place in less than 100 fs (resolution limit of the setup) followed by a back transfer on much longer timescales. Further, the lifetimes of the excitonic emission in Mn-doped and undoped samples shown in Figure 7.4 c) show that while the nanosecond components of P40 and MP40 are similar, MP40 also has a long-lived component for the excitonic emission, that is absent in the undoped counterpart. We observe that the lifetime of the Mn emission, shown in the inset of Figure 7.4 c), exactly matches that of the long-lived excitonic emission.

In order to understand the coupling of the Mn states with the host, we calculate the electronic band structure of 12.5% Mn-doped CsPbBr_3 using *ab initio* DFT as shown in Figure 7.5 a). The orbital character is extracted based on a projection onto atomic wavefunctions of Mn 3d (red), Pb 6p (green) and Br 4p (blue), and the intermediate colors indicate the degree of hybridization between these three states. It is interesting to note that the bottom of the conduction band is pulled considerably lower in energy due to spin-orbit coupling, resulting in the Mn levels being buried deep within the conduction band, unlike the situation in II-VI semiconductors. We also note that there are signatures of significant electronic coupling between Mn 3d and Pb 6p states, especially in the vicinity of the R point in the Brillouin zone. However, conservation of momentum (k) restricts the electron back transfer to the Γ point in the absence of vibrational assistance.

7. Vibrationally Assisted Delayed Fluorescence

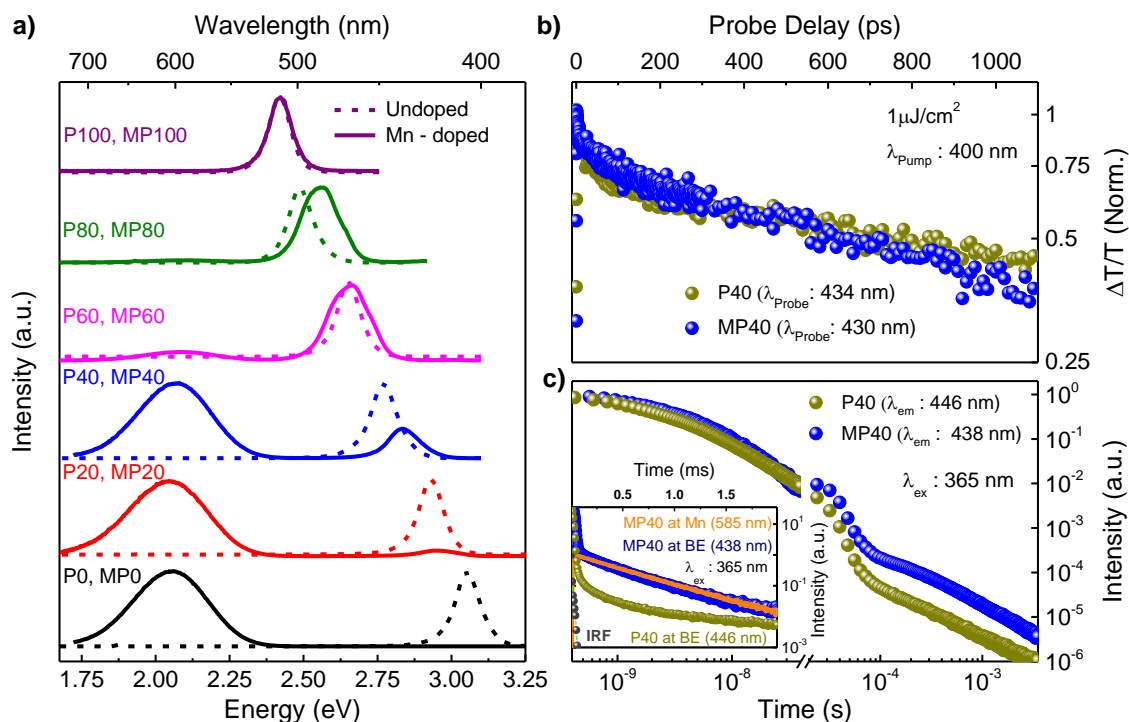


Figure 7.4 a) Steady-state PL emission for undoped and Mn-doped $\text{CsPb}(\text{Cl}/\text{Br})_3$ perovskite QDs b) Differential transmission ($\Delta T/T$) decay profiles for P40 and MP40 QDs at their respective band edge absorption energies. Pump photon energy is at 400nm c) Lifetime of excitonic emission for P40 and MP40; inset shows comparison of lifetime of long-lived band edge emission (blue circles) with Mn emission (orange circles) for MP40. Excitation energy is at 365 nm.

The vibrational coupling between the host and the Mn dopant atoms depends on the phonon band structure, which is calculated from density functional perturbation theory (DFPT) and is shown in Figure 7.5 b). The phonon branches are color coded according to the elemental contributions to the relevant mode, in a way analogous to the projections performed for the electronic band structure. Significant coupling of the Mn and Pb atoms (as observed from the intermediate colors) is observed in the frequency range of 90 to 135 cm^{-1} , corresponding to the modes b_1 to b_{11} (marked in Fig. 2b) at the Γ point. In contrast, similar phonon dispersion calculations on Mn doped CsPbCl_3 shown in Figure 7.5 c), (look at the analogous modes c_1 to c_{15} in the range of 100 to 150 cm^{-1}) demonstrate a very weak coupling of the Mn modes with the host, as shown by the predominantly blue color of the phonon modes at the Γ point.

7. Vibrationally Assisted Delayed Fluorescence

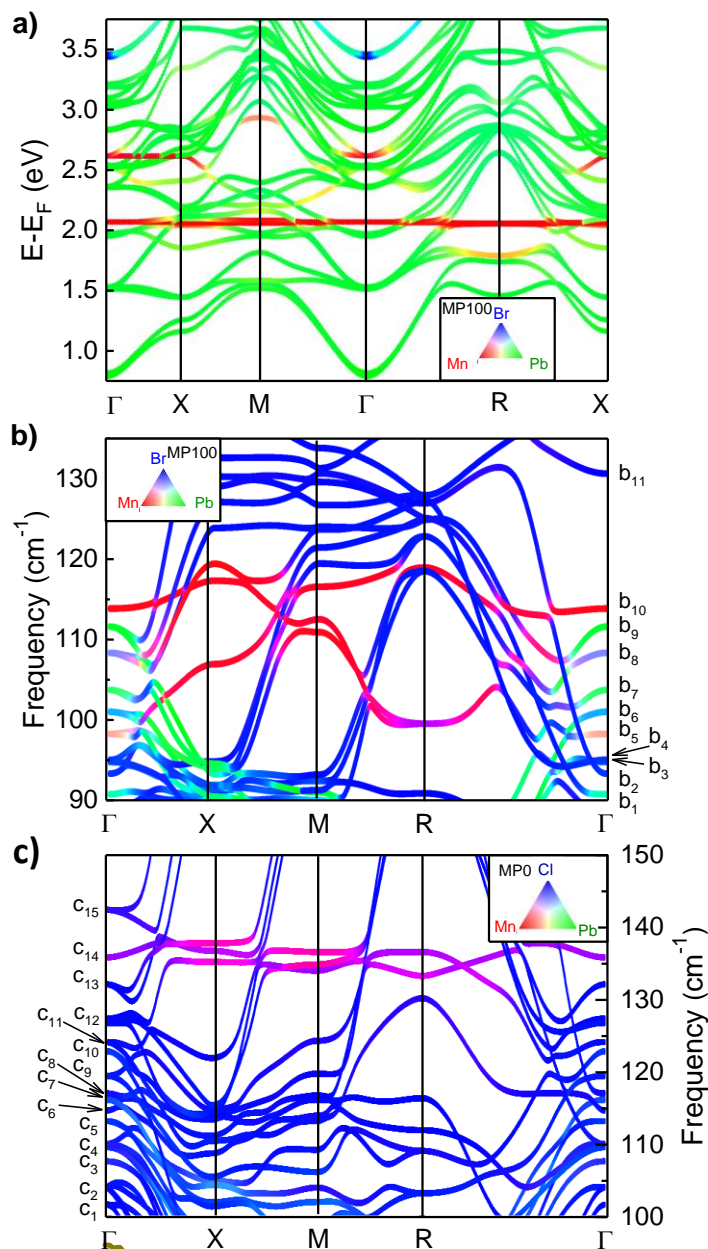


Figure 7.5 a) Electronic band structure of the conduction band, for Mn-doped CsPbBr₃. Red, green and blue colors indicate Mn 3d, Pb 6p and Br 4p like character, respectively, while intermediate colors indicate the degree of hybridization between these states. The Fermi level E_F is taken as the top of the valence band. b) Part of the phonon spectrum, as calculated from DFT, for 12.5% Mn-doped CsPbBr₃. The branches are colored according to their weights on the different atoms in the unit cell, as shown in the RGB color triangle. c) Part of the phonon spectrum, as calculated from DFT, for 12.5% Mn-doped CsPbCl₃. The branches are colored according to their weights on the different atoms in the unit cell, as shown in the RGB color triangle.

7. Vibrationally Assisted Delayed Fluorescence

While it is evident that the interatomic vibrational interactions of Mn doped CsPbBr₃ demonstrate the effect of Mn on the host phonon modes, it is important to see the coupling of these phonon modes with the electronic states. In order to investigate this, atoms were displaced along the eigenvectors of these modes, and the resulting effect on the electronic band structure was observed. As an example, in Figure 7.6 we show the perturbed electronic band structure after displacing the atoms according to the vibrational mode b_5 and standardizing with respect to the Cs 5s core level. Perceptible changes in the band structure upon perturbation confirm the existence of a strong electron-phonon coupling.

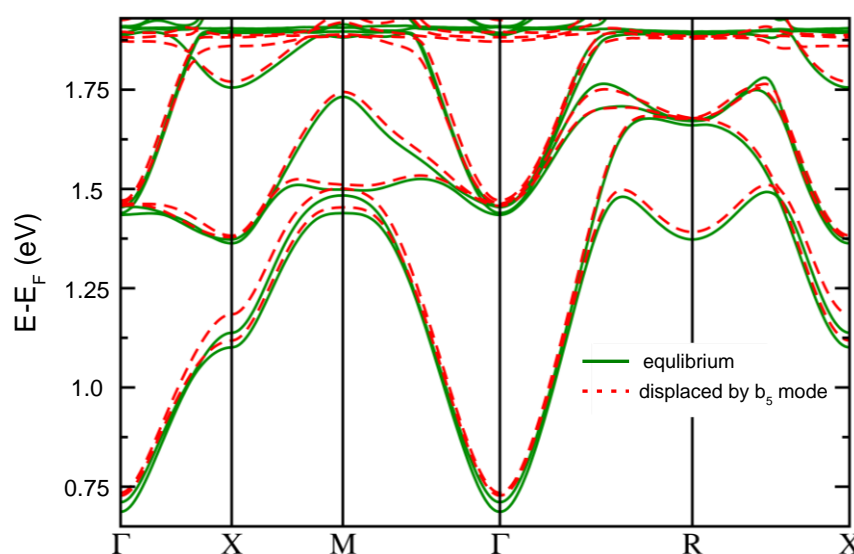


Figure 7.6 Strong electron - phonon coupling shown from shift in the electronic bands under atomic displacement of Mn atom (as obtained from the Eigen vector, b_5 in accordance to harmonic approximation) for Mn-doped CsPbBr₃.

These theoretical predictions are further verified by Raman spectroscopy, wherein similar modes were observed. Temperature dependent Raman studies on MP40 show a sharpening of the 132 cm⁻¹ [Pb-Br stretching mode (Transverse Optical phonon) in the octahedron^{32, 33} and 365 cm⁻¹ (second order combination mode of Transverse Optical phonon and Longitudinal Optical phonon³⁴) peaks on the Mn-doped samples compared to the undoped counterpart, as shown in Figure 7.7 a). This 132 cm⁻¹ peak is strongly coupled to the Mn²⁺ states as shown by the Raman spectra in this range in Figure 7.7 b). The width of the Raman peak is known to be inversely proportional to the phonon lifetime. A sharper peak as observed from Figure 7.7 b) as a function of temperature implies a longer phonon lifetime and hence a more efficient coupling between the Mn and the host. This non-monotonic change in the

7. Vibrationally Assisted Delayed Fluorescence

phonon lifetime as a function of temperature thus implies a non-monotonic coupling efficiency and accordingly, the back-transfer efficiency.³²

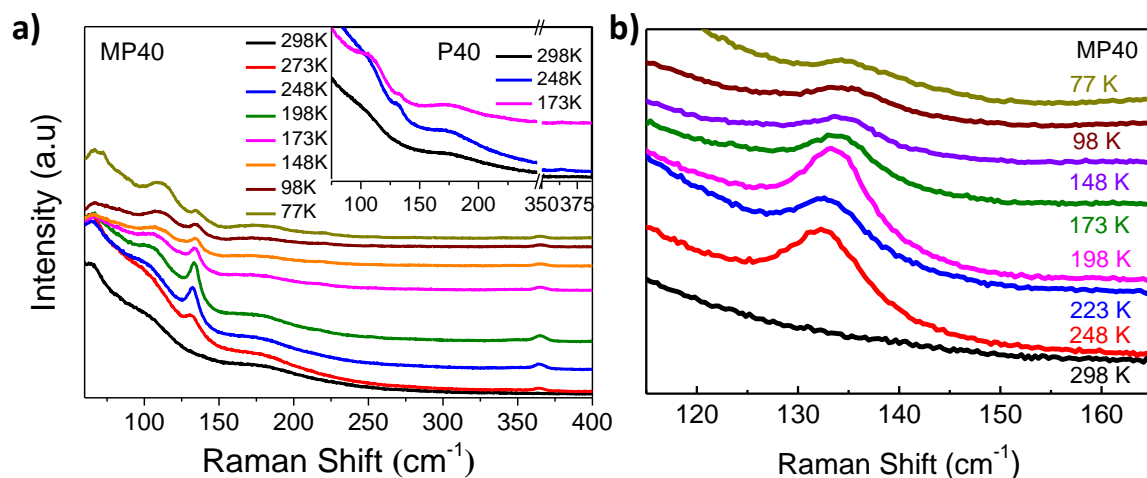


Figure 7.7 a) Temperature dependent Raman spectra for undoped (inset) and Mn doped perovskite QDs (P40 and MP40). b) Temperature dependent Raman spectra for MP40 perovskite QDs.

It should be noted here that the vibrational coupling is not very efficient in higher E_g hosts as compared to lower E_g materials, specifically at room temperature. However, statistically there is always a finite probability of back transfer even for the high E_g materials at room temperature. Once the electron reaches the excitonic states, due to its fast lifetime, it will decay through this pathway giving rise to finite excitonic emission as observed from a finite intensity of the excitonic emission in Figure 7.4 a). However, in a steady state emission process, one could also observe excitonic emission from the un-doped counterparts and hence the information regarding the back-transfer process may not be studied. Hence the most direct evidence of the delayed excitonic fluorescence is quantified by measuring the gated emission (schematic shown in Figure 7.8a), wherein excitonic luminescence obtained after a delay of 150 μ s is measured. Typical gated emission spectra at room temperature for various halide ion concentrations are shown in Figure 7.8 b). From the figure, it is apparent that irrespective of the E_g , all the samples show Mn emission in the gated fluorescence. Additionally, there is a substantial excitonic emission along with the Mn emission, specifically in low E_g materials like MP80. This delayed excitonic emission could either be due to delayed host excitation with energy provided by the non-radiative Mn decay or due to electron back-transfer from Mn leading to electron drip-feeding.

7. Vibrationally Assisted Delayed Fluorescence

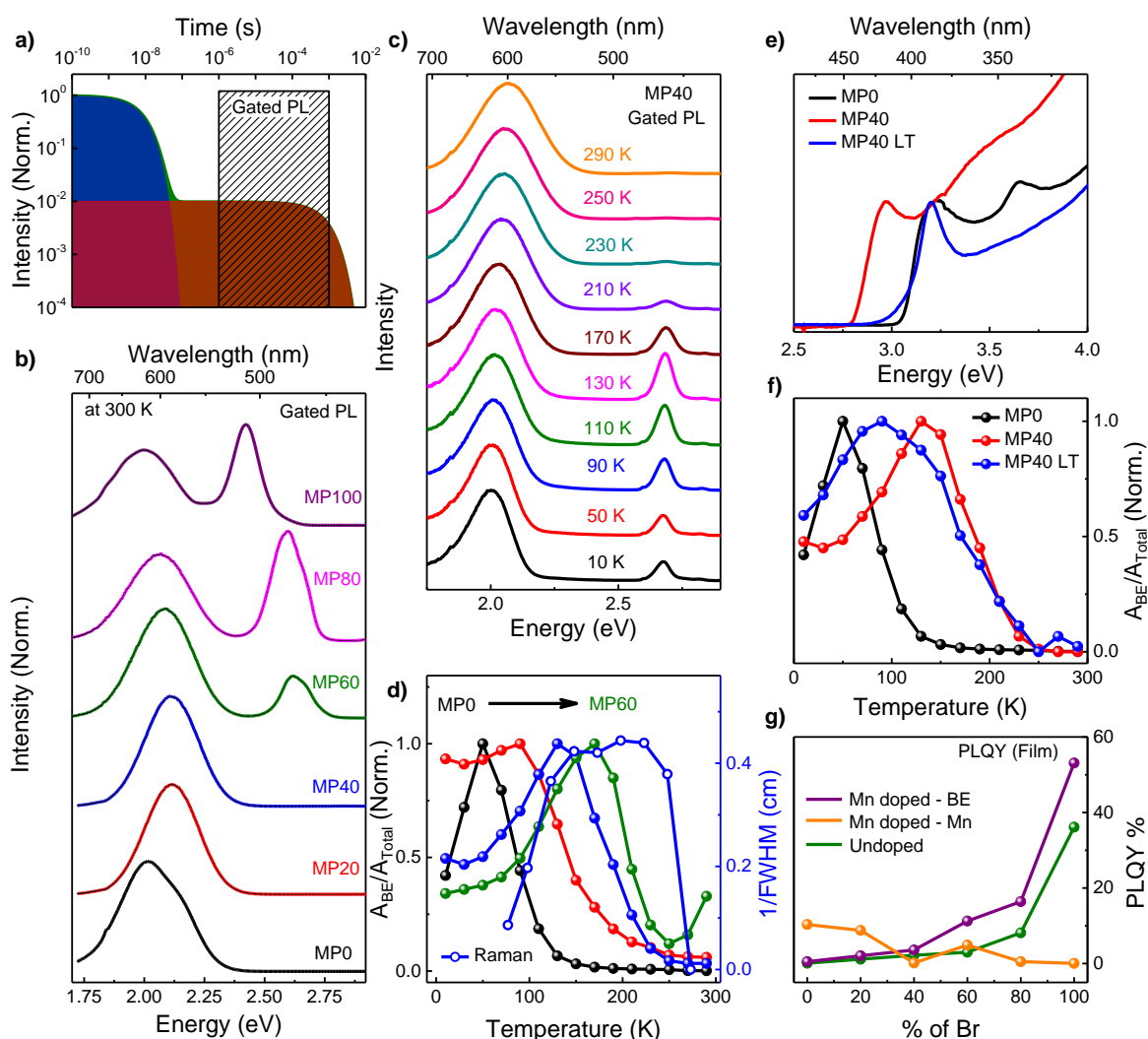


Figure 7.8 a) Schematic of gated emission (The blue region shows short lived nano-second emission, brown region shows long lived emission and green shaded region shows emission with both components of nano-second and milli-second emission. Shaded region shows gated PL measurement with a time delay of few micro-seconds.) b) Room temperature gated PL emission for Mn-doped $\text{CsPb}(\text{Cl}/\text{Br})_3$ perovskite QDs (MP0 to MP000) c) Temperature dependent Gated PL emission for MP40 QDs. d) Temperature dependent Gated PL area ratio of band edge emission (closed circles) vs total emission for Mn-doped $\text{CsPb}(\text{Cl}/\text{Br})_3$ perovskite QDs and inverse of FWHM of 132 cm^{-1} peak from Raman spectra of MP40 (open circles). e) Absorption spectra for smaller size of MP40 (MP40 LT) in comparison with MP40 and MP0 f) Intensity of delayed excitonic emission as a function of temperature for different sizes of MP40 along with MP0. g) Comparison of PLQY for the drop casted films of undoped and Mn-doped $\text{CsPb}(\text{Cl}/\text{Br})_3$ perovskite QDs.

7. *Vibrationally Assisted Delayed Fluorescence*

While both mechanisms are interesting from a fundamental perspective, the electron drip-feeding could lead to far-reaching consequences as it would couple selectively to the radiative pathways leading to decrease in energy loss pathways. The presence of Mn-coupled host phonon modes in the Raman spectra and the DFT calculations indeed suggests that there is significant phonon assistance to mediate charge transfer between the Mn and the host. Further, even though the Mn excitation is almost in resonance with the E_g of the sample P100, the Mn emission is much lower in energy and hence is unlikely to be capable of affecting delayed excitation. It is also evident that the back transfer is evident at room temperature for QDs with lower bandgap and hence we do not observe a Mn emission in the steady state PL as seen from Figure 7.4 a).

In order to provide convincing proof of the mechanism at play, we study the delayed excitonic fluorescence using gated emission as a function of temperature as well as quantum confinement. Typical spectra for Mn-doped sample (MP40) is shown in Figure 7.8 c), while the ratio of the area under the gated excitonic emission to the total area for varying halide ion concentrations as a function of temperature are shown in Figure 7.8 d). It should be noted here that in the absence of Mn, this is observed to be a flat line with no gated excitonic intensity. Though an increase in the area of the steady state excitonic feature as a function of temperature can be observed due to trapping and detrapping of charge carriers by defect states, this does not lead to an increase in the delayed excitonic feature. However, in the presence of Mn, due to back transfer from Mn states, the area under the gated excitonic emission peak increases with increasing temperature, possibly due to the low thermal energy, up to a certain maximum temperature determined by the E_g of the material. For temperatures above this maximum, we see a decrease in the intensity of the delayed excitonic emission, with the intensity finally becoming zero at sufficiently high temperatures. The detailed study of confinement effects are discussed in chapter 8. The observation of state specific back transfer and activation barriers, which is also supported by the Raman spectroscopy study in Figure 7.5, suggests the presence of real population kinetics, like an electron transfer. In order to compare this with the phonon lifetime as obtained from Raman spectra, we have also plotted the inverse of the full width at half maximum (FWHM) for a typical sample MP40, within the same plot. We observe that the phonon lifetime increases and reaches a maximum at the same temperature (123 K for MP40) as that of the optical signature. Further, with increasing temperature, this temperature-driven phonon assistance remains high until the gated excitonic emission reaches zero. This behavior of the lifetime suggests that phonon assistance and gated excitonic emission could respectively

7. *Vibrationally Assisted Delayed Fluorescence*

be in a cause-effect relation in a thermally activated phonon assisted electron transfer, further supporting the possible existence of an electron drip-feeding mechanism.

Additional confirmation of the mechanism is obtained by reducing the size of the QDs, wherein the E_g increases due to quantum confinement which also allows a relaxation of the phonon selection rules. Smaller MP40 LT QDs (12 nm as seen from TEM in Figure 7.1 a) show a higher E_g (3.15 eV) compared to the 16 nm MP40 ($E_g = 2.87$ eV) as shown in Figure 7.8 e). The absorption spectrum of MP0 ($E_g = 3.10$ eV) is also shown in the figure for comparison. The area ratios of the delayed excitonic emission as a function of temperature for MP40, MP40 LT and MP0 are compared in Figure 7.8 f). The similarity of the plots for MP40 and MP40 LT shows that the phonon assistance increases as expected in the smaller sized QDs, due to the relaxation of the phonon selection rules. This is unlike in the earlier case of II-VI semiconductors which, due to its thermally driven nature changed its nature as a function of quantum confinement.¹⁶ Figure 7.9 shows in the solution PLQY of the undoped QDs with lesser PLQY compared to the doped QDs providing a confirmatory proof for the back-transfer.

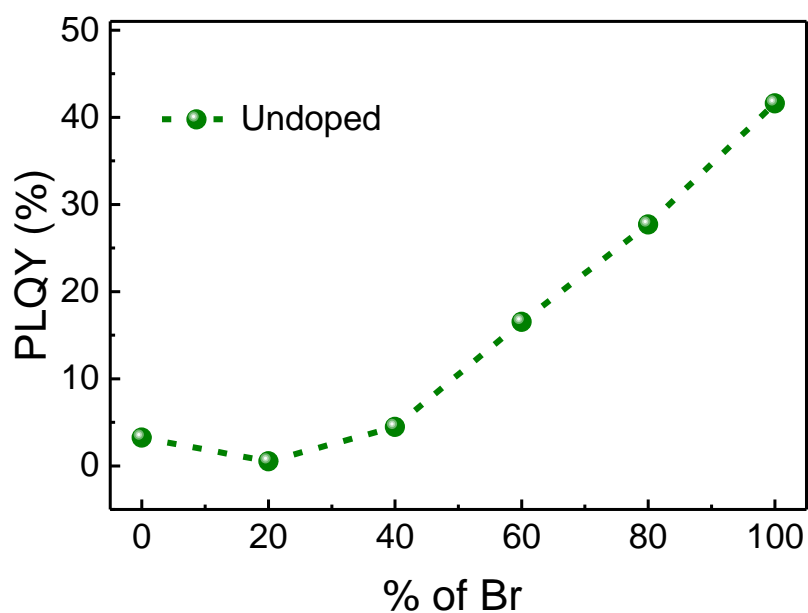


Figure 7.9 Solution PLQY for the undoped perovskite QDs.

7. Vibrationally Assisted Delayed Fluorescence

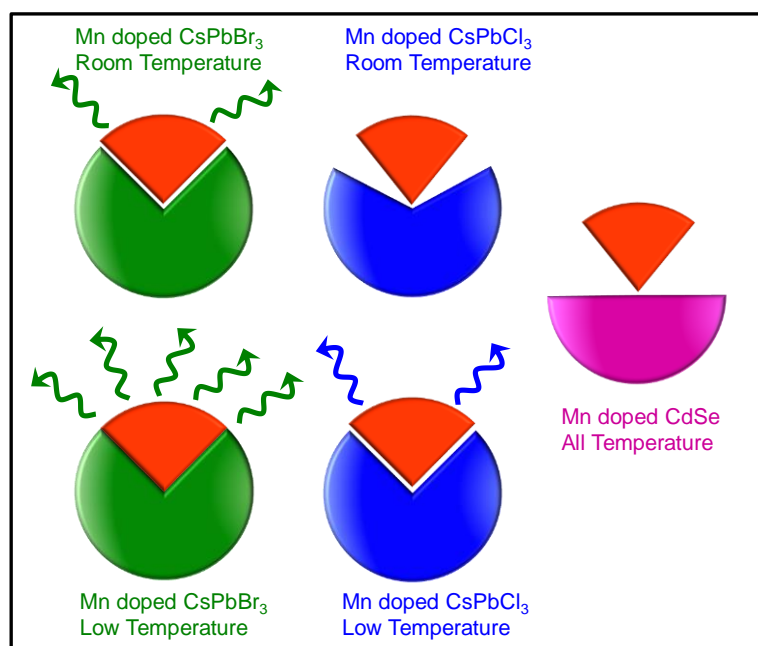


Figure 7.10 Visual analogy of phonon coupling for Mn-doped CsPbBr₃, CsPbCl₃ perovskite QDs and for Mn doped CdSe quantum dots.

In summary, Figure 7.10 symbolically depicts the two key players of this mechanism, vibrational coupling and the energy barrier for transfer to and from the Mn ion. The energy barrier is largely controlled by spin-orbit coupling, as the Mn energy levels are pushed deeper into the CB due to the spin-orbit coupling. However, the critical mechanism in these cases is the vibrational coupling. For CsPbBr₃, at room temperature, the coupling is efficient and hence we observe photons arising out of the back transfer. This coupling is further strengthened at low temperatures, leading to more efficient back transfer as shown in the visual analogy in Figure 7.10. In contrast, materials like mixed halides and chlorides show progressively weaker coupling, leading to back transfer only at lower temperature. This selective back transfer is favored when the lifetimes of the relevant phonon modes have increased, as observed from Raman spectroscopy and DFT calculations. However, in the case of most II-VI quantum dots (including quantum confined CdSe¹⁶ wherein thermally driven energy back transfer has been shown only in cases where the E_g is lower than the Mn transition energy), the coupling is not possible at any temperature and we do not observe back transfer from the Mn atom. Additionally, quantum confinement is not expected to change the coupling between the Mn and the host which is consistent with our experimental observations. This is fundamentally different than the case of CdSe¹⁶ which is driven by the thermal back transfer as well as quantum confinement and does not provide the additional advantage of selective drip-feeding to the radiative states.

7. *Vibrationally Assisted Delayed Fluorescence*

7.5. Conclusions

Finally, from a device perspective, Mn doping has been acknowledged to be superior due to the lack of self-absorption,³⁵ and improved colloidal stability³⁶⁻³⁹ as well as for air stable LED devices.⁴⁰ However, the major shortfall of Mn doping in devices is the presence of a single broad non-tunable emission at 590 nm (2.1 eV). By using Mn as a storehouse of excited electrons, all these advantages will be transferred to the excitonic features in addition to the tunability and the sharpness of the excitonic emission peak. This shutdown of the non-radiative channels increases the QY of the sharp tunable excitonic feature in the doped samples. In addition, the absence of self-absorption, due to electron drip-feeding, should retain high QY even on highly concentrated NC films. It should be noted that even though the solution QYs of the undoped QDs is about 30% for P80 (Figure 7.9), the same is reduced substantially in NC films (< 10%) due to self-absorption as shown in Figure 7.8 g) (green circles). However, the excitonic emission in Mn doped QDs is substantially greater (> 50% for MP80, MP100) due to absence of self-absorption. In conclusion, electron drip-feed leading to delayed excitonic emission adds an additional handle to increase and maintain a high QY with low losses. The immediate fallout of this is the reduction of overpotential losses and/or non-radiative loss leading to more efficient devices with Mn doping. Additionally, the formation of a magnetically coupled excitonic state also enables optical control of magnetism.

7. *Vibrationally Assisted Delayed Fluorescence*

Bibliography

1. Chernenko, A.; Dorozhkin, P.; Kulakovskii, V.; Brichkin, A.; Ivanov, S.; Toropov, A. *Phys. Rev. B* **2005**, 72, (4), 045302.
2. Krause, M. M.; Mooney, J.; Kambhampati, P. *ACS Nano* **2013**, 7, (7), 5922-5929.
3. Pinchetti, V.; Anand, A.; Akkerman, Q. A.; Sciacca, D.; Lorenzon, M.; Meinardi, F.; Fanciulli, M.; Manna, L.; Brovelli, S. *ACS Energy Lett.* **2018**, 4, (1), 85-93.
4. Zhou, Q.; Bai, Z.; Lu, W. g.; Wang, Y.; Zou, B.; Zhong, H. *Adv. Mater.* **2016**, 28, (41), 9163-9168.
5. Nedelcu, G.; Protesescu, L.; Yakunin, S.; Bodnarchuk, M. I.; Grotevent, M. J.; Kovalenko, M. V. *Nano Lett.* **2015**, 15, (8), 5635.
6. Song, J.; Li, J.; Li, X.; Xu, L.; Dong, Y.; Zeng, H. *Adv. Mater.* **2015**, 27, (44), 7162-7167.
7. Liu, W.; Lin, Q.; Li, H.; Wu, K.; Robel, I.; Pietryga, J. M.; Klimov, V. I. *J. Am. Chem. Soc.* **2016**, 138, (45), 14954-14961.
8. Meinardi, F.; Akkerman, Q. A.; Bruni, F.; Park, S.; Mauri, M.; Dang, Z.; Manna, L.; Brovelli, S. *ACS Energy Lett.* **2017**, 2, (10), 2368-2377.
9. Tan, Z.-K.; Moghaddam, R. S.; Lai, M. L.; Docampo, P.; Higler, R.; Deschler, F.; Price, M.; Sadhanala, A.; Pazos, L. M.; Credginton, D. *Nat. Nanotechnol.* **2014**, 9, (9), 687.
10. Uoyama, H.; Goushi, K.; Shizu, K.; Nomura, H.; Adachi, C. *Nature* **2012**, 492, (7428), 234.
11. Gahlot, K.; R, P. K.; Camellini, A.; Sirigu, G.; Cerullo, G.; Zavelani-Rossi, M.; Singh, A.; Waghmare, U. V.; Viswanatha, R. *ACS Energy Lett.* **2019**, 4, (3), 729-735.
12. Parobek, D.; Roman, B. J.; Dong, Y.; Jin, H.; Lee, E.; Sheldon, M.; Son, D. H. *Nano Lett.* **2016**, 16, (12), 7376-7380.
13. Van der Stam, W.; Geuchies, J. J.; Altantzis, T.; Van Den Bos, K. H.; Meeldijk, J. D.; Van Aert, S.; Bals, S.; Vanmaekelbergh, D.; de Mello Donega, C. *J. Am. Chem. Soc.* **2017**, 139, (11), 4087-4097.
14. Guria, A. K.; Dutta, S. K.; Adhikari, S. D.; Pradhan, N. *ACS Energy Lett.* **2017**, 2, (5), 1014-1021.
15. Chen, H.-Y.; Chen, T.-Y.; Son, D. H. *J. Phys. Chem. C* **2010**, 114, (10), 4418-4423.
16. Beaulac, R.; Archer, P. I.; van Rijssel, J.; Meijerink, A.; Gamelin, D. R. *Nano Lett.* **2008**, 8, (9), 2949-2953.

7. *Vibrationally Assisted Delayed Fluorescence*

17. Parobek, D.; Dong, Y.; Qiao, T.; Son, D. H. *Chem. Mater.* **2018**, 30, (9), 2939-2944.
18. Huang, G.; Wang, C.; Xu, S.; Zong, S.; Lu, J.; Wang, Z.; Lu, C.; Cui, Y. *Adv. Mater.* **2017**, 29, (29), 1700095.
19. Xu, K.; Meijerink, A. *Chem. Mater.* **2018**, 30, (15), 5346-5352.
20. De Siena, M. C.; Sommer, D. E.; Creutz, S. E.; Dunham, S. T.; Gamelin, D. R. *Chem. Mater.* **2019**, 7711-7722.
21. Protesescu, L.; Yakunin, S.; Bodnarchuk, M. I.; Krieg, F.; Caputo, R.; Hendon, C. H.; Yang, R.; Walsh, A.; Kovalenko, M. V. *Nano Lett.* **2015**, 15, (6), 3692-3696.
22. Kohn, W.; Sham, L. J. *Phys. Rev. A* **1965**, 140, (4A), A1133.
23. Hohenberg, P.; Kohn, W. *Phys. Rev. B* **1964**, 136, (3B), B864-B871.
24. Giannozzi, P.; Baroni, S.; Bonini, N.; Calandra, M.; Car, R.; Cavazzoni, C.; Ceresoli, D.; Chiarotti, G. L.; Cococcioni, M.; Dabo, I. *J. Phys.: Condens. Matter* **2009**, 21, (39), 395502.
25. Perdew, J. P.; Burke, K.; Ernzerhof, M. *Phys. Rev. Lett.* **1996**, 77, (18), 3865.
26. Vanderbilt, D. *Phys. Rev. B* **1990**, 41, (11), 7892.
27. Marzari, N.; Vanderbilt, D.; De Vita, A.; Payne, M. *Phys. Rev. Lett.* **1999**, 82, (16), 3296.
28. Butkus, J.; Vashishtha, P.; Chen, K.; Gallaher, J. K.; Prasad, S. K.; Metin, D. Z.; Laufersky, G.; Gaston, N.; Halpert, J. E.; Hodgkiss, J. M. *J. Chem. Mater.* **2017**, 29, (8), 3644-3652.
29. Monkhorst, H. J.; Pack, J. D. *Phys. Rev. B* **1976**, 13, (12), 5188.
30. Grote, C.; Ehrlich, B.; Berger, R. F. *Phys. Rev. B* **2014**, 90, (20), 205202.
31. Baroni, S.; de Gironcoli, S.; Dal Corso, A.; Giannozzi, P. *Rev. Mod. Phys.* **2001**, 73, (2), 515-562.
32. Yin, J.; Zhang, Y.; Bruno, A.; Soci, C.; Bakr, O. M.; Brédas, J.-L.; Mohammed, O. F. *ACS Energy Lett.* **2017**, 2, (12), 2805-2811.
33. Liao, M.; Shan, B.; Li, M. *J. Phys. Chem. Lett.* **2019**, 10, 1217-1225.
34. Calistru, D. M.; Mihut, L.; Lefrant, S.; Baltog, I. *J. Appl. Phys.* **1997**, 82, (11), 5391-5395.
35. Pandey, A.; Sarma, D. D. *Z. Anorg. Allg. Chem.* **2016**, 642, (23), 1331-1339.
36. Wang, Q.; Zhang, X.; Jin, Z.; Zhang, J.; Gao, Z.; Li, Y.; Liu, S. F. *J. A. E. L. ACS Energy Lett.* **2017**, 2, (7), 1479-1486.
37. Zhu, J.; Yang, X.; Zhu, Y.; Wang, Y.; Cai, J.; Shen, J.; Sun, L.; Li, C. *J. Phys. Chem. Lett.* **2017**, 8, (17), 4167-4171.

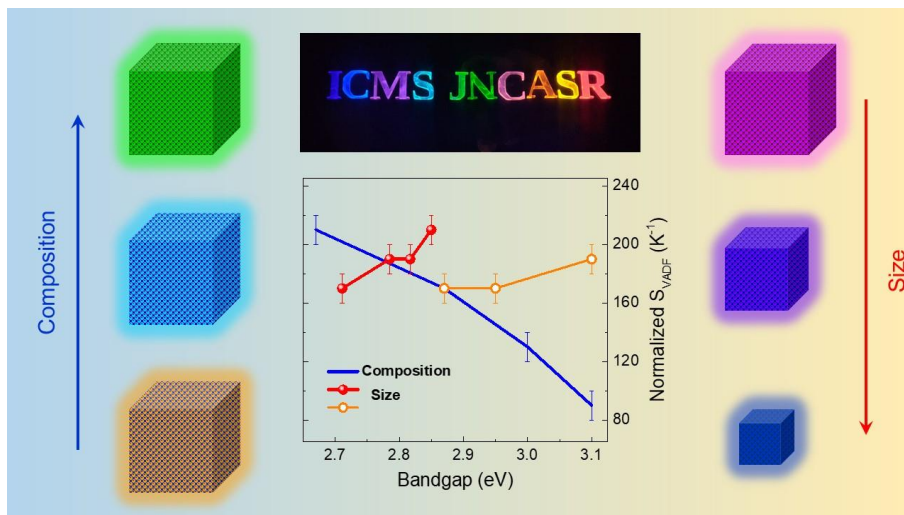
7. Vibrationally Assisted Delayed Fluorescence

38. Akkerman, Q. A.; Meggiolaro, D.; Dang, Z.; De Angelis, F.; Manna, L. J. A. e. l. *ACS Energy Lett.* **2017**, 2, (9), 2183-2186.
39. Zou, Y.; Yuan, Z.; Bai, S.; Gao, F.; Sun, B. J. M. T. N. *Materials Today Nano* **2019**, 100028.
40. Zou, S.; Liu, Y.; Li, J.; Liu, C.; Feng, R.; Jiang, F.; Li, Y.; Song, J.; Zeng, H.; Hong, M. J. *Am. Chem. Soc.* **2017**, 139, (33), 11443-11450.

7. Vibrationally Assisted Delayed Fluorescence

Chapter 8

Composition Modulation vs Quantum Confinement: Effect on VADF in Mn Doped Perovskite Quantum Dots



8. Composition Modulation vs Quantum Confinement

8. Composition Modulation vs Quantum Confinement

8.1. Abstract

The bandgap of perovskite quantum dots (QDs) can be tuned by halide composition modulation or by varying the size. In this chapter, we have studied the effect of composition modulation and quantum confinement in Mn doped mixed halide perovskite QDs on delayed excitonic emission. The delayed excitonic emission arises due to strong vibrational coupling between Pb and Mn levels leading to back-transfer of photo-excited carriers known as vibrationally assisted delayed fluorescence (VADF). The delayed excitonic emission intensities are strongly dependent on host bandgap. The host bandgap is tuned by composition modulation and by size modulation using halide ion ratio and temperature modulation respectively. The delayed band edge vs Mn emission efficiencies in the gated photoluminescence (PL) which is defined by entropy of VADF is studied by looking at the rate of change of VADF with respect to temperature. Gated photoluminescence excitation PLE studies also proved that the back transfer of photoexcited electrons are assisted by state specific higher excited levels, that cannot be changed by size variation as per quantum confinement effects.

8.2. Introduction

Inorganic lead halide perovskite QDs are in high favour among recent energy materials due to their efficient light emitting and photovoltaic applications.¹⁻¹¹ Capabilities of promising perovskite QDs are enhanced via chemical and structural modification. Recent works have shown bandgap tuning by anion exchange¹²⁻¹⁴ resulting in high photoluminescence quantum yield (PLQY). Multi-colour emission was also strategically obtained by doping the inorganic perovskite QDs expanding their functionality.¹⁵⁻²⁰ Mn doping in perovskite QDs is explored as the most common strategy to modify the spectroscopic properties recently.²¹ The uniqueness of this dopant is the spin forbidden long lived Mn d-d emission around 585 nm. Doping with Mn in inorganic perovskite QDs have also shown improved PLQY,^{22, 23} structural stability,^{24, 25} and improved size distribution²⁶ as an added advantage. However, Mn emission has not been observed in hosts with high Br content such as CsPb(Cl/Br)₃ and CsPbBr₃^{15, 16, 21, 27} due to lattice instabilities arising from size mismatch between anion and cation,¹⁵ disparity of bond dissociation energies of the metal and halide,¹⁶ and back energy transfer from Mn²⁺ states to the host band states.^{22, 27} However, strong dopant emission is observed when the host bandgap is increased by introducing quantum confinement in to the QDs irrespective of the halide composition.^{22, 28} Such quantum confinement of charge carriers enhances the sp-d exchange

8. Composition Modulation vs Quantum Confinement

interactions between the host and dopant ion yielding high orange emission from Mn d electrons.²⁹ Apart from the changes observed in the intensities of Mn d-d emission in mixed halide perovskites, presence of high band edge emission with a lifetime as long as milli seconds were under scrutiny. It was found that due to the drip feeding of photoexcited electron arising due to VADF from the dopant back to hosts radiative levels lead to the increased PLQY and lifetime of the excitonic emission in the Mn doped mixed halide perovskite QDs.²² However, it is not clear if photophysical properties, specifically VADF is a function of bandgap and/or electronic band structure. Hence, the photo-physics of PL features in mixed halide Mn doped perovskite QDs is rather interesting when there is opportunity of tuning the host bandgap by halide ion composition modulation and by size variation by introducing quantum confinement in the QDs makes the inorganic mixed halide perovskite QDs perfect candidate to study the consequences on both delayed Mn emission and delayed band edge emission.

Introducing controlled quantum confinement and doping Mn in to the perovskite QDs have been significantly more challenging than achieving the goals individually. Here in this chapter we study the effect of band gap tuning arising from quantum confinement as well as composition variation on dopant related delayed emission in Mn doped perovskite mixed halide QDs. Mn doped mixed halide perovskite QDs were synthesized by modifying the hot injection procedure followed by Protesescu *et al.*³⁰ Briefly, stoichiometric mixture of Pb-halides and Mn-halides were used for the synthesis in 1-octadecene (ODE) solvent as well as, 1.5 ml of oleic acid (OA), 1.5 ml of oleylamine (OLA). The size tuning of the doped QDs were achieved by carefully controlling the Cs-OA injection temperature. Synthesis, purification and isolation of the QDs are described in the experimental section in detail.

Gamelin and co-workers reported striking observation in the dopant emission in Mn doped CsPbCl₃ perovskite QDs at low temperature.³¹ Anomalous quenching of Mn emission was observed at low temperature unlike observed in Mn doped II-VI semiconductor quantum dot counterparts. Similar quenching of Mn emission effect is also observed in Br-incorporated QDs at low temperature.³² The reduction in Mn emission intensity at low temperature specifically in perovskite as a host is due to faster radiative decay of excitonic emission at cryogenic temperature^{27, 31, 33} and also due to effective back transfer of photoexcited electron from Mn to host because of VADF.²² The competition of these recombination rates as a function of temperature, host band gap variation by composition modulation and quantum confinement can give raise to the efficiency of back transfer and vibrational coupling between host and dopant at varying conditions. Quantification of the delayed emission for the

8. Composition Modulation vs Quantum Confinement

composition modulated QDs and quantum confined QDs is required to gain in-depth understanding in the back-transfer processes by eliminating the thermal vibrations at cryogenic temperature. Hence, this chapter discusses about the efficiency of VADF as a function of temperature using the spectroscopic delayed emission tools such as gated PL and gated PL excitation.

8.3. Experimental Methods

Chemicals used in the experiments include Cs_2CO_3 (99.99%), octadecene (ODE, 90%), oleic acid (OA, 90%), oleylamine (OLAm, 70%), PbBr_2 (99.999%), PbCl_2 (99.999%), MnBr_2 (99.9%), $\text{MnCl}_2 \cdot 4\text{H}_2\text{O}$ (99 %), n-hexane (>97.0%), trioctylphosphine (TOP), and are used straight after purchasing from Sigma Aldrich. All solvents and reagents were of analytical grade and directly used without further purification.

Cesium oleate was prepared using standard literature methods³⁰ using Cs_2CO_3 and OA in presence of ODE at high temperature of 150°C until all Cs_2CO_3 reacted with OA forming a clear solution of Cs-oleate.

8.3.1. Synthesis of Mn-doped $\text{CsPb}(\text{Br}/\text{Cl})_3$ perovskite quantum dots (QDs): Perovskite QDs were prepared according to the method described by Protesescu *et al.*³⁰ Stoichiometric mixtures of PbCl_2 and PbBr_2 , with $\text{MnCl}_2 \cdot 4\text{H}_2\text{O}$ and MnBr_2 were taken for the synthesis of both size and composition modulation of Mn-doped $\text{CsPb}(\text{Br}/\text{Cl})_3$ perovskite QDs. ODE (5mL) and the required Pb/Mn salts were loaded into a 3-neck flask and dried under vacuum for 1 hour at 120°C . Dried OLAm (1.5 mL), dried OA (1.5 mL) and TOP (1 mL) were injected at 120°C under Argon flow. After the complete solubilization of the precursors added and obtaining a clear solution, the temperature was raised up to 180°C for composition modulation and Cs-oleate solution (0.4mL preheated to 100°C) was quickly injected and cooled down by ice water bath within a few seconds. The Cs-oleate injection temperature decides the final size of the QDs formed. Hence, for the size variation sample Cs-oleate is injected at lower temperature (120 - 180°C). The QDs were purified by centrifuging the crude solution for 10 minutes at 5000 rpm. The precipitated QDs were redispersed in hexane and centrifuged for 5 min at 10000 rpm. Following this the precipitate, containing unreacted precursors, larger QDs and agglomerates, was discarded. The sequential centrifugation and discarding the precipitate containing unreacted precursors and larger size QDs is repeated to obtain monodisperse and stable QDs. The supernatant comprising the QDs was then stored under refrigeration.

8.4. Results and Discussion

Figure 8.1 shows the X-ray diffraction (XRD) pattern for quantum confined MP50-7 to MP50-13. The XRD peaks gets broad as the size of QDs decreases as seen from the figure. And Figure 8.2 a) and b) shows the corresponding size from TEM images for quantum confined Mn doped $\text{CsPb}(\text{Cl}/\text{Br})_3$.

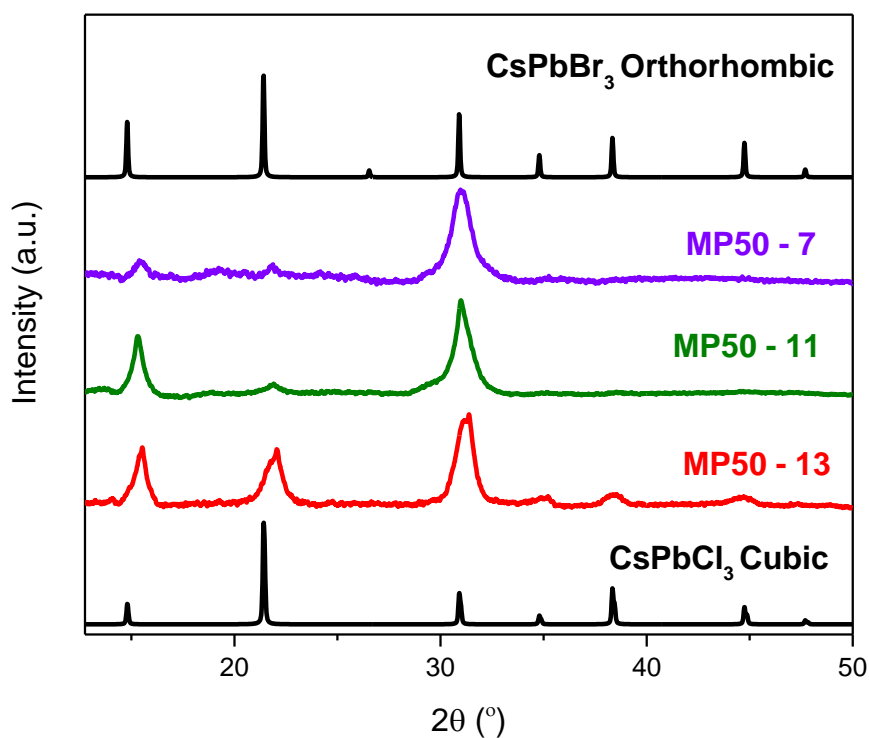


Figure 8.1 XRD patterns of Mn doped $\text{CsPb}(\text{Cl}/\text{Br})_3$ QDs.

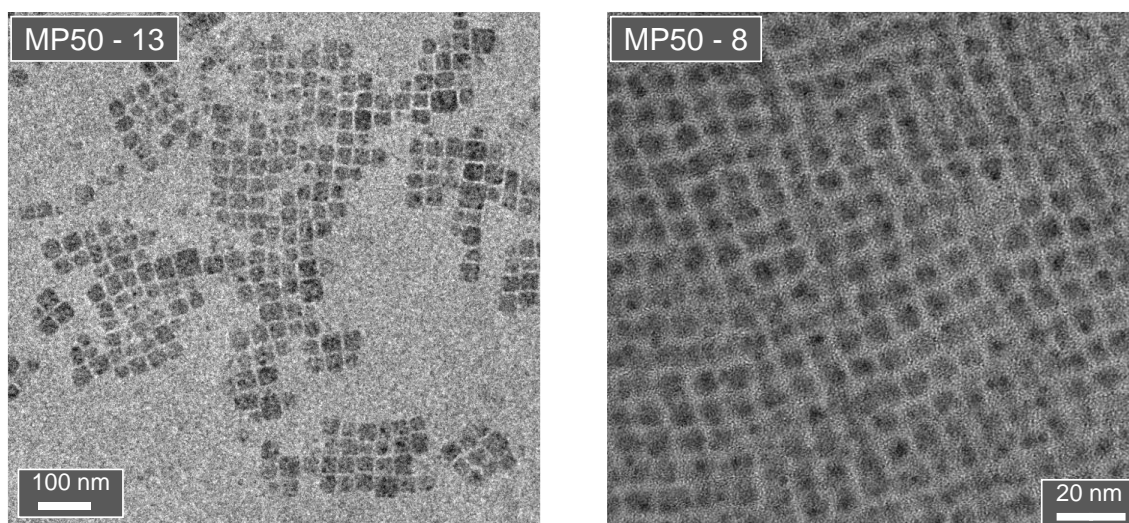


Figure 8.2 a) and b) TEM images for quantum confined QDs of Mn doped $\text{CsPb}(\text{Cl}/\text{Br})_3$.

8. Composition Modulation vs Quantum Confinement

Figure 8.3 a) shows the absorption and steady state PL spectra for Mn doped CsPb(Cl/Br)₃ mixed halide perovskite QDs (MP0-MP80) at room temperature. The consistent redshift in the absorbance is due to composition modulation obtained by Br incorporation in Mn doped mixed halide perovskite QDs. Like earlier reports, decrease in intensities of Mn d-d emission is also observed upon decreasing the host bandgap by Br incorporation. Upon composition modulation the film PLQY of excitonic emission increases and Mn emission decreases as shown in Table 8.1.

Sample	Composition (% of Br in Mn doped CsPb(Cl/Br) ₃)	Bandgap (eV)	PLQY BE (%)	PLQY Mn (%)	PLQY Total (%)
MP0	0	3.1	0.5	10.3	10.8
MP20	20	2.97	2	8.7	10.7
MP40	40	2.8	2.3	0.2	3.8
MP50	50	2.71	27.5	2.4	29.9
MP60	60	2.67	11.2	4.9	16.1
MP80	80	2.56	16.4	0.5	16.9

TABLE 8.1 Sample composition, bandgap and PL QY for composition modulated Mn doped CsPb(Cl/Br)₃ mixed halide perovskite QDs.

Sample	Size (nm)	Bandgap (eV)	PLQY BE (%)	PLQY Mn (%)	PLQY Total (%)
MP50-7	7	2.85	26.4	0.2	26.6
MP50-8	8	2.81	34.3	0.5	34.8
MP50-11	11	2.78	29.1	4.2	33.3
MP50-13	13	2.71	27.5	2.4	29.9

TABLE 8.2 Sample size, bandgap and PL QY for size variation of Mn doped CsPb(Cl/Br)₃ mixed halide perovskite QDs with 50 % Br content.

8. Composition Modulation vs Quantum Confinement

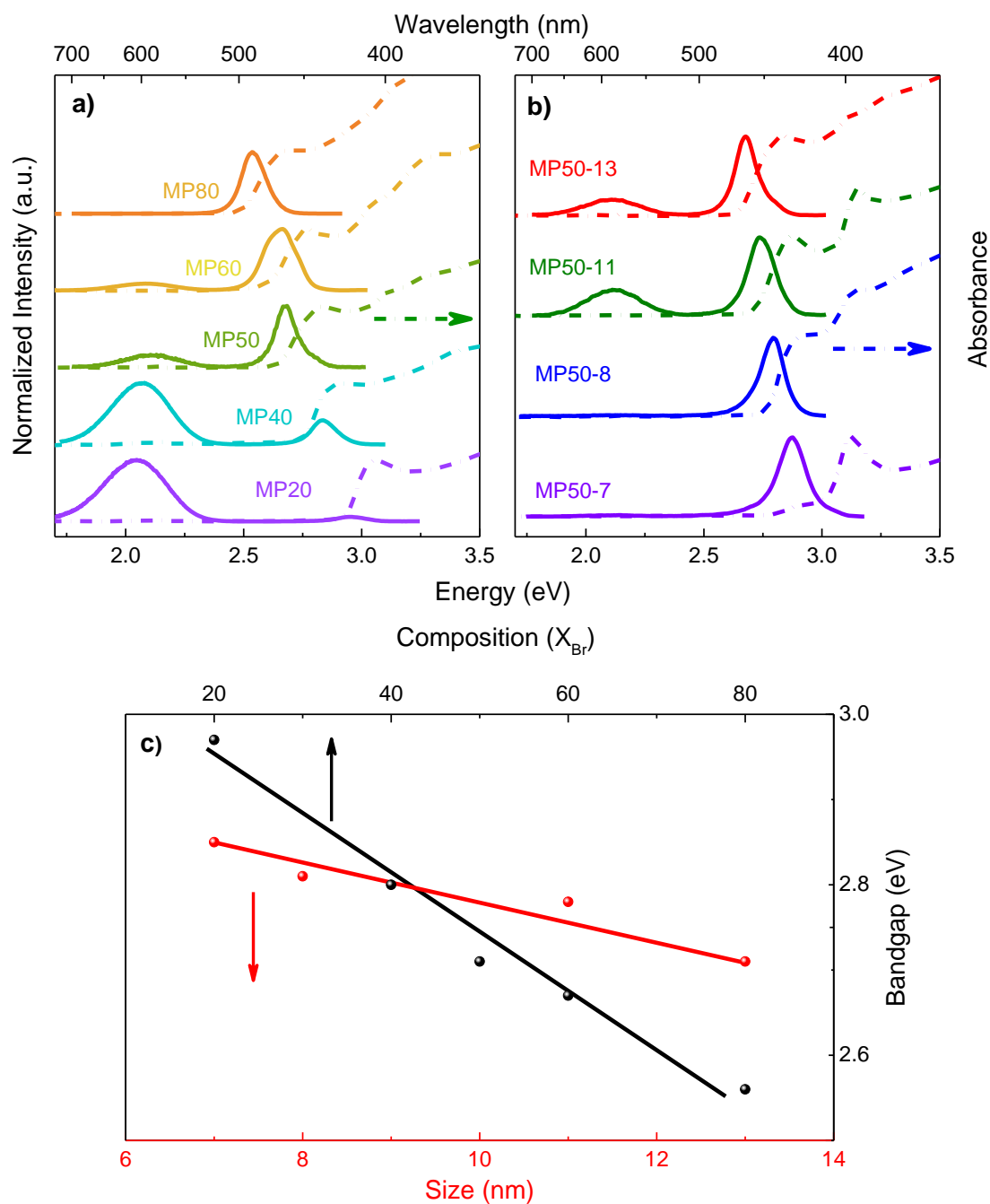


Figure 8.3 a) Absorption and steady state PL emission spectra for mixed halide perovskite QDs. b) Absorption and PL emission spectra for various sizes of Mn doped $\text{CsPb}(\text{Cl}_{1.5}\text{Br}_{1.5})$ (MP-50) c) The bandgap tuning in Mn doped perovskite QDs as a function of composition modulation and size variation.

Figure 8.3 b) shows the absorption and steady state PL spectra for quantum confined sized modulated Mn doped $\text{CsPb}(\text{Cl}/\text{Br})_3$ mixed halide perovskite QDs (MP50-7 to MP50-13) with 50 % of Br incorporation at room temperature. MP50-13 is synthesized at Cs-OA injection temperature of 180°C before ice-cooling. By decreasing the hot-injection temperature

8. Composition Modulation vs Quantum Confinement

the bandgap is blue shifted subsequently to increase the host bandgap from 2.71 to 2.85 eV. The blue shift along with the sharp excitonic features in the absorption spectra shows clear evidence of quantum confinement of charge carriers in Mn doped QDs. Substantial decrease in Mn emission intensities upon increasing the host bandgap is observed from the Figure 8.3. b). Attempt to increase the bandgap further by reducing the Cs-OA injection temperature were made but the obtained samples were highly unstable. The bandgap of MP50-7 (2.85 eV) is comparable to the bandgap of MP40 (2.8 eV), However, the intensities of Mn d-d emission in both the QDs are very different showing clear difference in the energy transfer efficiencies of QDs of similar bandgap. Mn doped perovskites QDs with similar bandgap synthesised at a higher temperature have very intense Mn emission. Figure 8.3 c) shows the tunability of bandgap in perovskite QDs by size variation and composition modulation. The bandgap tunability and corresponding changes in the film PLQY of excitonic PL and Mn emission is tabulated in Table 8.2.

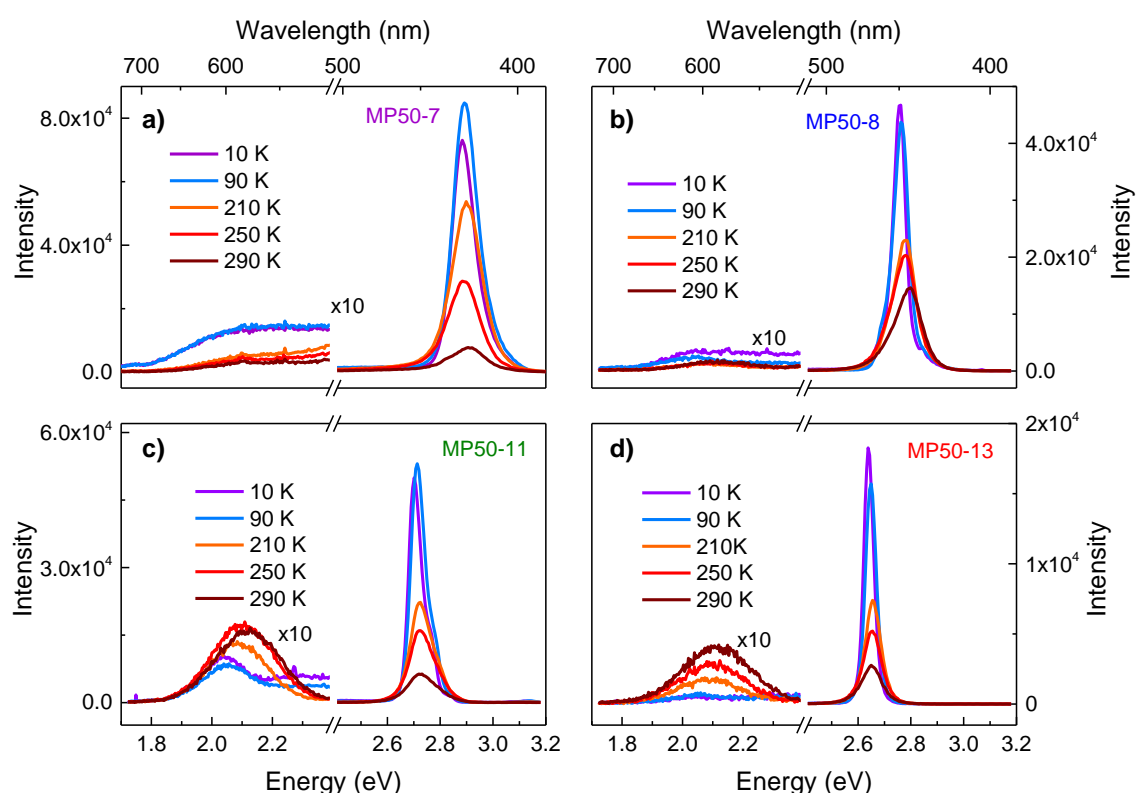


Figure 8.4 a)-d) Temperature dependent steady state PL spectra of Mn doped perovskite QDs with size ranging from 7 nm to 13 nm (MP50-7 to mp50-13).

8. Composition Modulation vs Quantum Confinement

To investigate optical properties of these QDs in more detail, low temperature (ranging from 10 K to 290 K) steady state PL measurements were performed. Figure 8.4 a) to d) shows the temperature dependent steady state PL spectra for QDs of various sizes ranging from 7 nm to 13 nm (MP50-7 to MP50-13). While the decrease in PL intensities of band edge emission with increase in temperature is due to thermal quenching, the anomalous increase in the Mn emission with increasing temperature as seen in recent studies are consistent with mixed halide perovskite QDs as well. In order to quantify the data, the area under the curves for band edge PL as function of temperature and Mn emission for a typical sample of MP50-13 are summarized in Figure 8.5. The inverse correlation of these temperature dependence in the area under the curve for band edge emission and Mn emission for the MP50 shows the competition between the radiative recombination rate, energy transfer from host to dopant and back transfer at various temperatures and are consistent with studies.³¹

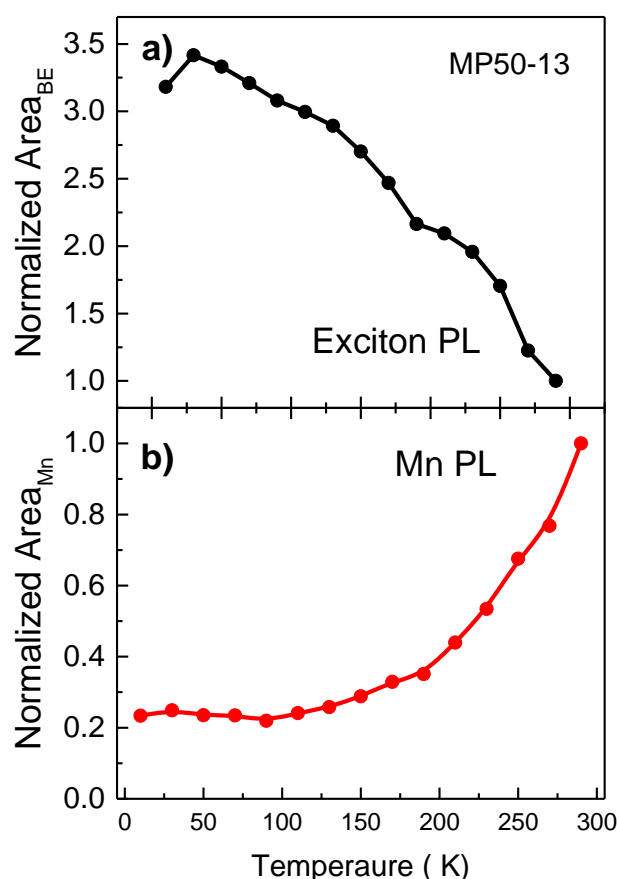


Figure 8.5 Temperature dependent PL area of excitonic and Mn emission peak for MP50-13 normalized at room temperature.

8. Composition Modulation vs Quantum Confinement

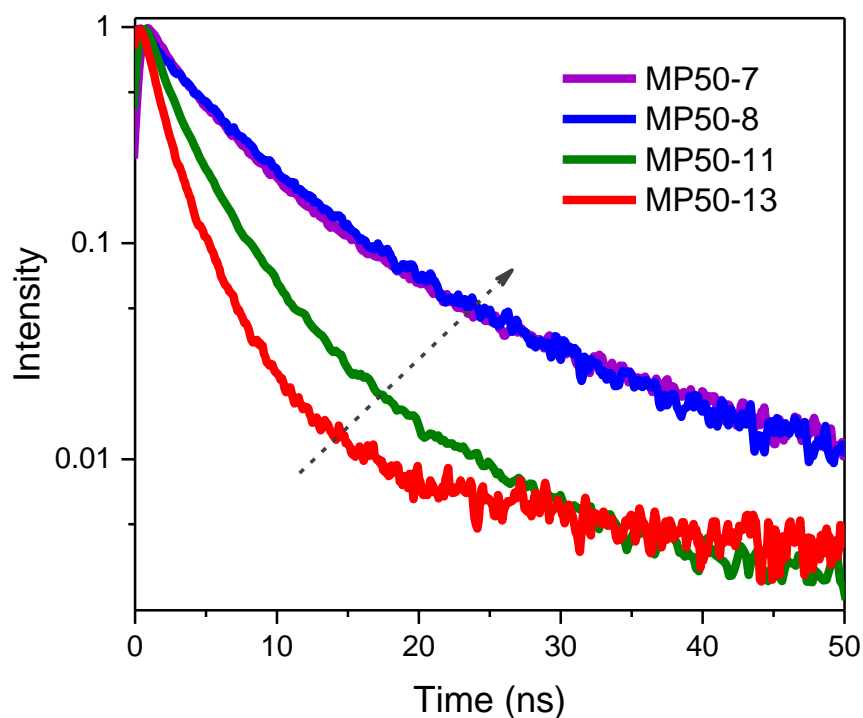


Figure 8.6 Time resolved PL decay of excitonic emission for size variation of Mn doped QDs (MP50-7 to MP50-13).

Figure 8.6 plots PL decay curves for the band edge PL for MP50-7 to MP50-13 QDs at room temperature. The decay lifetime of the band edge increases as the size of the QDs decreases due to the confinement effects and shows signatures of lesser non radiative emission pathways. These results are similar to the band edge lifetimes of lead halide perovskite QDs reported earlier.^{30, 34} However, although the band edge emission seems to decay within a few ns, there is a non-negligible intensity in the μs regime as observed from the lifetime obtained from micro-flash lamp. The temperature dependent lifetime measured for excitonic emission of MP50-8 over a range of milli seconds using micro flash lamp is shown in Figure 8.7 a).

As seen from the figure, the band edge emission also has a long-lived component which is similar to the lifetime of Mn emission due to VADF as also seen from quantum confined MP50-8. Interestingly, extremely fast component in (substantially slower than the IRF, also shown in the Figure) PL lifetime at lower temperature is observed from Figure 8.7 a) and b) and their respective inset is showing the same in a smaller time frame.

8. Composition Modulation vs Quantum Confinement

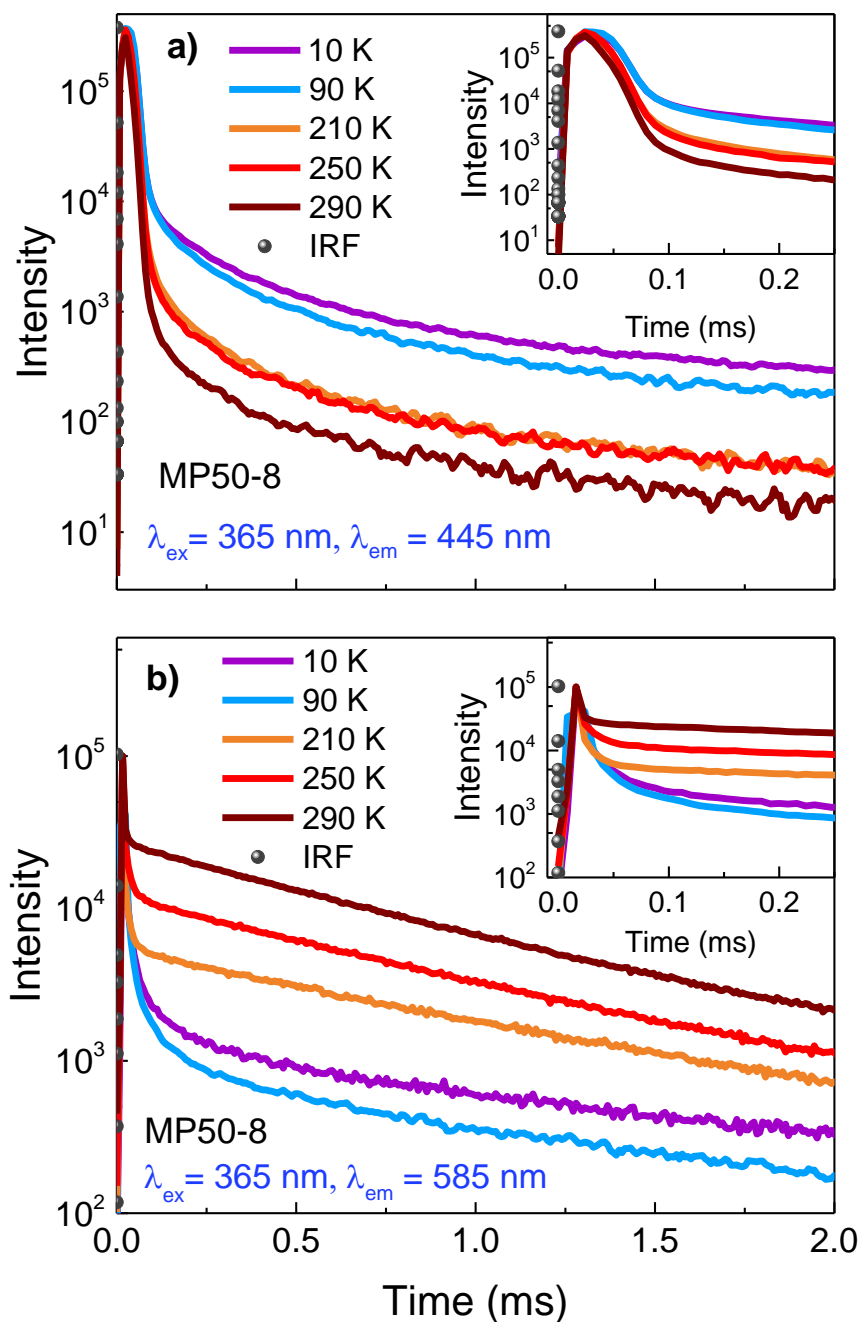


Figure 8.7 a) Decay curves of Mn doped QDs of size 8 nm at excitonic emission at 445 nm. b) decay curve for Mn-PL (585 nm) for the same sample.

To understand this change in decay better, we have integrated over the entire region from 0.2 ms to 2 ms to study the effect of delayed emission characteristics as a function of temperature using gated PL emission and gated PL excitation. Figure 8.8 shows the room temperature gated PL after a delay of 150 μ s for both compositions modulated (MP20-MP80) and quantum confined (MP50-7 to MP50-13) perovskite QDs. From the figure it is apparent that irrespective of the host bandgap there is intense Mn emission in the gated fluorescence.

8. Composition Modulation vs Quantum Confinement

However, it is also seen that irrespective of the host bandgap or size, there is substantial excitonic emission in the gated emission spectra. Presence of excitonic emission in the delayed gated PL studies are attributed to VADF in Mn doped perovskite QDs.²²

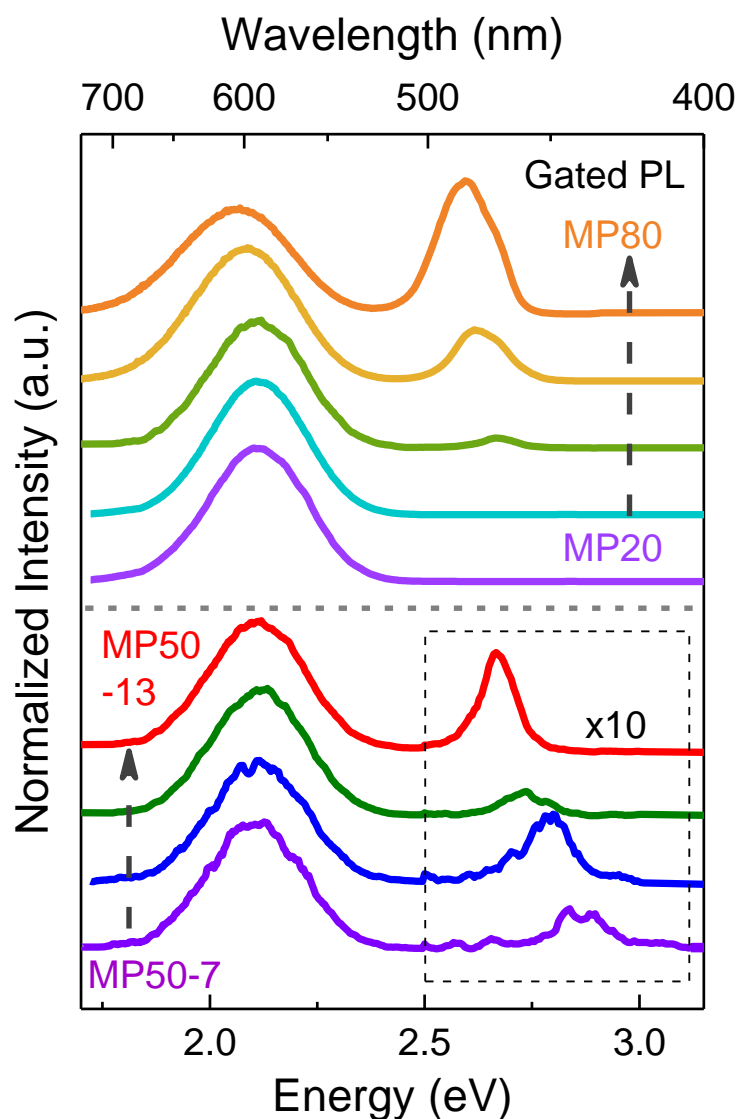


Figure 8.8 Room temperature gated PL emission for Mn doped mixed halide perovskite QDs with composition modulation (MP20 -MP80) and size modulation (MP50-7 to MP50-13)

The direct consequence of composition modulation and confinement effects on the delayed emission and drip-feeding rates were studied using gated PL emission as a function of temperature. Temperature dependant gated PL spectrum for the quantum confined samples MP50-7 to MP50-13 are shown in the Figure 8.9 a) to d). All the samples show delayed band edge emission at low temperatures and is persistent over the entire temperature range with varying intensity. Figure 8.10 shows area of excitonic delayed emission over total area in the

8. Composition Modulation vs Quantum Confinement

gated PL spectra at various temperature for various QDs with bandgap tuned by quantum confinement (Thick lines). Figure 8.10 also shows the area of band edge delayed emission over total area in the gated PL spectra at various temperature for QDs with composition modulation (dotted lines).

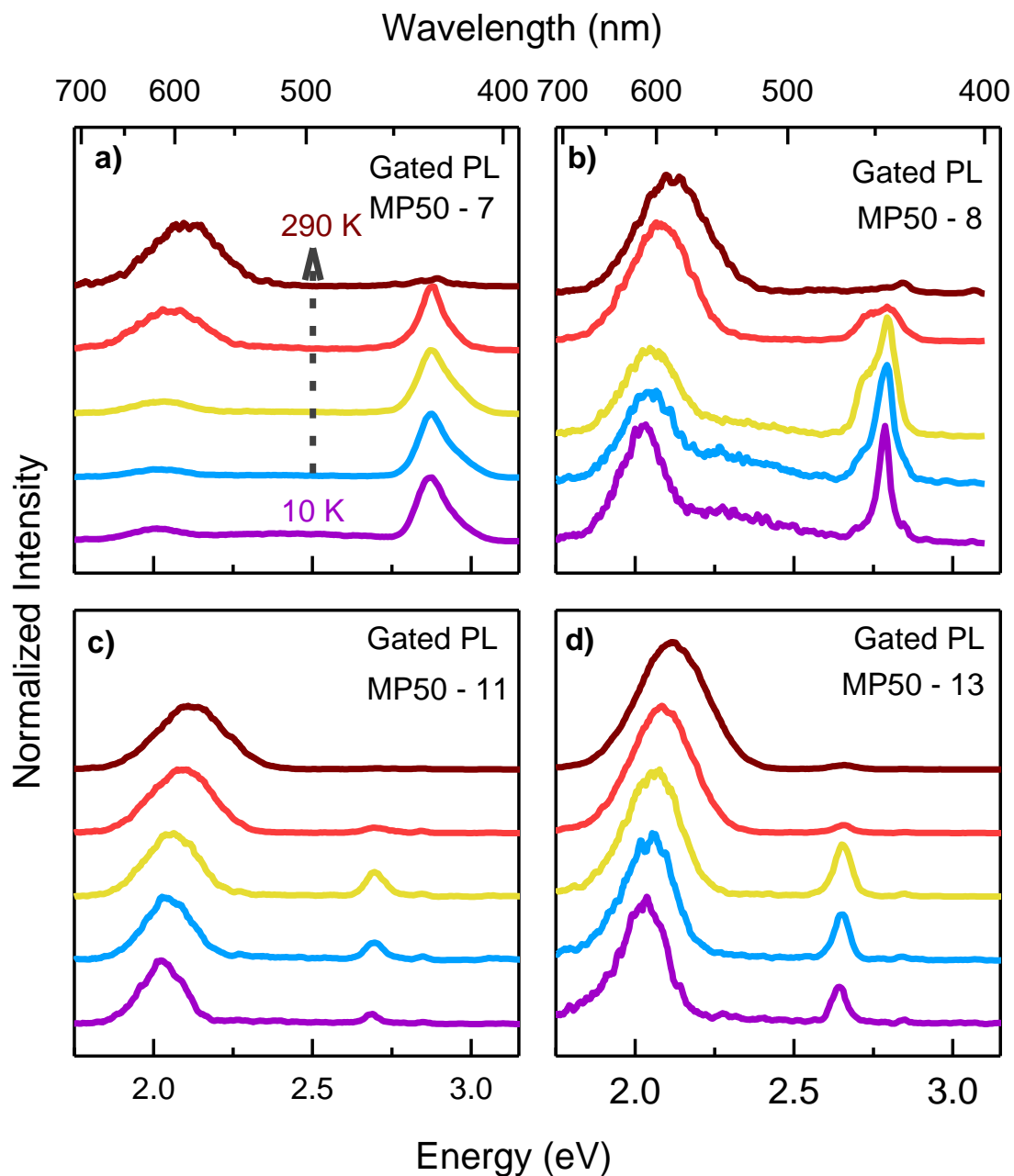


Figure 8.9 a) to d) Temperature dependent gated PL spectra for quantum confined QDs of Mn doped $\text{CsPb}(\text{Cl}/\text{Br})_3$ of size 7 nm (MP50-7), 8 nm (MP50-8), 11 nm (MP50-11) and 13 nm (MP50-13) respectively.

8. Composition Modulation vs Quantum Confinement

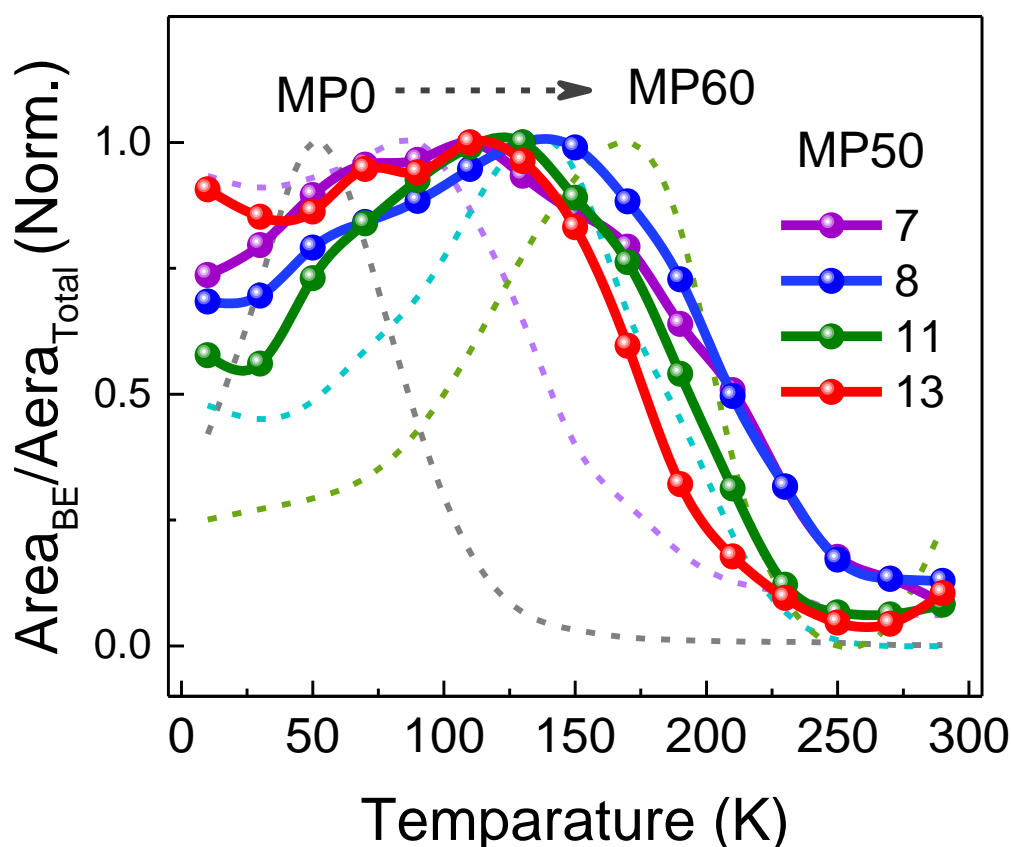


Figure 8.10 Temperature dependent gated PL area ratio of band edge emission vs total emission for Mn doped $\text{CsPb}(\text{Cl}/\text{Br})_3$ QDs with quantum confinement (thick lines) and composition modulation (thin dashed lines) in the background for comparison.

As seen from the Figure 8.9 and 8.10, we observe a rise in the intensities of the band edge emission at lower temperatures for both the smaller QDs (MP50-8) with strong confinement and larger QDs (MP50-13) with same halide ion composition. The Cl rich hosts shows weaker band edge delayed emission at higher temperatures compared to Br rich hosts are due to the stronger vibrational coupling that is observed for Mn doped CsPbBr_3 compared to weaker vibrational coupling in the case of Mn doped CsPbCl_3 .²² However, the scenario is quite different in the case of size variation of QDs with same halide composition. Thick line and scattered plots in Figure 8.10 b) also compare the ratio of the area under the band edge emission to the total area for various sizes (MP50-7 to MP50-13) of same halide composition of 50 % Br with mixed halides with composition modulation (MP0-MP60).

8. Composition Modulation vs Quantum Confinement

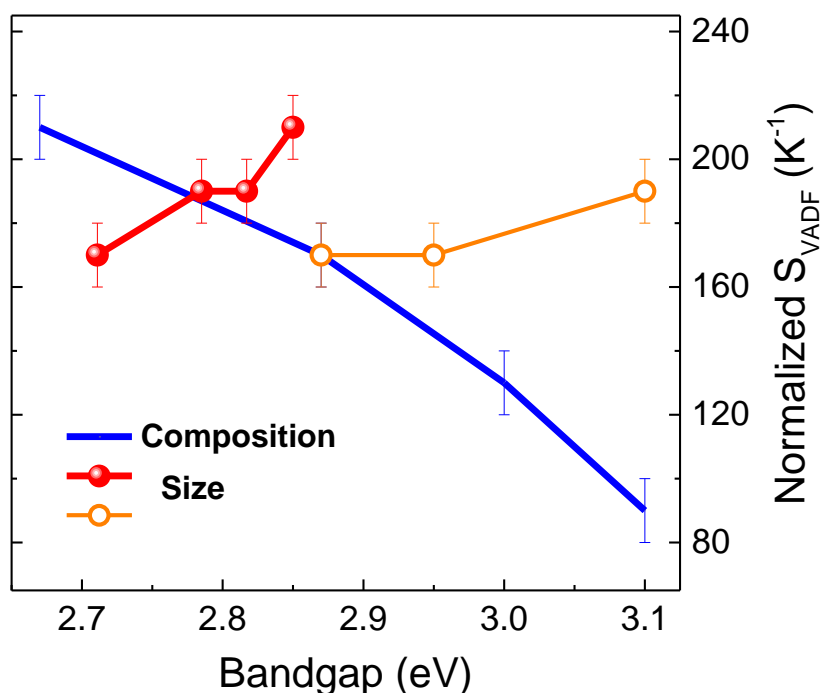


Figure 8.11 The entropy of VADF (S_{VADF}) as a function of temperature for Mn doped mixed halide QDs MP0-MP60 (blue line) and MP50-7 to MP50-13 (red solid line with closed circles) and also MP20-6 to MP20-14 (orange lines with open circles).

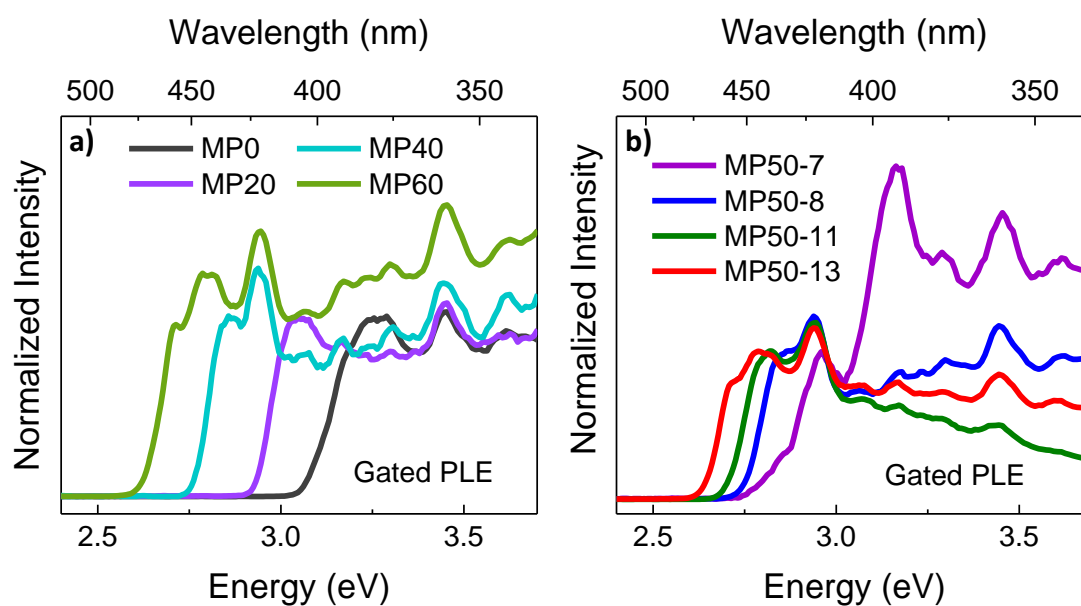


Figure 8.12 a) and b) Room temperature gated PL excitation spectra for samples with composition modulation (MP0-MP60) and size variation (MP50-7 to MP50-13) respectively.

8. Composition Modulation vs Quantum Confinement

Hence, we plotted the change in VADF as a function of temperature defined as VADF driven entropy (S_{VADF}) for both compositions modulated (MP0-MP60) and sized varied quantum confined (MP50-7 to MP50-13). As shown in Figure 8.11 the S_{VADF} is lesser for Cl rich hosts compared to mixed halide Br rich hosts, (blue line in figure) but when the bandgap of the host is tuned by varying the size (both MP50-7 to MP50-13 (red line with closed circles) and MP20-6 to MP20-14 (orange line with open circles)) the entropy of VADF (S_{VADF}) remained almost the same. As seen from the gated PL studies for both quantum confined and mixed halide composition tuned Mn doped QDs, host bandgap is not the only parameter deciding the efficiency of Mn emission and back transfer to the host radiative channels. In fact, the effective coupling between the host and Mn levels at various temperatures decide the rate of VADF.

In addition to the vibrational coupling between Mn and host which results in room temperature delayed band edge emission feature, due to quantum confinement, increased phonon assistance is also playing a role as expected due to the relaxation of phonon selection rules.

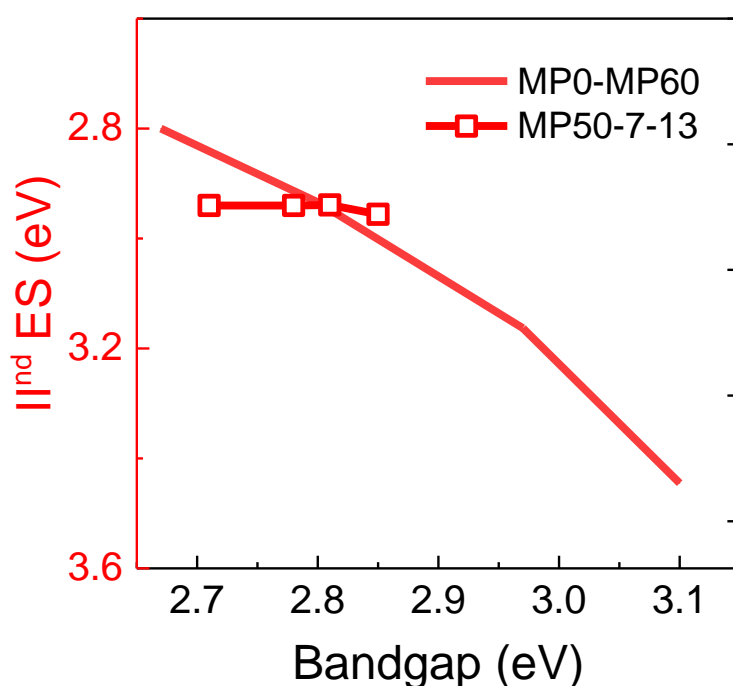


Figure 8.13 Comparison of II^{nd} excited state energy obtained from gated PLE for MP0-MP60 with composition modulation (red line) and MP50-7 to MP50-13 with quantum confinement (red line with open squares).

8. Composition Modulation vs Quantum Confinement

More specific proof of this hypothesis for state specific photoexcited charge transfer is obtained from gated PL excitation (PLE) measurement. Figure 8.12 a) and b) shows gated PLE spectra for composition modulated mixed halide QDs (MP0-MP60) and for quantum confined QDs (MP50-7 to MP50-13). A similar trend in Π^{nd} excited state energy of PL excitation plot is also observed as shown in Figure 8.13. As bandgap increases by synthesizing Cl rich hosts the higher excited state peaks also gets blue shifted (red line). Whereas, irrespective of the host bandgap, for the size tuned QDs (MP50-7 to MP50-13) with fixed halide composition the Π^{nd} excited state energy remained the same (red line with open squares). Comparing the higher excited state contributing for the delayed emission through gated PLE shows well defined peak positions indicating the drip feed mechanism of photoexcited carriers channelized through state specific levels of dopant and the host.

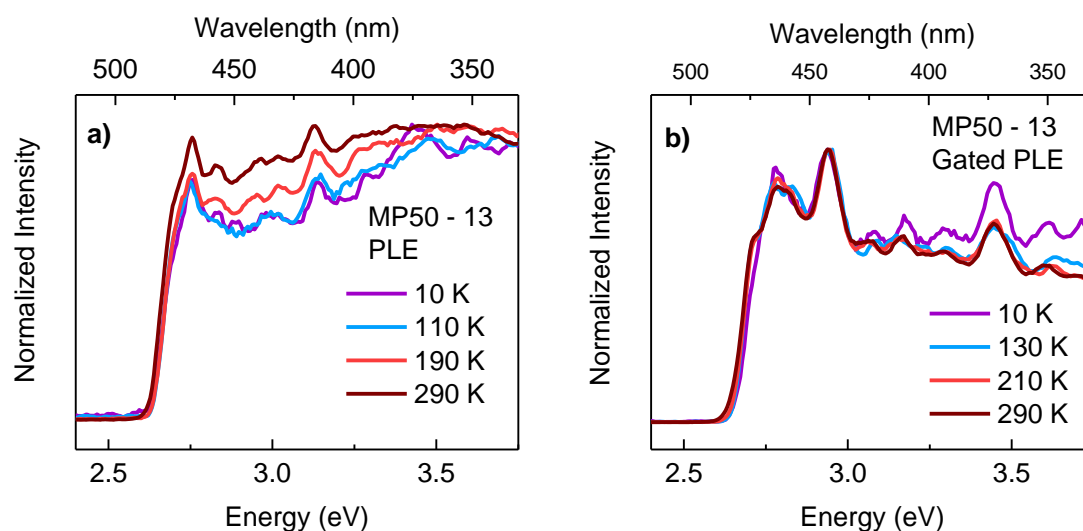


Figure 8.14 a) and b) Temperature dependent PL excitation and gated PL excitation spectra for Mn doped $\text{CsPb}(\text{Cl}/\text{Br})_3$ QDs (MP50-13) with quantum confinement.

It is also interesting to study the effect of temperature on the PLE spectra and variation of Π^{nd} excitation energy in the gated PLE spectra for QDs as seen from Figure 8.14 a) and b). However, temperature dependent PLE and gated PLE studies on a typical sample shows very similar peaks with no peak shift showing the state specific coupling levels are fixed between Mn and host and purely dependent on the nature of the host levels.

8. Composition Modulation vs Quantum Confinement

8.5. Conclusions

We have studied the effect of composition modulation and quantum confinement in Mn doped mixed halide perovskite QDs on delayed excitonic emission. The host bandgap is tuned by composition modulation and by controlling the reaction temperature to obtain various sizes with fixed halide ion concentration. Room temperature gated PL studies showed that even though the bandgap is blue shifted by decreasing the average size of the nano cube, QDs still showed substantial delayed band edge fluorescence with high PLQY due to VADF. Temperature dependent studies of band edge vs Mn emission efficiencies in the gated PL is defined by entropy of VADF by looking at the rate of change of VADF with respect to temperature clarified and quantified the difference between the photoexcited carrier back transfer efficiency. Gated PLE studies also proved that the back transfer of photoexcited electrons are assisted by state specific higher excited levels. The results and analyses presented here aid to elucidate the underlying factors contributing to the photo-physical properties of this new class of Mn doped perovskite mixed halide QDs and should help in further development of these materials for potential optoelectronic applications.

8. Composition Modulation vs Quantum Confinement

Bibliography

1. Manser, J. S.; Saidaminov, M. I.; Christians, J. A.; Bakr, O. M.; Kamat, P. V. *Acc. Chem. Res.* **2016**, 49, (2), 330-338.
2. Huang, H.; Bodnarchuk, M. I.; Kershaw, S. V.; Kovalenko, M. V.; Rogach, A. L. *ACS Energy Lett.* **2017**, 2, (9), 2071-2083.
3. Zhou, Q.; Bai, Z.; Lu, W. g.; Wang, Y.; Zou, B.; Zhong, H. *Adv. Mater.* **2016**, 28, (41), 9163-9168.
4. Zou, S.; Liu, Y.; Li, J.; Liu, C.; Feng, R.; Jiang, F.; Li, Y.; Song, J.; Zeng, H.; Hong, M. *J. Am. Chem. Soc.* **2017**, 139, (33), 11443-11450.
5. Hu, Y.; Bai, F.; Liu, X.; Ji, Q.; Miao, X.; Qiu, T.; Zhang, S. *ACS Energy Lett.* **2017**, 2, (10), 2219-2227.
6. Kovalenko, M. V.; Protesescu, L.; Bodnarchuk, M. I. *Science* **2017**, 358, (6364), 745-750.
7. Meinardi, F.; Akkerman, Q. A.; Bruni, F.; Park, S.; Mauri, M.; Dang, Z.; Manna, L.; Brovelli, S. *ACS Energy Lett.* **2017**, 2, (10), 2368-2377.
8. Lau, C. F. J.; Zhang, M.; Deng, X.; Zheng, J.; Bing, J.; Ma, Q.; Kim, J.; Hu, L.; Green, M. A.; Huang, S. *ACS Energy Lett.* **2017**, 2, (10), 2319-2325.
9. Cho, H.; Kim, Y. H.; Wolf, C.; Lee, H. D.; Lee, T. W. *Adv. Mater.* **2018**, 30, (42), 1704587.
10. Zhang, C.; Wang, S.; Li, X.; Yuan, M.; Turyanska, L.; Yang, X. *Adv. Funct. Mater.* **2020**, 1910582.
11. Bai, L.; Wang, S.; Zhang, Y.; Zhang, K.; Li, H.; Ou, K.; Yi, L. *Journal of Luminescence* **2020**, 117422.
12. Nedelcu, G.; Protesescu, L.; Yakunin, S.; Bodnarchuk, M. I.; Grotevent, M. J.; Kovalenko, M. V. *Nano Lett.* **2015**, 15, (8), 5635-5640.
13. Akkerman, Q. A.; D'Innocenzo, V.; Accornero, S.; Scarpellini, A.; Petrozza, A.; Prato, M.; Manna, L. *J. Am. Chem. Soc.* **2015**, 137, (32), 10276-10281.
14. Parobek, D.; Dong, Y.; Qiao, T.; Rossi, D.; Son, D. H. *J. Am. Chem. Soc.* **2017**, 139, (12), 4358-4361.
15. Van der Stam, W.; Geuchies, J. J.; Altantzis, T.; Van Den Bos, K. H.; Meeldijk, J. D.; Van Aert, S.; Bals, S.; Vanmaekelbergh, D.; de Mello Donega, C. *J. Am. Chem. Soc.* **2017**, 139, (11), 4087-4097.

8. Composition Modulation vs Quantum Confinement

16. Liu, M.; Zhong, G.; Yin, Y.; Miao, J.; Li, K.; Wang, C.; Xu, X.; Shen, C.; Meng, H. *Adv. Sci.* **2017**, 4, (11), 1700335.
17. Parobek, D.; Roman, B. J.; Dong, Y.; Jin, H.; Lee, E.; Sheldon, M.; Son, D. H. *Nano Lett.* **2016**, 16, (12), 7376-7380.
18. Liu, W.; Lin, Q.; Li, H.; Wu, K.; Robel, I.; Pietryga, J. M.; Klimov, V. I. *J. Am. Chem. Soc.* **2016**, 138, (45), 14954-14961.
19. Xing, K.; Yuan, X.; Wang, Y.; Li, J.; Wang, Y.; Fan, Y.; Yuan, L.; Li, K.; Wu, Z.; Li, H. *J. Phys. Chem. Lett.* **2019**, 10, (15), 4177-4184.
20. Rana, P. J. S.; Swetha, T.; Mandal, H.; Saeki, A.; Bangal, P. R.; Singh, S. P. *J. Phys. Chem. C* **2019**, 123, (27), 17026-17034.
21. Guria, A. K.; Dutta, S. K.; Adhikari, S. D.; Pradhan, N. *ACS Energy Lett.* **2017**, 2, (5), 1014-1021.
22. Pradeep, K.; Acharya, D.; Jain, P.; Gahlot, K.; Yadav, A.; Camellini, A.; Zavelani-Rossi, M.; Cerullo, G.; Narayana, C.; Narasimhan, S. V., Ranjani. *ACS Energy Lett.* **2019**, 5, (2), 353-359.
23. Das Adhikari, S.; Guria, A. K.; Pradhan, N. *J. Phys. Chem. Lett.* **2019**, 10, (9), 2250-2257.
24. Zou, S.; Liu, Y.; Li, J.; Liu, C.; Feng, R.; Jiang, F.; Li, Y.; Song, J.; Zeng, H.; Hong, M. *J. Am. Chem. Soc.* **2017**, 139, (33), 11443-11450.
25. Chen, D.; Fang, G.; Chen, X.; Lei, L.; Zhong, J.; Mao, Q.; Zhou, S.; Li, J. *J. Mater. Chem. C* **2018**, 6, (33), 8990-8998.
26. Paul, S.; Bladt, E.; Richter, A. F.; Döblinger, M.; Tong, Y.; Huang, H.; Dey, A.; Bals, S.; Debnath, T.; Polavarapu, L.; Feldmann, J. *Angew. Chem.* **2020**, 59, (17), 6794-6799.
27. Xu, K.; Meijerink, A. *Chem. Mater.* **2018**, 30, (15), 5346-5352.
28. Parobek, D.; Dong, Y.; Qiao, T.; Son, D. H. *Chem. Mater.* **2018**, 30, (9), 2939-2944.
29. Mir, W. J.; Jagadeeswararao, M.; Das, S.; Nag, A. *ACS Energy Lett.* **2017**, 2, (3), 537-543.
30. Protesescu, L.; Yakunin, S.; Bodnarchuk, M. I.; Krieg, F.; Caputo, R.; Hendon, C. H.; Yang, R. X.; Walsh, A.; Kovalenko, M. V. *Nano Lett.* **2015**, 15, (6), 3692-3696.
31. Yuan, X.; Ji, S.; De Siena, M. C.; Fei, L.; Zhao, Z.; Wang, Y.; Li, H.; Zhao, J.; Gamelin, D. R. *Chem. Mater.* **2017**, 29, (18), 8003-8011.
32. Fei, L.; Yuan, X.; Hua, J.; Ikezawa, M.; Zeng, R.; Li, H.; Masumoto, Y.; Zhao, J. *Nanoscale* **2018**, 10, (41), 19435-19442.

8. Composition Modulation vs Quantum Confinement

33. Ji, S.; Yuan, X.; Cao, S.; Ji, W.; Zhang, H.; Wang, Y.; Li, H.; Zhao, J.; Zou, B. *J. Phys. Chem. Lett.* **2020**, 11, (6), 2142-2149.
34. Ravi, V. K.; Swarnkar, A.; Chakraborty, R.; Nag, A. *Nanotechnology* **2016**, 27, (32), 325708.

Chapter 9

Temperature and Fluence Dependent Carrier Dynamics in Mn Doped Perovskite Quantum Dots

9. Carrier Dynamics in Mn Doped Perovskite Quantum Dots

9.1. Abstract

Manganese (II) doped perovskite quantum dots (QDs) because of their unique dual colour emission property are promising materials for various optoelectronic applications. To date, light emitting applications based on these materials have shown great promise. However, there is plenty of room for improvement especially in the device performances despite showing great promise in solution. One of many limiting factors is fast non radiative multiexciton Auger recombination. Using time resolved photoluminescence (PL) spectroscopy and ultrafast spectroscopic techniques we investigate multicarrier interactions in Mn doped perovskite QDs. We observe that compared to undoped perovskite QDs, Mn doped counterparts show lesser multiexciton lifetime suggesting the involvement of Mn as a dopant in excited state carrier dynamics. This understanding in the dopant host interactions could beneficially be applied to design new doped perovskite QDs with the goal of increasing their potential in light emitting applications.

9.2. Introduction

Semiconductor QDs doped with transition metal ions have attracted great attention for their exceptional optical, electronic magnetic properties.¹⁻⁵ For example, Mn^{2+} and Cu^+ in II-VI semiconductor QDs can introduce dopant emission with high PL quantum yield with large stoke shift and better colloidal stability.⁵⁻⁸ Recently, Pb based organic/inorganic perovskite QDs have emerged as promising materials for photovoltaics, light emitting diodes and lasers and other optoelectronic applications.⁹⁻¹⁴ The potential of perovskite QDs for optoelectronic applications in the various fields have triggered many research focusing on modifying the optical properties of this class of materials through transition metal doping.¹⁵⁻¹⁸ Recently, many reports have demonstrated successful doping of Mn^{2+} in lead halide perovskite QDs leading to dual colour emission from host and dopant Mn d-d states.¹⁹⁻²⁵

The Mn d-d emission arises from doped perovskite QDs is due to the spin forbidden 4T_1 to 6A_1 state of Mn^{2+} . Thus, the PL lifetime of the dopant emission is in milliseconds timescales which is few orders of magnitude longer than host exciton lifetime.^{26, 27} However, due to strong vibrational coupling between the Mn and Pb levels, there exists a possibility of back transfer of photoexcited carriers from Mn to the host leading to longer excitonic lifetime for the host emission. In addition to the increased PL quantum yield it is shown that the lifetime of the excitonic emission increases by sever order of magnitude due to continuous and slow back transfer of photoexcited carriers from Mn to Pb levels due to vibrationally assisted

9. Carrier Dynamics in Mn Doped Perovskite Quantum Dots

delayed fluorescence (VADF) as discussed in chapter 7. Additionally, upon photoexcitation, it is shown that the capture of photoexcited electrons by Mn from the hosts are quicker than capture of photoelectron by trap states showing efficient energy transfer dynamics at the excited state.²⁸ While the conducted studies indicate considerable promise of these novel QDs for applications that rely on light emission, their practical utilization in light-emitting devices would benefit from a more complete understanding of spectral and dynamical properties of electronic excitations in these materials. Particularly for perovskite-based light emitting diodes (LED), the low external quantum efficiency and poorer device performance despite showing great promise in solution is due to generation of multiexciton interaction causing non radiative decay due to Auger recombination. In addition, trion formation can also lead to low EQE in perovskite-based LEDs.²⁹ The carrier dynamics and the exciton dopant interaction due to vibrational coupling can be varied by change of several factors such as chemical composition, bandgap and excitation fluence. Recently Marakov et al.³⁰ reported the strong multi exciton interaction in perovskite QDs.

To seek clearer understanding of how the vibrational coupling due to Mn doping in perovskite QDs influences the multiexciton interactions in this particular class of QDs, we investigate, in the present work, excitation fluence dependent carrier dynamics for a series of undoped and Mn doped QDs having various halide composition. Also, the exciton Mn electron transfer dynamics for hosts with various halide composition are also analysed using temperature dependent time resolved photoluminescence spectroscopy giving complete understanding about the carrier recombination pathways. Thus, this work provides a novel foundation for understanding the photo-physics of Mn doped perovskite QDs.

9.3. Experimental Methods

Chemicals used in the experiments include Cs_2CO_3 (99.99 %), octadecene (ODE, 90 %), oleic acid (OA, 90 %), oleylamine (OLAm, 70 %), PbBr_2 (99.999 %), PbCl_2 (99.999 %), MnBr_2 (99.9 %), $\text{MnCl}_2 \cdot 4\text{H}_2\text{O}$ (99 %), n-hexane (>97.0 %), trioctylphosphine (TOP), and are used straight after purchasing from Sigma Aldrich. All solvents and reagents were of analytical grade and directly used without further purification.

Cesium oleate was prepared using standard literature methods³¹ using Cs_2CO_3 and OA in presence of ODE at high temperature of 150 °C until all Cs_2CO_3 reacted with OA forming a clear solution of Cs-oleate. Mn doped $\text{CsPb}(\text{Cl}/\text{Br})_3$ perovskite QDs were synthesized and purified by following the same method discussed in the previous chapters.

9.4. Results and Discussion

Figure 9.1 a) shows the absorption and b) steady state PL spectra for Mn doped CsPb(Cl/Br)₃ mixed halide perovskite QDs (MP0-MP100) at room temperature. The consistent redshift in the absorbance is due to composition modulation obtained by Br incorporation in Mn doped mixed halide perovskite QDs. Decrease in intensity of Mn d-d emission is also observed upon decreasing the host bandgap by Br incorporation.

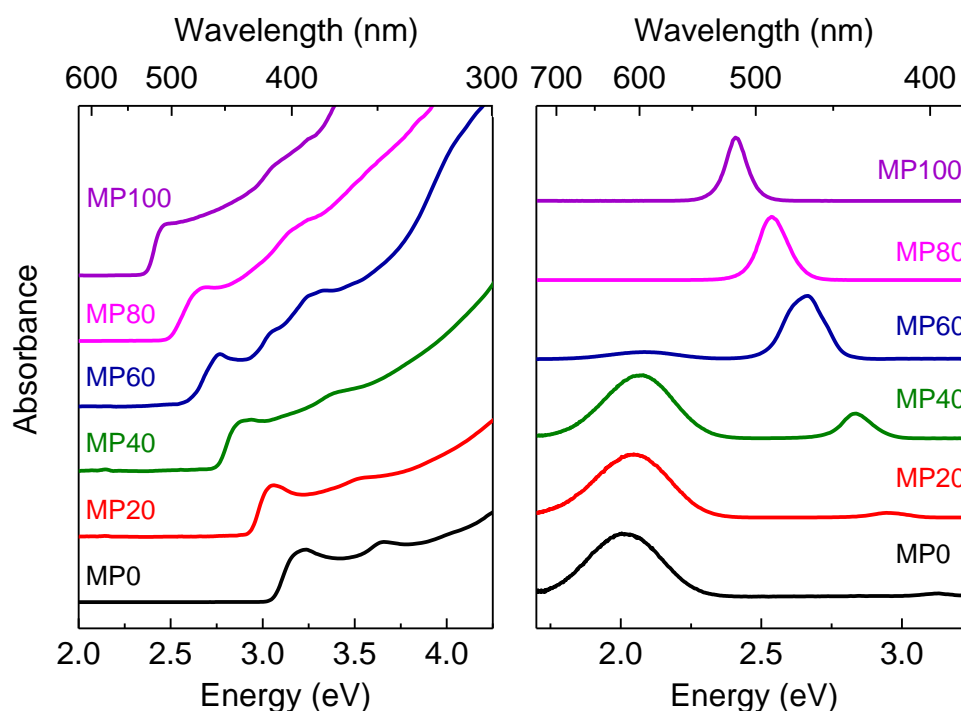


Figure 9.1 a) Absorption and b) steady state PL emission for Mn doped mixed halide perovskite QDs (MP0-MP100).

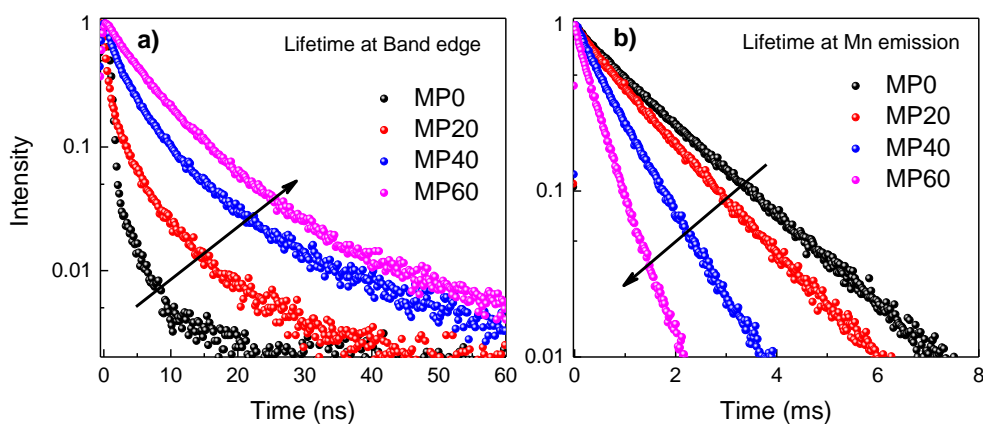


Figure 9.2 (a) Time resolved PL decay of excitonic emission and b) Time resolved PL decay of Mn emission for Mn doped mixed halide perovskite QDs (MP0 to MP100).

9. Carrier Dynamics in Mn Doped Perovskite Quantum Dots

To further study the change in the PL decay upon Br incorporation for both the excitonic emission and dopant emission fluorescent lifetimes of Mn doped CsPb(Cl/Br)₃ QDs were investigated and are shown in Figure 9.2 a) and b). The average PL lifetime of the band edge emission tend to increase with increasing Br percentage and Mn emission lifetime decreases. The absence of Mn emission in Br rich perovskite hosts has been intriguing and study on delayed emission using gated PL studies have shown that the absence of Mn emission is due to VADF as shown in chapter 7. Delayed excitonic emission observed in the Br rich hosts due to VADF is also observed in the excitonic lifetime studies done for prolonged time up to milliseconds as seen from Figure 9.3 a). As seen from the figure, the lifetime of the Mn doped QDs at band edge have a long component which is similar to the lifetime of Mn emission. The state selective back transfer of photoexcited electrons from Mn is understood by the temperature dependent lifetime studies. Figure 9.3 a) shows the temperature dependant lifetime data and the corresponding change in the long-lived component of the emission lifetime is plotted against temperature and shown in Figure 9.3 b) as well. The observation of host bandgap, excitonic back transfer from Mn levels to the host again confirms the VADF driven photoexcited carrier dynamics.

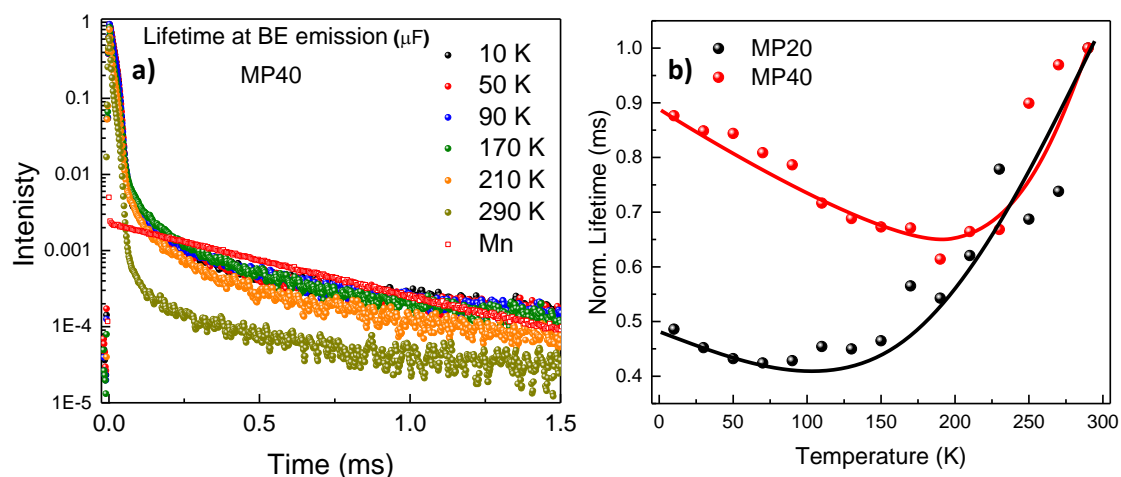


Figure 9.3 a) Temperature dependent PL decay at excitonic emission (excited at 365 nm using micro flash lamp (μF)) for MP40 with PL decay of Mn emission at 585 nm (red) and b) Change in temperature dependent lifetime of the long-lived component of excitonic emission for MP20 and MP40. (Red and black lines are guide to eye)

9. Carrier Dynamics in Mn Doped Perovskite Quantum Dots

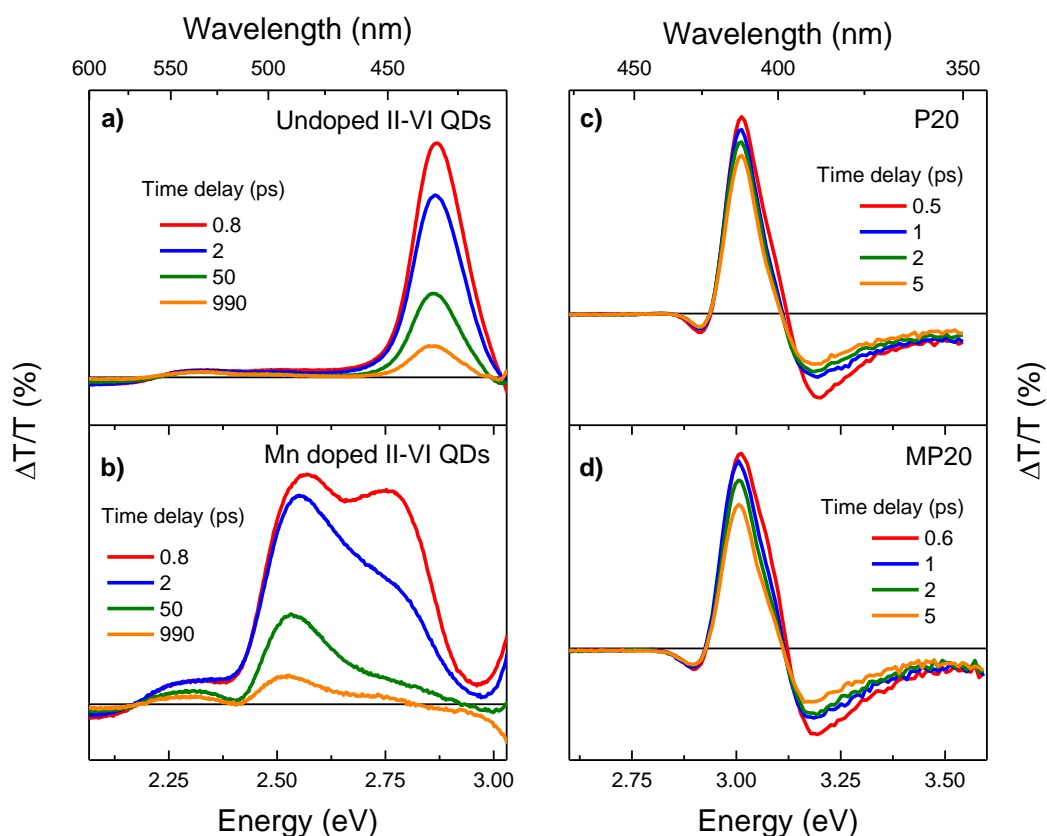


Figure 9.4 Differential transmission spectra at different delay times for the a) undoped and c) Mn doped mixed halide perovskite QDs. Differential transmission spectra at different delay times for the b) undoped and d) Mn doped II-VI semiconductor QDs.

Figure 9.4 a) and b) shows the TA spectra for a typical undoped and Mn doped II-VI semiconductor QDs clearly showing the transfer of photoexcited electron from host to dopant. However, in the case of perovskite as a host signature of quick transfer is not observed through any such depletion pathways. That doesn't directly imply that there is no such transfer of photoexcited electrons to the dopant because there is a strong Mn emission observed for these set of QDs. Figure 9.4 c) and d) shows the TA spectra of the undoped (P20) and Mn doped (MP20) perovskite QDs probed at different delay times at $5 \mu\text{J}/\text{cm}^2$. As seen from the figure the TA spectra are dominated by the exciton bleach feature due to the state filling effect by the band edge electrons and holes. Surprisingly the TA spectra are very identical for undoped and perovskite QDs. As we notice that the TA kinetics for both the undoped and Mn doped QDs exhibit a similar decay, it is possible only if there exist a continuous back transfer of photoexcited electron back to the host levels always maintaining high population at the host levels which is evident from the similarity observed between undoped and Mn doped QDs. This further confirms that the identical wavelength dependence observed for undoped and Mn

9. Carrier Dynamics in Mn Doped Perovskite Quantum Dots

doped perovskite QDs even when there is a strong Mn emission for these QDs under study (unlike II-VI semiconductor QDs scenario) is indeed due to the back transfer assisted by the strong vibrational coupling between Mn and Pb levels.

Further evidence for the absence of Mn emission in Br rich hosts and the presence of delayed excitonic emission due to vibrational coupling can be observed using ultrafast transient absorption (TA) spectroscopy. It is interesting to note that there exists a similarity in the differential transmission decay profiles for undoped and Mn doped perovskite QDs as shown in Figure 9.5. It is seen that the characteristic of Mn doping in QDs is a presence of a faster decay component especially where there is a strong Mn emission as seen from chapter 4.²⁸ As the dopant species is known to capture the photoexcited carriers at very early times as shown in chapter 4, the TA spectra at early times is expected to show exciton to dopant energy transfer providing an additional depletion pathway. Such a feature is absent in the case of Mn doped perovskite QDs. However, the absence of such a decay shows that there exists an efficient and fast transfer of photoexcited carriers from the host to dopant and followed by slow and continuous back transfer from Mn to host levels. Figure 9.5 also shows that the resemblance in the differential transmission decay profiles are very close for P100 and MP100 as there exists a strong back transfer at room temperature whereas for P20 and MP20 there is a slight difference in the longer times scales due to weak back transfer.

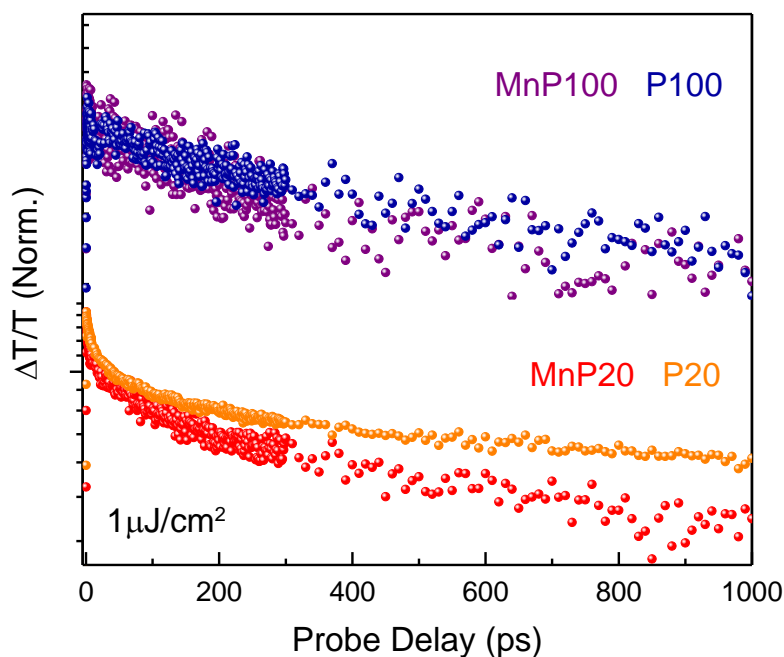


Figure 9.4 Differential transmission decay profiles for undoped (P20 and P100) and Mn doped (MP20 and MP100) at their respective band edge absorption energies.

9. Carrier Dynamics in Mn Doped Perovskite Quantum Dots

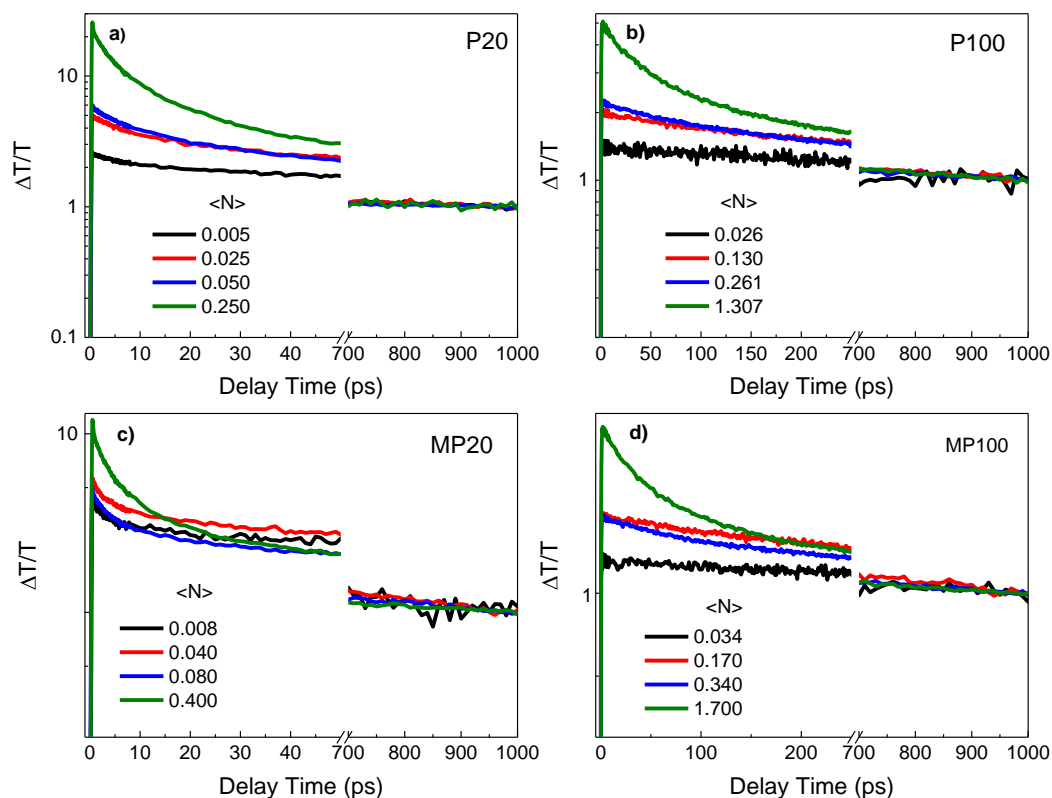


Figure 9.6 Fluence dependent differential transmission decay profiles for undoped (P20 and P100) and Mn doped (MP20 and MP100) mixed halide perovskite QDs. The data is normalized to match their long-term decay values.

In order to understand the difference between the doped and undoped perovskites in the excited state, it was necessary to track the excess carriers. Hence, we performed fluence dependent ultrafast transient absorption spectroscopy to study the multiexcitonic dynamic behaviour of carriers in undoped and Mn doped perovskite QDs. At very low excitation fluences, when the photoexcited QDs are dominated by single exciton states, the signal is generally long lived. With increase in excitation fluence, the amplitude of the new fast decay component becomes progressively larger, consistent with Auger recombination of multiple exciton states. Figure 9.6 a) to d) shows fluence dependent transient absorption decay profiles for undoped perovskite QDs with Cl rich (P20) and Br rich (P100) halide composition and Mn doped perovskite QDs with Cl rich (MP20) and Br rich (MP100) halide composition respectively. In order to estimate the multiexciton lifetime for both undoped and Mn doped perovskite QDs, it is essential to calculate the average number of excitons per QD per exciton pulse ($\langle N \rangle$). Average number of photons absorbed per QD per exciton pulse were calculated by using the expression

9. Carrier Dynamics in Mn Doped Perovskite Quantum Dots

$$\langle N \rangle = j_p \sigma_A,$$

where j_p is the pump photon fluence, and σ_A is the QD absorption cross section.

The absorption cross section of the undoped and Mn doped QDs were determined by elemental analysis method. Firstly, the absorption coefficient of the QDs were determined using Beer's law from the measured absorption spectrum and molar concentration of the QDs. Absorption cross section was then calculated from molar absorption coefficient using the conversion factor of $2303/N_A$ where N_A is Avogadro's number.

For low pump fluences where $\langle N \rangle \ll 1$, excited NCs only contain a single exciton and the resulting transient absorption spectra are well described by mono-exponential decay function which corresponds to the lifetime of single band edge excitons. To estimate the biexciton lifetime, Klimov et.al³² developed a simple subtractive procedure to extract single exponential dynamics that are characteristic of the decay of different multiple-pair QD states from the measured $\langle N(t) \rangle$ time transients for various sizes of CdSe QDs. According to this method, to extract single exponential multiparticle dynamics, firstly the data is normalized at long time after the photoexcitation as shown in Figure 9.6. Secondly, low pump intensity trace ($\langle N \rangle = \ll 1$) is subtracted from traces with $\langle N \rangle > 0.1$ which yields dynamics due to relaxation of multiple pair states and the data is fit to single exponential decay giving rise to biexciton lifetime (τ_2).

Sample	τ_2 (ps)	Trion lifetime (ps)	Sample	τ_2 (ps)	Trion lifetime (ps)
P20	4.76	33.61	MP20	3.19	20.38
P40	7.06	38.87	MP40	4.57	19.87
P80	37.81	293.45	MP80	13.28	204.18
P100	33.41	204.83	MP100	28.70	157.26

TABLE 9.1 Biexciton and trion lifetime for undoped and Mn doped perovskite QDs.

9. Carrier Dynamics in Mn Doped Perovskite Quantum Dots

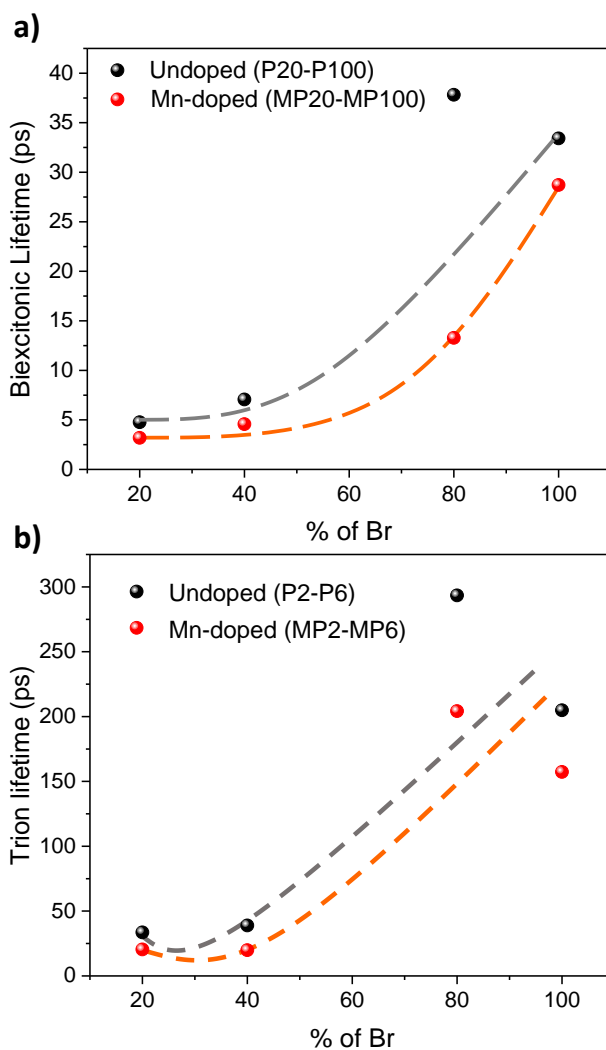


Figure 9.7 a) Biexciton lifetime and b) trion lifetime as a function of halide composition for undoped and Mn doped mixed halide perovskite QDs.

We have adapted the above-mentioned method of estimating the biexciton lifetime by subtracting the single exciton contribution from the lowest intensity scan and fitted data to single exponential decay for both undoped and Mn doped perovskite QDs. The fits obtained were not accurate as there was an additional long-lived component to be added to the fit (data not shown). To obtain more accurate results, the data is fit by considering the long-lived component present in the data which shows presence of trions. It is also seen from the study on emission properties and ultrafast carrier dynamics of CsPbCl₃ perovskite QDs, that more accurate values of biexciton lifetime (20 ps) by fitting the data with additional long lived component.³³ Similarly, for CsPbBr₃ QDs (P100), trion decay component with a lifetime of ~ 200 ps in addition to a biexciton decay component with a 40 ps lifetime, has been previously observed.³⁴ As seen from Table 9.1 and Figure 9.7, The biexciton lifetime (3-35 ps) with trion

9. Carrier Dynamics in Mn Doped Perovskite Quantum Dots

contribution (20-300 ps) increases from P20 to P100 and MP20 to MP100. Biexciton lifetime and trion lifetime of the undoped perovskites are in agreement with the available literature on perovskite QDs.^{30, 33, 34} Interestingly, the biexciton lifetime is lesser for Mn doped samples compared to their undoped counterparts as seen from Figure. 9.7. The lesser biexciton lifetime for the Mn doped perovskite QDs suggests that the excess population of photoexcited carriers at high fluence decays quickly through the radiative decay rather than Auger recombination when compared to undoped perovskite QDs. This fluence dependent carrier dynamics comparative study between undoped and Mn doped perovskite QDs establishes the influence of Mn as a dopant in drip-feeding the photo excited carriers back to the host through VADF and sheds light on to ultrafast processes involved perovskite QDs which is essential to design promising materials for light emission.

9.5. Conclusions

In summary, we have performed a systematic investigation on the photoinduced carrier dynamics in Mn-doped perovskite NCs by using temperature dependent time resolved PL spectroscopy and ultrafast transient absorption spectroscopy. From the temperature dependent delayed exciton lifetime studies, we observe that there exists a host bandgap dependent state specific back transfer from Mn levels to the host through vibrational coupling suggesting complex photoexcited carrier dynamics. We also observed huge differences between the TA spectra of Mn doped perovskite QDs and II-VI semiconductor confirming the differences photoexcited electron transfer mechanisms between these materials. We then observed strong fluence dependent biexciton generation and difference between the multiexciton lifetimes between undoped and Mn doped perovskite QDs. Also, the role of Mn as a dopant in drip-feeding the photo excited carriers back to the host through VADF is validated through ultrafast carrier dynamics studies in undoped and Mn doped perovskite QDs.

Bibliography

1. Norris, D. J.; Yao, N.; Charnock, F. T.; Kennedy, T. A. *Nano Lett.* **2001**, 1, (1), 3-7.
2. Pradhan, N.; Goorskey, D.; Thessing, J.; Peng, X. *J. Am. Chem. Soc.* **2005**, 127, (50), 17586-17587.
3. Norris, D. J.; Efros, A. L.; Erwin, S. C. *Science* **2008**, 319, (5871), 1776-1779.
4. Kittilstved, K. R.; Gamelin, D. R. *J. Am. Chem. Soc.* **2005**, 127, (15), 5292-5293.
5. Beaulac, R.; Archer, P. I.; van Rijssel, J.; Meijerink, A.; Gamelin, D. R. *Nano Lett.* **2008**, 8, (9), 2949-2953.
6. Pradhan, N.; Peng, X. *J. Am. Chem. Soc.* **2007**, 129, (11), 3339-3347.
7. Nag, A.; Chakraborty, S.; Sarma, D. *J. Am. Chem. Soc.* **2008**, 130, (32), 10605-10611.
8. Brovelli, S.; Galland, C.; Viswanatha, R.; Klimov, V. I. *Nano Lett.* **2012**, 12, (8), 4372-4379.
9. Yang, W. S.; Park, B.-W.; Jung, E. H.; Jeon, N. J.; Kim, Y. C.; Lee, D. U.; Shin, S. S.; Seo, J.; Kim, E. K.; Noh, J. H. *Science* **2017**, 356, (6345), 1376-1379.
10. Zolfaghari, Z.; Hassanabadi, E.; Pitarch-Tena, D.; Yoon, S. J.; Shariatinia, Z.; van de Lagemaat, J.; Luther, J. M.; Mora-Seró, I. n. *ACS Energy Lett.* **2018**, 4, (1), 251-258.
11. Veldhuis, S. A.; Ng, Y. F.; Ahmad, R.; Bruno, A.; Jamaludin, N. F.; Damodaran, B.; Mathews, N.; Mhaisalkar, S. G. *ACS Energy Lett.* **2018**, 3, (3), 526-531.
12. Fang, Y.; Dong, Q.; Shao, Y.; Yuan, Y.; Huang, J. *Nat. Photonics* **2015**, 9, (10), 679-686.
13. Yakunin, S.; Protesescu, L.; Krieg, F.; Bodnarchuk, M. I.; Nedelcu, G.; Humer, M.; De Luca, G.; Fiebig, M.; Heiss, W.; Kovalenko, M. V. *Nat. Commun.* **2015**, 6, (1), 1-9.
14. Utzat, H.; Sun, W.; Kaplan, A. E.; Krieg, F.; Ginterseder, M.; Spokoyny, B.; Klein, N. D.; Shulenberger, K. E.; Perkinson, C. F.; Kovalenko, M. V. *Science* **2019**, 363, (6431), 1068-1072.
15. Yong, Z.-J.; Guo, S.-Q.; Ma, J.-P.; Zhang, J.-Y.; Li, Z.-Y.; Chen, Y.-M.; Zhang, B.-B.; Zhou, Y.; Shu, J.; Gu, J.-L. *J. Am. Chem. Soc.* **2018**, 140, (31), 9942-9951.
16. Náfrádi, B.; Szirmai, P.; Spina, M.; Lee, H.; Yazyev, O.; Arakcheeva, A.; Chernyshov, D.; Gibert, M.; Forró, L.; Horváth, E. *Nat. Commun.* **2016**, 7, (1), 1-8.
17. Milstein, T. J.; Kroupa, D. M.; Gamelin, D. R. *Nano Lett.* **2018**, 18, (6), 3792-3799.

9. Carrier Dynamics in Mn Doped Perovskite Quantum Dots

18. Pan, G.; Bai, X.; Xu, W.; Chen, X.; Zhou, D.; Zhu, J.; Shao, H.; Zhai, Y.; Dong, B.; Xu, L. *ACS Appl. Mater. Interfaces* **2018**, 10, (45), 39040-39048.
19. Liu, W.; Lin, Q.; Li, H.; Wu, K.; Robel, I.; Pietryga, J. M.; Klimov, V. I. *J. Am. Chem. Soc.* **2016**, 138, (45), 14954-14961.
20. Akkerman, Q. A.; Meggiolaro, D.; Dang, Z.; De Angelis, F.; Manna, L. *ACS Energy Lett.* **2017**, 2, (9), 2183-2186.
21. Das Adhikari, S.; Dutta, S. K.; Dutta, A.; Guria, A. K.; Pradhan, N. *Angew. Chem., Int. Ed.* **2017**, 129, (30), 8872-8876.
22. Wang, Q.; Zhang, X.; Jin, Z.; Zhang, J.; Gao, Z.; Li, Y.; Liu, S. F. *ACS Energy Lett.* **2017**, 2, (7), 1479-1486.
23. Zou, S.; Liu, Y.; Li, J.; Liu, C.; Feng, R.; Jiang, F.; Li, Y.; Song, J.; Zeng, H.; Hong, M. *J. Am. Chem. Soc.* **2017**, 139, (33), 11443-11450.
24. Meinardi, F.; Akkerman, Q. A.; Bruni, F.; Park, S.; Mauri, M.; Dang, Z.; Manna, L.; Brovelli, S. *ACS Energy Lett.* **2017**, 2, (10), 2368-2377.
25. Zhu, J.; Yang, X.; Zhu, Y.; Wang, Y.; Cai, J.; Shen, J.; Sun, L.; Li, C. *J. Phys. Chem. Lett.* **2017**, 8, (17), 4167-4171.
26. Parobek, D.; Roman, B. J.; Dong, Y.; Jin, H.; Lee, E.; Sheldon, M.; Son, D. H. *Nano Lett.* **2016**, 16, (12), 7376-7380.
27. Yuan, X.; Ji, S.; De Siena, M. C.; Fei, L.; Zhao, Z.; Wang, Y.; Li, H.; Zhao, J.; Gamelin, D. R. *Chem. Mater.* **2017**, 29, (18), 8003-8011.
28. Gahlot, K.; KR, P.; Camellini, A.; Sirigu, G.; Cerullo, G.; Zavelani-Rossi, M.; Singh, A.; Waghmare, U. V.; Viswanatha, R. *ACS Energy Lett.* **2019**, 4, (3), 729-735.
29. Castañeda, J. A.; Nagamine, G.; Yassitepe, E.; Bonato, L. G.; Voznyy, O.; Hoogland, S.; Nogueira, A. F.; Sargent, E. H.; Cruz, C. H. B.; Padilha, L. A. *ACS Nano* **2016**, 10, (9), 8603-8609.
30. Makarov, N. S.; Guo, S.; Isaienko, O.; Liu, W.; Robel, I.; Klimov, V. I. *Nano Lett.* **2016**, 16, (4), 2349-2362.
31. Protesescu, L.; Yakunin, S.; Bodnarchuk, M. I.; Krieg, F.; Caputo, R.; Hendon, C. H.; Yang, R. X.; Walsh, A.; Kovalenko, M. V. *Nano Lett.* **2015**, 15, (6), 3692-3696.
32. Klimov, V. I.; Mikhailovsky, A. A.; McBranch, D.; Leatherdale, C. A.; Bawendi, M. *G. Science* **2000**, 287, (5455), 1011-1013.
33. Ahumada-Lazo, R.; Alanis, J. A.; Parkinson, P.; Binks, D. J.; Hardman, S. J.; Griffiths, J. T.; Wisnivesky Rocca Rivarola, F.; Humphrey, C. J.; Ducati, C.; Davis, N. J. *J. Phys. Chem. C* **2019**, 123, (4), 2651-2657.

9. Carrier Dynamics in Mn Doped Perovskite Quantum Dots

34. Castañeda, J. A.; Nagamine, G.; Yassitepe, E.; Bonato, L. G.; Voznyy, O.; Hoogland, S.; Nogueira, A. F.; Sargent, E. H.; Cruz, C. H. B.; Padilha, L. A. *ACS nano* **2016**, 10, (9), 8603-8609.

9. Carrier Dynamics in Mn Doped Perovskite Quantum Dots

Chapter 10

Summary

10. Summary

10. Summary

10.1. Quantum Dots for Optoelectronics

Quantum dots (QDs), with their unique properties have given rise to a variety of new applications that have been very useful. These semiconductor nanoparticles have electronic properties that are significantly different from their bulk counterparts as a consequence of constrained electron and hole wavefunctions. These properties are of interest both from a fundamental perspective as well as from the perspective of many optoelectronic applications.

Despite its history of more than 30-years, the science of colloidal QDs still represents an exciting area of research that appeals to scientists with a various range of backgrounds, including inorganic and colloidal chemistry, condensed matter physics, optoelectronics, biological and medical sciences. With the introduction of perovskite inorganic QDs the possibility is further increased by a recent demonstration of their applications in different technologies ranging from photovoltaics, QD-LEDS, lasers, bio-imaging etc. Colloidal QDs are rapidly generating attention not only in the scientific community but also engineering and entrepreneurial communities due to their potential in various applications.

10.2 Present Study

II-VI semiconductor QDs and perovskite QDs have been investigated extensively for optoelectronic applications. Transition metal doping adds additional advantage in designing quantum dots (QDs) for various optoelectronic applications. In the era that is driven by quest for energy efficiency, understanding of the photo physics is very essential. The thesis is divided into nine chapters along with methodology chapter where experimental techniques employed throughout these chapters are discussed. Rest of the thesis is divided in to two parts. The first part discusses about the decade long debate about mechanism of Mn emission in Mn doped II-VI semiconductors and the second part of the thesis discusses about various issues related to stability and structure of perovskite QDs and harvesting delayed fluorescence using Mn as a dopant in mixed halide perovskite QDs.

Chapter 1 highlights various applications of the semiconductors QDs of the II-VI elements and perovskites and provides an outline of the chapter-wise organization of the thesis. Chapter 2 describes the procedures for synthesis of Mn-doped group II-VI semiconductor QDs and perovskite QDs, their characterization techniques and details of spectroscopic tools used in this study. Chapter 3 and 4 constitute the first part of the thesis and deal with the mechanism of Mn emission in Mn doped II-VI semiconductor QDs. Chapter 5 to 9 form the second part

10. Summary

of the thesis and are devoted to the Mn-doped perovskite QDs. While Chapter 5 and 6 focus on the structural aspects and doping in perovskites. Chapter 7-9 are devoted mainly to the mechanism of Mn emission and harvesting delayed fluorescence Mn doped perovskites.

10.3. Mn Doped Quantum Dots: Present Status and Outlook for the Future

Mn as an optically active dopant in QDs, it has been studied for 30 years and achieved several milestones due to their unique feature of spin forbidden Mn d-d emission. The doping was first performed with different chalcogenide materials, and it has also been extended to recently emerged perovskite nanocrystals. The large absorption cross section and long lifetime of Mn doped semiconductors made them a particular curiosity during the early years of development. The large Stokes shift in Mn emission reduces self-absorption as an added advantage. Understanding the Mn excitation and emission mechanism provides a fundamental viewpoint about the potential of these excellent materials for optoelectronic applications. understanding of the mechanism of Mn emission has an immediate consequence in overcoming internal energy losses and spin driven opto-electronics may be a new strategy for designing optimal devices for photo-emissive and photo-voltaic applications.

The enigma over the mechanism of Mn excitation and emission around Mn doped II-VI semiconductor QDs and perovskite QDs are clarified using various extensive optical spectroscopic techniques. However, there are several anomalies and unanswered missing links present in this field. The presence of excitonic emission in the low bandgap perovskite hosts in gated PL, the presence of a 2.5 eV emission in Mn doped II-VI QDs can be well resolved and understood using single molecule spectroscopy where the origin of such peaks can be understood and can eliminate the possibility of the presence of any fraction of undoped counterparts. In addition to that, understanding in the reason behind the non-zero excitonic emission even in Mn doped CsPbCl₃ is essential to obtain major differences between the mechanism of Mn emission in II-VI QDs and perovskite QDs as hosts. Hence, there is still more rooms for understanding and investigating the fundamentals of the emission properties of these materials.

Additionally, even though perovskite nanocrystals synthesis is widely established, slowing down the growth process could not be achieved yet. Precise control over the synthesis process and dopant insertion needs to be deeply investigated. Also, the doping can be extended to a wide variety of shapes, though cubes and platelets are already reported. Beyond Mn, other

10. Summary

optically active dopants (for example, Ni, Cu) and also dual doping systems need to be developed to understand the process of VADF in perovskite QDs.

The emergence of perovskite QDs in the recent years keeps the applicability of QDs for various optoelectronics at a high scale. From a device perspective Mn doping has been acknowledged to be superior due to the lack of self-absorption, and improved colloidal stability as well as for air stable LED devices. However, the major shortfall of Mn doping in devices is the presence of a single broad non-tunable emission at 590 nm (2.1 eV). By using Mn as a storehouse of excited electrons, all these advantages will be transferred to the excitonic features in addition to the tunability and the sharpness of the excitonic emission peak. However, there are still many challenges to overcome before Mn doped QDs can be used in consumer devices. The additional advantage of using Mn as a dopant apart from using as a store house of photoexcited carriers for VADF, the formation of a magnetically coupled excitonic state also enables optical control of magnetism.

One of the main problems with perovskite QDs is that they contain lead, which is an extremely toxic metal. Due to the highly polar nature of perovskites, they can be easily dissolved in polar solvents (like water), leading to serious health and safety issues. So far, no feasible alternatives have been found for replacing lead in these QDs, as most replacements lead to stability issues, decreases in the PLQY, large stokes shifts, and a significant broadening of the PL. Thus, future work on perovskite QDs will mainly focus on finding sufficient replacements for lead.

10. Summary

LIST OF PUBLICATIONS

1. “Stability of Sn based inorganic perovskite quantum dots” **Pradeep K R**, Saptarshi Chakraborty, Ranjani Viswanatha **Materials Research Express** **2019** **6** 114004
DOI: 10.1088/2053-1591/ab5121
2. “Transient Species Mediating Energy Transfer to Spin Forbidden Mn d States in II-VI Semiconductor Quantum Dots” Kushagra Gahlot, **Pradeep K R**, Andrea Camellini, Gianluca Sirigu, Giulio Cerullo, Margherita Zavelani-Rossi, Anjali Singh, Umesh V. Waghmare, and Ranjani Viswanatha **ACS Energy Letters** **2019** **4** (3), 729-735
DOI: 10.1021/acseenergylett.9b00064
3. “Harvesting Delayed Fluorescence in Perovskite Nanocrystals using Spin Forbidden Mn d states” **Pradeep K R**, Debdipto Acharya, Priyanka Jain, Kushagra Gahlot, Anur Yadav, Andrea Camellini, Margherita Zavelani-Rossi, Giulio Cerullo, Chandrabhas Narayana, Shobhana Narasimhan, and Ranjani Viswanatha **ACS Energy Letters** **2020** **5**, 353-359
DOI: 10.1021/acseenergylett.9b02399
4. “Mechanism of Mn emission: Energy transfer vs charge transfer dynamics in Mn-doped quantum dots” **Pradeep K R**, Ranjani Viswanatha **APL Materials** **2020** **8**, 020901
DOI: 10.1063/1.5140888
5. “Doped or Not Doped? Importance of the Local Structure of Mn (II) in Mn Doped Perovskite Nanocrystals” **Pradeep K R**, Ranjani Viswanatha **Materials Research Bulletin** **2021**, (Under review)
6. “Solid Solution or Alloy? Understanding the Structure of Perovskite Quantum Dots at Various Length Scales” **Pradeep K R**, Priyanka Jain, Murzin Vadim, Chandrabhas Narayana, and Ranjani Viswanatha. (Manuscript under preparation)
7. “Band Gap Tuning due to Quantum Confinement vs Composition Variation: Consequences on Delayed Fluorescence in Mn Doped Perovskite Nanocrystals.” **Pradeep K R**, Abhinaya Elumuri, Ranjani Viswanatha. (Manuscript under preparation)

8. “Temperature and Fluence dependent Carrier Dynamics in Mn doped Perovskite Quantum Dots.” **Pradeep K R**, Andrea Camellini, Margherita Zavelani-Rossi Giulio Cerullo, Ranjani Viswanatha. (Manuscript Under Preparation)

LIST OF PUBLICATIONS NOT PART OF THIS THESIS

1. “Solvent Adaptive Dynamic Metal-Organic Soft Hybrid for Imaging and Biological Delivery” Debabrata Samanta, Syamantak Roy, Ranjan Sasmal, Nilanjana Das Saha, **Pradeep K R**, Ranjani Viswanatha, Sarit S. Agasti, Tapas Kumar Maji **Angew. Chem.** **2019**, **131**, **5062**.

DOI: 10.1002/ange.201900692

2. “Safeguarding long-lived excitons from excimer traps in H-aggregated dye-assemblies” Samaresh Samanta, Subir Kumar Ray, Shubham Deolka, Sudipta Saha, **Pradeep K R**, Rohit Bhowal, Nirmalya Ghosh, Debangshu Chaudhuri **Chemical Science** **2020** **11**, **5710-5715**

DOI: 10.1039/D0SC01784A

LIST OF BOOK CHAPTERS

1. **Chapter 3: “Opportunities and Challenges in Quantum Dots” Pradeep K R and Ranjani Viswanatha *Advances in the Chemistry and Physics of Materials*, pp. 55-77 (2019)**
https://doi.org/10.1142/9789811211331_0003

